THEORETICAL AND COMPUTATIONAL MODELLING OF WETTING PHENOMENA IN SMOOTH GEOMETRIES

ÉLFEGO RUIZ GUTIÉRREZ

PhD

2017

Theoretical and Computational Modelling of Wetting Phenomena in Smooth Geometries

Élfego Ruiz Gutiérrez

A thesis submitted in partial fulfilment
of the requirements of the
University of Northumbria at Newcastle
for the degree of
Doctor of Philosophy

Research undertaken in the
Faculty of Engineering and Environment

December 2017

Abstract

Capillarity and wetting are the study of the interfaces that separate immiscible fluids and their interaction with solid surfaces. The interest in understanding capillary and wetting phenomena in complex geometries has grown in recent years. This is partly motivated by applications, such as the micro-fabrication of surfaces that achieve a controlled wettability, but also because of the fundamental role that the geometry of a solid surface can play in the statics and dynamics of liquids that come into contact with it.

In this work, the statics and dynamics of liquids in contact with smooth, but non-planar geometries is studied. The approach is theoretical, and include mathematical modelling and numerical simulations using a new lattice-Boltzmann simulation method. The latter can account for solid boundaries of arbitrary geometry and a variety of boundary conditions relevant to experimental situations.

The focus is directed to two model systems. First, an analysis on the statics and dynamics of a droplet inside wedge is performed, this is accomplished by proposing the shape of the droplet, a new shape that will be referred in this document as a "liquid barrel". Using this assumption, the static position and shape of the droplet in response to an external body force is predicted. Then, the analysis is extended to include to dynamical situations in the absence of external forces, in which the translational motion of the liquid barrel towards equilibrium it is described. The proposed analytical model was validated by comparison with full 3D lattice-Boltzmann simulations and with recent experimental results. The applicability of these ideas is materialised with the purpose of achieving energy-invariant manipulation of a liquid barrel in a reconfigurable wedge.

As a second model system, the evaporation of a sessile droplet in contact with a wavy solid surface was studied. Due to the non-planar solid topography, the droplet position in equilibrium is restricted to a discrete set of positions. It is shown that when the amplitude of the surface is sufficiently high, the droplet can suddenly readjust its shape and location to a new equilibrium configuration. These events occur in a time-scale much shorter than the evaporation time-scale, a "snap". With numerical simulations and theoretical analysis, the study reveals the causes for the snap transitions, which lie in shape bifurcations of the droplet shapes, The analysis and results are compared against recent experiments of droplets evaporating on smooth sinusoidal surfaces.

With the advent of low-friction surfaces, in which static friction is practically absent, the mobility of droplets is close to ideal, and with this, predicting and controlling them in static cases becomes a challenge. The analysis and results presented in this work can be used for manipulating the position and defining the shape of droplets via the geometry of their confinements.

Contents

Acknowledgements

I would like to express my sincere gratitude to my principal supervisor Dr. Rodrigo Ledesma Aguilar for continuous support, patience and guidance during my PhD study, and for having interesting discussions. I would also like to thank my second supervisor Prof. Glen McHale for support and valuable comments.

I would like to extend my gratitude to Northumbria University for providing me with the scholarship and facilities to carry out my research, and for the financial support that allowed me to attend conferences.

A big thank to colleagues and members of staff: Dr. Gary Wells and Dr. Ciro Semprebon and Dr. Nicasio Geraldi, and PhD students: James Guan, Xinya Xu, Arezoo Amirkhalili, Lamine Mohamadi, Khald Werfli, and Bethany Orme, for their collaborations, friendship and support.

My special thanks to my family: my wife, daughter, parents, and brother for their unconditional love and kindness and continuous support. Many thanks to Prof. Rafael Ángel Barrio Paredes, for his early teachings in Physics.

Declaration

I declare that the work contained in this thesis has not been submitted for any other award and that it is all my own work. I also confirm that this work fully acknowledges opinions, ideas and contributions from the work of others. The work was done in collaboration with the *Smart Materials and Surfaces Laboratory* in Northumbria University.

Any ethical clearance for the research presented in this thesis has been approved. Approval has been sought and granted by the University Ethics Committee on the 27th of October 2015.

I declare that the word count of this thesis is 42,286 words.

Name:

_____

Date:

_____

Introduction

The interest for understanding capillary phenomena has grown in recent years. This can be attributed to the increasing number of applications that require a precise control and manipulation of small volumes of fluids [1] and to the micro-fabrication of surfaces that achieve controlled wettability [2]. At small scales, surface forces become comparable, or even dominant, to volume forces. Therefore, capillarity, which studies the effects of the interfaces of multicomponent fluids, becomes a key aspect in the behaviour of these systems [3].

The forces that the interface of two liquids produce have drawn the attention of many renowned mathematicians and scientists; attempts of a formal description of this phenomenon can be traced back to the 18th century [4]. Interfacial forces are one of the most astonishing manifestations of forces at a microscopic level, but are also elusive and difficult to treat. A major breakthrough in the modern theory of capillarity is due to van der Waals [5]. In his doctoral thesis, he modelled the concentration of molecules by a mean field approximation which led him to predict that the interface of a liquid coexisting with a gas is necessarily smooth and that it carries an energy cost which is now understood as surface energy or surface tension.

In order to minimise their surface energy, liquids can acquire stable closed shapes without a container. As a requirement, the interface must have a constant mean curvature [3], this implies the existence of an underlying symmetry in the surface energy. Depending on the physical constraints, the energy in equilibrium of a capillary system may be invariant upon a continuous or a discrete transformation. In this work two possibilities are explored: a droplet bridging two non-parallel planes, exhibiting energy invariance upon continuous variation of the angle between the planes, and a sessile droplet on a wavy surface, which relaxes to equilibrium by centring itself at either a peak or a trough in the topography. Although these systems appear in a number of real-life situations, their study, from a Theoretical Physics perspective, has remained relatively unexplored. Moreover, they constitute archetypes whose understanding can lead to advances in more complex situations.

The relevant aspects of the Theory of Capillarity that will give the foundations of our analytical and numerical models is summarised in §1. This includes the thermodynamic and mechanical aspects of capillarity.

In §2, a description and validation of the computer simulations that will be used is presented as part of the methodology. For that, the lattice-Boltzmann method (LBM) was chosen, which is a well-established numerical method that has proven to give an accurate description when it comes to the details at a small scale for the behaviour of liquids or gases and their interaction [6, 7, 8]. The LBM was enhanced to model open boundaries and a new algorithm was introduced to model the wetting behaviour on solid surfaces of an arbitrary shape.

Then, for the system exhibiting continuous symmetry, in Part I, an analysis of the statics and dynamics of a droplet inside a wedge is conducted. This analysis allows to understand ways of manipulating droplets as a direct application. The analysis begins in §3, by proposing the shape of the droplet: the *liquid barrel*. Then, in §4 numerical simulations to validate the liquid barrel assumption are carried out. The simulations also reveal further details of the motion of the droplet. In §5, the analytical model is compared against experimental results to later on propose a direct application to these ideas.

In Part II, a system that exhibits a discrete symmetry is studied: a sessile droplet on a wavy surface. Due to the patterned topography, the droplet finds equilibrium at a discrete set of positions that depend on its volume. As a consequence, if the droplet is changing in volume, it is observed to spontaneously reconfigure its shape and location to find equilibrium, in a *snap*. In §6, lattice-Boltzmann simulations are carried out to study this system, and in §7 an analytical model to study constructed with the aim of revealing the causes for the snap transitions.

Finally, the general conclusions of this work are presented.

Chapter 1

Review of the Theory of Capillarity

1.1 Thermodynamics of Multiphase Fluids

Capillarity is the study of the interfaces between two immiscible fluids [3]. A starting point for understanding capillarity is the thermodynamics of phase separation.

Consider a system composed of molecules of two different species. The components can be labelled by an *order parameter*, ϕ, which is defined as

$$\phi \stackrel{\text{def}}{=} \frac{n_2 - n_1}{n_2 + n_1}, \tag{1.1}$$

where n_1 and n_2 are the particle number densities of the two species [9, 10]. The intermediate values of the order parameter describe the relative concentrations of species in a mixture. This concept can be used to describe single component fluids that undergo a phase transition, in such a case, n_1 and n_2 correspond to the densities, e.g., of the vapour and liquid phases, respectively.

In a fluid, the molecules are free to move and interact with each other through collisions. If attractive interactions between two molecules of different species are weaker than same-species interactions, the mixed state will have a higher energy compared to the pure states [11, 12]. Therefore, mixed states are less stable, and, the system separates into pure phases.

The thermal equilibrium of the system occurs when the temperature, T, pressure, p, and chemical potential, μ, are equal in the two phases [11, 13]. To obtain the thermodynamic quantities of the equilibrium state, Maxwell's construction rule can be applied to the μ–ϕ isotherm (see figure 1.1(a)) [14].[1]

Equivalently, equilibrium is reached when the Helmholtz free energy, $F = F(\phi, T)$, which is the relevant thermodynamic potential for fixed volume and temperature situations, is minimised. For a given number of molecules, the stationary values in the free energy are obtained by writing

$$\mathrm{d}[F(\phi, T) - \mu_0 \phi] = 0, \tag{1.2}$$

where μ_0 is a Lagrange multiplier that is introduced to satisfy the constraint of a conserved order parameter. As a consequence, Eq. 1.2 shows that $\mu_0 = \mathrm{d}F/\mathrm{d}\phi$, is the chemical

[1] Maxwell's construction or equal-area rule is usually applied to the p–v isotherm, where v is the specific volume; however, if the control parameter is ϕ, the same procedure can be applied to the isotherm of its conjugate variable, μ.

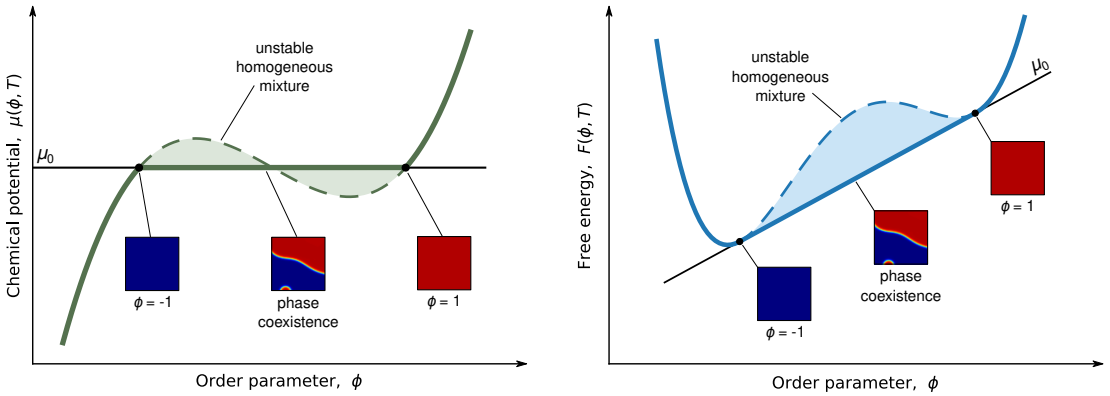

(a) (b)

Figure 1.1: (b) The chemical potential and (a) the Helmholtz free energy of a binary mixture. The homogeneous mixture (dashed curves) has a higher energy than the inhomogeneous mixture (thick line). The equilibrium chemical potential, μ_0, is such that the signed area of the shaded region is zero.

potential of the coexisting phases, which is represented by the slope of the line that interpolates the two pure states (see figure 1.1(b)).

1.1.1 The Sharp-Interface Approximation

In the sharp-interface approximation, the Helmholtz free energy of a capillary system is defined by [3, 15, 4],

$$\mathrm{d}F \overset{\text{def}}{=} S\mathrm{d}T - p\mathrm{d}V + \mu\mathrm{d}N + \gamma\mathrm{d}A, \tag{1.3}$$

where S, V, and N are the entropy, volume and number of particles, and γ and A are the *surface tension* and surface area of the interface, respectively. The first three terms in Eq. (1.3) give the usual bulk contributions of the coexisting phases as described before, whereas the last term corresponds to the energy cost for increasing the interface area by $\mathrm{d}A$. If creation of surface area results in work, then, γ, is also a force per unit length that pulls in direction parallel to the interface.

In a gently curved interface, surface tension produces a net force density,

$$\boldsymbol{f} = -2\gamma\kappa\hat{\boldsymbol{n}}_\mathrm{i}, \tag{1.4}$$

where $\hat{\boldsymbol{n}}_\mathrm{i}$ is the orthonormal vector to the interface, and $\kappa = \boldsymbol{\nabla}\cdot\hat{\boldsymbol{n}}_\mathrm{i}/2$ its mean curvature (see figure 1.2(a)) [16]. Therefore, in equilibrium, $\boldsymbol{f}$ is balanced by a change in pressure, Δp, which leads to the Young-Laplace condition [3, 16],

$$\Delta p = 2\gamma\kappa. \tag{1.5}$$

With the change in the pressure, the chemical potential varies accordingly by

$$\Delta\mu = -\frac{2\gamma\kappa}{\Delta\phi}, \tag{1.6}$$

where $\Delta\phi$ is the change of the order parameter across the interface. Eq. (1.6) is called the Gibbs-Thomson condition [17, 16].

The contact of a fluid phase with a solid surface creates an interface, and with it, a surface tension, γ_sf, thus adding the term $\gamma_\mathrm{sf}\mathrm{d}A_\mathrm{sf}$ to the free energy. If two coexisting fluids, e.g., 1 and 2, come in contact with a solid, the three interfaces meet at the *triple line* (also called *contact line*). The angle of intersection of the fluid-fluid interface with respect to the solid is called the *contact angle*, θ. At the contact line, the three surface tensions compete. Then, equilibrium is possible if the forces balance (see figure 1.2(b)), i.e.,

$$\gamma\cos\theta_\mathrm{e} = \gamma_{\mathrm{s}2} - \gamma_{\mathrm{s}1}, \tag{1.7}$$

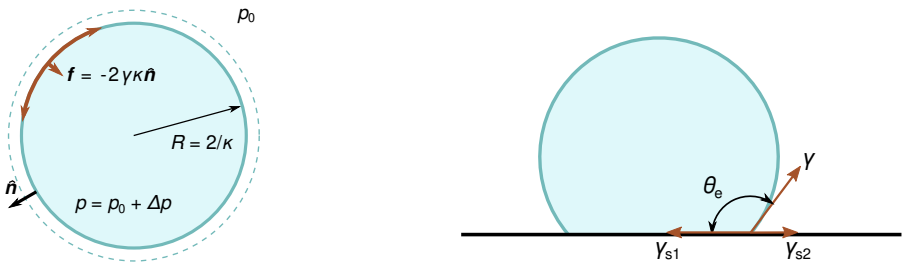

(a) (b)

Figure 1.2: Illustration of (a) the Laplace pressure inside a spherical droplet and (b) the equilibirum contact angle of a sessile droplet.

where θ_e is the *equilibrium contact angle*. Eq. (1.7) is called the Young-Drupé relation [18].

In situations where the temperature, number of molecules and volume are constant, the free energy of two immiscible liquids in contact with a solid becomes

$$F = \gamma A - \gamma A_{s1} \cos\theta_e + \text{const.}, \tag{1.8}$$

where A and A_{s1} are the surface areas the fluid-fluid and the solid-fluid (phase 1) interfaces. To produce Eq. (1.8), Eqs. (1.3) and (1.7) are combined, it is also assumed that the total surface area of the solid is constant. In the absence of the constant term, Eq. (1.8) will be refer to as the *interfacial energy*.

1.1.2 The Diffuse-Interface Approximation

In reality, the transition between one phase to another cannot be infinitely sharp. Molecules have an interaction potential energy which gradually fades out. In addition, due to thermal fluctuations, the molecules of a liquid cannot remain packed. This implies that a sharp interface cannot be in equilibrium [4], and consequently, the order parameter must change smoothly, over a distance that depends on the range of interactions between molecules. This characteristic length, which defines the width of a fluid-fluid interface, has been measured to be only a few nanometres across for simple liquids and gases [4, 17, 19, 20]. Consequently, for many practical purposes, the sharp-interface formalism is a good approximation to treat capillary systems. However, it will be shown that there are factors at the microscopic level that influence the physics at large scale [17], most notably, in the motion of the contact lines. Therefore, a microscopic description is also necessary.

The long-range effects of the interaction between molecules is captured by considering an energy contribution due to spatial variations in the order parameter [21, 16]. Therefore, $\phi = \phi(\boldsymbol{x})$, is now a scalar field, also called, the *phase field*. Henceforth, the Helmholtz free energy of a binary mixture must depend on the phase field and on its gradients, i.e.,

$$F[\phi(\boldsymbol{x})] = \int_\Omega \psi(\phi, \boldsymbol{\nabla}\phi)\, \mathrm{d}V + \int_{\partial\Omega} \zeta(\phi)\, \mathrm{d}S. \tag{1.9}$$

The first term is the volumetric contribution to the energy of the fluid mixture contained in a domain Ω. The second term is the contribution due to the interaction of fluid molecules in contact with a bounding surface, $\partial\Omega$ (e.g., a solid wall).

The free-energy density, ψ, in Eq. (1.9), can be modelled as [20, 19, 21]

$$\psi(\phi, \boldsymbol{\nabla}\phi) = \frac{1}{4}B(\phi^2 - 1)^2 + \mu_0\phi - p_0 + \frac{1}{2}K|\boldsymbol{\nabla}\phi|^2, \tag{1.10}$$

where B and K are a constants, and μ_0 and p_0 are the reference chemical potential and pressure. The first term in Eq. (1.10) is *excess free energy*, and gives the energy contributions of short range interactions. The excess free energy, together with the next two terms in Eq. (1.10), reproduce the dashed curve in figure 1.1(a) which corresponds to the energy of a uniform binary system. The last term of Eq. (1.10) models the free energy contribution due to phase-field gradients.

From Eq. (1.9), it is possible to calculate the chemical potential field,

$$\mu(\boldsymbol{x}) \overset{\text{def}}{=} \frac{\delta F}{\delta \phi} \tag{1.11}$$

$$= \mu_0 + B\phi(\phi^2 - 1) - K\nabla^2\phi, \tag{1.12}$$

and the pressure tensor field, [19, 15],

$$\mathbf{P}(\boldsymbol{x}) \stackrel{\text{def}}{=} [\,\phi\mu - \psi\,]\,\mathbf{I} + K\boldsymbol{\nabla}\phi\boldsymbol{\nabla}\phi \tag{1.13}$$

$$= \left[p_0 + \frac{1}{4}B(\phi^2-1)(3\phi^2+1) - K\phi\nabla^2\phi - \frac{1}{2}K|\boldsymbol{\nabla}\phi|^2\right]\mathbf{I} + K\boldsymbol{\nabla}\phi\boldsymbol{\nabla}\phi, \tag{1.14}$$

where $\mathbf{I}$ is the identity matrix.

For two phases separated by a flat interface in equilibrium, $\mu(\boldsymbol{x}) = \mu_0$ and $\boldsymbol{\nabla}\cdot\mathbf{P} = 0$. Thus, the distribution of the phase field follows after solving the differential equations; one finds the equilibrium profile

$$\phi(x) = \tanh\left[\frac{x}{\sqrt{2}\ell}\right], \tag{1.15}$$

where x is the normal coordinate to the interface, and

$$\ell \stackrel{\text{def}}{=} \sqrt{K/B}, \tag{1.16}$$

is the *interface thickness* (see figure 1.3(a)).

For a flat interface profile (Eq. (1.15)), one finds that the pressure tensor, $\mathbf{P}$, can be decomposed into two different quantities: the pressure component normal to the interface $P_\perp = \mathbf{P}_{xx}$, and the pressure component tangential to the interface $P_\parallel = \mathbf{P}_{yy} = \mathbf{P}_{zz}$, all other components of the pressure tensor are zero. Using the solution of Eq. (1.15), these read

$$P_\perp(x) = p_0, \tag{1.17}$$

which gives the equilibrium pressure of the mixture, and

$$P_\parallel(x) = p_0 - \frac{1}{2}B\cosh^{-4}\left[\frac{x}{\sqrt{2}\ell}\right]. \tag{1.18}$$

As discussed in §1.1.1, $P_\parallel$ corresponds to a pulling force per unit length by the interface (see figure 1.3(b)).

The transition from one phase to the other has an energy cost, [20]

$$\gamma \stackrel{\text{def}}{=} \int_{-\infty}^{\infty}\left[\psi(\phi,\boldsymbol{\nabla}\phi) - \mu_0\phi + p_0\right]\mathrm{d}x. \tag{1.19}$$

This is the energy per unit area which is identified as the surface tension. For the flat interface profile, this results in

$$\gamma = \frac{2}{3}\sqrt{2KB}, \tag{1.20}$$

Graphically, this is equal to twice the shaded region in figure 1.1(a) and also equal between the curves $P_\perp$ and $P_\parallel$ in figure 1.3(b), i.e., one can also define the surface tension as [22, 23]

$$\gamma \stackrel{\text{def}}{=} \int [P_\perp(x) - P_\parallel(x)]\,\mathrm{d}x. \tag{1.21}$$

Moreover, for gently curved interfaces, $\kappa \ll \ell^{-1}$, it can be shown that the Young-Laplace (Eq. (1.5)) and Gibbs-Thomson (Eq. (1.6)) laws are reproduced [15, 24].

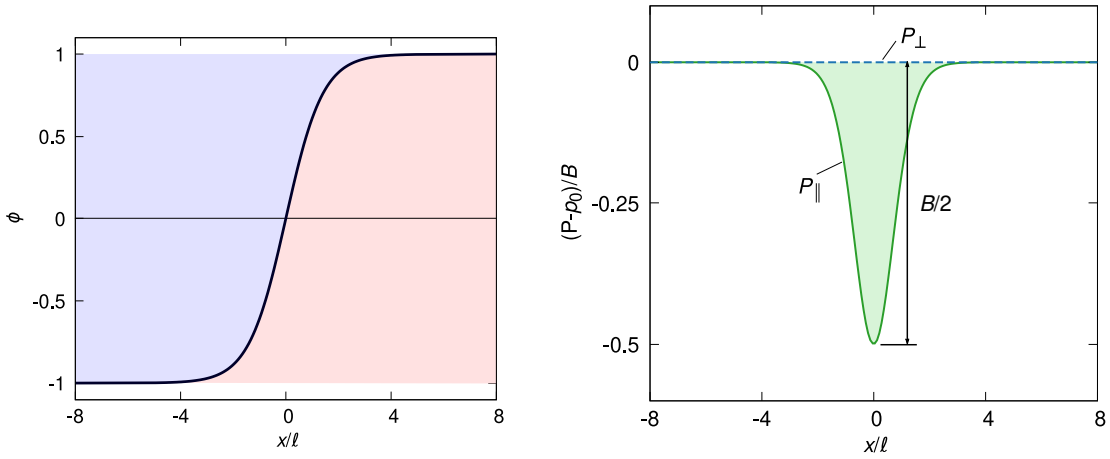

(a) (b)

Figure 1.3: Profiles of (a) the order parameter and (b) the components of the pressure tensor in the neighbourhood of a flat interface.

The second term in Eq. (1.9) is the surface contribution to the free energy, where $\zeta(\phi)$ is the binding energy of the fluid to the solid, i.e. [25, 26]

$$\zeta(\phi) = -\chi\,\phi, \tag{1.22}$$

where the constant χ, called the *wetting potential*, controls the energy cost incurred when the fluid phases come in contact with a solid boundary. Using the standard tools of Variational Calculus, this results in the equilibrium boundary condition,

$$K\hat{\boldsymbol{n}}\cdot\boldsymbol{\nabla}\phi = \chi, \tag{1.23}$$

where $\hat{\boldsymbol{n}}$ is the normal vector to the surface pointing towards the solid.

Eq. (1.23) has the effect of altering the profile of the order parameter in the vicinity of a boundary. It induces an increment in the energy of the fluid that is proportional to the contact area with the solid [25, 26], i.e., the surface tension of the solid with a fluid phase. In equilibrium, one can show that the solid-fluid surface tensions obey

$$\gamma_{s\pm} = \frac{\gamma}{2}\left[1 - \left(1 \pm \frac{4\chi}{3\gamma}\right)^{3/2}\right], \tag{1.24}$$

where the $+$ $(-)$ sign corresponds to phase 2 (1). Due to Eq. (1.13), it can be observed that the component of the pressure tensor parallel to the solid surface produces an effective pulling force per unit length, $\gamma_{s\pm}$. From the balance of forces and the Young-Dupré relation (Eq. (1.7)), the wetting potential be can expressed in terms of the contact angle, θ_e,

$$\chi(\theta_e) = \frac{3}{2}\,\gamma\,\mathrm{sgn}(\pi/2 - \theta_e)\left\{\alpha(\theta_e)\left[1 - \alpha(\theta_e)\right]\right\}^{1/2}, \tag{1.25}$$

where $\alpha(\theta_e) = \cos[\arccos(\sin^2\theta_e)/3]$ [25, 26].

1.2 Dynamics of Capillary Systems

1.2.1 The Navier-Stokes and Cahn-Hilliard Equations

Out of equilibrium, a gradient in the chemical potential will cause a diffusive current $-M\boldsymbol{\nabla}\mu$, where the constant M is called the mobility. In addition, the phase field will be advected by the velocity field, $\boldsymbol{u}$. Therefore, the local conservation of ϕ is given by the Cahn-Hilliard equation [20, 16]:

$$\partial_t \phi + \boldsymbol{u} \cdot \boldsymbol{\nabla}\phi = M\nabla^2\mu. \tag{1.26}$$

The local conservation of momentum is governed by the Navier-Stokes equation, i.e.,

$$\rho(\partial_t \boldsymbol{u} + \boldsymbol{u} \cdot \boldsymbol{\nabla}\boldsymbol{u}) = -\boldsymbol{\nabla} \cdot \mathbf{P} + \eta\nabla^2\boldsymbol{u} + \boldsymbol{f}, \tag{1.27}$$

where ρ and η are the local density and dynamic viscosity of the fluid, $\boldsymbol{f}$ is an external force [27], and incompressibility is assumed, i.e.,

$$\boldsymbol{\nabla} \cdot \boldsymbol{u} = 0, \tag{1.28}$$

The local fluid mass density and kinematic viscosity, $\nu \stackrel{\text{def}}{=} \eta/\rho$, is defined in terms of the phase field *via* the profiles

$$\rho(\boldsymbol{x}) = \frac{\rho_2 - \rho_1}{2}\phi(\boldsymbol{x}) + \frac{\rho_2 + \rho_1}{2}, \tag{1.29}$$

and

$$\nu(\boldsymbol{x}) = \frac{\nu_2 - \nu_1}{2}\phi(\boldsymbol{x}) + \frac{\nu_2 + \nu_1}{2}, \tag{1.30}$$

where ρ_1, ρ_2, ν_1, and ν_2 are the saturation mass densities and kinematic viscosities of phases 1 and 2.

1.2.2 Energy and Dissipation

The total energy of a coexisting fluid mixture in motion is the sum of the kinetic energy and the Helmholtz free energy [27], i.e.,

$$\mathcal{E} = \frac{1}{2}\int_\Omega \rho(\boldsymbol{x})\, u^2(\boldsymbol{x})\, \mathrm{d}V + F[\phi(\boldsymbol{x})], \tag{1.31}$$

where $u = |\boldsymbol{u}|$. As the fluid moves, energy will be dissipated to the surroundings. The rate of change in the energy, $\dot{\mathcal{E}}$, can be obtained by writing the time derivative of $\mathcal{E}$ in terms of $\dot{\phi}$ and $\dot{\boldsymbol{u}}$. Then, using the equations of motion (Eqs. (1.26) and (1.27)), $\dot{\mathcal{E}}$ can be expressed as:

$$\begin{aligned}\dot{\mathcal{E}} = &-\int_\Omega \left\{\frac{1}{2}\eta\, \mathbf{D} : \mathbf{D} + M|\boldsymbol{\nabla}\mu|^2\right\} \mathrm{d}V \\ &-\int_{\partial\Omega} \left\{\left[\frac{1}{2}\rho\, u^2 \mathbf{I} + \mathbf{P} - \eta\, \mathbf{D}\right] \cdot \boldsymbol{u} - M\mu\boldsymbol{\nabla}\mu\right\} \cdot \hat{\boldsymbol{n}}\, \mathrm{d}S,\end{aligned} \tag{1.32}$$

where $\mathbf{D} \stackrel{\text{def}}{=} \boldsymbol{\nabla}\boldsymbol{u} + \boldsymbol{\nabla}\boldsymbol{u}^T$, is called the *deformation tensor* [9]. The first integral in Eq. (1.32) is a volume integral and corresponds to the total energy dissipation in the bulk of the

fluid due to viscous friction and diffusion. The second integral in Eq. (1.32) is a surface integral and is composed by two terms. The first of these corresponds to the flow of mechanical energy at the boundary. The second term in the integrand corresponds to change in energy due to the flow of the chemical potential across the boundary (e.g., due to gain or loss of molecules). Often, the system might be closed, thus, energy exchange with its surroundings is impossible. Then, the surface integral in Eq. (1.32) vanishes, and dissipation occurs due to viscosity and diffusion in the bulk.

1.2.3 Flow Due to Interfaces

In the sharp-interface formalism, the domain of the fluid mixture is subdivided into separate phases. From a dynamical point of view, the interface is a surface of concentrated capillary force, $\boldsymbol{f}$. Each of this subdomains must be treated separately, however, they must be joined by adequate boundary conditions. One condition states that the velocity of the flow must be continuous across the interface, and thus, [28, 29]

$$\Delta \boldsymbol{u}(\boldsymbol{x}_\mathrm{i}) = 0, \tag{1.33}$$

where Δ represents the discontinuity at the interface point, $\boldsymbol{x}_\mathrm{i}$. Eq. (1.33) also describes the boundary condition at a fluid-solid surface. On the other hand, the capillary forces have an effect on the stresses of a free interface and produce a discontinuity [27, 29] given by

$$\Delta p(\boldsymbol{x}_\mathrm{i}) - \Delta(\eta \mathbf{D})(\boldsymbol{x}_\mathrm{i}) : \hat{\boldsymbol{n}}_\mathrm{i}\hat{\boldsymbol{n}}_\mathrm{i} = 2\gamma\kappa. \tag{1.34}$$

The first term in the left-hand side of Eq. (1.34) corresponds the pressure jump across the interface, and the second term, gives the discontinuity due to viscous stresses. For a fluid at rest, where $\mathbf{D} = 0$, Eq. (1.34) reduces to the Young-Laplace condition (see Eq. (1.5)).

1.2.4 Overdamped Flow

If the flow is characterised by a low Reynolds number, $Re \overset{\text{def}}{=} \rho U L/\eta \ll 1$, where U and L are the characteristic velocities and length-scales of the capillary system, the inertial terms in the Navier-Stokes equation (left-hand side of Eq. (1.27)) can be neglected, this is called the overdamped regime [30, 27, 28]. In such a case, the Navier-Stokes equations reduce to

$$0 = -\boldsymbol{\nabla} p + \eta \nabla^2 \boldsymbol{u} + \boldsymbol{f}, \tag{1.35}$$

$$0 = \boldsymbol{\nabla} \cdot \boldsymbol{u}. \tag{1.36}$$

Eq. (1.35) is called the Stokes equation. In the absence of external forces ($\boldsymbol{f} = 0$), if follows after taking the divergence of Eq. (1.35), that the pressure is a harmonic function, i.e.,

$$\nabla^2 p = 0. \tag{1.37}$$

Analogously, the *vorticity*, $\boldsymbol{\omega} \overset{\text{def}}{=} \boldsymbol{\nabla} \times \boldsymbol{u}$, which is a measure of the rotation of the flow, is also a harmonic function, i.e.,

$$\nabla^2 \boldsymbol{\omega} = 0. \tag{1.38}$$

Eqs (1.35)—(1.38) form a linear set of partial differential equations for the vector field, $\boldsymbol{u}(\boldsymbol{x})$, and the scalar field, $p(\boldsymbol{x})$. This implies that, the superposition of solutions can be

Table 1.1: List of free-space Green functions for the linearised viscous flow for two and three dimensions. ($\tilde{x} = |\tilde{\boldsymbol{x}}|$, $\tilde{\boldsymbol{x}} \stackrel{\text{def}}{=} \boldsymbol{x}' - \boldsymbol{x}$, and ε is the Levi-Civita symbol.)

	$\mathbf{G}(\boldsymbol{x}, \boldsymbol{x}')$	$\boldsymbol{p}(\boldsymbol{x}, \boldsymbol{x}')$	$\boldsymbol{\Omega}(\boldsymbol{x}, \boldsymbol{x}')$	$\mathbf{T}(\boldsymbol{x}, \boldsymbol{x}')$
2D	$-\mathbf{I}\log\tilde{x} + \frac{\tilde{\boldsymbol{x}}\tilde{\boldsymbol{x}}}{\tilde{x}^2}$	$2\frac{\tilde{\boldsymbol{x}}}{\tilde{x}^2}$	$2\varepsilon\cdot\frac{\tilde{\boldsymbol{x}}}{\tilde{x}^2}$	$-4\frac{\tilde{\boldsymbol{x}}\tilde{\boldsymbol{x}}\tilde{\boldsymbol{x}}}{\tilde{x}^4}$
3D	$\frac{\mathbf{I}}{\tilde{x}} + \frac{\tilde{\boldsymbol{x}}\tilde{\boldsymbol{x}}}{\tilde{x}^3}$	$2\frac{\tilde{\boldsymbol{x}}}{\tilde{x}^3}$	$2\varepsilon\cdot\frac{\tilde{\boldsymbol{x}}}{\tilde{x}^3}$	$-6\frac{\tilde{\boldsymbol{x}}\tilde{\boldsymbol{x}}\tilde{\boldsymbol{x}}}{\tilde{x}^5}$

applied, and with this, a *Green function*, can be defined. For example, the flow field due to a point force $\boldsymbol{f}(\boldsymbol{x}) = \boldsymbol{f}_0\delta(\boldsymbol{x} - \boldsymbol{x}')$, is given by

$$\boldsymbol{u}(\boldsymbol{x}) = \frac{1}{8\pi\eta}\mathbf{G}(\boldsymbol{x} - \boldsymbol{x}')\cdot\boldsymbol{f}_0, \tag{1.39}$$

where $\delta(\boldsymbol{x})$ is the three-dimensional Dirac delta function and $\mathbf{G}$ is the Green function. Similarly, the vorticity, pressure and stress tensor fields are given by,

$$\boldsymbol{\omega}(\boldsymbol{x}) = \frac{1}{8\pi\eta}\boldsymbol{\Omega}(\boldsymbol{x} - \boldsymbol{x}')\cdot\boldsymbol{f}_0, \tag{1.40}$$

$$p(\boldsymbol{x}) = \frac{1}{8\pi}\boldsymbol{p}(\boldsymbol{x} - \boldsymbol{x}')\cdot\boldsymbol{f}_0, \tag{1.41}$$

$$\boldsymbol{\Sigma}(\boldsymbol{x}) = \frac{1}{8\pi}\mathbf{T}(\boldsymbol{x} - \boldsymbol{x}')\cdot\boldsymbol{f}_0. \tag{1.42}$$

The corresponding Green functions, $\mathbf{G}$, $\boldsymbol{\Omega}$, $\boldsymbol{p}$, and $\mathbf{T}$, are summarised in table 1.1

1.2.5 Contact-Line Dynamics

A fundamental aspect of the theory of capillarity is the motion of contact lines [18, 31, 32, 33]. To formulate this problem, let us begin with the sharp-interface formalism.

Consider a fluid-fluid interface of characteristic length-scale ℓ_{M}, reaching a solid surface, and suppose fluid 1 is displacing fluid 2. Let us assume a stationary regime so that the contact line is moving at a constant velocity, v_{cl} (see figure 1.4) [34].

If adhesion of the fluid molecules with the solid is expected, the fluid is at rest with respect to the wall, this would require that the velocity of a contact line, v_{cl}, should vanish [35]. Under this assumption, the motion of the contact line would be impossible, in other words, the displacement of the contact line would produce an infinite stress [36]. To alleviate this singularity, it has been proposed to allow the fluids to slide over the solid surface [37] in a small region near the contact line of a characteristic length-scale, ℓ_{m} [34, 35]. Moreover, v_{cl} is considered small enough so that the contact angle is in equilibrium at the microscopic level. Nonetheless, further away from the contact line, the slope of the interface will vary due to its local curvature until reaching ℓ_{M} where the *dynamic contact angle* is defined.

According to Cox [34] and Voinov [35], the flow field shows a rolling structure (see figure 1.4) (as described in the seminal experiments by Dussan and Davis [32, 36, 38]); the flow is described by the relation [34, 35]

$$\int_{\theta_{\mathrm{e}}}^{\theta}\frac{\mathrm{d}\vartheta}{f_{\mathrm{CV}}(\vartheta, \eta_2/\eta_1)} = \frac{\eta_1 v_{\mathrm{cl}}}{\gamma}\log\frac{\ell_{\mathrm{M}}}{\ell_{\mathrm{m}}}, \tag{1.43}$$

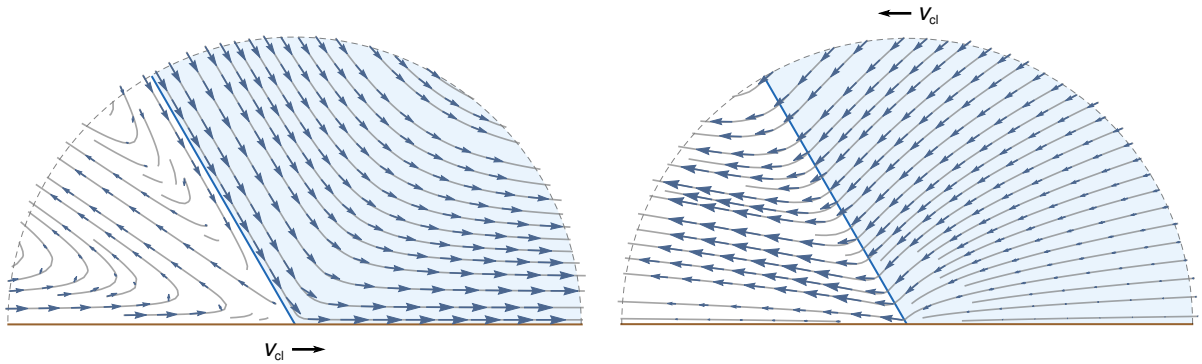

(a) (b)

Figure 1.4: Flow structure in the vicinity of a contact line, for a liquid (blue phase) and a gas (white phase) of negligible viscosity ($\eta_2 = 0$). (a) Shows the flow velocity in the reference frame of the triple line, therefore the solid surface moves at velocity $v_{\rm cl}$ to the right; and (b) is settled in the reference frame of the solid, where the contact line is advancing at $v_{\rm cl}$ to the left. The stream lines are depicted in grey and the magnitude of the velocity field is plotted as blue arrows.

that predicts the dynamic contact angle, θ, for a given velocity of the contact line, $v_{\rm cl}$, where

$$f_{\rm CV}(\vartheta,\lambda) = \frac{2\sin\vartheta[\lambda^2(\vartheta^2-\sin^2\vartheta)+2\lambda\{\vartheta(\pi-\vartheta)+\sin^2\vartheta\}+\{(\pi-\vartheta)^2-\sin^2\vartheta\}]}{\lambda(\vartheta^2-\sin^2\vartheta)\{(\pi-\vartheta)+\sin\vartheta\cos\vartheta\}+\{(\pi-\vartheta)^2-\sin^2\vartheta\}(\vartheta-\sin\vartheta\cos\vartheta)}, \tag{1.44}$$

and η is the viscosity of the fluid from which θ is measured.

The length-scale $\ell_{\rm M}$, in Eq. (1.43), is a characteristic size beyond which the details of the Cox-Voinov flow are no longer dominant. It is expected to extend from a few micros up to a few millimetres depending on the details of the flow. On the other hand, at length-scales bellow $\ell_{\rm m}$, a purely hydrodynamic description fails to model the motion of the contact lines. Therefore, a complementary theory is required to continue the description of the physics at smaller scales, and thus set a value of $\ell_{\rm m}$ depending on properties of the fluids involved and the microscopic structure of the solid surface [33].

To continue the analysis from here on, a theory that models the behaviour of the contact line at the microscopic level is necessary; this leads to the diffuse-interface formalism. Within the diffuse-interface model, the motion of the contact line occurs by virtue of diffusive currents caused by a local imbalance in the chemical potential field [39]. This is because, while the velocity field vanishes at the solid-fluid interface by virtue of Eq. (1.33), the diffusive term in Eq. (1.26) does not. This regularises the singularity that stems from the no-slip boundary condition [40]. More specifically, a distortion of the equilibrium configuration of the contact line will cause a change in the chemical potential $\Delta\mu$ according to the Gibbs-Thomson condition (see Eq. (1.6)). From Eq. (1.26), a small peak in the chemical potential will result in the local evaporation of the phase field, whereas a dimple will lead to condensation. As shown by [26], the combination of both features leads to a region where the contact line "slips" past the solid surface, thus, identifying the origin of $\ell_{\rm m}$ [40, 41, 42, 43].

Several authors have studied the dependence of $\ell_{\rm m}$ on the diffuse-interface model parameters [41, 42, 44, 40]. Kusumaatmaja [45] showed the existence of two scaling

regimes in relation to the interface width, ℓ, the mobility, M, and the average viscosity of the fluids, η:

- The *diffuse-interface regime*, which occurs if $\ell \gg (M\eta)^{1/2}$, and leads to $\ell_{\mathrm{m}} \sim (M\eta)^{1/4}$, and
- The *sharp-interface regime*, which occurs if $\ell \ll (M\eta)^{1/2}$, and leads to $\ell_{\mathrm{m}} \sim (M\eta)^{1/2}$.

In both regimes, however, the slip length obeys

$$\log \ell_{\mathrm{m}} \propto \log(M\eta) + \text{const.} \tag{1.45}$$

Apart from the hydrodynamic effect, the motion of the contact line also depends on the spreading of a submicrometre film that precedes the motion of the contact line, this is called, the *precursor film* [46, 31]. It has been found that the precursor film produces a lubricating effect and advances due to van der Waals forces between the solid and the fluid [47], and because of this, most of the spreading energy is burnt in this process. However, the precursor film does not always appear, it has been found that its development depends on the volatility of the fluids and the contact angle with respect to the solid [46, 47].

On the other hand, Blake and Haynes [33], proposed that, due to motion, the triple line becomes more diffuse. According to their model, it is predicted a the drag force, of a non-hydrodynamic origin, restricts the spreading of liquids. This force depends on the temperature and the density of absorption sites in the solid surface that are able to capture fluid molecules [48, 49, 50].

In the diffuse-interface model, a material-dependent mobility allows the chemical potential to relax [42, 41, 43, 40]. Therefore, it is the chemical potential that induce breaking of bonds between the adsorption sites of the solid surface that capture fluid molecules and therefore allows motion of the contact line [42].

All the aforementioned mechanisms motivates the inclusion of an additional drag force, f_{cl}, that acts independent of the hydrodynamic dissipation [38, 42, 41]. At low velocities, the form of f_{cl} must be proportional to the velocity of the contact line to a first approximation, i.e.,

$$f_{\mathrm{cl}} = -\zeta_0 v_{\mathrm{cl}}, \tag{1.46}$$

where ζ_0 is a contact-line friction coefficient. The value of ζ_0 depends on the transport properties of the fluids, but also on the properties of the solid [38]. In view that the contact-line motion is enhanced by the mobility, thus it is expected that the friction coefficient is of the form

$$\zeta_0 \propto \eta/M. \tag{1.47}$$

1.3 Concluding remarks

In this chapter, a condensed review of the theory of capillarity has been provided for both static and dynamic situations. First, the sharp-interface formalism is presented, which gives a sensible approximation to the diffuse-interface model of phase transitions described afterwards. Then, the equations of motion for capillary systems are provided, these are the Navier-Stokes for incompressible fluids, which stems from the conservation of momentum in continuum media, and the Cahn-Hilliard equation, which models diffusive processes

in multiphase flows. Finally, the behaviour of flows due to interfaces, which include the dynamics of contact lines is briefly discussed. With this, the theoretical background that will give base to the analysis and simulations for the following chapters has been defined.

Chapter 2

The Lattice-Boltzmann Method

2.1 General Framework

The lattice-Boltzmann method (LBM) is a fluid dynamics simulator that earns its name by numerically solving the Boltzmann equation [7, 51, 10]. The Boltzmann equation, from the Kinetic Theory of Gases, is a statistical description of the evolution of a fluid at a mesoscopic level (see figure 2.1) [52, 53]. Its main ingredient is a particle distribution function, $f(\boldsymbol{x}, \boldsymbol{v})$, that counts the mean number of particles that have certain velocity, $\boldsymbol{v}$, at a certain position in space, $\boldsymbol{x}$ [6, 54].

The discretised Boltzmann equation, also called the *lattice-Boltzmann equation* reads [55, 56, 6, 57]

$$f_q(\boldsymbol{x} + \boldsymbol{c}_q, t + 1) = f_q(\boldsymbol{x}, t) + \mathcal{J}[f], \tag{2.1}$$

where $f_q(\boldsymbol{x}, t)$ is a *particle distribution function* that represents the average number of fluid particles with position $\boldsymbol{x}$ and velocity $\boldsymbol{c}_q$ at time t; and $\mathcal{J}[f]$ is called the *collision operator*. The terms in the right-hand side of Eq. (2.1) are often referred to as the *post-collision distribution*, $f_q^\star$, i.e.,

$$f_q^\star(\boldsymbol{x}, t) \stackrel{\text{def}}{=} f_q(\boldsymbol{x}, t) + \mathcal{J}[f]. \tag{2.2}$$

Space and time are discretised, and the velocity space is restricted to a set $C = \{\boldsymbol{c}_q\}_{q=0}^{Q-1}$ (see Appendix A) where Q is the number of directions in which particles can move after a unitary time step (see figure 2.1). Therefore, C defines the neighbourhood of each lattice site, and Q its degree.

The dimension, D, of the simulation, together with the degree, Q, uniquely identifies the geometry and topology of the lattice. Therefore, the notation D-Q- is commonly used to define an LBM model, e.g., the D3Q15 model consists of a 3D lattice with 15 velocity vectors.

The collision operator, $\mathcal{J}[f]$ in Eq. (2.1), models how particle populations are re-distributed due to interactions such that it increases the entropy of the fluid and thus approaches thermodynamic equilibrium. In this work the *single-relaxation time* collision operator will be used [58], which is based on the so-called BGK approximation [59],

$$\mathcal{J}[f] = -\frac{1}{\tau_f}\left[f_q - f_q^{\mathrm{e}}\right](\boldsymbol{x}, t). \tag{2.3}$$

The time evolution of the distribution function in Eq. (2.1) consists of a collision step where f_q relaxes to an equilibrium value f_q^{e} over a time-scale determined by the collision

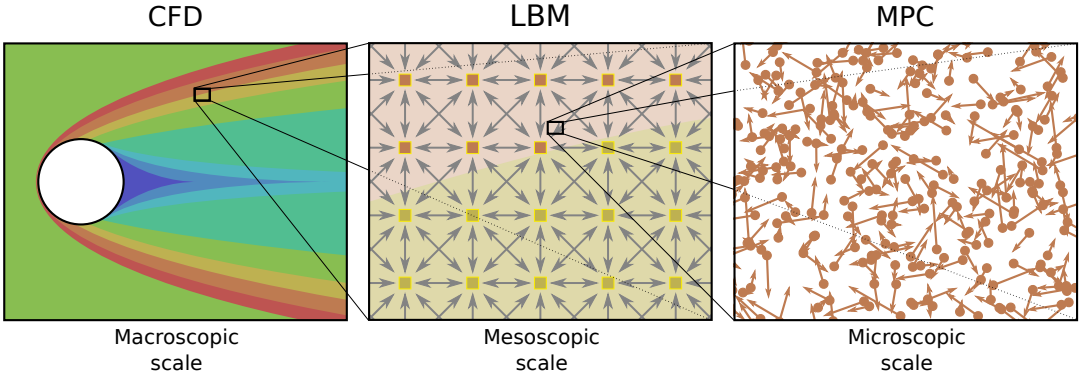

Figure 2.1: The lattice-Boltzmann is a mesoscopic method that operates at a scale between the macroscopic Computer Fluid Dynamics (CFD) and the microscopic Multi-Particle Collision (MPC) methods. It uses discrete particle populations, $f_q(\boldsymbol{x})$, (gray arrows) in a lattice (coloured squares).

parameter τ_f (Eq. (2.3)), followed by a streaming step where f_q is propagated along the direction of $\boldsymbol{c}_q$ over a unitary time increment (left-hand side of Eq. (2.1)). Over large length-scales and long time-scales the LB method integrates the macroscopic equations of motion, i.e., the Navier-Stokes and Cahn-Hilliard equations [52, 53, 6].

2.1.1 Numerical Integration of the Navier-Stokes Equation

The Navier-Stokes equation, Eq. (1.27),

$$\rho(\partial_t \boldsymbol{u} + \boldsymbol{u}\cdot\boldsymbol{\nabla}\boldsymbol{u}) = -\boldsymbol{\nabla}\cdot\mathbf{P} + \eta\nabla^2\boldsymbol{u} + \boldsymbol{f}, \tag{2.4}$$

is recovered by means of a Chapman-Enskog expansion [10, 52, 53, 60] of Eq. (2.1). The local momentum density is related to the first moment of the distribution function, i.e.,

$$\rho\boldsymbol{u} \stackrel{\text{def}}{=} \sum_q f_q \boldsymbol{c}_q. \tag{2.5}$$

The equilibrium distribution function, f_q^{e}, is constructed to convey the thermodynamic behaviour of the fluid and to ensure local mass and momentum conservation. This is done by requiring that the moments of f_q^{e} obey $\sum_q f_q^{\text{e}} = \rho$, $\sum_q f_q^{\text{e}}\boldsymbol{c}_q = \rho\boldsymbol{u}$, and $\sum_q f_q^{\text{e}}\boldsymbol{c}_q\boldsymbol{c}_q = \mathbf{P} + \rho\boldsymbol{u}\boldsymbol{u}$. A suitable choice for the equilibrium distribution is,

$$f_q^{\text{e}}(\rho,\boldsymbol{u},\mathbf{P}) \stackrel{\text{def}}{=} w_q\left[\text{tr}\mathbf{P}H_q^{(0)} + \frac{\rho\boldsymbol{u}}{c_s}\cdot H_q^{(1)} + \frac{1}{2c_s^2}\left(\mathbf{P} - c_s^2\text{tr}\mathbf{P}\,\mathbf{I} + \rho\boldsymbol{u}\boldsymbol{u}\right) : H_q^{(2)}\right] \tag{2.6}$$

for $q \neq 0$, and

$$f_0^{\text{e}}(\rho,\boldsymbol{u},\mathbf{P}) \stackrel{\text{def}}{=} \rho - \sum_{q=1}^{Q-1} f_q^{\text{e}}(\rho,\boldsymbol{u},\mathbf{P}), \tag{2.7}$$

where w_q are weighting factors determined by the geometry of the lattice [61], c_s is the speed of sound (see Appendix A), and $H_q^{(n)} = H^{(n)}(\boldsymbol{c}_q)$ is the tensor Hermite polynomial of n-th degree [10, 61, 62]. Explicitly, $H_q^{(0)} = 1$, $H_q^{(1)} = \boldsymbol{c}_q/c_s$, and $H_q^{(2)} = \boldsymbol{c}_q\boldsymbol{c}_q/c_s^2 - \mathbf{I}$.

The mass density of the fluid, $\rho(\boldsymbol{x})$, is determined by means of the phase field, $\phi(\boldsymbol{x})$, as in Eq. (1.29),

$$\rho(\boldsymbol{x}) = \frac{\rho_2 - \rho_1}{2}\phi(\boldsymbol{x}) + \frac{\rho_2 + \rho_1}{2}, \tag{2.8}$$

where ρ_i, $i = 1, 2$, are constants that correspond to the bulk densities. The Chapman-Enskog expansion provides a relation between the relaxation parameter, τ_f, and the kinematic viscosity of the fluid,

$$\nu = c_s^2(\tau_f - 1/2). \tag{2.9}$$

Therefore, τ_f can be specified, by means of Eq. (2.9), as a function of the phase field (Eq. (2.10)),

$$\nu(\boldsymbol{x}) = \frac{\nu_2 - \nu_1}{2}\phi(\boldsymbol{x}) + \frac{\nu_2 - \nu_1}{2}, \tag{2.10}$$

where ν_i, $i = 1, 2$, correspond to the kinematic viscosities.

To model a body force, $\boldsymbol{f}$, acting on the fluid, a term is included to the lattice-Boltzmann equation,

$$f_q(\boldsymbol{x} + \boldsymbol{c}_q, t + 1) = f_q(\boldsymbol{x}, t) + \mathcal{J}[f] + \Delta f_q. \tag{2.11}$$

Following Lee [7, 60], the forcing term, Δf_q, is defined as

$$\Delta f_q \stackrel{\text{def}}{=} \frac{w_q}{c_s^2}\left[1 + \frac{\boldsymbol{u}\cdot\boldsymbol{c}_q}{c_s^2} + \frac{(\boldsymbol{u}\cdot\boldsymbol{c}_q)^2}{2c_s^4} - \frac{u^2}{2c_s^2}\right](\boldsymbol{c}_q - \boldsymbol{u})\cdot\boldsymbol{f}. \tag{2.12}$$

The lattice-Boltzmann method is known to break Galilean invariance in situations where the fluid has density inhomogeneities [63]. Following Swift [10] and Holdych [64], to reduce this effect, the correction term is added

$$\boldsymbol{\Pi} = \nu\left[(\boldsymbol{u}\cdot\boldsymbol{\nabla}\rho)\,\mathbf{I} - (\boldsymbol{u}\boldsymbol{\nabla}\rho) - (\boldsymbol{u}\boldsymbol{\nabla}\rho)^T\right] \tag{2.13}$$

when calculating the equilibrium distribution function, i.e.,

$$f_q^{\mathrm{e}} = f_q^{\mathrm{e}}(\rho, \boldsymbol{u}, \mathbf{P} + \boldsymbol{\Pi}). \tag{2.14}$$

2.1.2 Numerical Integration of the Cahn-Hilliard equation

To integrate the Cahn-Hilliard equation, Eq. (1.26),

$$\partial_t\phi + \boldsymbol{u}\cdot\boldsymbol{\nabla}\phi = M\nabla^2\mu, \tag{2.15}$$

a second lattice-Boltzmann equation is introduced,

$$g_q(\boldsymbol{x} + \boldsymbol{c}_q, t + 1) = g_q(\boldsymbol{x}, t) - \frac{1}{\tau_g}\left[g_q - g_q^{\mathrm{e}}\right](\boldsymbol{x}, t), \tag{2.16}$$

where g_q is a distribution function with a collision parameter $\tau_g = 1$, whose zeroth moment defines the phase field,

$$\phi \stackrel{\text{def}}{=} \sum_q g_q. \tag{2.17}$$

The corresponding equilibrium distribution function, g_q^{e}, is defined as

$$g_q^{\mathrm{e}}(\phi, \boldsymbol{u}, \mu) \stackrel{\mathrm{def}}{=} w_q \left[\frac{M'\mu}{c_s^2} H_q^{(0)} + \frac{\phi \boldsymbol{u}}{c_s} \cdot H_q^{(1)} + \frac{\phi \boldsymbol{u}\boldsymbol{u}}{2c_s^2} : H_q^{(2)} \right] \tag{2.18}$$

if $q \neq 0$, and

$$g_0^{\mathrm{e}}(\phi, \boldsymbol{u}, \mu) \stackrel{\mathrm{def}}{=} \phi - \sum_{q=1}^{Q-1} g_q^{\mathrm{e}}(\phi, \boldsymbol{u}, \mu), \tag{2.19}$$

thus satisfying $\sum_q g_q^{\mathrm{e}} = \phi$, $\sum_q g_q^{\mathrm{e}} \boldsymbol{c}_q = \phi \boldsymbol{u}$ and $\sum_q g_q^{\mathrm{e}} \boldsymbol{c}_q \boldsymbol{c}_q = M'\mu \mathbf{I} + \phi \boldsymbol{u}\boldsymbol{u}$, where $M' = M(\tau_g - 1/2)^{-1}$.

2.1.3 Calculating the Equations of State

To compute the pressure tensor, $\mathbf{P}$, and the chemical potential, μ, in Eqs. (2.6) and (2.18) the expressions in Eqs. (2.20) and (1.12) are used, i.e.,

$$\mathbf{P}(\boldsymbol{x}) = \left[p_0 + \frac{1}{4} B(\phi^2 - 1)(3\phi^2 + 1) - K\phi\nabla^2\phi - \frac{1}{2} K |\boldsymbol{\nabla}\phi|^2 \right] \mathbf{I} + K \boldsymbol{\nabla}\phi \boldsymbol{\nabla}\phi, \tag{2.20}$$

$$\mu(\boldsymbol{x}) = \mu_0 + B\phi(\phi^2 - 1) - K\nabla^2\phi, \tag{2.21}$$

where the reference pressure and chemical potential are set to $p_0 = 1/3$, and $\mu_0 = 0$.

To calculate the equations of state, it is required to compute the gradient and the Laplacian of the phase field. These are approximated using the finite-differences stencils

$$\boldsymbol{\nabla}\phi(\boldsymbol{x}) \approx \frac{1}{c_s^2} \sum_{q \neq 0} w_q \boldsymbol{c}_q \, \phi(\boldsymbol{x} + \boldsymbol{c}_q), \tag{2.22}$$

$$\nabla^2\phi(\boldsymbol{x}) \approx \frac{2}{c_s^2} \sum_{q \neq 0} w_q \left[\phi(\boldsymbol{x} + \boldsymbol{c}_q) - \phi(\boldsymbol{x}) \right], \tag{2.23}$$

where the w_q are used as weighting factors to optimise the accuracy of the approximation [65] (see Appendix A).

2.1.4 Structure of the Lattice-Boltzmann Algorithm

The LBM algorithm can be summarised in the following sequence of steps (see figure 2.2) [51, 54].

1. *Initialisation*: in which the density, order parameter, pressure, and chemical potential fields are set to an initial value.
2. *Main loop*: where the integration over time of the lattice-Boltzmann equation is done, this is subdivided in the following.
   (a) *Calculation of the equilibrium distributions* f_q^{e} and g_q^{e}, in which Eqs. (2.6)-(2.7) and (2.18)-(2.19) are evaluated in terms of the hydrodynamic fields.
   (b) *Collision*, in which the collision operators, $\mathcal{J}[f]$ and $\mathcal{J}[g]$ from Eq. (2.3) are applied, this results in the post-collision distribution functions $f_q^\star$ and $g_q^\star$.

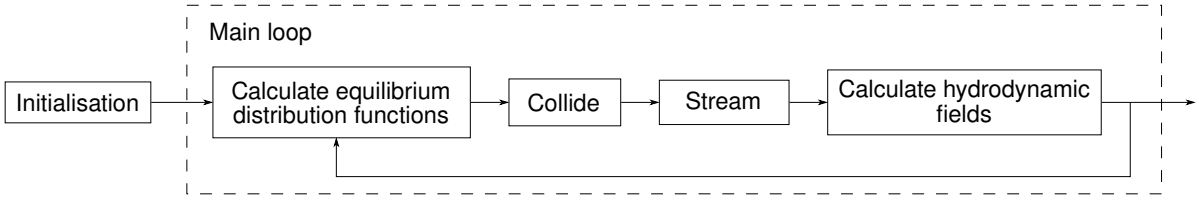

Figure 2.2: Flow diagram of the lattice-Boltzmann algorithm.

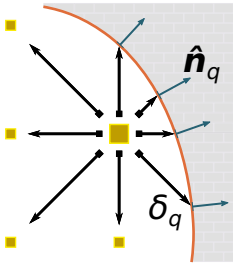

Figure 2.3: Schematics of solid boundaries in the lattice-Boltzmann method. A near-boundary lattice node (large square) has at least one lattice link that intersects the solid boundary. Each of such cut links is defined by its direction, and by the fractional distance to the wall, δ_q. At the intersection, the boundary is defined by a local normal vector $\hat{\boldsymbol{n}}_q$.

(c) *Streaming*, in which the post-collision distribution functions are propagated to the neighbouring sites, e.g., $f_q^\star(\boldsymbol{x}, t) \to f_q(\boldsymbol{x} + \boldsymbol{c}_q, t + 1)$, and similarly for g_q.

(d) *Calculation of the hydrodynamic fields* by means of the distribution functions f_q and g_q according to Eqs. (2.17), (2.8), (2.5), (2.20) and (2.21).

2.2 Boundary Conditions

Boundary conditions in the lattice-Boltzmann method arise in the streaming steps of Eqs. (2.1) and (2.16), and in the spatial derivatives of the phase field needed to compute the pressure tensor and chemical potential. In the following, these two types of boundary conditions will be referred as *kinetic boundary conditions* and *finite-differences boundary conditions*.

A near-boundary node, of position vector $\boldsymbol{x}_\mathrm{b} \in \Omega$, is defined as a node that has at least one lattice vector that crosses the boundary of the simulation domain (see figure 2.3). These lattice vectors define a set of *cut links*, Γ_c [66]. Each cut link is characterised by its length, $|\delta_q \boldsymbol{c}_q|$, where $0 < \delta_q \leq 1$, and by a local normal vector to the boundary, $\hat{\boldsymbol{n}}_q = \hat{\boldsymbol{n}}(\boldsymbol{x}_\mathrm{b} + \delta_q \boldsymbol{c}_q)$.

2.2.1 Kinetic Boundary Conditions

The kinetic boundary conditions consist of specifying the particle population $f_{\bar{q}}$ streaming into the simulation domain opposite to the cut link, where $\bar{q} \in \{q' \mid \boldsymbol{c}_{q'} = -\boldsymbol{c}_q;\ q \in \Gamma_\mathrm{c}\}$ is the direction of streaming from the boundary into the simulation domain. Two types of boundary conditions are considered: *no-slip walls* and *open boundaries*.

For no-slip (solid) walls the corresponding boundary conditions are,

$$\begin{aligned} \boldsymbol{u}(\boldsymbol{x}_{\rm w}) &= \boldsymbol{u}_{\rm w}, && (2.24)\\ \hat{\boldsymbol{n}}\cdot\boldsymbol{\nabla}\cdot\mathbf{P}(\boldsymbol{x}_{\rm w}) &= 0, && (2.25)\\ \hat{\boldsymbol{n}}\cdot\boldsymbol{\nabla}\mu(\boldsymbol{x}_{\rm w}) &= 0, && (2.26)\end{aligned}$$

where $\boldsymbol{x}_{\rm w} = \boldsymbol{x}_{\rm b} + \delta_q \boldsymbol{c}_q$ is the location of the solid wall, and $\boldsymbol{u}_{\rm w}$ is the boundary value of the velocity. Eqs. (2.24)–(2.26) are satisfied by the *bounce-back algorithm* [66, 67, 68]; specifically, the YLI bounce-back algorithm was implemented [69, 70], which reads

$$\begin{aligned} f_{\bar{q}}(\boldsymbol{x}_{\rm b}, t+1) =& \frac{\delta_q}{1+\delta_q} f_q^{\star}(\boldsymbol{x}_{\rm b}, t) + \frac{1-\delta_q}{1+\delta_q} f_q^{\star}(\boldsymbol{x}_{\rm b} - \boldsymbol{c}_q, t) \\ &+ \frac{\delta_q}{1+\delta_q} f_{\bar{q}}^{\star}(\boldsymbol{x}_{\rm b}, t) - \frac{2}{1+\delta_q}\frac{w_q}{c_s^2}\rho_{\rm w}\boldsymbol{u}_{\rm w}\cdot\boldsymbol{c}_q, \end{aligned} \tag{2.27}$$

where the boundary value of the density $\rho_{\rm w}$ is taken from the boundary node, i.e., $\rho_{\rm w} = \rho(\boldsymbol{x}_{\rm b})$. The same algorithm is used for $g_{\bar{q}}$.

Open boundaries correspond to situations in which the fluid is allowed exchange mass and energy with its surroundings. The pressure and the chemical potential are prescribed at an open boundary, i.e.,

$$\begin{aligned} \phi(\boldsymbol{x}_{\rm w}) &= \phi_{\rm w}. && (2.28)\\ \boldsymbol{\nabla}\cdot\boldsymbol{u}(\boldsymbol{x}_{\rm w}) &= 0, && (2.29)\\ \mathbf{P}(\boldsymbol{x}_{\rm w}) &= \mathbf{P}_{\rm w}, && (2.30)\\ \mu(\boldsymbol{x}_{\rm w}) &= \mu_{\rm w}, && (2.31)\end{aligned}$$

where the notation $\boldsymbol{x}_{\rm w} = \boldsymbol{x}_{\rm b} + \delta_q \boldsymbol{c}_q$ holds for the actual position of the boundary; $\phi_{\rm w}$, $\mathbf{P}_{\rm w}$ and $\mu_{\rm w}$ are the boundary values of the order parameter, pressure tensor and the chemical potential. For the distribution function f_q, the unknown particle populations are computed according to the *anti-bounce back* algorithm [69], which reads

$$f_{\bar{q}}(\boldsymbol{x}_{\rm b}, t+1) = \frac{1}{2}\left[f_q^{\rm e} + f_{\bar{q}}^{\rm e}\right](\rho_{\rm w}, \boldsymbol{u}_{\rm w}, \mathbf{P}_{\rm w}), \tag{2.32}$$

where the distribution functions, $f_q^{\rm e}$ and $f_{\bar{q}}^{\rm e}$, are given by Eq. (2.6), the velocity at the boundary, $\boldsymbol{u}_{\rm w}$, is computed as

$$\boldsymbol{u}_{\rm w} = \boldsymbol{u}(\boldsymbol{x}_{\rm b}) - \hat{\boldsymbol{n}}_q \cdot \boldsymbol{u}(\boldsymbol{x}_{\rm b})\hat{\boldsymbol{n}}_q \tag{2.33}$$

to satisfy Eq. (2.29), and $\rho_{\rm w}$ is determined by Eq. (2.8). The same algorithm is used to build the boundary populations of g, i.e.,

$$g_{\bar{q}}(\boldsymbol{x}_{\rm b}, t+1) = \frac{1}{2}[g_q^{\rm e} + g_{\bar{q}}^{\rm e}](\phi_{\rm w}, \boldsymbol{u}_{\rm w}, \mu_{\rm w}). \tag{2.34}$$

The boundary values $\phi_{\rm w}$, $\mu_{\rm w}$, and $\mathbf{P}_{\rm w}$ are not independent, but constrained by the equation of state. Namely, from Eq. (1.13), a relation for the three boundary values needs to be satisfied,

$$\mathbf{P}_{\rm w} = [\,\phi_{\rm w}\mu_{\rm w} - \psi(\phi_{\rm w})\,]\,\mathbf{I}, \tag{2.35}$$

where it is assumed that $\boldsymbol{\nabla}\phi_{\rm w} = 0$ at the open boundaries.

2.2.2 Finite-Differences Boundary Conditions

The wetting behaviour at the solid walls depends on the derivatives of the phase field at a boundary node in such a way that Eq. (1.23),

$$\hat{\boldsymbol{n}}_q \cdot \boldsymbol{\nabla}\phi(\boldsymbol{x}_b + \delta_q \boldsymbol{c}_q) = \frac{\chi}{K}, \tag{2.36}$$

is satisfied. To impose Eq. (2.36) as a boundary condition, the derivatives of ϕ are computed at the boundary node $\boldsymbol{x}_\mathrm{b}$. Specifically, the Taylor expansion of Eq. (2.36) around the node $\boldsymbol{x}_\mathrm{b}$ reads [71],

$$\hat{\boldsymbol{n}}_q \cdot \boldsymbol{\nabla}\phi(\boldsymbol{x}_\mathrm{b}) + \delta_q \hat{\boldsymbol{n}}_q \boldsymbol{c}_q : \boldsymbol{\nabla}\boldsymbol{\nabla}\phi(\boldsymbol{x}_\mathrm{b}) = \frac{\chi}{K}, \tag{2.37}$$

if $q \in \Gamma_c$, and

$$\boldsymbol{c}_q \cdot \boldsymbol{\nabla}\phi(\boldsymbol{x}_\mathrm{b}) + \frac{1}{2}\boldsymbol{c}_q \boldsymbol{c}_q : \boldsymbol{\nabla}\boldsymbol{\nabla}\phi(\boldsymbol{x}_\mathrm{b}) = \phi(\boldsymbol{x}_\mathrm{b} + \boldsymbol{c}_q) - \phi(\boldsymbol{x}_\mathrm{b}) \tag{2.38}$$

otherwise. In Eqs. (2.37) and (2.38) the gradient vector, $\boldsymbol{\nabla}\phi(\boldsymbol{x}_\mathrm{b})$, and the Hessian matrix, $\boldsymbol{\nabla}\boldsymbol{\nabla}\phi(\boldsymbol{x}_\mathrm{b})$, are unknown. In 3D, the gradient vector and the Hessian matrix comprise 3+6 independent components, forming a set of $U = 9$ unknowns; in 2D, $U = 5$. Eqs. (2.37) and (2.38), however, give $Q - 1$ equations. Therefore, the system is overspecified.

To determine $\boldsymbol{\nabla}\phi(\boldsymbol{x}_\mathrm{b})$ and $\boldsymbol{\nabla}\boldsymbol{\nabla}\phi(\boldsymbol{x}_\mathrm{b})$, a pseudo-inverse algorithm will be introduced. First, Eqs. (2.37) and (2.38) are expressed in the same units by multiplying every instance of Eq. (2.37) by $\delta_q|\boldsymbol{c}_q|^2/\hat{\boldsymbol{n}}\cdot\boldsymbol{c}_q$, this will allow to build linear combinations of the equations. Then, the system of equations is expressed in matrix form:

$$\mathbf{G}\,\boldsymbol{\Lambda} = \boldsymbol{\Phi}, \tag{2.39}$$

where $\boldsymbol{\Lambda}$, is a $U \times 1$ vector containing the unknown entries of the gradient vector and the Hessian matrix, e.g., in 3D,

$$\boldsymbol{\Lambda} = \left(\partial_x\phi,\ \partial_y\phi,\ \partial_z\phi,\ \partial_x^2\phi,\ \partial_y^2\phi,\ \partial_z^2\phi, \partial_x\partial_y\phi,\ \partial_y\partial_z\phi,\ \partial_z\partial_x\phi\right)^T(\boldsymbol{x}_\mathrm{b}). \tag{2.40}$$

In Eq. (2.39), $\boldsymbol{\Phi}$ is a $(Q-1)\times 1$ vector of known field values and boundary conditions whose entries read

$$\Phi_q = \begin{cases} \chi\delta_q|\boldsymbol{c}_q|^2/K\hat{\boldsymbol{n}}\cdot\boldsymbol{c}_q, & \text{if } q \in \Gamma_c. \\ \phi(\boldsymbol{x}_\mathrm{b} + \boldsymbol{c}_q) - \phi(\boldsymbol{x}_\mathrm{b}), & \text{otherwise,} \end{cases} \tag{2.41}$$

and $\mathbf{G}$ is a $(Q-1)\times U$ matrix of coefficients that reflects the local structure of ϕ, including the boundaries. The pseudo-inverse algorithm consists of estimating the solution, $\boldsymbol{\Lambda} = \mathbf{G}^{-1}\,\boldsymbol{\Phi}$, computing $\mathbf{G}^{-1}$ as

$$\mathbf{G}^{-1} \equiv (\mathbf{E}\,\mathbf{G})^{-1}\,\mathbf{E}. \tag{2.42}$$

In Eq. (2.42), $\mathbf{E}$ is a $U\times(Q-1)$ matrix which projects $\mathbf{G}$ into a $U\times U$ (square) matrix. This can be thought of as a weighting of the entries of $\mathbf{G}$ while preserving linear independence. In the spirit of Eqs. (2.22) and (2.23), in 3D, the columns of the projection matrix are defined as,

$$\boldsymbol{E}_q \equiv \frac{w_q}{\delta_q c_s^2}\left(\frac{c_{xq}}{\delta_q}, \frac{c_{yq}}{\delta_q}, \frac{c_{zq}}{\delta_q}, \frac{c_{xq}^2}{c_s^2}, \frac{c_{yq}^2}{c_s^2}, \frac{c_{zq}^2}{c_s^2}, \frac{c_{xq}c_{yq}}{c_s^2}, \frac{c_{yq}c_{zq}}{c_s^2}, \frac{c_{zq}c_{xq}}{c_s^2}\right)^T, \tag{2.43}$$

where the generalisation $\delta_q = 1$ for $q \notin \Gamma_c$ is made. The structure of the $\mathbf{E}$ matrix in 2D is similar, and it is obtained by removing every entry where z appears in Eq. (2.43). Although the expression of $\mathbf{E}$ is not unique, it was found that Eq. (2.43) produces the expected interface profile near the solid boundaries, which was quantified using the equilibrium contact angle.

Because the matrix $\mathbf{G}$ stores the structure of the lattice and of the solid boundary (which do not change over time), the pseudo-inverse algorithm, Eq. (2.42), is applied numerically at the initialisation of a simulation, and is therefore not more expensive than the usual application of a finite-differences stencil.

2.3 Validation of the Lattice-Boltzmann Method

The lattice-Boltzmann method is validated by representative reference systems; these are, the Couette Flow, the Poiseuille Flow, and the Jeffery-Hamel Flow for the dynamics of a single phase fluid, whereas simulations for the interface width, equilibrium contact angle, and evaporation of a sessile droplet were carried out to validate the two-phase fluid model and mass transfer boundary conditions.

2.3.1 Couette Flow

A Couette Flow consists of a 2D flow between two parallel plates that have different tangential velocity. The flow is driven by the difference of the velocity between the two plates, see figure 2.4(a). The tangential velocity, u_x, as a function of the transverse coordinate y, is given by the following expression [72, 29],

$$u_x(y) = 2u_{\mathrm{w}}\frac{y}{L_y} - u_{\mathrm{w}}, \tag{2.44}$$

where $\pm u_{\mathrm{w}}$ is the velocity at the top $(+)$ and bottom $(-)$ walls respectively, and L_y is the separation between the two plates.

D2Q9 lattice-Boltzmann simulations of a single phase fluid ($\phi(\boldsymbol{x}) = 1$) were carried out for a simulation box of width, $N_x = 32$ lattice sites, and variable height, $N_y = L_y + 1$. The no-slip boundary conditions are set at the planes $y = 0.5$ and $y = L_y + 0.5$, where the velocity of the solid wall is set to $u_{\mathrm{w}} = 10^{-3}$. The ends of the channel are connected by periodic boundary conditions. The density of the fluid is set to unity, i.e., $\rho = 1$, and the collision parameters are: $\tau_f = 1.0, 1.5$ and $\tau_g = 1$.

Initially, the flow is at rest, and after 10^6 iterations, the flow asymptotically reached a stationary state.

In figure 2.4(b), the results of the simulation are shown and the solution given by Eq. (2.44). In the simulations the viscosity was varied by choosing different values of the relaxation time. This is in good agreement with the analytical solution, Eq. (2.44), and therefore, validates the velocity boundary conditions, Eq. (2.27).

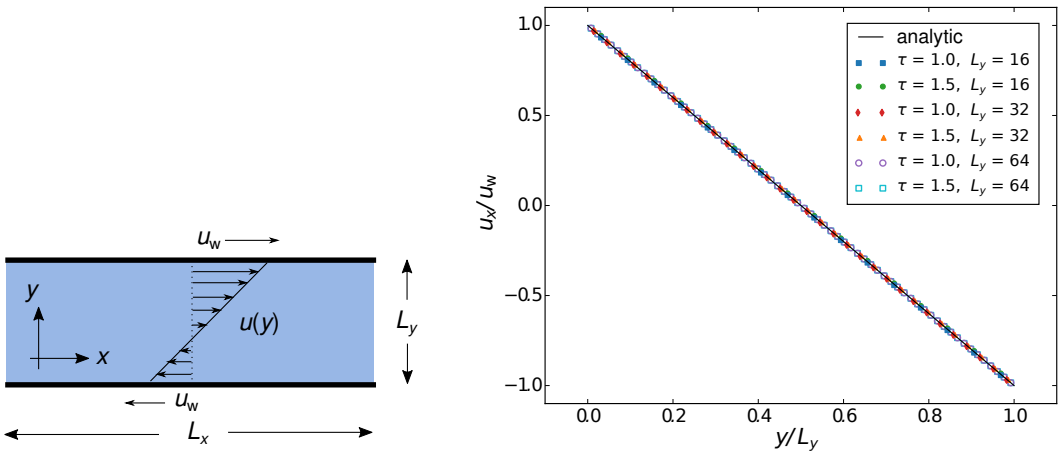

Figure 2.4: (a) Schematic representation of the Couette-Flow simulation. The top plate is moving with horizontal velocity u_w and the bottom plate with $-u_\mathrm{w}$. This creates a profile in the velocity of the fluid. (b) Lattice Boltzmann simulations of the velocity profile of the Couette flow in comparison with the theory, for different system sizes and relaxation times.

2.3.2 Poiseuille Flow

Similar to the Couette Flow, the Poiseuille Flow consists of a 2D flow between parallel planes. However, the fluid is driven by either a difference of pressure between the opposite ends of the cavity, Δp, or by an external force density throughout the volume, $\boldsymbol{f}$, see figure 2.5(a). In both cases, the velocity profile in this system is given by [72, 29],

$$u_x(y) = 4\,u_\mathrm{max}\,\frac{y}{L_y}\left(1-\frac{y}{L_y}\right) \tag{2.45}$$

where

$$u_\mathrm{max} = -\frac{\Delta p}{2\eta L_x L_y^2}, \tag{2.46}$$

in case of a pressure driven flow, and

$$u_\mathrm{max} = \frac{f_x}{2\eta L_y^2}, \tag{2.47}$$

in case the flow is driven by a body force.

For the Poiseuille system, D2Q9 LB simulations of a single phase fluid contained in a simulation box of width, $N_x = L_x + 1$, where $L_x = 20$, and variable height, $N_y = L_y + 1$ were carried out. The solid walls are at rest, and are located at the planes $y = 0.5$ and $y = L_y + 0.5$.

The open boundaries are specified at the endpoints of the channel, i.e., $x = 0.5$ and $x = L_x + 0.5$ when the flow is driven by a pressure difference, $\Delta p = -10^{-4}$ and the base pressure, $p_0 = 1/3$. On the other hand, when a body force is applied, $f_x = 10^{-6}$, and the end-points of the channel are connected by periodic boundary conditions. The density of the fluid, and the collision parameters are set to unity, i.e., $\rho = 1$, and $\tau_f = \tau_g = 1$.

As an initial condition, the velocity of the flow is $\boldsymbol{u}(\boldsymbol{x}) = 0$ everywhere, and it was left for 10^6 iterations to reach a steady state.

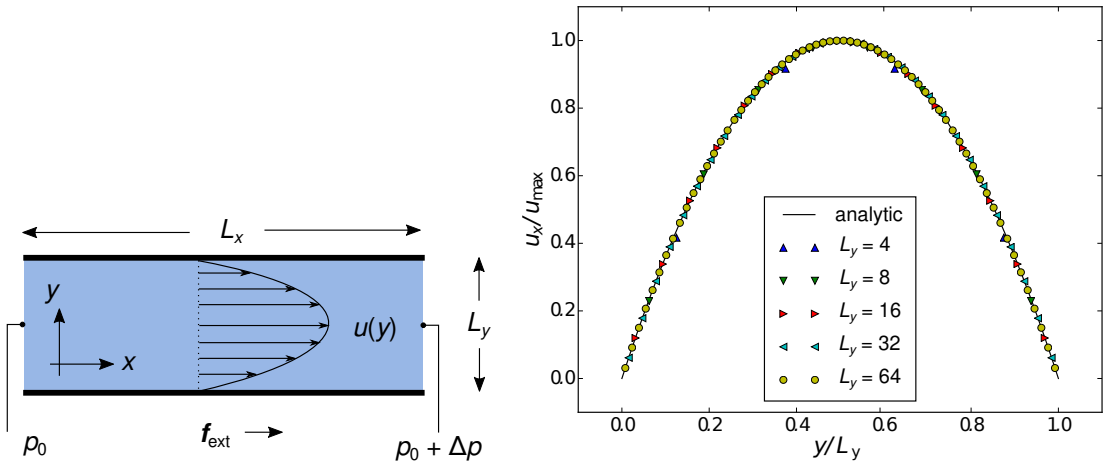

(a) (b)

Figure 2.5: (a) Schematic representation of the Poiseuille Flow for the simulation setup. The flow is driven either by a difference of pressure between the two open ends of the channel or by an external force. (b) LBM simulations of the Poiseuille velocity profile driven by a constant force density. The simulation results for the pressure driven Poiseuille flow reproduce the same velocity profile.

In the simulations, the width of system was varied, and measure the velocity at a cross-section of the channel, a quantitative agreement with Eq. (2.45) can be observed in figure 2.5(b) where the profile of the velocity is plotted. Therefore, the implementation of the body forces, Eq. (2.12), and pressure driven boundary conditions, Eq. (2.32), give the expected results.

2.3.3 Jeffery-Hamel Flow

In a Jeffery-Hamel flow, a fluid is contained between two planes that form a wedge geometry of opening angle 2β. The flow is driven by a pressure difference. Due to the symmetry of the system, it is customary to use polar coordinates to describe the flow. A schematic illustration of the flow can be seen in figure 2.6. For a Jeffery-Hamel flow, the pressure profile along the bisector reads [27],

$$p(r, \theta = 0) = p_0 + \Delta p \frac{r_1^2}{r^2} \frac{r^2 - r_2^2}{r_1^2 - r_2^2}, \tag{2.48}$$

where r_1 and r_2 are the distances from the openings to the apex of the channel, p_0 is the pressure at r_2 and $\Delta p + p_0$ is the pressure at r_1, where Δp if the pressure difference between the two ends [73, 74]. For more details on the derivation of the Jeffery-Hamel flow, see Appendix §B.

D2Q9 LBM simulations for a single phase Jeffery-Hamel flow were carried out. The simulation domain is contained in a box of width $N_x = 100$ and height $N_y = 48$. the open boundaries are specified at $x = 0.5$ and $x = 99.5$, and the no-slip boundaries at $y = 24 \pm \tan(\beta) \pm 5$, where $\beta = 10°$. The simulations parameters and initial condition are the same as in the Poiseuille flow simulations §2.3.2.

In the simulations, an increment in the pressure was set at the narrow end of the channel, then, the system is left to relax near equilibrium. In figure 2.7(a), the pressure

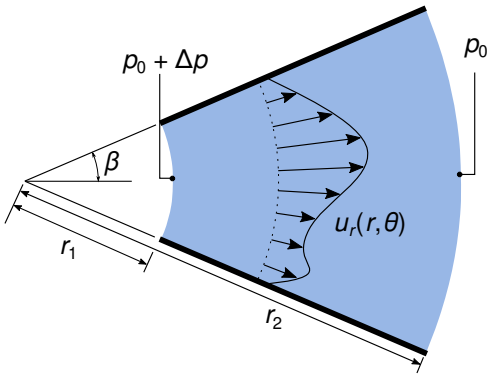

Figure 2.6: Schematic representation of the Jeffery-Hamel simulation set-up. The top plate forms an angle β with the horizontal line. The flow is driven by a pressure difference between the two ends of the channel.

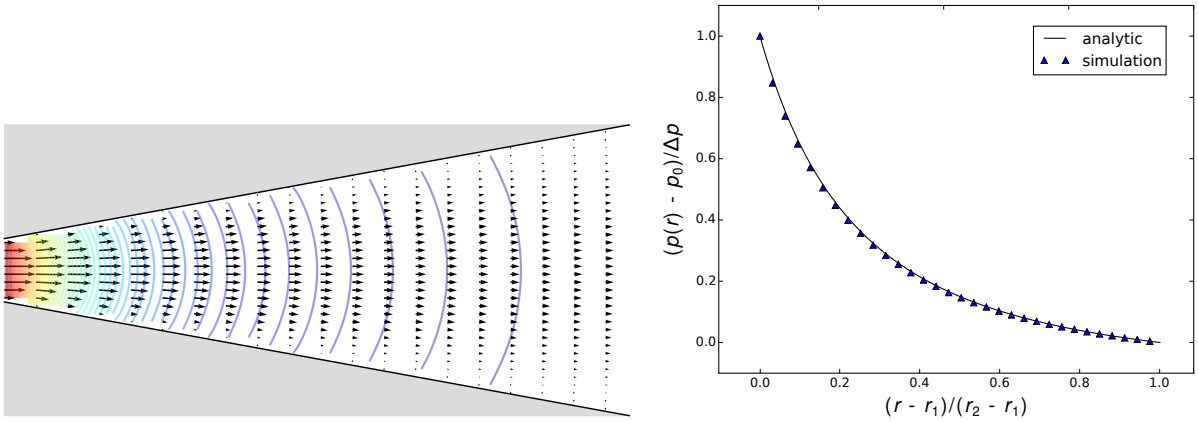

(a) (b)

Figure 2.7: Simulation results of a Jeffery-Hamel flow. (a) In coloured lines, the contour plot of the pressure field and the velocity profile depicted with arrows. (b) Barometric pressure profile of the channel at the bisector and comparison with the analytical prediction.

field is shown with contour lines and the velocity field is drawn with arrows, qualitatively it can be observed that the arrows of the velocity field are radial, while the contour lines are circular sections as expected. In figure 2.7(b), the pressure profile from the simulations is plotted and compared with the analytical prediction displaying good agreement. This shows that the interpolation scheme in the bounce-back algorithm make an accurate representation for off-lattice solid walls.

2.3.4 Interface Profile Between Two Fluid Phases

Simulations of the equilibrium phase field profile, $\phi(\boldsymbol{x})$, of a two-phase system were carried out. A D3Q15 LBM model was used, with a simulation box of $N_y = N_z = 1$, and $N_x = 100$, with closed boundaries at $x = 0.5$ and $x = 99.5$, and periodic boundaries for y and z. The saturation density of both phases is $\rho_i = 1$, $i = 1, 2$. The collision parameters are $\tau_f = \tau_g = 1$. The mobility is set to $M = 10^{-2}$, and the thermodynamic constant K

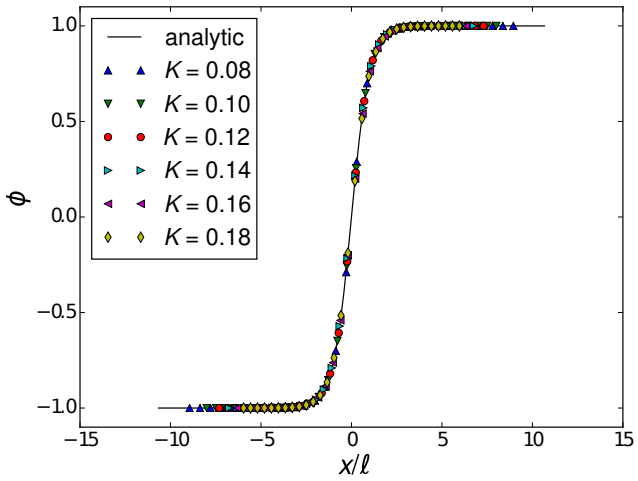

Figure 2.8: LBM simulations for the interface profile and the comparison with the prediction by the theory.

was varied from 0.08 to 0.18, and $B = (3\gamma)^2/8K$, in order to keep a constant value of the surface tension, $\gamma = 10^{-3}$.

Initially, the fluid is at rest, and the profile of the phase field

$$\phi(\boldsymbol{x}) = 2\Theta(x - 50) - 1, \tag{2.49}$$

where Θ is the Heaviside function. The system was left for 10^4 iterations to equilibrate.

Initially, the system is spatially divided into two halves, for one half, the concentration is set to one equilibrium value, whereas for the other half, the concentration is set to the other value in order to make a discontinuity at the middle point. As the system evolves in time, the discontinuity smooths out until it reaches equilibrium. The resulting profile is plotted in figure 2.8 for different values of the constant K, the agreement with the theory, Eq. (1.15), can be observed. This shows that the LBM is capable to simulate phase coexisting flows. Moreover, by tuning the constants B and K, in Eqs. (2.20) and (2.21), the interface width, ℓ (and also the surface tension, γ) can be adjusted.

2.3.5 Equilibrium Contact Angle

To measure the equilibrium contact angle of a sessile droplet on a solid surface, D2Q9 LBM simulations of two-phase fluids were carried out. The simulation domain was contained in a box of dimensions 100×50, where the solid boundaries were placed at the planes $y = 1 - \delta$, with variable $0 < \delta < 1$ and $y = 49.5$, and periodic boundary conditions in the x direction.

The initial condition for the order parameter is,

$$\phi(\boldsymbol{x}) = -\tanh\left(\frac{2}{\ell}\left[|\boldsymbol{x} - \boldsymbol{x}_c| - 60\right]\right), \tag{2.50}$$

which represents a circular droplet with centre at $\boldsymbol{x}_c = (50, 0.5)$ and radius of 60 lattice sites. The interface width $\ell = 2.12$, and the surface tension is set to $\gamma = 1.0 \times 10^{-3}$, thus setting the constants $B = 5.0 \times 10^{-4}$ and $K = 2.25 \times 10^{-3}$. The parameter χ was varied from -5×10^{-4} to 5×10^{-4}.

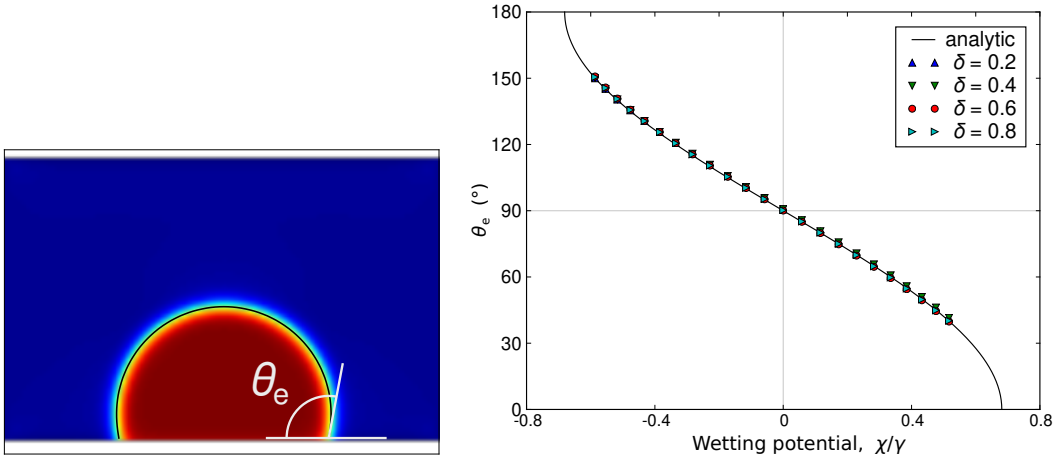

(a) (b)

Figure 2.9: LBM simulation results for the contact angle of a sessile droplet in comparison with the prediction by the theory for different values of an off-site boundary at distance δ.

After 10^4 iterations, the system reaches the equilibrium and the drop forms a circular cap as shown in figure 2.9(a). The contact angle is measured by finding the centre of the circular segment. The simulations were carried out for different values for the wetting potential χ and different values of the off-site distance to the boundary δ, resulting in different contact angles (see figure 2.9(b)).

As expected, the variation of the surface constant resulted in the predicted contact angle with a negligible variation with respect to the off-site distance. This is evidence that the effect of the contact angle is well reproduced, that is, the finite-differences boundary conditions give the expected results regardless of the distance to the solid surface.

2.3.6 Evaporation of a Sessile Droplet

To assess the numerical method for evaporating boundary conditions of a binary fluid, 3D simulations in a $201 \times 201 \times 101$ simulation domain were carried out.

The initial condition for the order parameter is,

$$\phi(\boldsymbol{x}) = -\tanh\left(\frac{2}{\ell}\left[|\boldsymbol{x} - \boldsymbol{x}_c| - 60\right]\right), \tag{2.51}$$

where the centre of the droplet is placed at $\boldsymbol{x}_c = (50, 50, 0.5)$ for the 3D set, and the interface width $\ell = 2.12$. The surface tension is set to $\gamma = 1.0 \times 10^{-3}$ fixing the constants $B = 5.0 \times 10^{-4}$ and $K = 2.25 \times 10^{-3}$.

Evaporating boundary conditions, Eq. (2.32), are placed at the top plane, whereas the solid walls correspond to the bottom plane. The value of the thermodynamic fields at the boundaries were set to $\phi_w = -1.02$, $p_w = 1/3$, and thus, the chemical potential at the boundary is $\mu_w = -2.0604 \times 10^{-5}$. The value of the diffusion constant $M = 16$ and the relaxation time for both distribution functions was set to unity, i.e., $\tau_i = 1$, $i = f, g$.

As the droplet evaporates, diffusive currents transfer mass from the inner phase to the open boundaries (see figure 2.10). These currents are perpendicular to the interface of the droplet, and also to the open boundary plane. According to Cazabat [75], the evolution

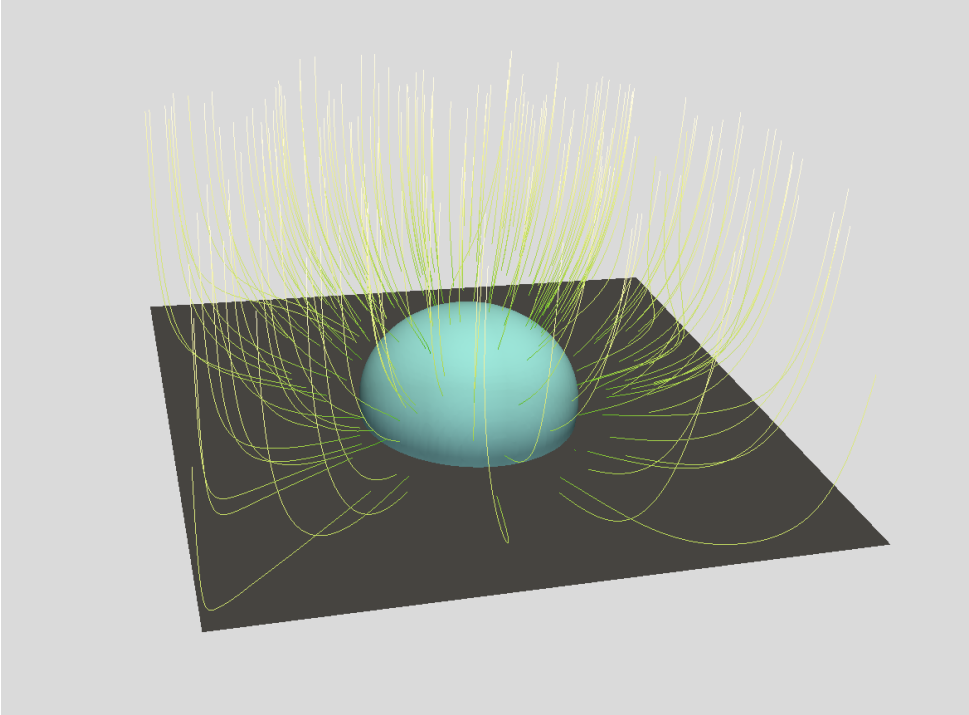

Figure 2.10: Snapshot after $t = 1.0 \times 10^6$ iterations for a 3D evaporating droplet (blue spherical cap) where the diffusive flows are shown as streamlines (yellow curves).

of the height is expected to be

$$h(t) = h_0 \sqrt{1 - t/T}, \tag{2.52}$$

where $h_0 = h(t = 0)$ is the initial height of the droplet, and T is the total evaporation time-lapse. In figure 2.11(a), the simulation result is compared with the theoretical prediction. The comparision with the theoretical curve is obtained by matching h_0 with the initial value of the height of the droplet in the simulations, and T is adjusted via curve fitting. A good agreement between the two curves is obtained. However, some discrepancies can be observed most prominently, at the final stages of the evaporation process where the simulation shows a faster evaporation rate. This is expected since the chemical potential inside the droplet obeys the Gibbs-Thomson rule, Eq. (1.6). As the droplet evaporates, its radius decreases, and therefore the chemical potential also increases (see figure 2.11(b)). Consequently, the magnitude of the diffusive flow increases and the droplet has a higher evaporation rate. Nonetheless, this effect is not captured by Eq. (2.52).

2.4 Concluding remarks

In this chapter, the lattice-Boltzmann algorithm was defined and validated. This is an LBM capable of modelling capillary systems in the presence of open and closed boundary conditions.

The LBM scheme is introduced in the context of the Boltzmann equation from Kinetic Theory, and it is shown how it solves the diffuse-interface Navier-Stokes and Cahn-Hilliard equations. By doing this, the tool that will model capillary phenomena in later chapters

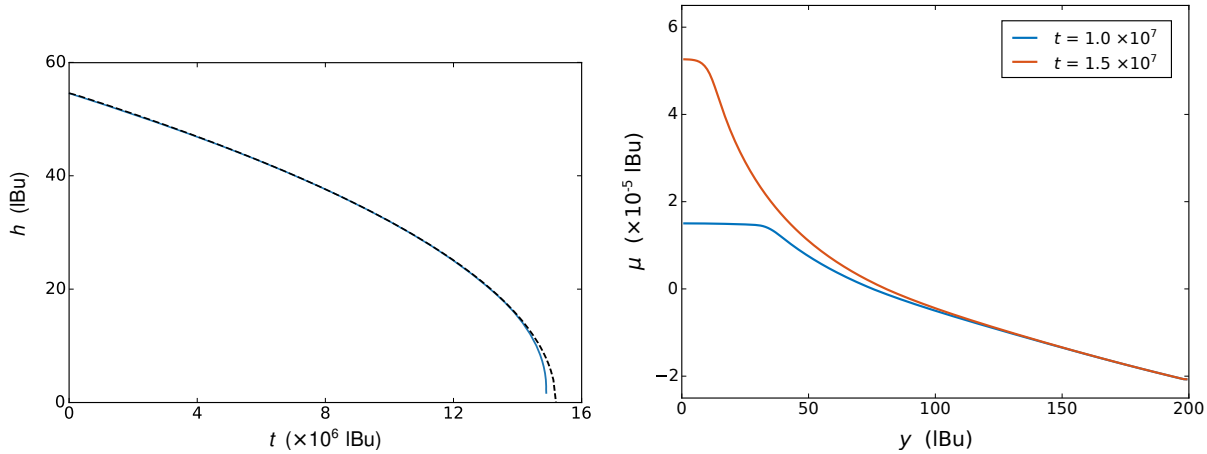

Figure 2.11: (a) Evolution of the height of the droplet, h, as a function of time, t, (blue solid line) and comparison with the prediction (black dashed line). (b) The chemical potential profile at the centre vertical line, $x = y = 50$.

has been constructed. The lattice-Boltzmann algorithm can be used to model fluids composed of coexisting phases, including the effects of surface tension and wetting.

Boundary conditions play an important role in the dynamics of capillary systems. For this reason, the LBM has been equipped to model different types of boundary conditions. These include moving boundaries, such as no-slip walls, but also open boundaries, in which the pressure, order parameter and chemical potential are prescribed.

The LBM was validated against reference systems for which an analytical prediction of the fluid dynamics is available; therefore, this allows the use the present LBM in the to study capillary phenomena in complex situations.

Part I

Droplets in Wedges

Introduction to Part I

Droplets in wedge geometries appear in many natural environments. For example, many shorebird species have wedge-shaped beaks that allow them to feed on water-bound organisms [76], water striders have arrays of tapered bristles that help them brush-off droplets from their legs [77], and the material properties of wet granular media depend on the adhesion and lubrication provided by capillary bridges wedged between solid grains [78, 79, 80].

Understanding the motion of droplets in wedges is important to improve technologies that use the geometry of the confinement for purposes of transport, positioning or actuation of small volumes of liquid. Wetting droplets inside tapered capillary tubes [81] or wedge-shaped channels [82] self-propel towards regions of stronger confinement, while non-wetting droplets trapped in non-parallel channels migrate to regions of weaker confinement [83, 82]. Such principles have been used to transport capillary bridges using mechanical [84] or photo-induced [85] actuation and even to separate droplets formed by two immiscible liquids [86].

When a liquid droplet is brought into contact with the inner walls of a wedge-shaped channel, the system will tend to minimise its total surface energy. In general, the transient dynamics and the final equilibrium state of the droplet can be characterised in terms of two main parameters, corresponding to the opening angle of the wedge, β, which characterises the confinement geometry, and the equilibrium contact angle of the liquid with the solid, θ_e, which quantifies the wetting properties of the liquid.

Broadly speaking, one can identify four qualitatively different regimes for the behaviour of droplets in wedges depending on the interplay between β and θ_e, as summarised in figure 2.12. The first corresponds to a complete invasion regime, where $0^\circ \leq \theta_e \leq 90^\circ - \beta$. In which case, the liquid forms a transient *capillary bridge* that completely invades the apex of the wedge where they form an *edge spread*. It was first noted by Hauksbee [87] that the free motion of such structures (i.e., in the absence of external forces, such as gravity) always results in their migration towards the apex of the wedge. Concus and Finn [88] and Concus *et al.* [89] showed that a global equilibrium for capillary bridges is not possible. Recently, Reyssat [82] studied the motion of completely-wetting capillary bridges ($\theta_e = 0$) within wedge-shaped channels and identified two regimes in the dynamics of the liquid. Close to the apex, the main source of energy dissipation is the viscous friction in the bulk of the liquid, which balances the rate of work done by capillary forces. As a result, the time evolution of the position of the capillary bridge is linear. This picture changes when the liquid is far from the apex of the wedge, where the main source of dissipation is the corner flow near the apparent contact lines. The result is a different equation of motion, which is given by a power-law dependence of the position of the liquid as a function of time with an exponent 4/13 [82].

A second regime occurs when $90^\circ - \beta < \theta_e \leq 90^\circ + \beta$. In such a case the liquid-gas interface forms an equilibrium shape that touches the apex of the wedge, sometimes

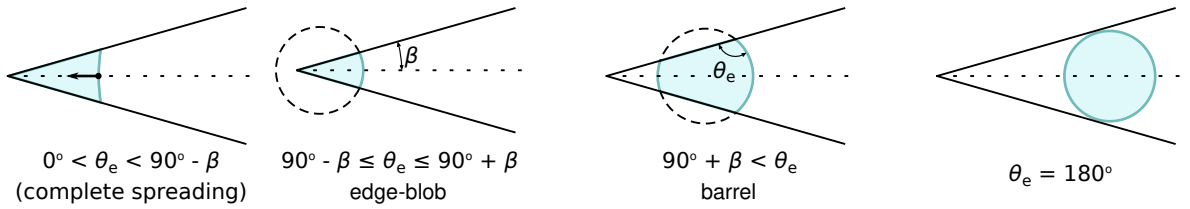

(a) (b) (c) (d)

Figure 2.12: Wetting regimes for a liquid droplet in a wedge geometry. (a) Edge spread. (b) Edge blob. (c) Liquid barrel. (d) Drop.

referred to as an *edge blob* [90, 89, 91].

A third regime corresponds to the completely non-wetting case, where $\theta_e = 180°$, and for which a liquid in a wedge-shaped channel will form a suspended droplet, a situation also found for gas bubbles. In such a case, a confined droplet will always migrate away from the apex of the wedge [83]. In sharp contrast to the complete-wetting limit, the equilibrium shapes of suspended droplets or bubbles correspond to perfect spheres. The dynamics of such systems involve the interplay between the liquid/gas and the surrounding fluid [92, 93]. However, in the specific case of a low-viscosity fluid (air bubble) suspended in a liquid of relatively high viscosity (silicone oil), Reyssat [82] showed that the main sources of dissipation during the motion within a wedge originate from the liquid, and that the same equations of motion that hold for completely wetting capillary bridges also hold for completely non-wetting bubbles.

The fourth regime, which is the main focus in this work, corresponds to a mostly non-wetting situation, where $90° + \beta < \theta_e < 180°$. In such a case, the liquid-gas interface is convex, i.e., it has a positive mean curvature, and forms a closed surface in equilibrium that avoids the apex of the wedge.

Concus *et al.* [89] studied the equilibria of partially wetting droplets in wedge geometries. They showed that, in contrast to the wetting regime, droplets form closed equilibrium shapes avoiding the apex of the wedge, and that, in the absence of external forces, such shapes correspond to sections of spheres. Experimentally, Baratian [94] recently observed such equilibrium configurations using an electrowetting setup. They show that a spherical equilibrium shape implies a vanishing net force acting on the liquid and that non-spherical static shapes appear when subjecting the liquid to the action of gravity.

The behaviour of droplets inside wedges is just beginning to be explored [82, 84, 95]. In this part, the statics and dynamics of partially-wetting drops in a wedge geometry is studied. The approach taken in §3, is to represent the statics and dynamics of the droplet is by relying on the Lagrangian formalism and by assuming the shape of the liquid-gas interface. Then, in §4, lattice-Boltzmann simulations are performed to gather further information and gain a deeper understanding of how the motion of the droplet inside the wedge occurs. In §5, the manipulation on the position a droplet as an example of the potential applications for this system is proposed. For the latter, an experimental set-up grounding our analytical and numerical results is used. Finally, in §I the conclusions of this part are presented.

Chapter 3

Theoretical Analysis

The analysis of the droplet inside the wedge will be based on the Lagrangian formulation detailed in §1.1.1. The starting point of the analysis is to determine the free energy of the system. For this purpose, the shape of the droplet will be proposed and it will be shown that it is a valid approximation for both static and dynamic situations. This shape is intended to describe the configuration of the liquid close to equilibrium, where curvature gradients are small: such shapes will be referred as *liquid barrels*.

3.1 Sharp-Interface Formulation

3.1.1 Droplet Morphology: Liquid Barrels

The focus is directed at droplets confined in hydrophobic narrow wedges ($\theta_e > 90°$), where β is of the order of a few degrees. Specifically, the interest lies on droplets of characteristic linear size $\beta V^{1/3} \sim 10^{-2}\,\mathrm{mm}$, where $V \sim 10\,\mu\mathrm{L}$ is the volume of the droplet, made of liquids such as water, glycerol, or oils, for which the density is $\rho \sim 10^3\,\mathrm{kg\ m^{-3}}$, the dynamic viscosity is $\eta \sim 1\,\mathrm{mPa\ s}$, and the surface tension is $\gamma \sim 20\text{—}70\,\mathrm{mN\ m^{-1}}$.

Based on the experiments carried out by Reyssat [82], it is expected that the droplet relaxes asymptotically to equilibrium, and thus, the translational motion of the droplet can be arbitrarily slow. For a typical speed $U \sim 1\text{—}10\,\mathrm{mm\ s^{-1}}$, the Reynolds number is $Re \overset{\text{def}}{=} \rho U V^{1/3}/\eta \sim 10^{-1}\text{—}10^{0}$, the capillary number is $Ca \overset{\text{def}}{=} \eta U/\gamma \sim 10^{-5}\text{—}10^{-3}$, and the Weber number is $We \overset{\text{def}}{=} Re\,Ca \sim 10^{-6} - 10^{-3}$. For droplets under the action of gravity along the axis of translation (as in the experiments of Baratian, *et al.* [94]), the Bond number is $Bo \overset{\text{def}}{=} \rho g V^{2/3}\gamma^{-1} \sim 10^{-1}$, where $V^{1/3}$ has been used as the characteristic length, and $g = 9.81\,\mathrm{m\ s^{-2}}$. If the action of gravity is perpendicular to the bisector plane, the characteristic length can be taken to be the height of the droplet giving a Bond number $Bo \sim \rho g \beta^2 V^{2/3}\gamma^{-1} \sim 10^{-3}$.

The smallness of the Reynolds number implies that inertial effects are negligible relative to viscous stresses. On the other hand, the magnitude of the Weber number indicates that short-wavelength (and thus high frequency) perturbations of the liquid-gas interface should decay over a short time-scale compared to the translational time-scale [96, 97, 27]. Finally, the smallness of the Bond number implies that the action of gravity has a negligible effect over the shape of the interface.

In summary, the magnitudes of the capillary, Weber and Bond numbers imply that the shape of the liquid-gas interface is dominated by surface tension. In conclusion, close

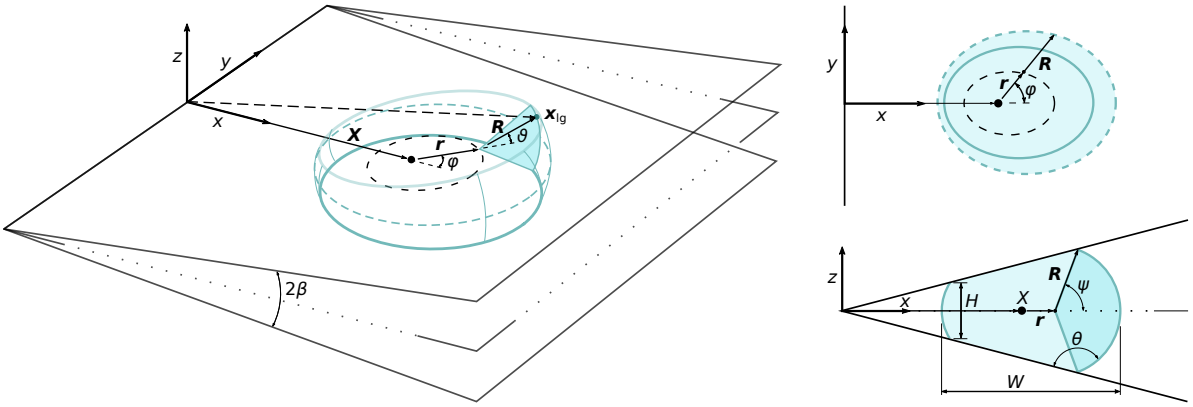

Figure 3.1: Schematics of the geometry of a liquid barrel inside a solid wedge of opening angle 2β. (a) 3D view of the system. The position vector of the liquid-gas interface, $\boldsymbol{x}_{\mathrm{lg}}$, is described using the vectors $\boldsymbol{X}$, $\boldsymbol{r}$ and $\boldsymbol{R}$, and the azimuthal and polar angles φ and ϑ. (b) View of the barrel's cross section along the bisector plane, $z = 0$. The short-dashed line corresponds to the equator of the barrel. The solid line corresponds to the contact lines. (c) View of the barrel's cross section along the transverse plane, $y = 0$. The intersection with the solid occurs at a contact angle θ. The aspect ratio of the transverse cross section of the barrel is determined by its minimum thickness, H and equatorial width, W.

to equilibrium, the liquid-gas surface must have small gradients in its curvature.

The description of the liquid-gas interface begins by setting the coordinate system. This will be a Cartesian coordinate system in which the wedge planes are located as half planes intersecting the y-axis and opening at the angles $+\beta$ and $-\beta$ from the xy-plane (see figure 3.1). Therefore, the normal vector to the upper plane is defined as

$$\hat{\boldsymbol{n}} \overset{\text{def}}{=} (-\sin\beta,\, 0,\, \cos\beta), \tag{3.1}$$

which points outwards from the fluid domain.

It is assumed that the walls of the wedge are identical and perfectly uniform. Furthermore, the shape of the droplet follows two planes of symmetry: the *bisector plane*,

$$z = 0, \tag{3.2}$$

and the *transverse plane*,

$$y = 0. \tag{3.3}$$

The intersection of the two planes occurs at the x-axis, and defines the *bisector line* which is the principal axis of symmetry of the droplet.

Let $\boldsymbol{x}_{\mathrm{lg}}$ be the position vector of a point on the liquid-gas interface. This vector can be expressed as the sum of three displacements from the origin,

$$\boldsymbol{x}_{\mathrm{lg}} = \boldsymbol{X} + \boldsymbol{r} + \boldsymbol{R}. \tag{3.4}$$

The vector $\boldsymbol{X} = (X,\, 0,\, 0)$ defines the position of the geometric centre of the droplet, X, relative to the apex of the wedge. The vector $\boldsymbol{r} = r(\varphi)\hat{\boldsymbol{r}}$, where $\hat{\boldsymbol{r}} = (\cos\varphi,\, \sin\varphi,\, 0)$, is a displacement vector from the geometric centre of the droplet (point X in figure 3.1) confined to the bisector plane. The vector $\boldsymbol{R} = R(\varphi)\hat{\boldsymbol{R}}$, where $\hat{\boldsymbol{R}} = (\cos\varphi\cos\vartheta,\, \sin\varphi\cos\vartheta,\, \sin\vartheta)$,

is a displacement vector that joins the vector $\boldsymbol{r}$ and a point on the liquid-gas interface (see figure 3.1 for a defintion of the azimuthal and polar angles, φ and ϑ).

The sum of the vectors $\boldsymbol{r} + \boldsymbol{R}$ is restricted such that, at the bisector plane ($\vartheta = 0$), it draws an *equatorial circle* of radius $R_o = |\boldsymbol{r} + \boldsymbol{R}|$ centred at $\boldsymbol{X}$.

For each value of φ, the vector $\boldsymbol{R}$ draws a circular section parametrised by the polar angle, ϑ, on a plane perpendicular bisector plane. The centre of each circular section is the endpoint of $\boldsymbol{X} + \boldsymbol{r}$, and its radius, $R(\varphi)$, is set such that the liquid-gas interface intersects the solid planes at a prescribed contact angle θ.

Whilst the azimuthal angle varies in the interval $\varphi \in [0, 2\pi)$, the polar angle is restricted by the intersection of the liquid-gas interface with the solid walls, i.e., $\vartheta \in [-\psi, \psi]$, where the maximum angle, ψ, can be found by the intersection with the bounding planes, i.e.,

$$\hat{\boldsymbol{n}} \cdot \boldsymbol{x}_{\mathrm{lg}}(\varphi, \vartheta = \psi) = 0. \tag{3.5}$$

The normal vector to the liquid-gas surface is expressed as,

$$\hat{\boldsymbol{n}}_{\mathrm{lg}}(\varphi, \vartheta) = \frac{\partial_\varphi \boldsymbol{x}_{\mathrm{lg}} \times \partial_\vartheta \boldsymbol{x}_{\mathrm{lg}}}{|\partial_\varphi \boldsymbol{x}_{\mathrm{lg}} \times \partial_\vartheta \boldsymbol{x}_{\mathrm{lg}}|}. \tag{3.6}$$

From Eq. (3.5) and Eq. (3.6), a condition that specifies ψ in terms of the contact angle is obtained, i.e.,

$$-\cos\theta = \hat{\boldsymbol{n}} \cdot \hat{\boldsymbol{n}}_{\mathrm{lg}}(\varphi, \vartheta = \psi). \tag{3.7}$$

Here it is assumed that

$$\theta \to \theta_{\mathrm{e}}; \tag{3.8}$$

this is consistent with static situations where the local shape of the interface is not affected by pinning effects, and with dynamic situations where the contact line undergoes a slow translational motion, corresponding to the limit of small Ca.

Furthermore, it is assumed that the equatorial radius is constant. Therefore, Eq. (3.7) reduces to

$$-\cos\theta_{\mathrm{e}} \approx \hat{\boldsymbol{n}} \cdot \hat{\boldsymbol{R}}. \tag{3.9}$$

Following these assumptions, the following expressions for the inner and outer radii of the droplet are obtained,

$$r(\varphi) = \frac{\alpha R_o - X}{\alpha + \cos\varphi}, \tag{3.10}$$

and

$$R(\varphi) = \frac{R_o \cos\varphi + X}{\alpha + \cos\varphi}, \tag{3.11}$$

where

$$\alpha \overset{\mathrm{def}}{=} -\frac{\cos\theta_{\mathrm{e}}}{\sin\beta}. \tag{3.12}$$

Figure 3.1 shows a typical droplet shape as given by Eqs. (3.10) and (3.11), the name *liquid barrel* is assigned because this is similar to an old-style wooden barrel. It will be shown that the liquid barrel is a good approximation to the shape of the interface in both static and dynamic situations.

Whilst it is possible to analyse the liquid barrels in Cartesian coordinates, the shape of the liquid-gas interface is better described using toroidal coordinates (σ, ϕ, ω). Geometrically, in toroidal coordinates a point in space, (x, y, z), is determined by the intersection of three surfaces [98]: a torus,

$$x^2 + y^2 + z^2 + a^2 = 2a(x^2 + z^2)^{1/2} \coth \sigma, \qquad (\sigma = \text{const}); \tag{3.13}$$

a sphere,

$$x^2 + (y - a \cot \phi)^2 + z^2 = \frac{a^2}{\sin^2 \phi}, \qquad (\phi = \text{const}); \tag{3.14}$$

and a half plane

$$\frac{z}{x} = \tan \omega, \qquad (\omega = \text{const}); \tag{3.15}$$

which defines the coordinates σ, ϕ, and ω. From Eq. (3.13), it can be seen that higher values of σ form tori with shrinking tubular radius that asymptotically approach the *reference circle*,

$$x^2 + z^2 = a^2, \quad \text{as } \sigma \to \infty. \tag{3.16}$$

In terms of these coordinates, the position vector $\boldsymbol{x}$ reads

$$\boldsymbol{x}(\sigma, \phi, \omega) = \frac{a}{\Delta}(\sinh \sigma \, \cos \omega, \, -\sin \phi, \, \sinh \sigma \, \sin \omega), \tag{3.17}$$

where $\Delta = \cosh \sigma - \cos \phi$.

In toroidal coordinates, the apex of the wedge corresponds to the axis of revolution of the angle ω. The two solid planes forming the wedge are located at $\omega = \pm\beta$. Therefore, $\omega = 0$, corresponds to the bisector plane. The liquid-gas interface of the droplet is given by the surface

$$\sigma_{\text{lg}} = \sigma_{\text{lg}}(\phi, \omega), \tag{3.18}$$

and the position vector of a point and the liquid-gas interface is thus given by

$$\boldsymbol{x}_{\text{lg}}(\phi, \omega) = [\boldsymbol{x} \circ \sigma_{\text{lg}}] \, (\phi, \omega) \tag{3.19}$$

(see figure 3.2). The contact lines follow after evaluating $\boldsymbol{x}_{\text{lg}}$at $\omega = \pm\beta$, i.e.,

$$\boldsymbol{x}_{\text{cl}\pm}(\phi) = \boldsymbol{x}_{\text{lg}}(\phi, \, \omega = \pm\beta), \tag{3.20}$$

or, equivalently,

$$\sigma_{\text{cl}}(\phi) \stackrel{\text{def}}{=} \sigma_{\text{lg}}(\phi, \omega = \pm\beta). \tag{3.21}$$

In order to specify $\sigma_{\text{lg}}(\phi, \omega)$ in terms of the liquid barrel shape, the parameter a is identified with the radius of the equatorial circle; using Eq. (3.13) at $z = 0$ gives,

$$a^2 = R_o^2(\xi^2 - 1), \tag{3.22}$$

and

$$\cosh \sigma = \xi, \tag{3.23}$$

where

$$\xi \stackrel{\text{def}}{=} \frac{X}{R_o}. \tag{3.24}$$

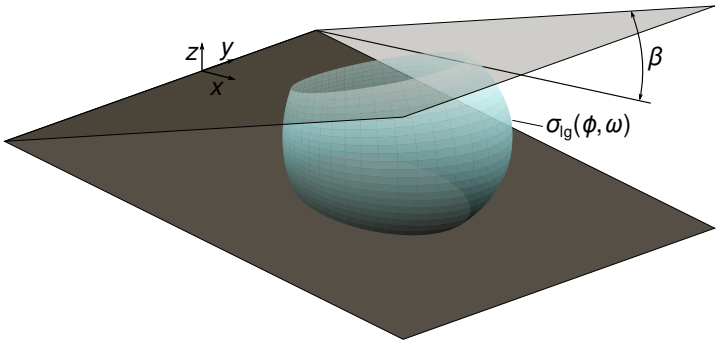

Figure 3.2: Representation of the liquid-gas interface using toroidal coordinates. Surface plot of an example of a parametric function $\sigma_{\mathrm{lg}}(\phi,\omega)$ for the liquid-gas interface (teal) and the solid planes (grey).

By calculating the angle of a point in the perimeter of the equatorial circle with respect to its centre, a relation between ϕ and φ is obtained, i.e.,

$$\cos\varphi = \frac{\xi\cos\phi - 1}{\xi - \cos\phi}. \tag{3.25}$$

Considering that the liquid-gas interface is formed by arcs of constant radii, R, and centres at $\boldsymbol{X} + \boldsymbol{r}$, then, Eq. (3.4) satisfies

$$[x - (X + r\cos\varphi)]^2 + [y - r\sin\varphi]^2 + z^2 = R^2; \tag{3.26}$$

which, by substitution of Eqs. (3.17), (3.10), (3.11) and (3.25), yields

$$\sigma_{\mathrm{lg}}(\omega) = \log\left[\frac{\alpha - \xi - (\xi^2-1)^{1/2}(1-\alpha^2\sin^2\omega)^{1/2}}{\alpha\xi - 1 - \alpha(\xi^2-1)^{1/2}\cos\omega}\right]. \tag{3.27}$$

Eq. (3.27) gives the liquid barrel interface in the toroidal parametrisation. The centre of the droplet, X, and contact angle, θ_{e} are specified by the parameters ξ and α, which follow from Eqs. (3.12) and (3.24).

Note that, while Eqs. (3.10) and (3.11) contain a singularity whenever $|\alpha| < 1$, under the parametrisation based on toroidal coordinates, these singularities are removed. Moreover, using Eq. (3.27), one can introduce a variation in the contact angle, i.e., $\alpha = -\cos\theta/\sin\beta$. This offers an effective generalisation of the liquid barrel shape to model situations where the contact angle varies in space or time.

Having defined the shape of the liquid barrel, some useful geometrical quantities are at hand. The height-to-width aspect ratio of the droplet is defined as (see figure 3.1),

$$h \overset{\mathrm{def}}{=} \frac{H}{W}, \tag{3.28}$$

where the droplet height,

$$H \overset{\mathrm{def}}{=} \min_{\{\phi\}} |\boldsymbol{x}_{\mathrm{lg}}(\phi,\omega=+\beta) - \boldsymbol{x}_{\mathrm{lg}}(\phi,\omega=-\beta)|, \tag{3.29}$$

is the length of the line connecting the contact lines at the narrow end of the wedge and the droplet width,

$$W \overset{\mathrm{def}}{=} \max_{\{\phi\}} |\boldsymbol{x}_{\mathrm{lg}}(\phi,0) - \boldsymbol{x}_{\mathrm{lg}}(0,0)|, \tag{3.30}$$

is the distance between the leading and trailing points of the equator of the droplet. For the liquid barrel shape, the aspect ratio reads

$$h = -\frac{\xi - 1}{\alpha - 1}\cos(\theta_{\mathrm{e}} - \beta). \tag{3.31}$$

The volume of the droplet can be found using the divergence theorem,

$$V = \frac{1}{3}\int_{\mathrm{liq.}} \boldsymbol{\nabla}\cdot\boldsymbol{x}\,\mathrm{d}x\,\mathrm{d}y\,\mathrm{d}z = \frac{1}{3}\int_{\mathrm{lg}} \boldsymbol{x}_{\mathrm{lg}}\cdot\mathrm{d}\boldsymbol{A}_{\mathrm{lg}}, \tag{3.32}$$

where, according to Eq. (3.17), the liquid-gas interface is $\boldsymbol{x}_{\mathrm{lg}} = (\boldsymbol{x}\circ\sigma_{\mathrm{lg}})(\phi,\omega)$, and the differential element of area is given by,

$$\mathrm{d}\boldsymbol{A}_{\mathrm{lg}} = (\partial_\phi \boldsymbol{x}_{\mathrm{lg}} \times \partial_\omega \boldsymbol{x}_{\mathrm{lg}})\,\mathrm{d}\phi\mathrm{d}\omega. \tag{3.33}$$

After some calculations, the volume is found to be

$$V = \frac{a^3}{3}\int_{-\beta}^{\beta}\int_{-\pi}^{\pi}\left[\frac{\sinh^2\sigma_{\mathrm{lg}}}{\Delta^3}\left(\cos\phi - \coth\sigma_{\mathrm{lg}}\,\sin\phi\,\partial_\phi\sigma_{\mathrm{lg}}\right)\right]\mathrm{d}\phi\mathrm{d}\omega. \tag{3.34}$$

The surface energy of the droplet is obtained by computing the surface areas of the liquid-gas and liquid-solid interfaces (see §1.1.1). The liquid-gas surface area can be computed directly as

$$A_{\mathrm{lg}} = \int |\mathrm{d}\boldsymbol{A}_{\mathrm{lg}}|. \tag{3.35}$$

Using the parametrisation of the liquid-gas interface the liquid-gas interface area is

$$A_{\mathrm{lg}} = a^2\int_{-\beta}^{\beta}\int_{-\pi}^{\pi}\frac{1}{\Delta^2}\Big\{(\partial_\omega\sigma_{\mathrm{lg}})^2 + \sinh^2\sigma_{\mathrm{lg}}\left[1 + (\partial_\phi\sigma_{\mathrm{lg}})^2\right]\Big\}^{1/2}\mathrm{d}\phi\mathrm{d}\omega. \tag{3.36}$$

The contact area of the droplet with the walls of the wedge is computed in a similar fashion, i.e.,

$$A_{\mathrm{ls}} = 2\int \hat{\boldsymbol{n}}\cdot\mathrm{d}\boldsymbol{A}_{\mathrm{ls}}, \tag{3.37}$$

where the element of surface area is

$$\mathrm{d}\boldsymbol{A}_{\mathrm{ls}} = \frac{1}{2}\boldsymbol{x}_{\mathrm{cl}}\times\partial_\phi\boldsymbol{x}_{\mathrm{cl}}\,\mathrm{d}\phi. \tag{3.38}$$

Using the toroidal parametrisation, the solid-liquid interface is

$$A_{\mathrm{sl}} = a^2\int_{-\pi}^{\pi}\frac{1}{\Delta^2}\Big[\sinh\sigma_{\mathrm{cl}}\cos\phi - \cosh\sigma_{\mathrm{cl}}\,\sin\phi\,\partial_\phi\sigma_{\mathrm{cl}}\Big]\mathrm{d}\phi. \tag{3.39}$$

Finally, an expression for the curvature of the liquid-gas interface is derived as follows. The orthonormal vector to the liquid-gas interface can be calculated by

$$\hat{\boldsymbol{n}}_{\mathrm{lg}} = \left[\frac{\boldsymbol{\nabla}(\sigma - \sigma_{\mathrm{lg}})}{|\boldsymbol{\nabla}(\sigma - \sigma_{\mathrm{lg}})|}\right]_{\sigma=\sigma_{\mathrm{lg}}}, \tag{3.40}$$

where the gradient operator in toroidal coordinates (of a scalar function f) is

$$\boldsymbol{\nabla} f = \frac{\Delta}{a}\left(\hat{\boldsymbol{e}}_\sigma \partial_\sigma f + \hat{\boldsymbol{e}}_\phi \partial_\phi f + \frac{1}{\sinh\sigma}\hat{\boldsymbol{e}}_\omega \partial_\omega f\right), \tag{3.41}$$

and $\hat{\boldsymbol{e}}_i = \partial_i \boldsymbol{x}/|\partial_i \boldsymbol{x}|$ ($i = \sigma,\, \phi,\, \omega$) are the orthonormal coordinate vectors. Therefore, the vector normal to the liquid-gas interface is,

$$\hat{\boldsymbol{n}}_{\mathrm{lg}} = \frac{(\hat{\boldsymbol{e}}_\sigma - \hat{\boldsymbol{e}}_\phi\, \partial_\phi \sigma_{\mathrm{lg}})\sinh\sigma_{\mathrm{lg}} - \hat{\boldsymbol{e}}_\omega \partial_\omega \sigma_{\mathrm{lg}}}{\sqrt{(\partial_\omega \sigma_{\mathrm{lg}})^2 + [1 + (\partial_\phi \sigma_{\mathrm{lg}})^2]\sinh^2\sigma_{\mathrm{lg}}}}. \tag{3.42}$$

Using $\hat{\boldsymbol{n}}_{\mathrm{lg}}$, the curvature of the liquid-gas interface is calculated,

$$\kappa = -\frac{1}{2}\boldsymbol{\nabla}\cdot\hat{\boldsymbol{n}}_{\mathrm{lg}}, \tag{3.43}$$

where the divergence operator (of a vector function $\boldsymbol{B} = \sum_i B_i \hat{\boldsymbol{e}}_i$, $i = \sigma, \phi, \omega$) in toroidal coordinates is,

$$\boldsymbol{\nabla}\cdot\boldsymbol{B} = \frac{\Delta^3}{a\sinh\sigma}\left[\partial_\sigma\left(\frac{\sinh\sigma}{\Delta^2}B_\sigma\right) + \sinh\sigma\,\partial_\phi\left(\frac{B_\phi}{\Delta^2}\right)\right] + \frac{\Delta}{a\sinh\sigma}\partial_\omega B_\omega. \tag{3.44}$$

3.1.2 Energy Landscapes

Concus and Finn [90, 89] showed that the ground state of a partially-wetting liquid bridging two non-parallel plane walls is a truncated sphere. They found that the centre of the sphere, X_{e}, is related to its radius, R_0, by $\sin\beta X_{\mathrm{e}} = -\cos\theta_{\mathrm{e}} R_o$, and thus radius of the droplet is given by

$$R_o = \left[\frac{6V}{\pi(\cos 3\theta_{\mathrm{e}} - 9\cos\theta_{\mathrm{e}})}\right]^{1/3}. \tag{3.45}$$

Baratian, *et al.* [94] experimentally confirmed these findings and showed, by the effect of an external force, that the equilibrium state is stable. Nonetheless, further details of the behaviour of the droplet are still missing for both static and dynamic situations.

In this section, the surface energy of the liquid barrel close to its equilibrium position will be studied. Then, deviations from the equilibrium position will be quantified using the displacement $X - X_{\mathrm{e}}$, where X is the geometric centre of the barrel. The analysis begins by considering the Helmholtz free energy, which, for constant temperature and number of molecules, is

$$F = \gamma A_{\mathrm{lg}} - \gamma A_{\mathrm{sl}}\cos\theta_{\mathrm{e}}. \tag{3.46}$$

In terms of Eqs. (3.36) and (3.39), with σ_{lg} given by Eq. (3.27), the surface areas read

$$A_{\mathrm{lg}} = R_o^2(\xi^2 - 1)\int_{-\beta}^{\beta}\left[\frac{1}{\Delta^2}\sqrt{\sinh^2\sigma_{\mathrm{lg}} + (\partial_\omega\sigma_{\mathrm{lg}})^2}\right]\mathrm{d}\omega, \tag{3.47}$$

and

$$A_{\mathrm{sl}} = 2\pi R_o^2 \frac{\xi^2 - 1}{\sinh^2\sigma_{\mathrm{cl}}}. \tag{3.48}$$

The volume of the droplet is computed explicitly using Eq. (3.32) to ensure that it is kept constant,

$$V = R_o^3(\xi^2 - 1)^{3/2} \int_{-\beta}^{\beta} \frac{\cosh \sigma_{\mathrm{lg}}}{\sinh^3 \sigma_{\mathrm{lg}}} \, \mathrm{d}\omega, \tag{3.49}$$

so that is can be used as a constraint.

The integrals in Eqs. (3.47), (3.48) and (3.49) can be evaluated by introducing two perturbation parameters:

$$\epsilon \overset{\text{def}}{=} \frac{\alpha}{\xi} - 1 = \frac{R_o}{q} - 1, \tag{3.50}$$

and

$$q \overset{\text{def}}{=} \frac{X}{\alpha}. \tag{3.51}$$

Here, q is a rescaled position of the geometric centre of the barrel. The parameter ϵ can be thought of as a deviation from the equilibrium spherical shape: setting $\epsilon = 0$ gives $\alpha = \xi$ and thus using Eq. (3.24), $X = \alpha R_o$. Then, Eq. (3.10) gives $r = 0$ and Eq. (3.11) gives $R = R_o$.

The condition of a constant volume fixes a relation between ϵ and q; implicitly evaluating Eq. (3.49) gives the result

$$V(q, \epsilon) = q^3 \sum_{i=0}^{3} a_i \epsilon^i, \tag{3.52}$$

where the constants a_i are functions of β and θ_{e}. Their expressions, however, simplify considerably in the limit of small wedge angles (see Appendix C). Therefore,

$$a_0 = \frac{\pi}{6}(\cos 3\theta_{\mathrm{e}} - 9\cos\theta_{\mathrm{e}}), \tag{3.53}$$

$$a_1 = \pi(2\theta_{\mathrm{e}} - \pi - \sin 2\theta_{\mathrm{e}}) + O(\beta^2), \tag{3.54}$$

$$a_2 = -2\pi\cos\theta_{\mathrm{e}} + O(\beta^2), \tag{3.55}$$

$$a_3 = 0 + O(\beta^2). \tag{3.56}$$

Using this approximation, and inverting (3.52), is can be found

$$\epsilon(q) = \frac{1}{2a_2}\left(\left\{a_1^2 + 4a_2\left(\frac{V}{q^3} - a_0\right)\right\}^{1/2} - a_1\right). \tag{3.57}$$

In the same way, the surface energy is expressed in polynomial form in powers of ϵ, i.e.,

$$F(q, \epsilon) = \gamma q^2 \sum_{i=0}^{3} (3 - i) a_i \epsilon^i + O(\epsilon^4). \tag{3.58}$$

The constant-volume energy landscapes, $F_V(X)$, can be obtained by composing the functions Eq. (3.57) into Eq. (3.58) and recovering the definition of q from Eq. (3.51), i.e.,

$$F_V(X) \overset{\text{def}}{=} F \circ \epsilon \circ q \; (X). \tag{3.59}$$

In figure 3.3 a plot of the energy landscape of the liquid barrel is presented. These are convex curves thus showing the existence of a state of minimum energy and the

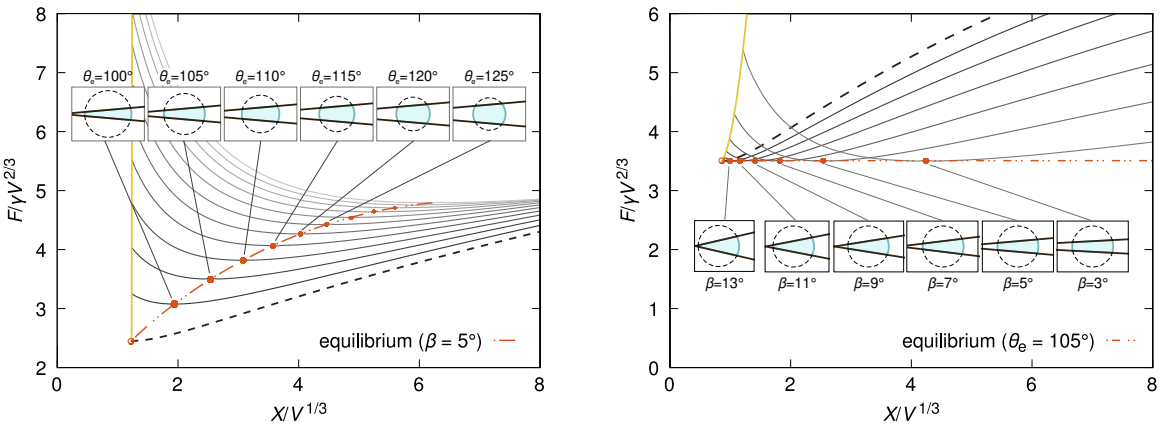

(a) (b)

Figure 3.3: Free energy landscapes along the position of the liquid barrel within the wedge, X, calculated analytically. (a) $F_V(X)$ curves for fixed $\beta = 5°$ and different equilibrium contact angles. (b) $F_V(X)$ curves for fixed $\theta_e = 105°$ and different wedge angles. The dots correspond to the minima in the analytical curves. The solid cut-off lines correspond to the limit where the liquid-gas interface touches the apex of the wedge.

corresponding equilibrium position. Figure 3.3(a) shows the energy landscapes for several values of θ_e but keeping $\beta = 5°$. The asymmetry in the landscapes about the equilibrium position arises from the intrinsic asymmetry of the geometry of the wedge. A displacement towards the apex of the wedge induces a comparatively larger increase in the solid-liquid surface area relative to the liquid-gas surface area, and results in a sharper increase in the surface energy. This same feature is observed in figure 3.3(b), where the energy landscapes at fixed $\theta_e = 105°$ and different values of β are presented.

Since the interfacial energy is conservative, Eq. (3.59) can be identified as a source of potential energy. Therefore, it can be used to derive total force that the liquid barrel exerts to restore its equilibrium state without the need of calculating the projected forces arising from the pressure and surface tension. This is a significant advantage for building simplified models that reduce the details of the configuration of the droplet into a single degree of freedom.

3.1.3 Force-Free Equilibrium

Figure 3.3 shows that the energy landscapes have a minimum, shown as the orange dotted-dashed curve. Formally, this can be obtained by finding the minimum of the energy, F_V, Eq. (3.59).

First, the free energy is expressed as $F_V(\epsilon) = FV^{-2/3}$ by eliminating q (using Eq. 3.52). Taking the total derivative with respect to ϵ gives

$$\frac{\mathrm{d}F_V(\epsilon)}{\mathrm{d}\epsilon} = \frac{1}{V^{5/3}}\left[(\partial_\epsilon F)\,V - \frac{2}{3}(\partial_\epsilon V)\,F\right]. \tag{3.60}$$

Using the expressions (3.52) and (3.58), Eq. (3.60) recasts into

$$\frac{\mathrm{d}F_V(\epsilon)}{\mathrm{d}\epsilon} = \frac{1}{V^{5/3}}\sum_{i,j=0}^{2}\left[(2-i)(i+1) - \frac{2}{3}(3-j)(i+1)\right]a_{i+1}a_j\epsilon^{i+j}. \tag{3.61}$$

Evaluating Eq. (3.61) at

$$\epsilon_{\mathrm{e}} = 0, \tag{3.62}$$

is a solution. Setting $\epsilon = 0$ in Eq. (3.50), the equilibrium value of

$$\xi_{\mathrm{e}} = \alpha; \tag{3.63}$$

using Eqs. (3.51) and (3.11) gives

$$q_{\mathrm{e}} = R_o. \tag{3.64}$$

The well-known result of references [89, 94] (see Eq. (3.45)) has been recovered: the equilibrium shape of the droplet is a sphere truncated by the walls of the wedge. In terms of Eqs. (3.10) and (3.11), this implies $r = 0$ and $R = R_o = R_{\mathrm{e}}$ which gives spherical surfaces. Such spherical shapes have a radius

$$R_{\mathrm{e}} = \left[\frac{6V}{\pi(\cos 3\theta_{\mathrm{e}} - 9\cos\theta_{\mathrm{e}})}\right]^{1/3}, \tag{3.65}$$

and centre (or equilibrium position),

$$X_{\mathrm{e}} = -\frac{\cos\theta_{\mathrm{e}}}{\sin\beta} R_{\mathrm{e}}. \tag{3.66}$$

The relations for the height-to-width ratio, h_{e}, and surface energy, F_{e} are also obtained:

$$h_{\mathrm{e}} = -\cos(\theta_{\mathrm{e}} - \beta), \tag{3.67}$$

$$F_{\mathrm{e}} = 3\gamma\left[\frac{\pi}{6}\left(\cos 3\theta_{\mathrm{e}} - 9\cos\theta_{\mathrm{e}}\right)V^2\right]^{1/3}. \tag{3.68}$$

Because the energy lanscape is a convex function of the position, as seen in figure 3.3, it can be ascertained that the equilibrium position, Eq. (3.66), is stable.

Figure 3.4 shows the equilibrium surface energy of liquid barrels at different positions within the wedge. For $\theta_{\mathrm{e}} < 180°$, a suspended droplet will always reduce the total surface energy by wetting the walls of the wedge. This wetted area is larger for smaller θ_{e}, and, because of volume conservation, the liquid settles at an equilibrium position closer to the wedge apex (see insets in figure 3.4). At first sight, one might expect a similar effect by increasing the wedge angle, β. Indeed, from Eq. (3.66), an increase in the wedge angle leads to a closer position of the barrel to the wedge apex. The surface energy, however, remains constant. Geometrically, this can be understood by noting that a change in β is equivalent to a rotation of the excluded portions of the truncated sphere (shown as dashed lines in the insets of figure 3.4) about the centre of the sphere, which does not alter the size of any of the interfaces of the barrel.

Note that for the droplet to form a closed barrel, that is, a structure that bridges the walls of the wedge avoiding its apex, one must have $R_{\mathrm{e}} < X_{\mathrm{e}}$, or, equivalently,

$$h_{\mathrm{e}} > 0. \tag{3.69}$$

From Eq. (3.67), this condition is satisfied only if

$$\theta_{\mathrm{e}} - \beta > 90°. \tag{3.70}$$

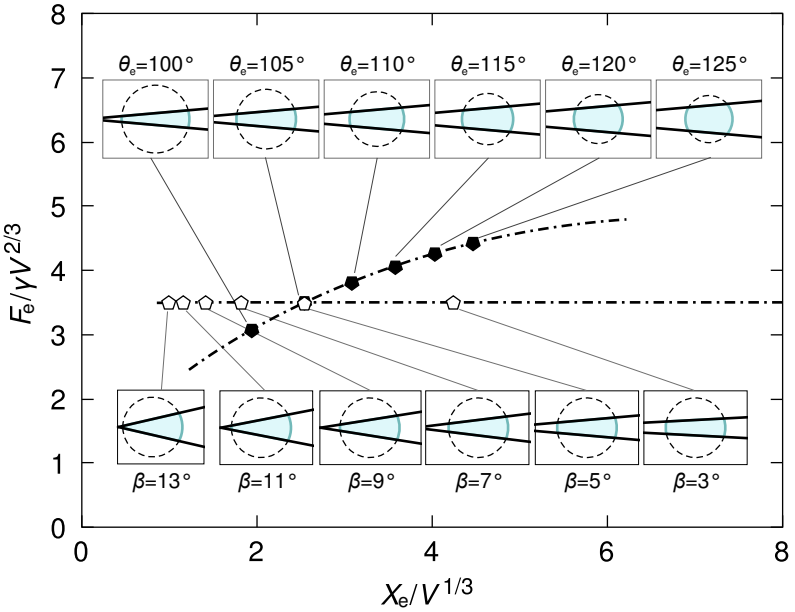

Figure 3.4: Equilibrium surface energy, F_e, as a function of the distance from the wedge apex, X_e, for different equilibrium contact angles at fixed $\beta = 5°$ (full symbols) and wedge angles at fixed $\theta_e = 105°$ (empty symbols). The insets correspond to cross sections of the barrels along the transverse plane.

Equilibrium states can also exist if $\theta_e - \beta \leq 90°$ but not as liquid barrel shapes. In such cases it has been shown that the liquid completely invades the wedge [82] and forms edge blobs [90, 89] or filaments that spread laterally along the wedge apex [91].

For a parallel-plate geometry ($\beta = 0°$), force-free barrels can exist provided that the separation between the solid walls matches the equilibrium height

$$H_e = 2h_e R_e, \tag{3.71}$$

which follows from Eq. (3.67). As noted by [99], a displacement of the solid wall from this equilibrium configuration will still result in mechanical equilibrium, albeit in the presence of a net external force. This situation can also occur for capillary bridges ($\theta_e < 90° - \beta$), for which no force-free equilibrium configurations can exist, and for which the net force exerted by the liquid on the solid plates is always attractive.

3.1.4 Pressure Distribution

In this section, the pressure distribution within the liquid barrel will be analysed for a displacement from equilibrium, $X - X_e \neq 0$. In the limit of small Reynolds and Weber numbers, the local conservation of momentum within the liquid is governed by the Stokes equation. For an incompressible fluid, the pressure field satisfies the Laplace equation,

$$\nabla^2 p = 0. \tag{3.72}$$

Eq. (3.72) is also valid for a static droplet under the action of a uniform external field, such as gravity.

The barrel shape presented in §3.1.1 provides a means to solving Eq. (3.72), i.e., to obtain the pressure distribution within the liquid in both static and dynamic situations.

Here, the geometry of the wedge and the configuration of the barrel provide the boundary conditions for the pressure field p. At the solid walls, the impenetrability condition is imposed,

$$\hat{\boldsymbol{n}} \cdot \boldsymbol{\nabla} p(\boldsymbol{x}_{\mathrm{sl}}) = 0, \tag{3.73}$$

and at the liquid-gas interface, the Young-Laplace law,

$$p(\boldsymbol{x}_{\mathrm{lg}}) = 2\gamma\kappa. \tag{3.74}$$

To determine the pressure profile, the boundary value problem posed by Eqs. (3.72)—(3.74) must be solved. The mean curvature, κ, follows from Eq. (3.43) after specifying the interface shape in Eq. (3.27); keeping terms up to second order in ω, it reads,

$$\kappa = \kappa(\phi, \omega = 0) + \frac{\alpha(\xi - \alpha)}{8R_o}\omega^2 + O(\omega^4), \tag{3.75}$$

where $\kappa(\phi, \omega = 0)$ is the curvature at the equatorial plane,

$$\kappa(\phi, \omega = 0) = \frac{1}{R_o}\left[1 + \frac{(\alpha - \xi)(\xi - \cos\phi)}{2(\xi^2 - 1)}\right]. \tag{3.76}$$

Considering that $|\omega| \leq \beta$ and $\xi \sim \alpha$ near equilibrium, the high-order correction terms in Eq. (3.75) are vanishingly small and thus can be dropped.

Eq. (3.72) can now be solved in toroidal coordinates. Laplace's equation reads [98]

$$\nabla^2 p = \frac{\Delta^3}{a^2 \sinh\sigma}\left[\partial_\sigma\left(\frac{\sinh\sigma}{\Delta}\partial_\sigma p\right) + \partial_\phi\left(\frac{\sinh\sigma}{\Delta}\partial_\phi p\right)\right] + \frac{\Delta^2}{a^2\sinh^2\sigma}\partial_\omega^2 p = 0. \tag{3.77}$$

This equation is separable using the *ansatz* $p = (\Delta/\sinh\sigma)^{1/2} S(\sigma)\Phi(\phi)\Omega(\omega)$. The general solution is given by Andrews [100], where $S(\sigma)$ is expressed as a linear combination of terms $P^{\mu}_{\nu-1/2}(\coth\sigma)$ and $Q^{\mu}_{\nu-1/2}(\coth\sigma)$, which are the Legendre and associate Legendre functions of the third kind; $\Phi(\phi)$ is expressed as a linear combination of the functions $\cos m\phi$ and $\sin m\phi$; and $\Omega(\omega)$ is expressed as a linear combination of $\cos\mu\omega$ and $\sin\mu\omega$ terms.

Periodicity in the angle ϕ demands that $p(\phi + 2\pi) = p(\phi)$ for all ϕ, therefore making m an integer, and, due to the plane symmetry ($y \leftrightarrow -y$), only the $\cos m\phi$ solutions are kept. Symmetry upon a reflection about the bisector plane ($z \leftrightarrow -z$) restricts the solutions of the form $\cos\mu\omega$. The boundary condition at the solid surface, $\partial_\omega p(\beta) = 0$, sets $\mu = \pi n/\beta$, for integer n. Interior solutions, i.e., finite value at the inner phase, demand discarding the $Q^m_{\mu-1/2}$ terms since such terms diverge at the reference circle (Eq. (3.16)). After these simplifications, the pressure field is expressed as,

$$p = \frac{2\gamma}{R_o}\sum_{m,\,n=0}^{\infty} A_{mn}\,\Psi_{mn}(\sigma, \phi, \omega), \tag{3.78}$$

where,

$$\Psi_{mn}(\sigma, \phi, \omega) = \left[\frac{\cosh\sigma - \cos\phi}{\sinh\sigma}\right]^{1/2} P^m_{\pi n/\beta - 1/2}(\coth\sigma)\cos(m\phi)\cos(\pi n\omega/\beta). \tag{3.79}$$

Note that for small β, the lower index in the Legendre function $(\pi n/\beta - 1/2)$ becomes large and so does its value at the boundary. This implies that the terms of higher order in n should carry a vanishingly small coefficient; and, even for $n = 1$, their contribution can be neglected. Therefore, the pressure at the equatorial circle of the droplet can be written as $(2\gamma/R_o)\sum_{k=0}^{1} c_k \cos k\phi$, where the coefficients $c_k = c_k(\xi, \alpha)$ are,

$$c_0 = \frac{\xi^2 + \alpha\xi - 2}{2(\xi^2 - 1)}, \tag{3.80}$$

$$c_1 = \frac{\xi - \alpha}{2(\xi^2 - 1)}. \tag{3.81}$$

As stated in [100], the pre-factor in square brackets from the general solution, Eq. (3.79), can be expressed as a Fourier cosine series using the identity

$$\frac{1}{\sqrt{\xi - \cos\phi}} = \sum_{m=0}^{\infty} b_m(\xi) \cos m\phi. \tag{3.82}$$

where $b_m = (2^{1/2}/\pi)(2 - \delta_{0m})Q_{m-1/2}(\xi)$.

The product of the two Fourier series resulting from substituting Eq. (3.82) into Eq. (3.79) and then into Eq. (3.78) can be recast into a single series by using the trigonometric equality, $2\cos m\phi \cos k\phi = \cos[(m+k)\phi] + \cos[(m-k)\phi]$. Then, rearranging terms, the A_{m0} coefficients in Eq. (3.78) follow as,

$$A_{m0}(\xi, \alpha) = \frac{(\xi^2 - 1)^{1/4}}{P^m_{-1/2}(\xi/\sqrt{\xi^2 - 1})} \times \begin{cases} c_0 b_0 + c_1 b_1/2, & m = 0, \\ c_0 b_1 + c_1(b_0 + b_2/2), & m = 1, \\ c_0 b_m + c_1(b_{m-1} + b_{m+1})/2, & m \geq 2. \end{cases} \tag{3.83}$$

The result is illustrated in figure 3.5, by plotting the solution of Laplace's equation, Eq. (3.78), along the bisector line. Evaluating the pressure profile at the points $\varphi = 0$ and $\varphi = \pi$ leads to an expression for the pressure difference along the bisector line (between the leading and trailing ends of the barrel), which, in terms of ϵ, reads

$$\Delta p = -\frac{2\gamma X \epsilon}{X^2 - R_o^2}. \tag{3.84}$$

Eq. (3.84) gives an indication of the structure of the pressure profiles along the bisector line. It is first noted that the sign of Δp is controlled by ϵ (since $X > R_o$). Inwards displacements, corresponding to $\epsilon > 0$, give $\Delta p < 0$, indicating that the barrel is subject to an outwards force due to the pressure gradient. The converse situation occurs for $\epsilon < 0$. The magnitude of Δp increases as $X \to R_o$, reflecting the stronger effect of confinement for inwards displacements from the equilibrium position. In equilibrium, where $\epsilon = 0$, the pressure profile is uniform ($\Delta p = 0$), and corresponds to $p(x, y = 0, z = 0) = 2\gamma/R_e$, as expected for a spherical barrel shape.

As shown in the contour plots of figure 3.6, the 3D pressure distribution broadly follows the same structure as the pressure profile along the bisector line. For barrels displaced inwards and outwards from their equilibrium position, the contour lines of the pressure field are denser towards the narrow end of the barrel, implying a stronger capillary force caused by the effect of confinement. This is confirmed by inspection of the pressure gradient force density, $-\boldsymbol{\nabla} p$, shown in figure 3.7, which is radial and decreases in magnitude with increasing distance from the apex of the wedge.

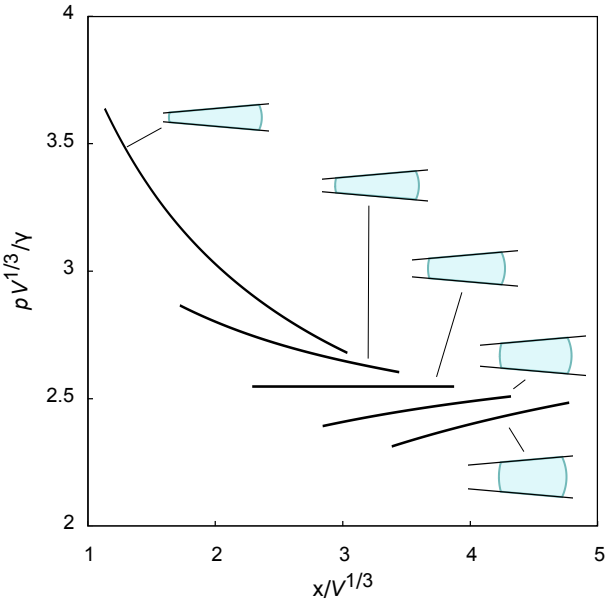

Figure 3.5: Pressure profiles along the bisector line $(x, 0, 0)$ for out-of-equilibrium barrel shapes of equilibrium contact angle $\theta_e = 110°$ and wedge angle $\beta = 5°$ (shown as insets). Each curve corresponds to a different displacement from equilibrium. From left to right, $(X - X_e)/V^{1/3} = -1,\ -1/2,\ 0,\ 1/2,\ 1$.

3.2 Comparison to Static Droplet Shapes Displaced by a Body Force

In the presence of an external force, the droplet is deformed from its equilibrium shape [94]. In this section, the liquid barrel model is compared to direct numerical calculations of the shape of a droplet subject to an applied force under static conditions.

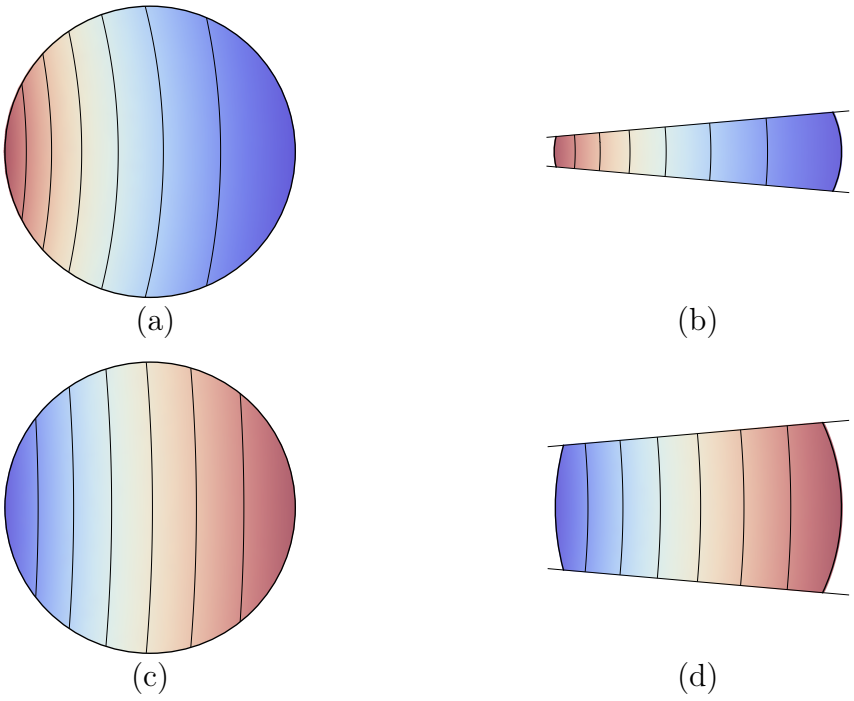

Figure 3.6: Pressure field, $p(\boldsymbol{x})$, for a barrel displaced inwards, (a and b), and outwards, (c and d), from the equilibrium position. (a) and (c): Projections of the pressure field on the bisector plane, $z = 0$. (b) and (d): Projections on the transverse plane, $y = 0$. The displacement in (a) and (b) is $(X - X_\mathrm{e})/V^{1/3} = -1$, and in (c) and (d), $(X - X_\mathrm{e})/V^{1/3} = +1$. The contact and tapering angles are $\theta_\mathrm{e} = 110^\circ$ and $\beta = 5^\circ$.

Figure 3.7: Pressure gradient force density, $-\boldsymbol{\nabla} p$, for a barrel displaced (a) inwards and (b) outwards from the equilibrium position. The plots correspond to cross sections along the transverse plane, $y = 0$. The displacements in (a) and (b) correspond to $(X - X_\mathrm{e})/V^{1/3} = -1$ and $(X - X_\mathrm{e})/V^{1/3} = +1$. The contact and tapering angles are $\theta_\mathrm{e} = 110^\circ$ and $\beta = 5^\circ$.

3.2.1 Energy and Shape of a Droplet in an External Forced Field

If a conservative force field is acting on the droplet, e.g. $-\boldsymbol{\nabla} U$, each differential volume element contributes with an additional potential energy, $U(\boldsymbol{x})\mathrm{d}V$. Therefore, the total energy, $\mathcal{E}$, reads

$$\mathcal{E}[\sigma_{\mathrm{lg}}] = F[\sigma_{\mathrm{lg}}] + \int_{\mathrm{liq.}} U(\boldsymbol{x})\,\mathrm{d}V. \tag{3.85}$$

In the following, static and constant external forces are exclusively considered. These forces model the gravitational field, $U(\boldsymbol{x}) = \rho \boldsymbol{g} \cdot \boldsymbol{x}$, where $\boldsymbol{g} = g\hat{\boldsymbol{e}}_x$ is the gravitational acceleration vector, oriented parallel to the bisector line.

The problem of finding the equilibrium surface is reduced to a similar minimisation problem as before, i.e.,

$$\frac{\delta}{\delta \sigma_{\mathrm{lg}}}\Big(\mathcal{E}[\sigma_{\mathrm{lg}}] - \tilde{p}\,V[\sigma_{\mathrm{lg}}]\Big) = 0, \tag{3.86}$$

where $\tilde{p}$ is a Lagrange multiplier.

Numerically, the minimisation problem can be solved using a finite element approach, this gives the droplet morphologies in mechanical equilibrium subject to a constraint in the position of the centre of mass. The data by C. Semprebon[1] is presented in figure 3.8. It was obtained using the public domain software Surface Evolver [101]. The data is plotted along with analytical predictions for the displaced droplet. The good agreement of the data with the liquid barrel analytical curves supports the liquid barrel is a good approximation of the morphology of a forced droplet.

[1] I thank Dr. Ciro Semprebon for kindly providing his data.

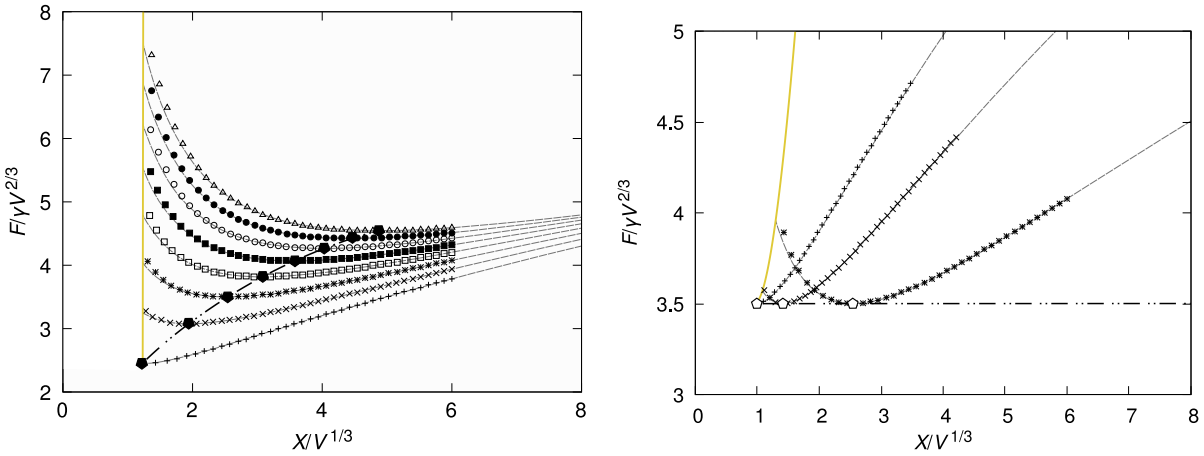

Figure 3.8: Energy landscapes along the position of the liquid barrel within the wedge, X, calculated analytically (dashed lines) and numerically *via* constrained minimisation of the surface energy (symbols). (a) Curves for fixed $\beta = 5°$ and different equilibrium contact angles: $\theta_e = 95°$ (+), $\theta_e = 100°$ (×), $\theta_e = 105°$ (∗), $\theta_e = 110°$ (□), $\theta_e = 115°$ (■), $\theta_e = 120°$ (○), $\theta_e = 125°$ (●), and $\theta_e = 130°$ (△). (b) Curves for fixed $\theta_e = 105°$ and different wedge angles: $\beta = 5°$ (+), $\beta = 9°$ (×) and $\beta = 13°$ (∗). The pentagons correspond to the minima in the analytical curves. The solid cut-off lines correspond to the limit where the liquid-gas interface touches the apex of the wedge.

3.2.2 Pressure Distribution within a Droplet in an External Force Field

Having compared the free energy of the droplet to the numerical results obtained from Surface Evolver, the pressure profiles are now compared to numerical results using the same method. In Surface Evolver, a Lagrange multiplier is introduced to enforce the volume constraint, λ_V, it plays the role of the Laplace pressure at the coordinate $x = 0$; another Lagrange multiplier is used to fixe the centre of mass, λ_X, which can be interpreted as an effective body force required to hold the droplet in place. Therefore, a linear hydrostatic pressure profile can be obtained, reading $p_{\mathrm{hs}}(x) = \lambda_V + \lambda_X V^{2/3} x/\gamma$.

In figure 3.9, an overlay the pressure profiles obtained numerically to the analytical curves can be observed. The range of each curve corresponds to the equatorial width of the barrel in each model. There is a good agreement with the magnitude of the pressure and the location of the edges close to equilibrium with the analytical model, particularly for for $X > X_e$.

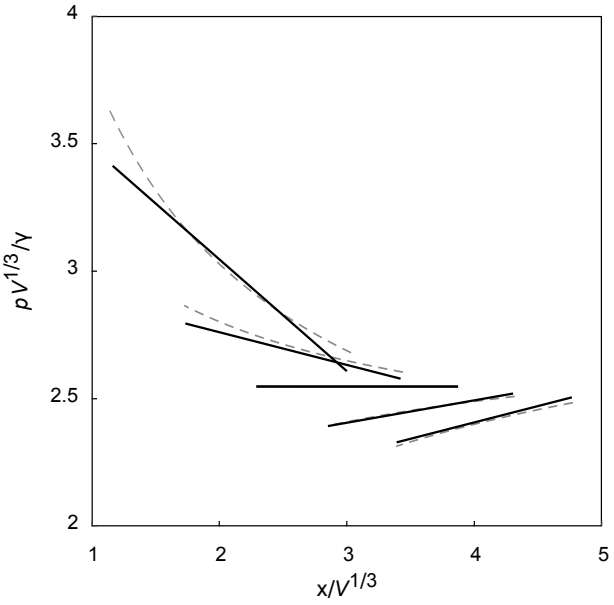

Figure 3.9: Comparison of the pressure profiles along the bisector line for out-of-equilibrium barrel shapes. The solid line represent the hydrostatic profiles obtained *via* constrained free-energy minimisation and the dashed lines are the analytical solution. From left to right, the curves correspond to the set of displacements $(X - X_e)/V^{1/3} = -1,\ -1/2,\ 0,\ 1/2,\ 1$. The equilibrium and wedge angles are $\theta_e = 110°$ and $\beta = 5°$.

3.2.3 Displacement of Equilibrium as Response to External Forces

After establishing that the liquid barrel shape gives a good representation of the shape of the droplet under the action of a uniform force field, a simple model to predict the displacement of the droplet in the presence of gravity is now derived. With numerical validation of the energy landscapes, the liquid-barrel model can be used to calculate the restitution force that the droplet experiences upon a displacement from equilibrium.

Eliminating the Lagrange multiplier term from Eq. (3.85) by using Eq. (3.59) instead, the energy of a droplet under a uniform potential field simplifies to,

$$\mathcal{E}_V(X) = F_V(X) - \rho V g X. \tag{3.87}$$

The new equilibrium position is obtained by finding the minimum of $\mathcal{E}_V$ in Eq. (3.87), which follows after solving

$$\frac{1}{\gamma V^{1/3}} \frac{\mathrm{d}F_V}{\mathrm{d}X}(X = X^*) - Bo = 0, \tag{3.88}$$

where X^* is the equilibrium position, and Eq. (3.88) is expressed in dimensionless form by introducing the Bond number, $Bo = \rho g V^{2/3}/\gamma$.

In figure 3.10, the equilibrium position as a function of Bo is plotted. When the force points inwards ($Bo < 0$), the droplet is monotonically displaced towards the apex of the wedge (see inset of figure 3.10). The force required to approach the apex increases with the contact angle. This is a consequence of the increased curvature in the narrow side of the droplet resulting from higher contact angles. The increase in curvature produces an increase in the Laplace pressure and therefore the net force increases as well. This can

occur until $X^* = R_o$, or equivalently, using Eq. (3.24), when

$$\xi^* = 1, \tag{3.89}$$

i.e., the position in which droplet reaches the apex. This has been previously shown in figures 3.3, 3.8 and 3.10 as the yellow cut-off line.

On the other hand, when the force is pointing outwards ($Bo > 0$), the droplet is displaced towards the wide end of the wedge. From the figure, there is a maximum force above which no equilibrium solution exists. This occurs because the force that the droplet can oppose due to an outwards displacement is finite; the total force is the sum of the pressure over the contact area, and the surface tension exerted over the contact lines. For a partially wetting liquid, the curvature of the droplet is positive, and thus, the pressure alone would push the droplet apart from the apex. The surface tension at the contact lines exerts an opposite force, that would tie the wedge and the droplet together. As the droplet is forced out of the wedge, it becomes narrower, the pressure wanes, and the contribution from the contact lines dominates. However, the same action also reduces the perimeter of the contact lines. For a liquid barrel, this happens as $\sigma_{\mathrm{lg}} \to \infty$, where the contact areas are reduced to points. From Eq. (3.27), the singularity appears when

$$X^* = -R_o \frac{1 + \cos\beta \sin\theta_{\mathrm{e}}}{\sin\beta \cos\theta_{\mathrm{e}}}, \tag{3.90}$$

which sets the upper bound to the parametrisation. Above this point, the liquid-barrel model fails.

Moreover, as a droplet becomes narrower, the curvature of the equatorial circle begins to increase, and thus, the average pressure inside the droplet raises again. Consequently, the restoring force that the droplet can oppose is not monotonic, and with further displacement, the droplet exerts less restoring force. This implies that the forced equilibrium position, which is given by the roots of Eq. (3.88), is not unique. This is observed for droplets of low θ_{e}. See inset of figure 3.10 for instance, where two forced equilibrium states with different displacement are found at the same force magnitude.

If the force that the droplet opposes due to the displacement is non-monotonic then it can reach an extreme. In this case, the extreme is a maximum, which implies the existence of a threshold set by

$$Bo_{\max} \overset{\mathrm{def}}{=} \frac{1}{\gamma V^{1/3}} \max_{\{X\}} \frac{\mathrm{d}F_V}{\mathrm{d}X}, \tag{3.91}$$

and whose position is at the inflection point of the energy landscape. Therefore, applying a force above the threshold would detach the droplet from the wedge.

3.3 Simplified Analysis of the Dynamics of the Liquid Barrel

The dynamic situation in which a droplet inside am hydrophobic wedge will be analysed. The droplet will be initially set at a distance away from its equilibrium position, and it is allowed to relax back to its equilibrium position X_{e}. The liquid barrel assumption is used to obtain an expression of the net capillary force that drives the relaxation of the droplet in dynamic situations. Then, the dynamics will be modelled using the Lagrangian approach, treating the position of the droplet as a function of time, $X(t)$, as the relevant degree of freedom for the dynamics.

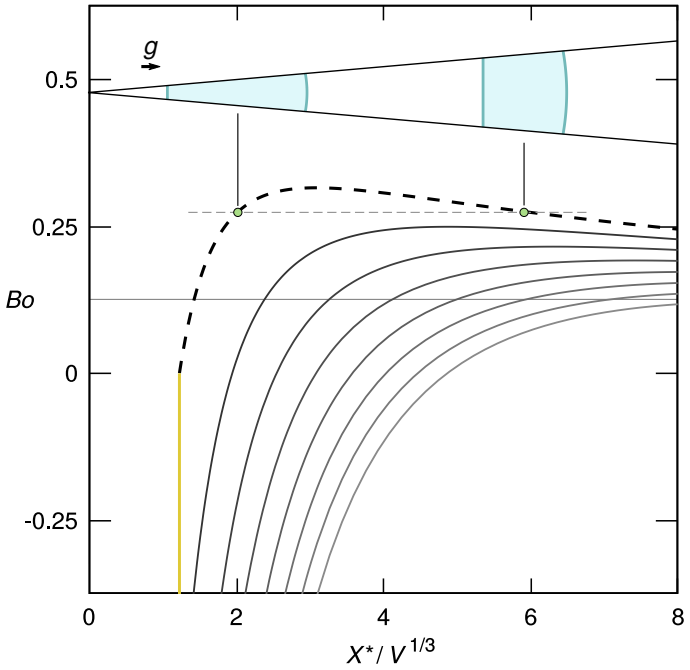

Figure 3.10: Equilibrium position of the droplet by the effect of an external force. From right to left, the thick curves represent the response in the position of droplet as a function of the Bond number, Bo, for the contact angles $\theta_e = 95°, 100°, ..., 135°$, at $\beta = 5°$. The cut-off line at the bottom represents the position in which the droplet reaches the apex of the wedge.

3.3.1 Simplified Equations of Motion

The Lagrangian functional of the system reads,

$$L[\sigma_{lg}, \boldsymbol{u}] = \frac{1}{2}\int \rho u^2 \, \mathrm{d}^3x - F[\sigma_{lg}] + \tilde{p}\, V[\sigma_{lg}], \tag{3.92}$$

where $u = |\boldsymbol{u}|$, and $\boldsymbol{u}$ is the velocity field of the fluid. The first term in the right-hand side of the equation corresponds to the total kinetic energy, the next term is the interfacial energy contribution, and the last term is included to satisfy the constant-volume constraint, where $\tilde{p}$ is the corresponding Lagrange multiplier. The equations of motion are derived from the principle of minimum action, and by adding dissipative forces caused by viscous friction and contact line motion.

The liquid barrel shape, constructed in §3.1.1, can be used to model the translational motion of the liquid. It is assumed that the velocity of the droplet is small, and thus, the kinetic energy term in Eq. (3.92) can be neglected. From Eqs. (3.52) and (3.58), the Lagrangian is reduced to

$$L(q, \epsilon, \dot{q}, \dot{\epsilon}) = -F(q, \epsilon) + \tilde{p}\, V(q, \epsilon). \tag{3.93}$$

Then, the equations of motion are

$$\partial_q F - \tilde{p}\, \partial_q V = K_q, \tag{3.94}$$
$$\partial_\epsilon F - \tilde{p}\, \partial_\epsilon V = K_\epsilon, \tag{3.95}$$

where $K_q = K_q(q, \epsilon, \dot{q}, \dot{\epsilon})$, and $K_\epsilon = K_\epsilon(q, \epsilon, \dot{q}, \dot{\epsilon})$ stand for non-conservative friction forces. The conservation of volume,

$$\dot{V} = \partial_q V \dot{q} + \partial_\epsilon V \dot{\epsilon} = 0, \tag{3.96}$$

is necessary to bring closure to the system and to determine the value of $\tilde{p}$.

From Noether's theorem [102], the energy flow of the system is calculated,

$$\frac{\mathrm{d}}{\mathrm{d}t}\left[F - \tilde{p}\, V\right] = \dot{\mathcal{E}}, \tag{3.97}$$

where the dissipation function, $\dot{\mathcal{E}} = \dot{\mathcal{E}}(q, \epsilon, \dot{q}, \dot{\epsilon})$, gives the rate of change of energy of the system, i.e.,

$$\dot{\mathcal{E}} = \dot{q} K_q + \dot{\epsilon} K_\epsilon. \tag{3.98}$$

The friction forces can be reconstructed on the basis of the dissipative contributions to Eq. (3.98). Therefore, the properties of the dissipation function, relevant to the equations of motion, will be derived.

For small velocities near equilibrium, the dissipation function can be expanded in a Taylor series,

$$\dot{\mathcal{E}} = -\sum_{l,m=1}^{2} \nu_{lm} \dot{w}_l \dot{w}_m + O(\dot{w}^4), \tag{3.99}$$

where the variables are $w_1 = q$ and $w_2 = \epsilon$, and the drag coefficients ν_{lm} are given by

$$\nu_{lm}(w_l, w_m) = -\frac{1}{2} \left. \frac{\partial^2 \dot{\mathcal{E}}}{\partial \dot{w}_l \, \partial \dot{w}_m} \right|_{(\dot{w}_l = 0,\, \dot{w}_m = 0)}. \tag{3.100}$$

The dissipation function, $\dot{\mathcal{E}}$, lacks a constant term since dissipation cannot occur while the system is at rest. The linear terms should also be zero, otherwise they would lead to the spontaneous creation of energy for a combination of values of $\dot{q}$ and $\dot{\epsilon}$. On that basis, and without loss of generality, the friction forces are expressed as

$$K_q = -\nu_{qq}\dot{q} - \nu_{q\epsilon}\dot{\epsilon} \qquad \text{and} \tag{3.101}$$

$$K_\epsilon = -\nu_{q\epsilon}\dot{q} - \nu_{\epsilon\epsilon}\dot{\epsilon}\,. \tag{3.102}$$

It can be verified that Eqs. (3.101) and (3.102) satisfy Eq. (3.99).

Substituting Eqs. (3.101) and (3.102) into Eqs. (3.94) and (3.95) respectively, and using the constraint of constant volume (Eq. 3.96), the equations of motion and the value of the Lagrange multiplier is obtained:

$$\nu\, \dot{q} = \left[-\partial_q F + (\partial_\epsilon F)\frac{\partial_q V}{\partial_\epsilon V}\right], \tag{3.103}$$

$$\nu\, \dot{\epsilon} = \left[-\partial_\epsilon F + (\partial_q F)\frac{\partial_\epsilon V}{\partial_q V}\right]\left(\frac{\partial_q V}{\partial_\epsilon V}\right)^2, \tag{3.104}$$

$$\tilde{p} = \frac{\nu_{qq}(\partial_\epsilon F)(\partial_\epsilon V) - \nu_{q\epsilon}[(\partial_\epsilon F)(\partial_q V) + (\partial_q F)(\partial_\epsilon V)] + \nu_{\epsilon\epsilon}(\partial_q F)(\partial_q V)}{\nu_{qq}(\partial_\epsilon V)^2 - 2\nu_{q\epsilon}(\partial_q V)(\partial_\epsilon V) + \nu_{\epsilon\epsilon}(\partial_q V)^2}; \tag{3.105}$$

where

$$\nu \overset{\text{def}}{=} \nu_{qq} - 2\nu_{q\epsilon}\frac{\partial_q V}{\partial_\epsilon V} + \nu_{\epsilon\epsilon}\left(\frac{\partial_q V}{\partial_\epsilon V}\right)^2. \tag{3.106}$$

The Lagrange multiplier, $\tilde{p}$, is the average pressure inside the liquid barrel. This can be seen by looking at the total energetic contribution of the pressure. As discussed in §1.2.2, the work done by the pressure of the fluid is $-\int p\,\mathrm{d}V$, integrated throughout the volume of the droplet. In this simplified model, the energy contribution corresponds to $-\tilde{p}\,V$. By construction, the two expressions must be equal, and thus, the Lagrange multiplier corresponds to the average pressure, i.e.,

$$\tilde{p} = \frac{1}{V}\int p\,\mathrm{d}V. \tag{3.107}$$

The equations of motion can be further simplified by reducing the system to a single degree of freedom, X. This eliminates the volume constraint but, because of that, knowledge of the average pressure is lost. The Lagrange function for this single degree of freedom is,

$$L(X,\dot{X}) = -F_V(X). \tag{3.108}$$

Following a similar procedure as above, the equation of motion now reads

$$\nu_X \dot{X} = -\frac{\mathrm{d}F_V}{\mathrm{d}X}. \tag{3.109}$$

The relation among the drag coefficients of Eqs. (3.101), (3.102) and (3.109) is found by means of the chain rule of the free-energy derivatives, i.e.,

$$\frac{\mathrm{d}F_V}{\mathrm{d}X} = \left[\partial_q F + (\partial_\epsilon F)\frac{\mathrm{d}\epsilon}{\mathrm{d}q}\right]\frac{\mathrm{d}q}{\mathrm{d}X}, \tag{3.110}$$

and the cyclic relation,

$$\frac{\partial_q V}{\partial_\epsilon V} = -\frac{\mathrm{d}\epsilon}{\mathrm{d}q}, \tag{3.111}$$

which, by comparison to Eqs. (3.94) and (3.106), gives

$$\nu_X(X) = \frac{1}{\alpha^2}\nu(q,\epsilon), \tag{3.112}$$

where the drag coefficient ν_X is defined by

$$\dot{\mathcal{E}} = -\nu_X \dot{X}^2. \tag{3.113}$$

In order to solve the equations of motion, an explicit expression of the friction coefficients is required. Strictly speaking, this task requires solving the hydrodynamic equations coupled with the equations that describe the motion of the contact lines. Nonetheless, within this coarse-grain approximation, the dissipation function will be estimated using a superposition of the friction forces arising from the motion of the contact lines and the flow pattern that develops during the translational motion of the droplet.

3.3.2 Flow Pattern

The friction forces that the droplet experiences depend on the details of the flow pattern within the liquid barrel, for this, the force-free Stokes equation will be used (see §1.2.4),

$$0 = -\boldsymbol{\nabla} p + \eta\nabla^2\boldsymbol{u}. \tag{3.114}$$

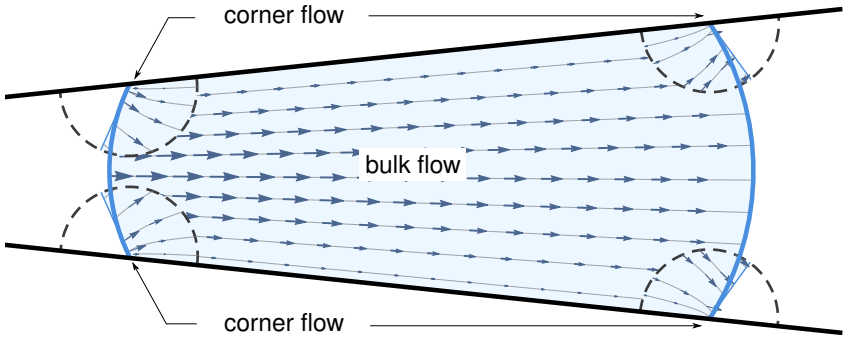

Figure 3.11: Decomposition of the flow field for the liquid barrel. The corner flow models the flow in the vicinity of the contact line which is described in the Cox-Voinov theory, and the bulk flow or the region far from the contact line, modelled by a Jeffery-Hamel flow.

This comprises a set of non-homogeneous linear partial different equations for the velocity field $\boldsymbol{u}$. Due to the linearity of the Stokes equation, $\boldsymbol{u}$ can be expressed in terms of a superposition of solutions. Therefore, a perturbative method can be applied to refine the approximation of the velocity field.

For this, two regions in the liquid can be differentiated: the region near the contact lines, and the bulk region of the barrel (see figure 3.11).

In the region near the contact lines, according to Voinov [35] and Cox [34], the flow pattern in the vicinity of the contact lines is generic for dynamic wetting problems [103]. It is determined by the competition between the capillary and viscous forces. As discussed in §1.2.5, this flow pattern is a corner flow defined by the contact angle, θ, at which the liquid-gas interface intersects the solid wall (see figure 3.12).

To describe the flow, a local reference frame to the contact line given by three unit vectors is defined: the vector orthonormal to the solid surface $\hat{\boldsymbol{n}}$, the vector parallel to the contact line tangent to the solid planes,

$$\hat{\boldsymbol{t}}(\phi) \stackrel{\text{def}}{=} \pm \frac{\partial_\phi \boldsymbol{x}_{\text{cl}\pm}}{|\partial_\phi \boldsymbol{x}_{\text{cl}\pm}|}(\phi), \tag{3.115}$$

as defined in Eq. (3.20), and the binormal vector perpendicular to both,

$$\hat{\boldsymbol{b}}(\phi) \stackrel{\text{def}}{=} \hat{\boldsymbol{n}} \times \hat{\boldsymbol{t}}(\phi). \tag{3.116}$$

These vectors serve as an orthonormal basis: a local system of coordinates is defined such that any position vector $\boldsymbol{r}'$ is given by the linear combination $\boldsymbol{r}' = x'\hat{\boldsymbol{b}} + y'\hat{\boldsymbol{t}} - z'\hat{\boldsymbol{n}}$.

Following Snoeijer [36], who focused on situations where the fluid of the outer phase has negligible viscosity, the velocity field of the viscous phase is expressed as

$$\boldsymbol{u}_{\text{corner}}(x', z') = \frac{v_{\text{cl}}}{\theta - \cos\theta \sin\theta} \left[-\frac{z'^2}{x'^2 + z'^2} \sin\theta\, \hat{\boldsymbol{b}} - \left(\frac{x'z'}{x'^2 + z'^2} - \phi' \sin\theta \right) \hat{\boldsymbol{n}} \right] + u_{\parallel}(z')\, \hat{\boldsymbol{t}}, \tag{3.117}$$

where $v_{\text{cl}} = \boldsymbol{v}_{\text{cl}} \cdot \hat{\boldsymbol{b}}$ is the velocity of the contact line, $u_{\parallel} = \boldsymbol{u} \cdot \hat{\boldsymbol{t}}$ is the velocity component of the fluid velocity (perpendicular to the $x'z'$–plane), and ϕ' is the angle of the point $(x',\, z')$ subtending from the solid wall ($\phi = 0$), and the interface ($\phi = \theta$).

The bulk of the barrel is the next region to be studied, i.e., the region far from the contact lines. Therefore, it is expected that fluid flow is governed by the geometry of

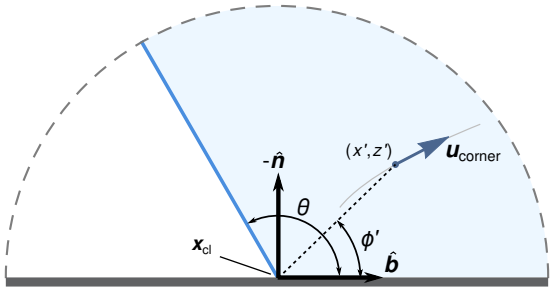

Figure 3.12: Local coordinate system for the corner flow. The origin of the local coordinate system, (x', z') is at the contact line $\boldsymbol{x}_{\mathrm{cl}}$. The liquid-gas interface makes an angle θ with respect to the vector $\hat{\boldsymbol{b}}$.

the solid planes and the structure of the pressure field. It will be analysed, first, by writing the flow between two non-parallel solid planes (see §2.3.3 and figure 3.6). For such a geometry, it is expected that the velocity profile forms a radial flow known as a Jeffery-Hamel flow [104, 105].

Using the result from Eq. (B.9) from Appendix B, the mean flow velocity of a Jeffery-Hamel flow is matched with the translational velocity of the barrel, $\dot{X}$. For a given a barrel configuration of width $2R_o$ and centre at X, the bulk flow velocity reads

$$\boldsymbol{u}_{\mathrm{bulk}}(\boldsymbol{x}) = \dot{X}\frac{X}{(x^2+z^2)^{1/2}} \cdot \frac{\cos 2\beta - \cos 2\omega}{\cos 2\beta - \beta^{-1}\sin 2\beta}(\cos\omega\,\hat{\boldsymbol{e}}_x + \sin\omega\,\hat{\boldsymbol{e}}_z). \tag{3.118}$$

The pressure profile of this flow reads

$$p_{\mathrm{bulk}}(\boldsymbol{x}) = \frac{2\gamma}{R_o}\left(\frac{\alpha+3\xi}{4\xi}\right) + \frac{\gamma}{2}\left(\frac{\alpha}{\xi}-1\right)\frac{R_o(\xi^2-1)}{x^2+z^2}. \tag{3.119}$$

To assess the quality of this approximation, the pressure profile of the barrel (Eq. (3.78)) and the Jeffery-Hamel pressure profile are compared (Eq. (3.119)). This is shown in figure 3.13. There can be observed a good match between both pressure profiles when $X \geq X_{\mathrm{e}}$, and larger deviations when the liquid barrel is closer to the apex of the wedge. This is expected at $X \ll X_{\mathrm{e}}$, since the shape of the droplet becomes increasingly distorted and the Jeffery-Hamel assumption begins to depart from the liquid barrel.

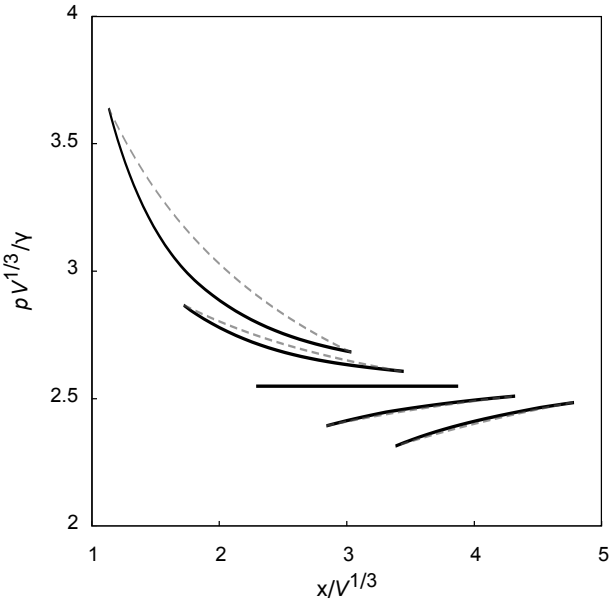

Figure 3.13: Comparison between the pressure profile of a liquid barrel along the bisector line (dashed curves), to the Jeffery-Hamel pressure profile (solid curves) for $\theta_e = 120°$, $\beta = 5°$ and barrel positions $(X - X_e)/V^{1/3} = -1, -1/2, 0, +1/2, +1$.

3.3.3 Effect of the Outer Phase in the Flow Field

It has been shown that the Jeffery-Hamel flow gives a good approximation of the flow in the bulk of the droplet at the transverse plane. In this section, the flow in the outer phase that surrounds the liquid is investigated.

The following analysis is based on the Boundary Integral Method [28], using the single-layer formulation (see §1.2.4). The general solution of the velocity of a fluid phase of viscosity η_{in} in contact with another phase of viscosity $\eta_{out} = \eta_{in}\lambda$, is given by

$$\boldsymbol{u}(\boldsymbol{x}) = \int \mathsf{G}(\boldsymbol{x}, \boldsymbol{x}') \cdot \boldsymbol{q}(\boldsymbol{x}')\, \mathrm{d}A_{lg}(\boldsymbol{x}'), \tag{3.120}$$

where G is a Green's tensor function that solves the Stokes equation, and the vector $\boldsymbol{q}(\boldsymbol{x})$ is the local *force density*, that drives the flow. The latter satisfies a Fredholm integral equation of the second kind,

$$\boldsymbol{q}(\boldsymbol{x}) = -\frac{1}{4\pi\eta_{in}} \cdot \frac{1}{1+\lambda} \Delta\boldsymbol{f}(\boldsymbol{x}) + \frac{\zeta}{4\pi}\, \hat{\boldsymbol{n}}_{lg} \cdot \int^{\mathscr{PV}} \mathsf{T}(\boldsymbol{x}, \boldsymbol{x}') \cdot \boldsymbol{q}(\boldsymbol{x}')\, \mathrm{d}A_{lg}(\boldsymbol{x}'), \tag{3.121}$$

where $\zeta = (1-\lambda)/(1+\lambda)$, $\Delta\boldsymbol{f} = 2\gamma\kappa\hat{\boldsymbol{n}}_{lg}$ is force discontinuity due to the surface tension, T is a third rank Green's tensor function, and the superscript $\mathscr{PV}$ indicates that the Cauchy Principal Value of the integral should be taken.

The Green's function relevant to the wedge geometry, i.e., one that vanishes at the solid planes, was given by Osano and Hasimoto [106]; using their result to compute the force density, however, has considerable difficulties. For that reason, the analysis is restricted to the flow in the bisector plane, and therefore, the 2D free-space Oseen tensor will be used as the Green function G, i.e.,

$$\mathsf{G}(\boldsymbol{x}, \boldsymbol{x}') = -\mathbb{I} \log \tilde{x} + \frac{\tilde{\boldsymbol{x}}\,\tilde{\boldsymbol{x}}}{|\tilde{\boldsymbol{x}}|^2}, \tag{3.122}$$

and for the third rank stress tensor Green function,

$$\mathbf{T}(\boldsymbol{x},\boldsymbol{x}') = -4\frac{\tilde{\boldsymbol{x}}\,\tilde{\boldsymbol{x}}\,\tilde{\boldsymbol{x}}}{\tilde{x}^4}, \tag{3.123}$$

where $\tilde{x} = |\tilde{\boldsymbol{x}}|$, and $\tilde{\boldsymbol{x}} = \boldsymbol{x}' - \boldsymbol{x}$.

Eq. (3.121) can be solved in polar coordinates. From Eq. (3.76), the force discontinuity can be expressed in the angular coordinate φ,

$$\Delta\boldsymbol{f} = \frac{\gamma}{R_o}\left(\frac{\alpha+\xi+2\cos\varphi}{\xi+\cos\varphi}\right)\hat{\boldsymbol{e}}_r, \tag{3.124}$$

and express the force density as a Fourier series

$$\boldsymbol{q}(\varphi) = \hat{\boldsymbol{e}}_r\sum_{m=0}^{\infty} b_m\cos m\varphi + \hat{\boldsymbol{e}}_\varphi\sum_{m=1}^{\infty} c_n\sin m\varphi, \tag{3.125}$$

where the terms that do not satisfy the reflection symmetry have been dropped ($\varphi \to -\varphi$). With this, Eq. (3.121) turns into an algebraic equation for the coefficients b_m and c_m.

After some simplifications, the force density results in

$$\boldsymbol{q}(\varphi,R_o,\xi,\alpha) = (b_0+b_1\cos\varphi)\,\hat{\boldsymbol{e}}_r - b_1\sin\varphi\,\hat{\boldsymbol{e}}_\varphi + \frac{1}{4\pi\eta_{\text{in}}(1+\lambda)}\Delta\boldsymbol{f}, \tag{3.126}$$

where the coefficients are

$$b_0 = \frac{\gamma\,\zeta}{4\pi\eta_{\text{in}}(1+\lambda)R_o}\cdot\frac{\alpha-\xi+2\sqrt{\xi^2-1}}{(\zeta+2)\sqrt{\xi^2-1}} \tag{3.127}$$

and

$$b_1 = \frac{\gamma\,\zeta}{4\pi\eta_{\text{in}}(1+\lambda)R_o}\cdot\frac{(\xi-\alpha)(\xi-\sqrt{\xi^2-1})}{(\zeta-2)\sqrt{\xi^2-1}}. \tag{3.128}$$

Eq. (3.126) can now be used in conjunction with Eq. (3.120) to integrate the velocity field. An example of this is shown in figure 3.14 by numerical integration of the force density. There, streamlines and vector plots are shown for droplets moving outwards and inwards for a vanishing viscosity ratio $\lambda = 0$. The structure of the flow shows a slow recirculating flow that vanishes in a short vicinity of the droplet. Also, the formation of two vortices at the sides of the liquid barrel can be observed. The velocity field vanishes at the centres of the vortices, reducing drag, and thus, their presence allow a faster motion of the centre of the droplet. Therefore, due to the interaction of the outer phase, a significant reduction of the bulk dissipation relative to the expected reference Jeffery-Hamel flow occurring throughout the volume of the droplet.

In the context of the boundary-layer, a fluid near a solid plane is expected to acquire a parabolic profile [107]. In this case, due to conservation of flux for a diverging confinement, a more adequate profile is the Jeffery-Hamel flow given in Eq. (3.118). The amplitude of such profile is governed by the gradients in the pressure [108]; in this case, prescribed by the curvature of the liquid-gas interface. Therefore, the structure of the flow in the bulk of a moving droplet is expected to be a Jeffery-Hamel flow in the transverse plane, which includes two side vortices in the orthogonal plane as shown in figure 3.14.

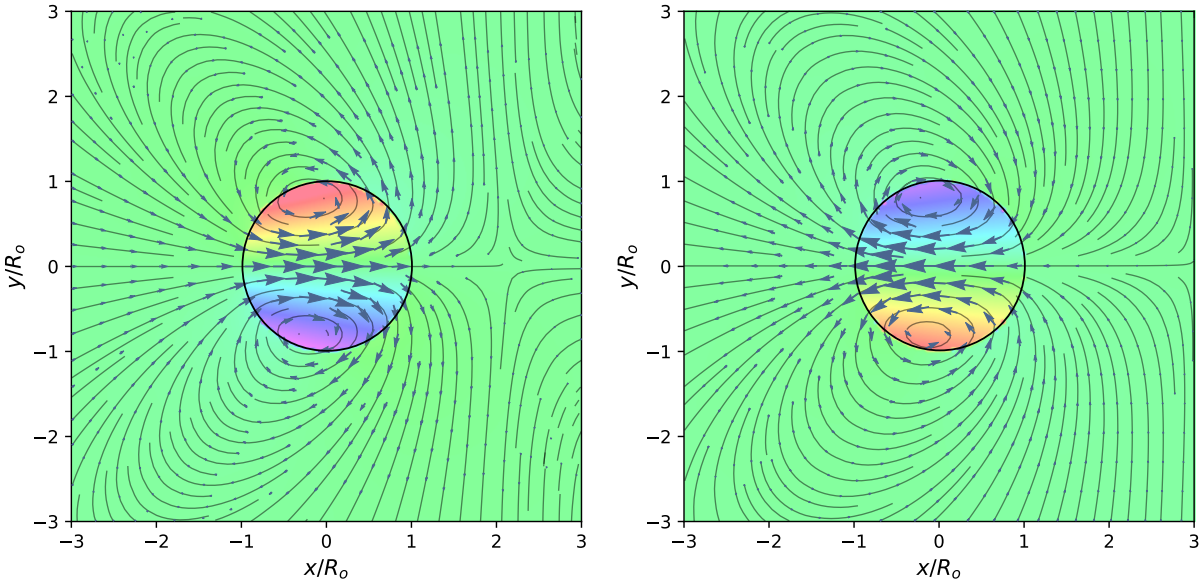

Figure 3.14: Stream and vector plots at the bisector plane of the droplet at positions (a) $X - X_e = -V^{1/3}$, and (b) $X - X_e = +V^{1/3}$ for outwards and inwards motion, respectively as the liquid barrel moves in the absence of external forces. The colour map shows the vorticity in the z direction. The viscosity ratio is set to $\lambda = 0$.

3.3.4 Estimating the Dissipation Function

Having developed a model for the flow pattern within the barrel, the dissipation function can now be derived. As discussed by de Gennes [18], the total dissipation will be the sum of the dissipations at three different length scales:

$$\dot{\mathcal{E}} = \dot{\mathcal{E}}_{\text{bulk}} + \dot{\mathcal{E}}_{\text{corner}} + \dot{\mathcal{E}}_{\text{cl}}, \tag{3.129}$$

The first two contributions, $\dot{\mathcal{E}}_{\text{bulk}}$, and $\dot{\mathcal{E}}_{\text{corner}}$, are hydrodynamic in origin, and $\dot{\mathcal{E}}_{\text{cl}}$ accounts for the dissipation that occurs at the microscopic scale, sometimes referred to as the 'true' contact line [18].

The dissipation in the bulk of the fluid can be readily obtained by evaluating Eq. (1.32) using the velocity field from Eq. (3.118), this is,

$$\dot{\mathcal{E}}_{\text{bulk}} = -\frac{1}{2}\eta_{\text{in}} \int (\boldsymbol{\nabla u}_{\text{bulk}} + \boldsymbol{\nabla u}_{\text{bulk}}^{T})^2 \, \mathrm{d}V. \tag{3.130}$$

The dissipation function in Eq. (3.130) considers a Jeffery-Hamel flow that is homogeneous along the y axis. Therefore, the integral is bounded to the region within the liquid barrel in which the dissipation of the Jeffery-Hamel flow takes place. This can be quantified as an effective volume, $V_{\text{eff}} \leq V$. The effective volume, V_{eff}, is an adjustable parameter that excludes the volume of the corner flow, and also the volume that contains the side vortices that facilitate the motion of the fluid (see §3.3.3). Then, from Eq. (3.130),

$$\dot{\mathcal{E}}_{\text{bulk}} = -\frac{6\pi\eta_{\text{in}}}{|\cos\theta_e|} \frac{V_{\text{eff}}}{V} \frac{\alpha\,\xi^2}{(\xi^2-1)^{3/2}} R_o \dot{X}^2 \tag{3.131}$$

is obtained (see Appendix D for details).

At the corner-flow length scale, the stresses that locally bend the interface are the main causes of dissipation [109]. This induces a change in the contact angle to a dynamic value of θ [34]. This deviation out of equilibrium results in a force per unit length in the perpendicular direction to the contact line given by

$$\boldsymbol{f}_{\text{corner}} = \gamma(\cos\theta_{\text{e}} - \cos\theta)\,\hat{\boldsymbol{b}} \approx \gamma(\theta - \theta_{\text{e}})\sin\theta_{\text{e}}\,\hat{\boldsymbol{b}}. \tag{3.132}$$

Then, the energy dissipated is

$$\dot{\mathcal{E}}_{\text{corner}} = 2\oint_{\text{cl}} \boldsymbol{f}_{\text{corner}} \cdot \boldsymbol{v}_{\text{cl}}\,\mathrm{d}l, \tag{3.133}$$

where $\mathrm{d}l$ is the differential arc-length element of the contact line.

The apparent contact angle is obtained from the Cox-Voinov expression (see 1.2.5). For small differences in the contact angle, the integral in Eq. (1.43) can be approximated as,

$$\frac{\theta - \theta_{\text{e}}}{f_{\text{CV}}(\theta_{\text{e}}, \lambda)} \approx \frac{\eta_{\text{in}}\, v_{\text{cl}}}{\gamma} \log\frac{\ell_{\text{M}}}{\ell_{\text{m}}}. \tag{3.134}$$

where $f_{\text{CV}}(\theta_{\text{e}}, \lambda)$ is given by Eq. (1.44). In the limit of vanishing outer viscosity ($\lambda \to 0$),

$$f_{\text{CV}}(\theta, 0) = \frac{2\sin\theta_{\text{e}}}{\theta_{\text{e}} - \sin\theta_{\text{e}}\cos\theta_{\text{e}}}. \tag{3.135}$$

The force per unit length is then obtained by eliminating the difference in contact angles in Eq. (3.134), i.e.,

$$\boldsymbol{f}_{\text{corner}} = \eta_{\text{in}} v_{\text{cl}}\, f_{\text{CV}}(\theta_{\text{e}}, 0)\sin\theta_{\text{e}} \log\frac{\ell_{\text{M}}}{\ell_{\text{m}}}\,\hat{\boldsymbol{b}}. \tag{3.136}$$

Therefore, the dissipation contribution due to the corner flow is,

$$\dot{\mathcal{E}}_{\text{corner}} = -\frac{4\eta_{\text{in}}\sin^2\theta_{\text{e}}}{\theta_{\text{e}} - \sin\theta_{\text{e}}\cos\theta_{\text{e}}} \log\frac{\ell_{\text{M}}}{\ell_{\text{m}}} \oint_{\text{cl}} v_{\text{cl}}^2\,\mathrm{d}l. \tag{3.137}$$

Note that the integrand of Eq. (3.137) is quadratic in v_{cl}, therefore regardless of the direction of motion of the contact line, the dissipation function is always negative. The closed-loop integral in Eq. (3.137) can be approximated as (see Appendix E),

$$\oint_{\text{cl}} v_{\text{cl}}^2\,\mathrm{d}l \approx \pi R_o \dot{X}^2. \tag{3.138}$$

At length scales below the microscopic length, ℓ_{m}, dissipative processes are determined by the motion of molecules of the two phases and the interaction with the solid surface. According to Ruijter [49], the corresponding friction force is proportional to v_{cl}, i.e.,

$$\boldsymbol{f}_{\text{cl}} = \zeta_0 v_{\text{cl}}\,\hat{\boldsymbol{b}}, \tag{3.139}$$

where the constant of proportionality, ζ_0, is described in §1.2.5. This leads to the dissipation contribution of the contact line,

$$\dot{\mathcal{E}}_{\text{cl}} = 2\zeta_0 \oint_{\text{cl}} v_{\text{cl}}^2\,\mathrm{d}l, \tag{3.140}$$

Adding all the dissipation contributions, Eqs. (3.131), (3.137), and (3.140), gives the total dissipation. Using Eq. (3.113), the friction coefficient is obtained,

$$\nu_X(X,R_o) \approx \left[\frac{6\pi\eta_{\rm in}}{|\cos\theta_{\rm e}|}\frac{V_{\rm eff}}{V}\frac{\alpha X^2 R_o}{(X^2-R_o^2)^{3/2}} + \frac{4\pi\eta_{\rm in}\sin^2\theta_{\rm e}}{\theta_{\rm e}-\sin\theta_{\rm e}\cos\theta_{\rm e}}\log\frac{\ell_{\rm M}}{\ell_{\rm m}} + 2\pi\zeta_0\right]R_o, \quad (3.141)$$

where the corrections that involve $\dot{R}_o$ have been neglected since they come with high-order powers of β and ϵ. This also implies that the generalised velocity $\dot{\epsilon}$ does not play significant role in the dissipation, as, $\nu_{q\epsilon} \approx \nu_{\epsilon\epsilon} \approx 0$. Consequently, the only friction coefficient, which dominates the translational motion of the barrel, is $\nu_{qq} = \nu = \alpha^2\nu_X$.

3.3.5 Near Equilibrium Relaxation

Having obtained the dissipation coefficients, the analysis of the motion of the liquid barrel can be completed. The equation of motion of the liquid barrel (Eq. (3.109)) reads,

$$\dot{X} = -\frac{1}{\nu_X(X)}\frac{{\rm d}F_V(X)}{{\rm d}X}. \quad (3.142)$$

The right hand side of Eq. (3.142) depends on the position X. In the vicinity of equilibrium, it can be expanded in terms of power of $(X - X_{\rm e})$ and the equation of motion reduces to

$$\dot{X} = -\frac{1}{\tau}(X-X_{\rm e}) + O(X-X_{\rm e})^2, \quad (3.143)$$

where

$$\tau \stackrel{\rm def}{=} \frac{\nu_X(X_{\rm e})}{k}. \quad (3.144)$$

Here,

$$k \stackrel{\rm def}{=} \left.\frac{{\rm d}^2F_V}{{\rm d}X^2}\right|_{X=X_{\rm e}}, \quad (3.145)$$

is defined from the expansion around equilibrium of the free energy,

$$F_V(X) = F_{\rm e} + \frac{1}{2}k\,(X-X_{\rm e})^2 + O(X-X_{\rm e})^3. \quad (3.146)$$

The role of k is to act as a restitution coefficient, a force per unit displacement that restores the barrel to equilibrium. From Eq. (3.59) and Eq. (3.57), it reads

$$k(\theta_{\rm e},\beta) = 6\gamma\frac{a_0}{\alpha^2}\left(1-\frac{3a_0a_2}{a_1^2}\right) \quad (3.147)$$

$$= \pi\gamma\frac{\sin^2\beta}{\cos^2\theta_{\rm e}}(\cos 3\theta_{\rm e} - 9\cos\theta_{\rm e})\left[1+\frac{2\cos^2\theta_{\rm e}(\cos 2\theta_{\rm e}-5)}{(2\theta_{\rm e}-\pi-\sin 2\theta_{\rm e})^2}\right]. \quad (3.148)$$

Evaluating the friction coefficient (Eq. (3.141)) close to equilibrium results in

$$\nu_X(X_{\rm e}) \approx \left(\frac{6\pi\eta_{\rm in}}{|\cos\theta_{\rm e}|}\frac{V_{\rm eff}}{V} + \frac{4\pi\eta_{\rm in}\sin^2\theta_{\rm e}}{\theta_{\rm e}-\sin\theta_{\rm e}\cos\theta_{\rm e}}\log\frac{\ell_{\rm M}}{\ell_{\rm m}} + 2\pi\zeta_0\right)\left[\frac{6V}{\pi(\cos 3\theta_{\rm e}-9\cos\theta_{\rm e})}\right]^{1/3}. \quad (3.149)$$

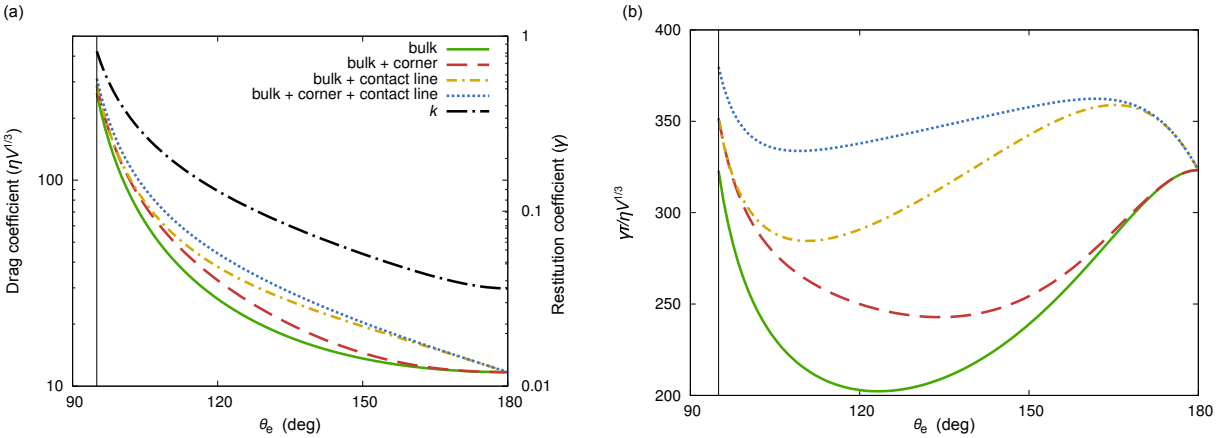

Figure 3.15: Bulk, corner flow and contact line contributions to (a) the drag coefficient, ν_X and (b) the relaxation time, τ, of the translational motion of barrels along the bisector plane of a wedge of angle $\beta = 5°$. In (a) the restitution coefficient, k, is superimposed on the right-hand side axis. The vertical lines in both plots correspond to the limiting wetting angle $\theta_e = 90° + \beta$.

The solution of Eq. (3.143) is,

$$X(t) = [\,X(0) - X_e\,]\,e^{-t/\tau} + X_e. \tag{3.150}$$

Consequently, near equilibrium, the liquid barrel relaxes at an exponential rate. The characteristic time scale, τ, in which this occurs, is determined by the ratio of the friction to restitution constants.

Figures 3.15(a) and (b) show plots of k, ν_X, and τ as functions of the equilibrium angle. In the limit $\theta_e \to 90° + \beta$, the barrel equilibrium position is closer to the apex of the wedge. Geometrically, this implies a stronger confinement, and thus both the bulk contribution to the friction coefficient and the restitution constant reach local maxima in this limit. For larger θ_e, both quantities decrease monotonically, leading to an initial decrease in the relaxation time. However, the rate at which k decreases becomes dominant with increasing θ_e. This is because at higher equilibrium contact angle the barrels keep an approximately spherical shape for larger displacements from equilibrium. As a result, the relaxation time reaches a minimum, beyond which it increases with θ_e until it reaches a maximum saturation value as $\theta_e \to 180°$.

The typical magnitude of the corner flow is controlled by the length scale separation between the macroscopic length scale ℓ_M, and the microscopic length scale ℓ_m. The microscopic length depends on the details of the liquid-gas interactions and the roughness of the solid surface [33] that characterise the motion of the interface at the level of the contact line [38]. Experiments by [110, 111], reveal that in narrow confinements, the relative velocity of a liquid near the bounding solid is not zero. The speed of this shear motion was found to be proportional to the viscous stress, [112] where the constant of proportionality manifests as a length-scale of a few nanometres.

For a macroscopic droplet, $\ell_M \sim R_e \sim 1$ mm can be fixed and comparing the microscopic length ℓ_m to the slip-length then, $\ell_M/\ell_m \approx 10^5$. As shown in figure 3.15(a), this additional contribution is important at intermediate angles, and vanishes in the limit $\theta_e \to 180°$. This is the combined effect of a vanishing contour length and a less confined corner flow at higher opening angle. As a result of the corner flow, the minimum in the

relaxation time is displaced to a higher contact angle, as shown in figure 3.15(b).

The contribution of contact line dissipation to the drag coefficient is controlled by the (constant) microscopic friction coefficient ζ_0 and the contour length of the contact line. Therefore, this term decays more slowly than the corner flow term in Eq. (3.149). Estimating ζ_0 will, in general, be subject to the details of a specific model [109, 113]. For the sake of illustration, the case where $\zeta_0 = 3\eta$ in (3.149) is examined as a specific example where the corner and contact line dissipation are comparable in magnitude. As shown in figures 3.15(a) and 3.15(b), the main effect of this term is a slower decay in the contact line dissipation with increasing contact angle, which in turn leads to an overall broadening of the maximum in the relaxation time.

3.4 Concluding remarks

In this chapter, an analytical model to study the statics and dynamics of droplets in hydrophobic wedges has been proposed. First, the shape that the droplet acquires is studied from a sharp-interface perspective based on a free energy approach. It was proposed that the "liquid barrel" gives a good approximation for a static case in the presence of an external force. This assumption is validated by comparing the energy landscapes and pressure profiles with numerical methods.

Having validated the liquid barrel assumption, the model is extended to analyse dynamic situations in the absence of external forces. Continuing with the free energy approach, the equations of motion were deduced by considering the restitutive forces and dissipative forces. The dissipative forces were estimated from three contributions: the viscous friction of bulk of the droplet, the dissipation in the vicinity of the contact lines, and the microscopic drag forces arising from the true contact lines.

Chapter 4

Lattice-Boltzmann Simulations

Diffuse-interface numerical simulations are amenable methods to study the dynamics of liquid barrels, as they have the capacity of modelling capillary phenomena, including the dynamic wetting of smooth solid surfaces [42, 26, 39, 44, 40, 45, 114]. The main advantage of this approach is that the interface dynamics occurs naturally through convection and diffusion—the latter driven by chemical potential gradients [41, 42, 9]. This contrasts with sharp-interface models, where one needs to track the evolution of the interface [115] and to specify a boundary condition for the contact line in an *ad hoc* manner [103].

Following §1, the relevant equation to analyse the translational motion of a droplet in a wedge is the Navier-Stokes equation. This equation models the evolution of the velocity field, in the incompressible limit, it reads (Eq. (1.27)),

$$\rho\left(\partial_t + \boldsymbol{u}\cdot\boldsymbol{\nabla}\right)\boldsymbol{u} = -\boldsymbol{\nabla}\cdot\mathsf{P} + \eta\nabla^2\boldsymbol{u}. \tag{4.1}$$

To model the behaviour of the interfaces with a continuous phase field, ϕ, the pressure tensor, P, is defined as in Eq. (2.20),

$$\mathsf{P} = \left[\frac{1}{4}B(\phi^2-1)(3\phi^2+1) - K\phi\nabla^2\phi - \frac{1}{2}K|\boldsymbol{\nabla}\phi|^2\right]\mathsf{I} + K\boldsymbol{\nabla}\phi\boldsymbol{\nabla}\phi, \tag{4.2}$$

where the parameters B and K are tuned according to Eqs. (1.20) and (1.16) to give values of surface tension and interface thickness, respectively.

Additionally, the Cahn-Hilliard equation (Eq. (1.26)),

$$(\partial_t + \boldsymbol{u}\cdot\boldsymbol{\nabla})\phi = M\nabla^2\mu, \tag{4.3}$$

preserves continuity of the phase field, and allows motion of the contact lines by diffusive processes. Similarly, the chemical potential, μ, is defined by the phase field as in Eq. (1.12),

$$\mu = B\phi(\phi^2-1) - K\nabla^2\phi. \tag{4.4}$$

The wettability of the wedge planes is determined by introducing the boundary condition of Eq. (1.23),

$$K\hat{\boldsymbol{n}}\cdot\boldsymbol{\nabla}\phi = \chi, \tag{4.5}$$

where, the wetting potential, χ, is specified by the equilibrium contact angle, θ_e, according to Eq. (1.25).

To integrate the Navier-Stokes coupled with the Cahn-Hilliard equations, the D3Q15 lattice-Boltzmann method, as presented in §2, was used.

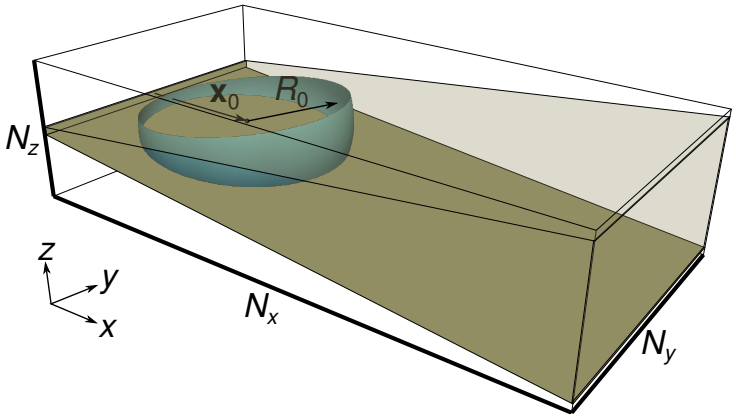

Figure 4.1: Schematics of the simulation set-up. Two planes forming a wedge with an opening angle β are contained in a simulation domain of dimensions $N_x \times N_y \times N_z$. The initial condition consists of a truncated spherical droplet of radius R_0 centred at a position $\boldsymbol{X}_0$.

4.1 Simulation Set-Up

A simulation domain contained in a box of dimensions $N_x \times N_y \times N_z$, as shown in figure 4.1, was set. In the frame of reference of the simulation box, the walls of the wedge are fixed at the planes $(\boldsymbol{x} - \boldsymbol{d}) \cdot \hat{\boldsymbol{n}} = 0$. The offset $\boldsymbol{d}$ is introduced to avoid that the solid walls intersect within the simulation domain, which was found to give rise to numerical errors. Setting $\boldsymbol{d} \cdot \hat{\boldsymbol{n}} = 1.72$ allowed at least two nodes of separation between the boundaries. Periodic boundary conditions were used along the y direction, and impose two other solid planes at $x = 1/2$ and $x = N_x - 3/2$.

As an initial condition, the fluid is at rest. The interface has a spherical configuration with radius R_0 and centre $\boldsymbol{X}_0$ as shown in figure 4.1. This corresponds to setting the following initial velocity and phase-field profiles

$$\boldsymbol{u}(\boldsymbol{x}, t = 0) = 0, \tag{4.6}$$

$$\phi(\boldsymbol{x}, t = 0) = \tanh\left[\frac{R_0 - |\boldsymbol{x} - \boldsymbol{X}_0|}{\sqrt{2}\ell}\right]. \tag{4.7}$$

Two initial values of the centre of sphere were used, $\boldsymbol{X}_0 = (0.75N_x, 0, 0)$ and $\boldsymbol{X}_0 = (0.24N_x, 0, 0)$, which, for the range of tapering and contact angles considered, correspond to the droplet initial positions, $X_0 > X_\mathrm{e}$ and $X_0 < X_\mathrm{e}$. These initial conditions allow the droplet to move inwards or outwards of its equilibrium position.

The instantaneous volume of the droplet, $V(t)$, and its position, $X(t)$, are computed as follows. To calculate the volume of the droplet, the formula

$$V(t) = \sum_{\boldsymbol{x} \in \Omega} \frac{\phi(\boldsymbol{x}, t) + 1}{2} \quad \text{if } \phi > -1, \tag{4.8}$$

was used. To calculate $X(t)$, a slice of the phase field is taken at the bisector plane, $\boldsymbol{x} = (x, y, 0)$, and use a linear interpolation scheme to find the interface—defined as the level curve $\phi = 0$. $X(t)$ is taken as the x coordinate of the centre of the circle that best fits the interface profile using a Least Mean Squares algorithm.

Parameter	Value*	Parameter	Value	Parameter	Value
N_x	256	γ	0.008	ρ_{in}	1.0
N_y	128	θ_{e}	100°—120°	ρ_{out}	0.4
N_z	32—76	ℓ	3.54	η_{in}	1/6—1
β	5°—8°	M	1.5×10^{-4}—5.0×10^{-3}	η_{out}	1/15

*Unless otherwise specified, values are reported in lattice-Boltzmann units (lBu).

Table 4.1: Lattice-Boltzmann simulation parameters.

The values of the simulation parameters used are summarised in table 4.1. For these parameter values, it was found that the system reaches equilibrium in a typical time-scale of $\sim 5 \times 10^6$ iterations.

4.2 Simulation Results

4.2.1 Equilibrium

First, the equilibrium configuration of the droplet as a quantitative validation of accuracy of the numerical method is performed.

As expected from §3.1.3, the interface adopts the shape of a sphere truncated by the solid planes of radius and position consistent with by Eqs. (3.65) and (3.66) (figure 4.2(a)); the simulations agree with the analytical prediction over the whole range of equilibrium and wedge angles considered (see figures 4.2(b) and 4.2(c)). This agreement holds regardless of the initial conditions (compare symbols to solid lines in the figure).

Beyond the configuration of the interface, the simulations provide details of the equilibrium hydrodynamic fields. The velocity field vanishes everywhere, except for small currents ($\sim 10^{-5}$ in lattice-Boltzmann units; see figure 4.3a) which arise due to spurious effects in the lattice-Botzmann method [116]. Despite being augmented by the lower density and viscosity of the outer phase, they have a negligible effect on the liquid barrel.

The scalar pressure profile, $p \equiv \text{tr}\mathbf{P}/3$, along the centre-line of the droplet, dips at two points (see figure 4.3(b)), these correspond to the interfacial regions (compare to the phase-field profile shown as a dashed line). As pointed out by Lee and Lin [7], this is due to the free-energy density contribution to the pressure and gives rise to the surface tension effect. The pressure is higher in the bulk of the inner phase than in the outer phase. This is the combined effect of surface tension and the curvature of the interface, as expected from the Young-Laplace relation [3].

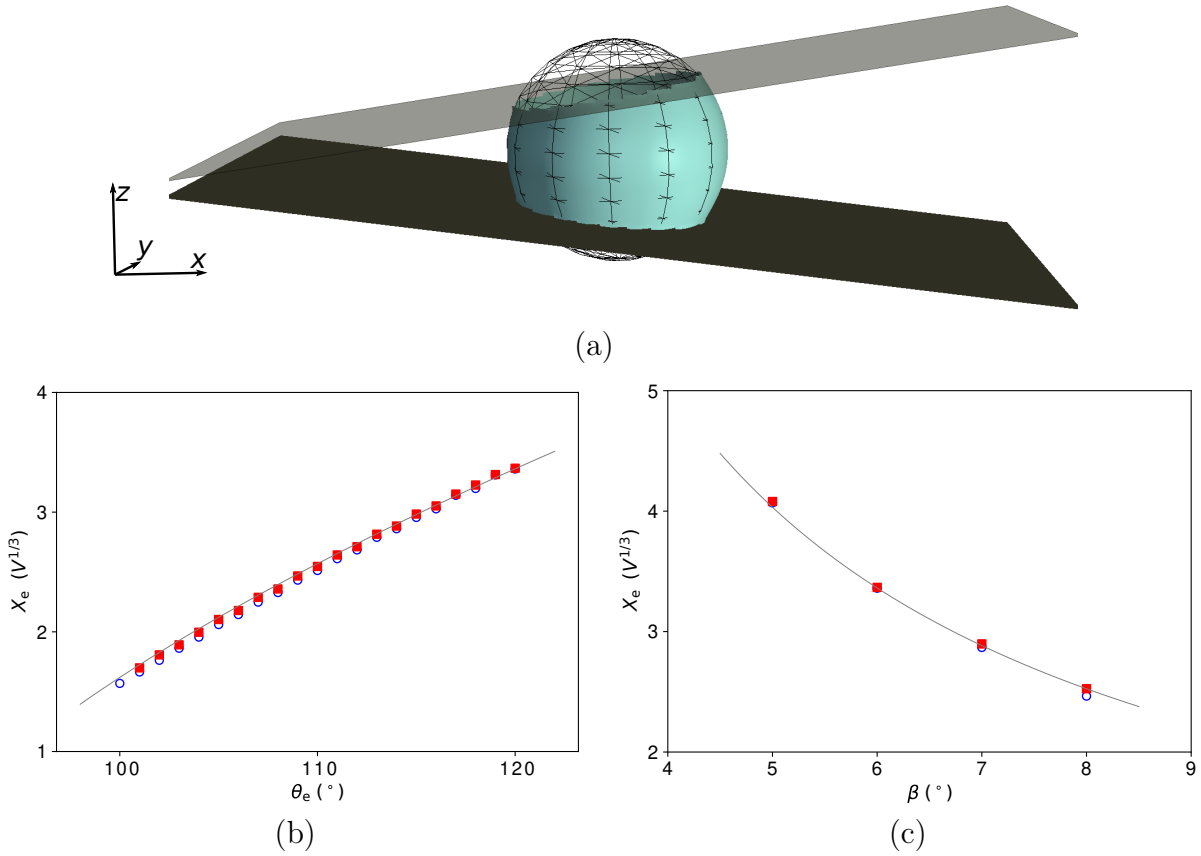

Figure 4.2: Equilibria of liquid barrels in wedges. (a) Interface configuration of a barrel of equilibrium contact angle $\theta_e = 110°$ in a wedge of opening angle $\beta = 6°$. The interface adopts the shape of a truncated sphere. The expected analytical result is shown as a wireframe. (b) Equilibrium position of the liquid barrel as a function of θ_e at constant $\beta = 6°$. (c) Equilibrium position as a function β at constant $\theta_e = 110°$. The symbols indicate the two types of initial conditions used in the simulations: $X_0 > X_e$ (○) and $X_0 < X_e$ (■). The solid lines correspond to the analytical prediction. The simulation parameters are $M = 5 \times 10^{-3}$ and $\eta_{in} = 1/3$.

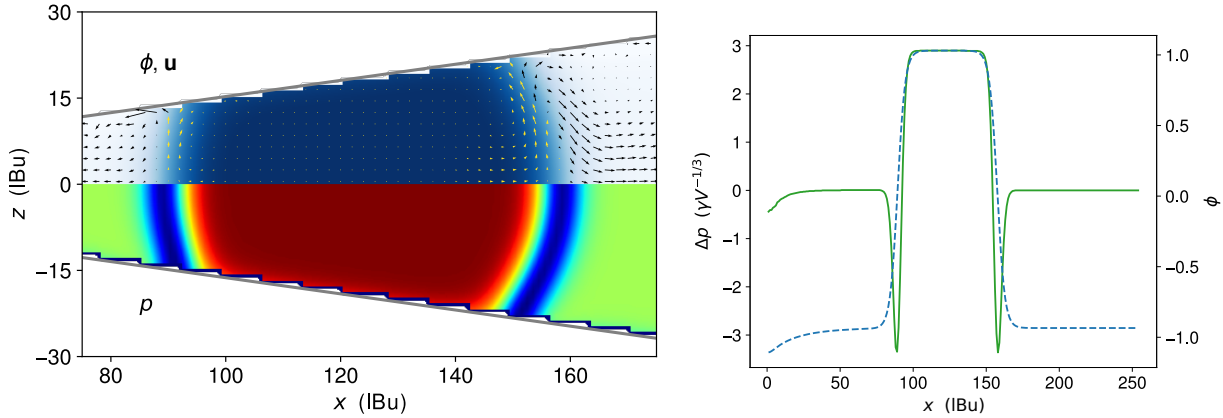

Figure 4.3: Equilibrium hydrodynamic fields of a liquid barrel of contact angle $\theta_e = 110°$ in a wedge of opening angle $\beta = 6°$. (a) Cross-sections of the phase field (colour plot, top) and velocity field (vector plot) and barometric pressure (colour plot, bottom). The magnitude of the arrows has been rescaled by a factor of 10^5 for visibility. (b) Pressure (solid line) and phase field (dashed line) profiles along the centre line (x-axis). The simulation parameters are $M = 5 \times 10^{-3}$ and $\eta_{in} = 1/3$.

4.2.2 Translational Motion along the Wedge

Now, the translational motion of the droplet during equilibration is analysed. Figure 4.4(a) shows a sequence of simulation snapshots at intervals of 8×10^5 time steps for droplets moving inwards and outwards to the same equilibrium position. In both cases, the position of the droplet as a function of time suggests an exponential relaxation (figure 4.4(b) and inset). For an exponential decay, (see §3.3.5), it is expected that the position of the droplet, X, obeys the relation,

$$\dot{X} = -\frac{1}{\tau}(X - X_\mathrm{e}), \tag{4.9}$$

where $\dot{X}$ is the translational velocity of the droplet and τ is the relaxation time. It was found that the linear relation in Eq. (4.9) is satisfied by the liquid barrels over the whole range of contact angles considered in the simulations, and that, for constant values of all other parameters (β, M and η_in), the data collapse onto a single line (see figure 4.5(a)). This implies that the relaxation time does not change significantly with the contact angle.

While at lower contact angles, a stronger restitutive force due to confinement is expected, and also a higher hydrodynamic dissipation near the contact lines due to the development of vortices in the inner (more viscous) phase. It can be inferred that the variation of the dissipative and conservative forces with the contact angle is therefore approximately equal, thus cancelling out a net dependence of τ on θ_e.

The dependence of τ with the wedge angle, β, was also tested; from the simulation results (figure 4.5(b)) it was found a scaling $-\dot{X}/\sin^2\beta \propto (X - X_\mathrm{e})$, and thus $\tau \propto 1/\sin^2\beta$. Physically, this functional dependence implies that as the wedge gets narrower by decreasing β, the droplet takes more time to reach its equilibrium point. After an analysis of the restoring forces [94], the projection of surface tension and pressure along coordinate of translational motion give a net capillary force proportional to $\sin^2\beta$. This implies that the dependence of β on the relaxation time is given by the restitutive forces alone and not on dissipative forces.

The plots in figures 4.4 (b, inset) and 4.5 show faint oscillations in the position of the droplet and velocity. These oscillations are unphysical, and their origin is attributed to an aliasing effect in the discretisation of the boundary. Due to the lattice structure of the simulation domain, the discretisation of a boundary deviated from a straight angle will create spatial aliasing on the boudnaries. This is because the wavelength of the oscillations coincide with the passing of the interface at every lattice site, and further amplified when crossing an aliasing step.

The numerical noise due to the aliasing of the boundary creates a small pinning effect to the contact lines, equivalent to roughness or imperfections in the surface. As the droplet relaxes, the restitutive forces become weaker and thus the effect is more contrasting. Applying the numerical algorithm presented in §2.2 substantially reduced the spatial aliasing effect and the relaxation process of the droplet to equilibrium can be analysed with a high degree of accuracy.

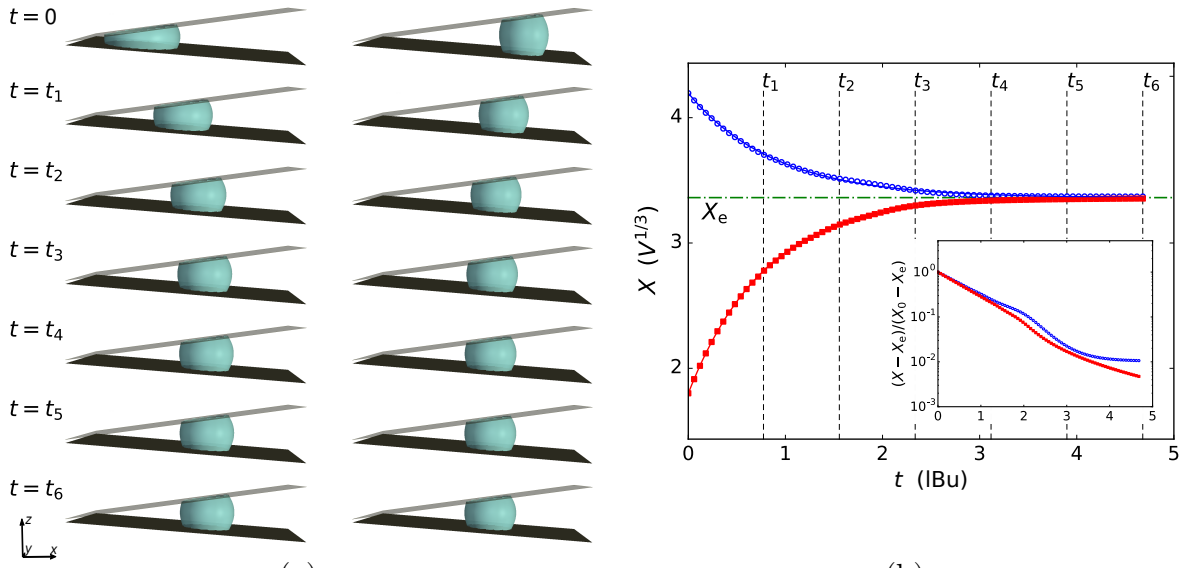

(a) (b)

Figure 4.4: Motion of the liquid barrel and relaxation to the equilibrium configuration. (*a*) Snapshots of the time evolution of the droplet. (*b*) Evolution in the position of the droplet, the symbols (■) denote outwards motion, in contrast with (○) that represent inward motion. The dot-dashed line indicates the equilibrium position. In the inset, a semilogarithmic plot of the the distance to equilibrium as a function of time is presented. The simulations were carried out for the angles $\beta = 6°$, and $\theta_e = 120°$, the snapshots are taken every 8×10^5 timesteps for a total of 4.8×10^6 iterations. The mobility and viscosity were set to $M = 0.005$ and $\eta_{in} = 1/3$.

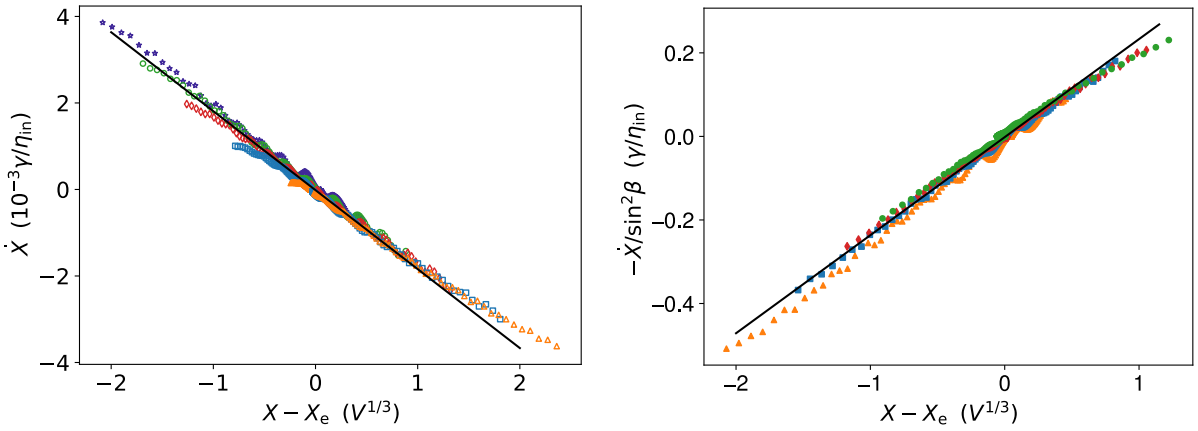

(a) (b)

Figure 4.5: Correlation of the instantaneous displacement and velocity of liquid barrels. (a) Data collapse for liquid barrels of different contact angles and fixed wedge angle $\beta = 5°$; the symbols correspond to $\theta_e = 100°$ (△), 105° (□), 110° (◇), 115° (○), and 120° (⋆). (b) Data collapse for different opening angles: $\beta = 5°$ (▲), 6° (■), 7° (◆) and 8° (●), and fixed contact angle $\theta_e = 120°$. The solid lines correspond to linear trends close to equilibrium.

4.2.3 Driving Forces

To better understand the mechanisms driving the relaxation process, the instantaneous pressure and chemical potential fields will now be considered. It was found that the slope of the pressure profile, $\partial p/\partial x$, is negative for droplets that move outwards and positive for droplets that move inwards (see figure 4.6). This indicates the action of a net capillary driving force resulting from Laplace pressure differences.

Along with the numerical results, the pressure profile derived in §3.1.4 and the average pressure from the Lagrange multiplier from §3.3.1 is presented for comparison in figure 4.6(b). It was found a good qualitative agreement of the numerical results (solid lines) with the analytical results (dashed lines). Quantitatively, however, it is found some differences, these discrepancies arise from the motion of the contact lines. According to Cox [34] and Voinov [35], the contact angle is expected to vary in dynamical situations. This has the effect of changing the curvature of the interface, most prominently, at the leading and trailing sections of the droplet where the velocity of the droplet is perpendicular to the contact line. At the leading section of the droplet, the curvature of the interface increases, whilst at trailing section it decreases. This has the effect of reducing the pressure gradient and consequently the main driving force acting on the liquid.

While the pressure gradient drives the dynamics in the bulk of the barrel, the contact lines move by virtue of the local pressure drop and an imbalance in the chemical potential. The chemical potential profile, $\mu(\boldsymbol{x})$, deviates from equilibrium more strongly near the contact lines (see figures 4.7a and 4.7b); it is found that μ dips at the advancing contact line, and peaks at the receding contact line (see figure 4.7c). From the Gibbs-Thomson condition [39], an increment in $\Delta\mu$ is expected at the interface due to a change in curvature,

$$\Delta\mu = -\frac{2\gamma\kappa}{\Delta\phi}, \tag{4.10}$$

where $\Delta\phi \approx 2$ is the change in the order parameter across the interface.

From the Cahn-Hilliard equation, Eq. (1.26), a small peak in the chemical potential will result in the local "evaporation" of the inner phase, whereas a dimple will lead to "condensation". As shown by Briant *et al.* [26], the combination of both features allows the motion of the contact lines.

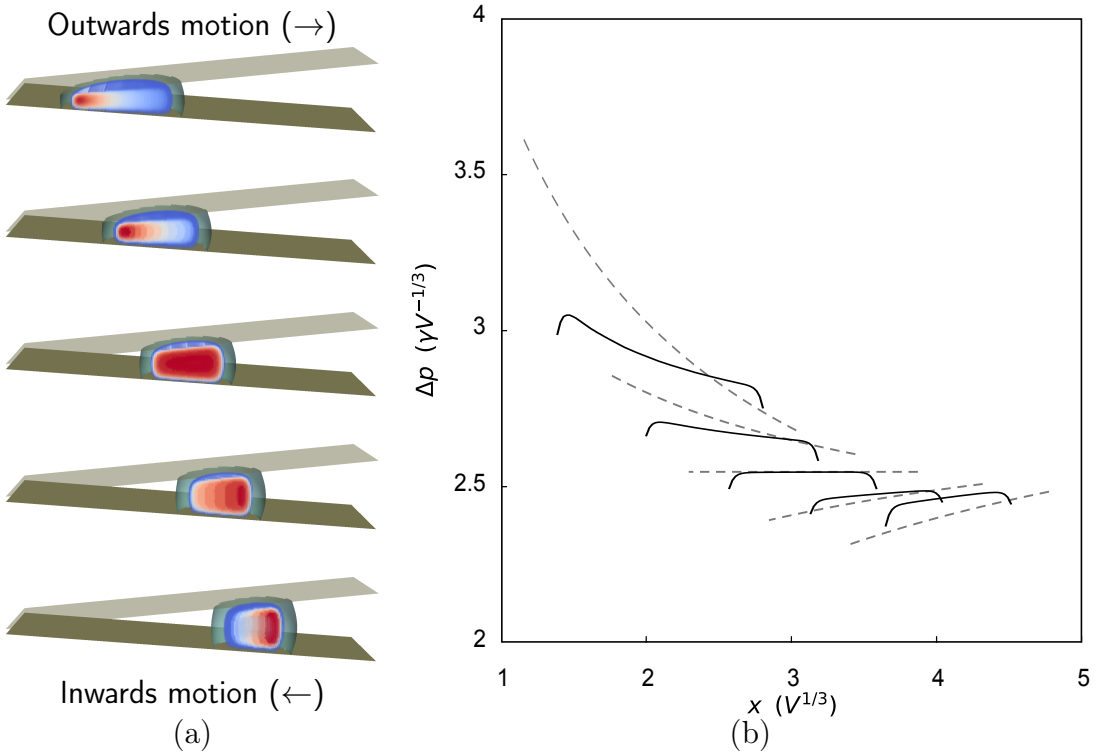

Figure 4.6: Instantaneous out-of-equilibrium pressure profiles for a liquid barrel of contact angle $\theta_e = 110°$ in a wedge of opening angle $\beta = 5°$. (a) The inset illustrations show a colour map of the pressure field at the cross-sectional plane $y = 0$ (decreasing from dark red to lightt blue) at the displacements $X(t) - X_e = \{-1, -1/2, 0, 1/2, 1\}V^{1/3}$ from top to bottom. (b) Plot of the pressure profile at the bisector line, $p(x, 0, 0)$ (solid black lines) for the snapshots shown in (a). Due to the surface tension of the liquid-gas interface, the pressure dips at the endpoints (see figure 4.3), therefore the pressure profile is plotted for the section where $\phi(x) > 0.9$ to highlight the area of interest. This result is compared with the theoretical prediction from the Young-Laplace equation (dashed gray lines). The simulation parameters are $M = 0.005$ and $\eta_{in} = 1/3$.

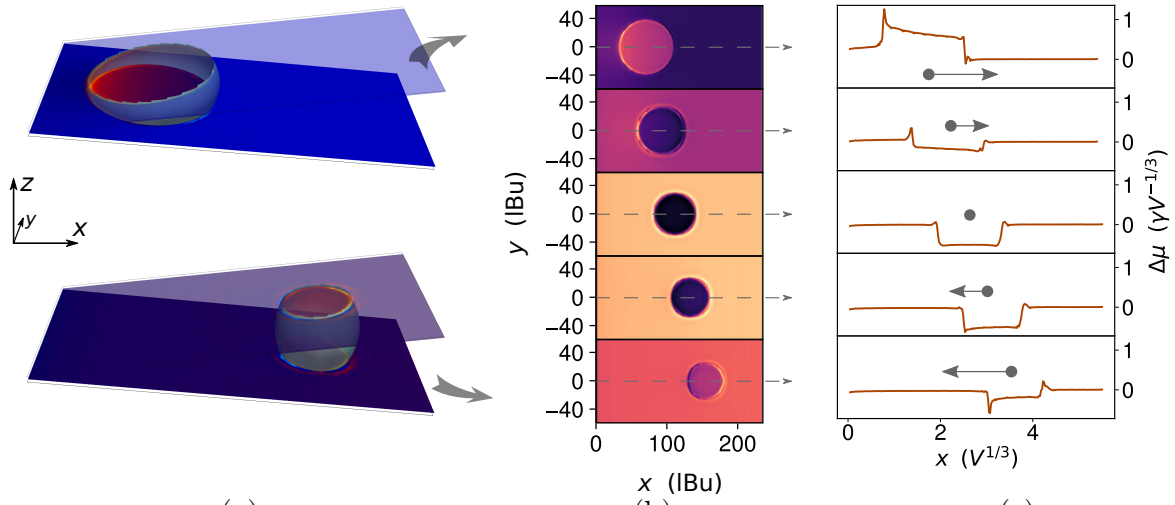

(a) (b) (c)

Figure 4.7: Chemical potential field of a liquid barrel of contact angle $\theta_e = 110°$ at different displacements from equilibrium in a wedge of opening angle $\beta = 5°$. (a) The colour map in the 3D images show the slicing plane $z = 0.82 - x \tan 5°$ (l.B.u.) for a displacement of the equilibrium position of the liquid barrel at $X - X_e = \pm V^{1/3}$. (b) Projections of the colour maps $\Delta\mu$ on the wedge walls at displacements $X - X_e = \{-1, -1/2, 0, 1/2, 1\}V^{1/3}$ (top to bottom). (c) Profile of the chemical potential along the x coordinate of the wall. The arrows indicate the direction of motion of the liquid barrel. The simulation parameters are $M = 0.005$ and $\eta_{in} = 1/3$.

4.2.4 Flow Field

The flow pattern resulting from the pressure gradient will now be discussed. In the surrounding phase, two recirculating streamlines at the sides of the droplet (see figure 4.8) can be observed as predicted by the analytical model presented in §3.3.2. These are also observed in figure 4.9, by means of a vector field and a vorticity colour map. It can be infer that these vortices occur close to the interface because of the difference in the viscosities, and reduce friction in the motion of the droplet.

The topology of the flow field is persistent over the whole set of simulations, with little variation in the details depending on the direction of motion or the velocity of translation. This is reasonable, as the dynamics in the simulations always fall in the exponential regime. Therefore, it is expect that, while the magnitude of these features decreases as the system approaches equilibrium, the overall structure of the flow remains the same [27].

The flow in the bulk of the droplet shows a remarkable laminar structure (see figure 4.8). This is in agreement with the theoretical model proposed in section §3.3.2, thus supporting that a Jeffery-Hamel flow gives a good approximation of the flow inside the droplet. This is a consequence of the relatively large viscosity of the outer phase, for which the vortices are located out of the droplet. This effect implies that by increasing the viscosity ratio, the inner flow becomes laminar, making the assumption of a Jeffery-Hamel flow more accurate. This also implies that the dissipation of the outer phase becomes more significant for a higher outer viscosity.

The flow in the transverse plane also shows a laminar structure (see figure 4.9(a)). The flow points in the direction of the apex, growing in magnitude from the walls to the bisector plane. This feature is distinctive of the Jeffery-Hamel flow, giving further support to the assumption of the bulk flow in §3.3.2.

As shown in the inset of figure 4.9(b), the flow pattern changes near the contact line. Here, the structure of the flow is consistent with the generic corner flow of wetting dynamics predicted by Cox [34] and Voinov [35], which results in a tread-milling motion of the interface [18, 38] as documented in experiments by Dussan and Davis [32] This is in agreement with the analytical model (see §3.3.2).

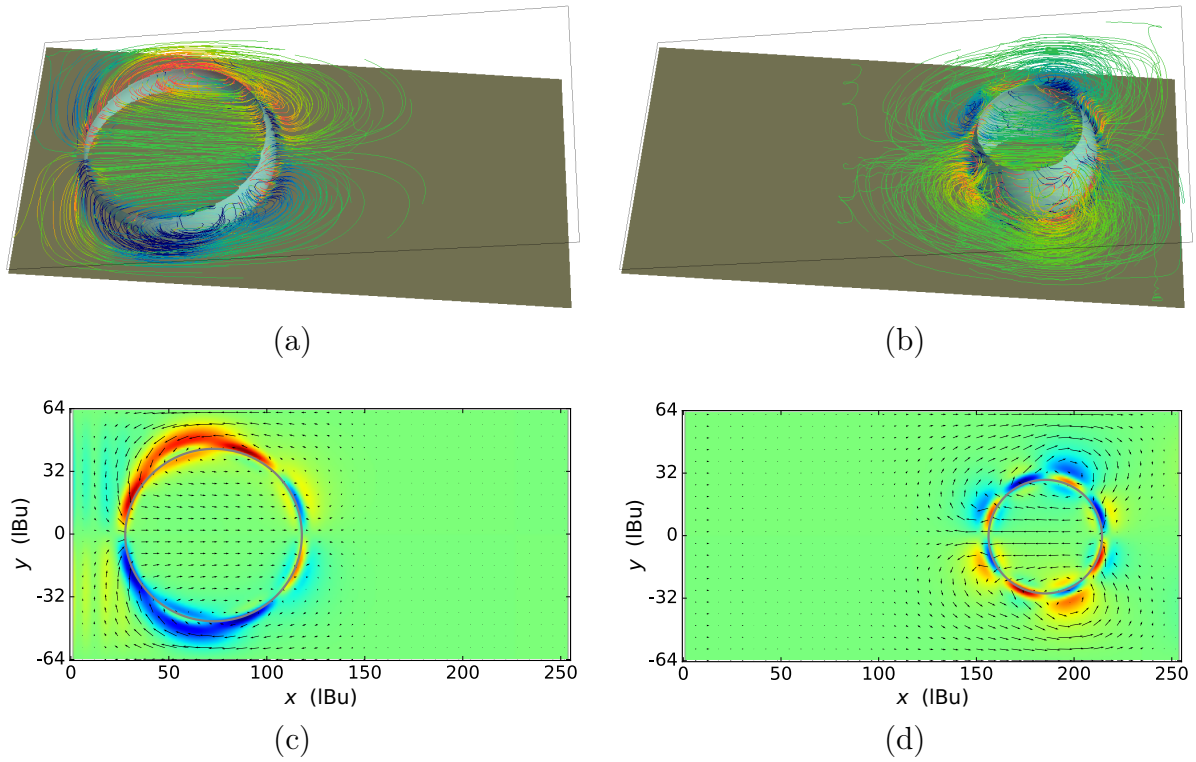

Figure 4.8: Instantaneous flow field at the bisector plane of a liquid barrel of contact angle $\theta_e = 120°$ moving outwards (a and c) and inwards (b and d) in a wedge of opening angle $\beta = 6°$. The streamlines of the velocity field (a and b) are coloured with the z component of the vorticity. The arrows of the vector field in the bisector projection (c and d) are amplified by 10^5 for visibility.

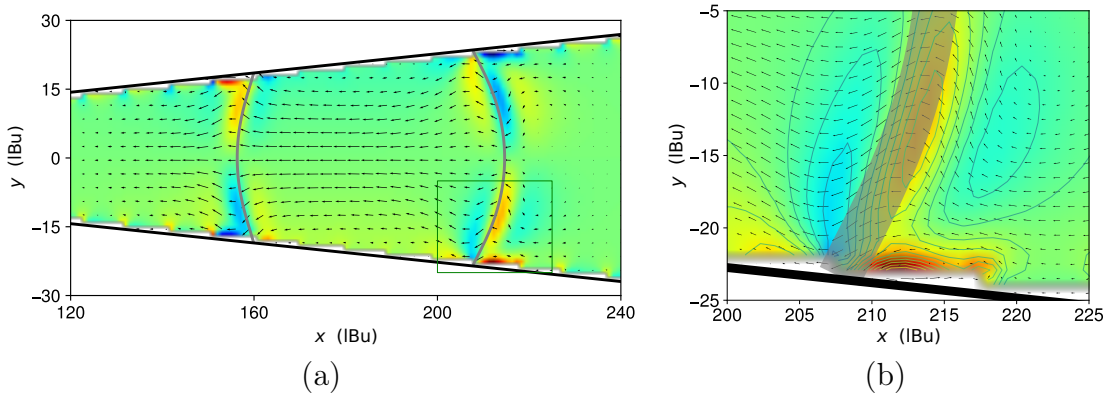

Figure 4.9: (a) Side view of the velocity and vorticity fields. The interface is plotted as a solid contour line, the vorticity field ω_y is plotted in colour map. The size of the arrows is augmented by 3.5×10^4 for visibility. (b) Close-up of the contact-line region indicated as a square in (a). The interface is plotted as a thick semi-transparent line. Contour lines of the vorticity field are plotted to enhance the visibility. The velocity field vectors are rescaled to 1.5×10^4. The simulation parameters are set to $M = 0.005$ and $\eta_{\text{in}} = 1/3$.

4.2.5 Contact Angle Variations

A dynamic contact angle, different from the its equilibrium value, results from the resistance of motion from either fluid in the vicinity of the contact line, and the contact line itself [33]. In the diffuse-interface model, the dynamics combines viscous and diffusive processes [42, 41, 43] and, for that reason, as discussed in §3.3.4, the energy dissipation provides relevant information at both levels.

In the lattice-Boltzmann simulations, the dynamic contact angle in the advancing and receding sections of the contact lines at the transverse plane was measured. Following Kusumaatmaja [45], this was done by finding the best circle that fits the fluid-fluid interface at the solid walls and then calculating the intersection angle with the solid walls.

As predicted by Cox [34] and Voinov [35], the contact angle varies with the local velocity of the contact lines, v_{cl}. The difference between the dynamic and the equilibrium contact angle can be estimated using in Eq. (3.134),

$$\theta - \theta_{\mathrm{e}} \approx \frac{\eta_{\mathrm{in}}}{\gamma} f_{\mathrm{CV}}(\theta_{\mathrm{e}}, \lambda)\, v_{\mathrm{cl}} \log \frac{\ell_{\mathrm{M}}}{\ell_{\mathrm{m}}}, \tag{4.11}$$

where the function f_{CV} is given in Eq. (1.44) for any value of the viscosity ratio $\lambda = \eta_{\mathrm{out}}/\eta_{\mathrm{in}}$.

In figure 4.10, the dynamic contact angle, θ, *vs* the velocity of the contact line, v_{cl}, is plotted for a set of prescribed contact angles, θ_{e}. It can be observed that, at vanishing velocity, the contact angle converges to the equilibrium value, and, when v_{cl} is positive (negative)—which corresponds to the advancing (receding) section of the contact line—θ increases (decreases) with respect to the base value θ_{e}. Moreover, it can be observed that the growth in the dynamic contact angle is linear with respect to the velocity of the contact line, which is in good agreement with the prediction in Eq. (4.11).

Looking at figure 4.10 in further detail reveals a difference in the slope of the contact angle, $\mathrm{d}\theta/\mathrm{d}v_{\mathrm{cl}}$, at the advancing and receding parts of the contact line. From Eq. (4.11), this can be attributed to the last term, i.e., $\log \ell_{\mathrm{M}}/\ell m$. Recall that ℓ_{M} plays the role of the macroscopic length-scale, in which the corner flow merges with the bulk flow, therefore it is expected to depend on the geometry of the droplet, and thus, scale with the height of the droplet. On the other hand, as shown by Jacqmin [42] and Kusumaatmaja [45], the microscopic length-scale ℓ_{m} has a power-law dependence with the viscosity and the mobility; the exponent varying between 1/2 and 1/4. Therefore,

$$\ell_{\mathrm{m}} \propto [M \eta_{\mathrm{in}}]^a \tag{4.12}$$

can be considered.

Combining Eq. (4.11) with Eq. (4.12), the rate of change of the contact angle is expected to have the form,

$$\frac{\mathrm{d}\theta}{\mathrm{d}v_{\mathrm{cl}}} \sim \frac{\eta_{\mathrm{in}}}{\gamma} \Big\{ b - a \log[M\, \eta_{\mathrm{in}}] \Big\}\, f_{\mathrm{CV}} \left(\theta_{\mathrm{e}}, \frac{\eta_{\mathrm{out}}}{\eta_{\mathrm{in}}} \right), \tag{4.13}$$

where the constants a and b are free parameters yet to be determined. The positive (negative) sign inside the cosine function corresponds to the farther (+) and closer (−) sections of the contact line relative to the apex of the wedge.

The numerical error due to spatial aliasing is evident in figure 4.10 and is more prevalent for the advancing section of the contact line. This is because, for a droplet moving

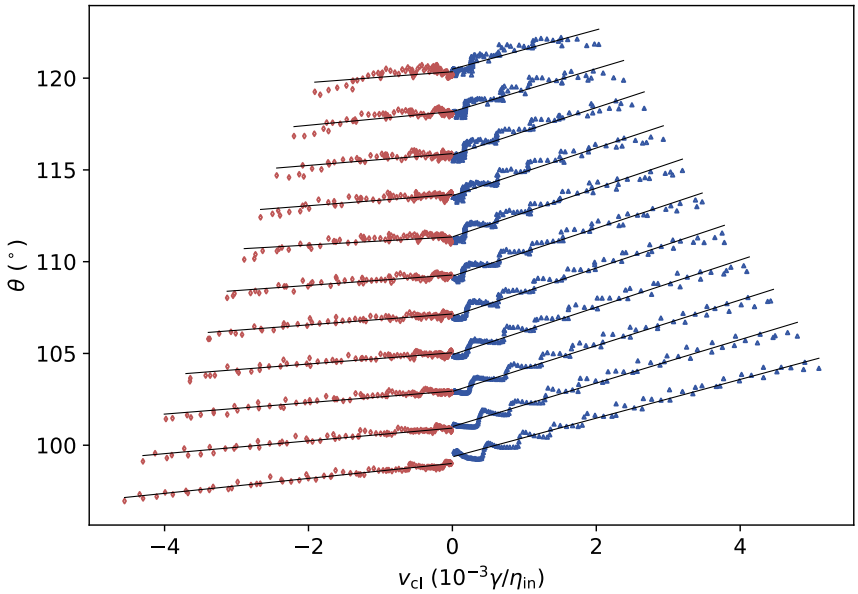

Figure 4.10: Variation of the contact angle with the velocity of the contact line. Scatter plot of the measured contact angle at varying prescribed θ_e while fixing the viscosity ($\eta_{in} = 1/3$) and mobility ($M = 5 \times 10^{-3}$). The symbol (▲) corresponds to the advancing section of the contact lines, whereas (♦) corresponds to the receding. The solid lines represent the fitting of a linear profile, where the slope is $d\theta/dv_{cl}$.

inwards, the advancing section of the fluid-fluid interface is more confined, and therefore, spurious effects in the contact angle are also amplified.

From figure 4.10, one can extract the slope of the linear fits to see its dependence on θ_e. Similarly, this can be done for a set of β, η_{in} and M. The rate of change of the contact angle is presented in figure 4.11 for both advancing and receding sections of the contact line as function of θ_e, β, η_{in} and M.

Figure 4.11(a) shows that $d\theta/dv_{cl}$ does not change significantly with respect θ_e. On the other hand, the effect of the wedge angle is apparent as one that varies with β (see figure 4.10(b)). The latter gives further support to the form of ℓ_M in Eq. (4.11) which models the effect of the geometry of the confinement in the structure of the corner flow.

Moreover, in figures 4.11(c) and (d) a predominantly linear dependence on η_{in} and $\log M$, respectively, can be observed. At higher viscosity, the contact angle has larger deviations from the equilibrium value, meaning that a greater difference in the curvature of the interface at the contact lines is necessary to allow a faster motion. In contrast, with higher mobility, the diffusion of the order parameter can occur at lower differences, and therefore less variation in the contact angles is necessary. Henceforth, the motion of the contact lines is hindered by viscosity and enhanced by mobility, and consequently, less dissipation is expected at higher values of M and lower values of η_{in}.

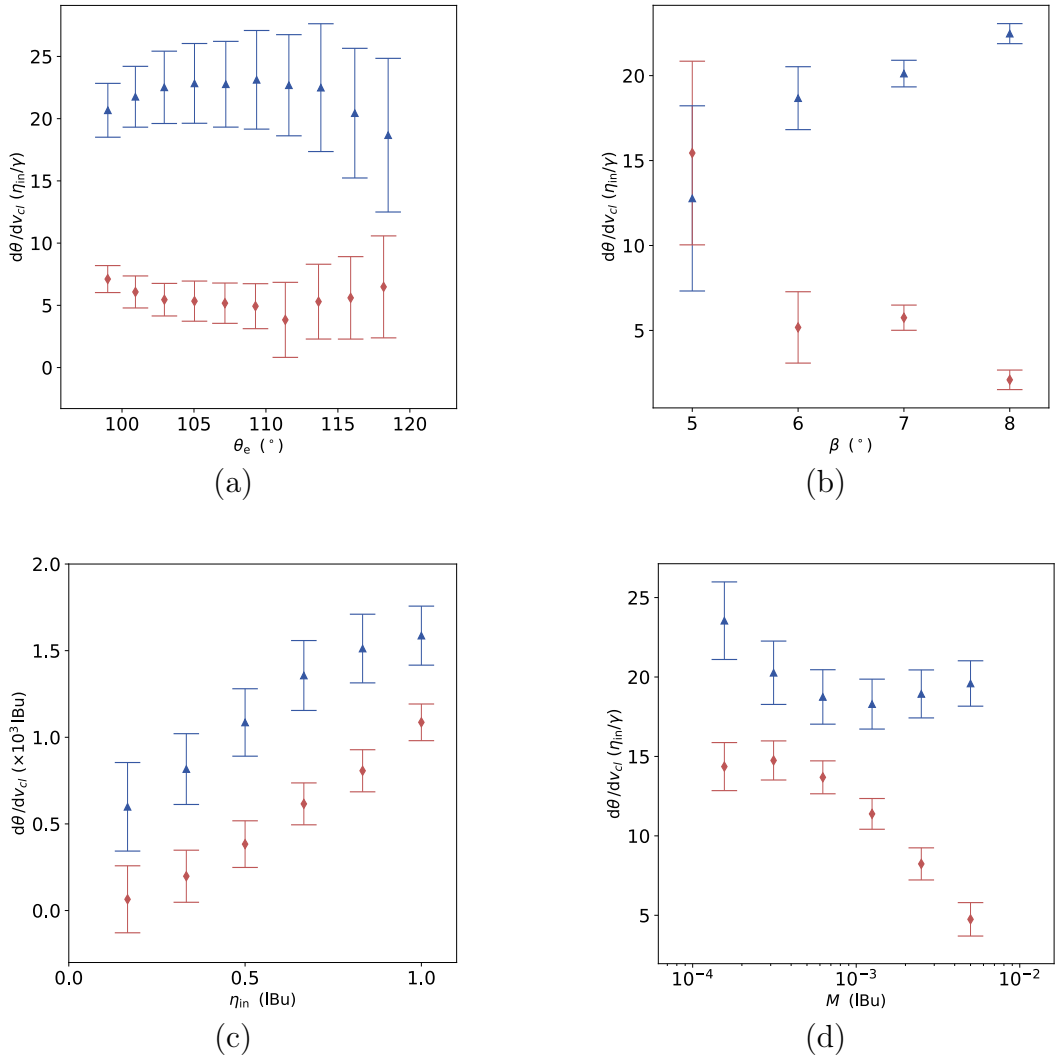

Figure 4.11: Plots of the variation of the contact angle response with respect to (a) the equilibrium contact angle, (b) wedge angle, (c) viscosity, and (c) mobility; the latter in logarithmic scale. The symbols correspond to (▲) advancing and (♦) receding sections of the contact lines. The dotted-dashed and dashed lines correspond to their respective curve fittings.

4.2.6 Reconstruction of the Energy Landscapes

The energy landscapes as the droplet travels to its equilibrium position will now be studied. As the liquid barrel equilibrates, the excess surface energy is dissipated not only by viscous friction, but also by the relaxation of the chemical potential field [9] (see §1.2.5 for further details).

Following §1.2.2, the total rate of energy dissipation reads,

$$\dot{\mathcal{E}} = -\int \left\{ \frac{1}{2}\eta \left(\boldsymbol{\nabla u} + \boldsymbol{\nabla u}^T \right)^2 + M \left| \boldsymbol{\nabla} \mu \right|^2 \right\} \mathrm{d}V, \tag{4.14}$$

which renders the term inside the brackets an energy dissipation density. It was found that the dissipation density is higher close to the interface, and peaks near the contact lines (see figure 4.12). The overall contribution to dissipation, however, is dominated by

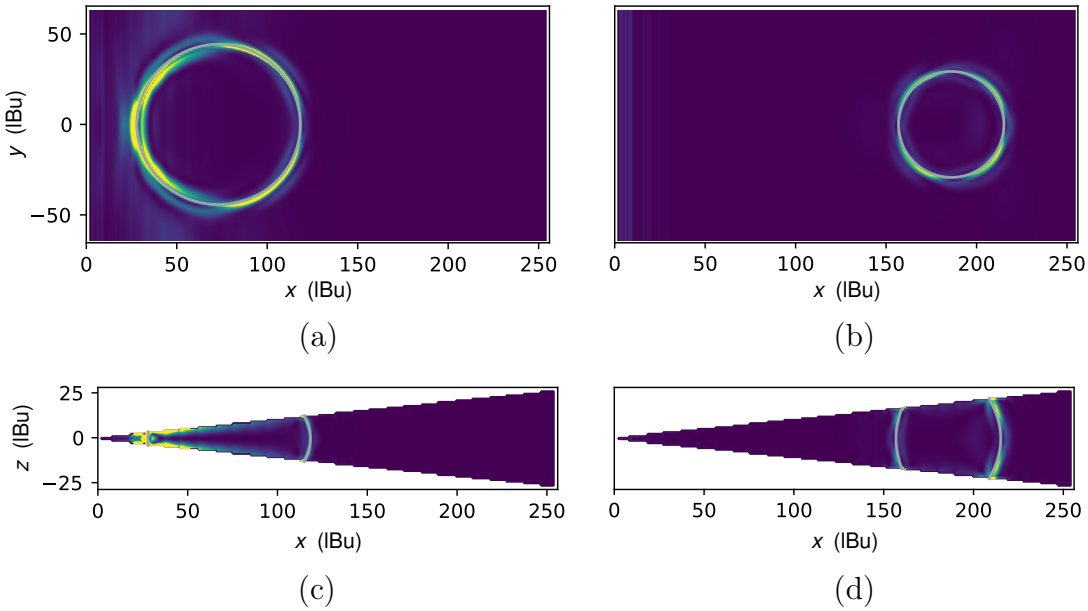

Figure 4.12: Energy dissipation density field of a liquid barrel with contact angle $\theta_e = 110°$ moving inwards in a wedge of opening angle $\beta = 6°$. Cross-section of the dissipation field at the bisector plane, $z = 0$, for a droplet moving (a) outwards and (b) inwards. Dissipation field at the transverse plane, $y = 0$, for a droplet moving (c) outwards and (d) inwards. The interface of the droplet is depicted with a grey solid line. The simulation parameters are $M = 0.005$ and $\eta_{in} = 1/3$.

viscous friction over the whole equilibration of the barrel—the contribution of the diffusive term is typically less than 10% (figure 4.13).

The total dissipation can be used to reconstruct the instantaneous free energy, $F(t)$, by integrating the dissipation rate, $\dot{\mathcal{E}}$, with respect to time (see §1.2.2). Yet, in the simulations, a constant residual dissipation at long times, $\dot{\mathcal{E}}_\infty$, which is unphysical (see figure 4.13) was found. The origin of the residual dissipation is in the spurious currents of the lattice-Boltzmann method, which it was found to increase in magnitude as the equilibrium contact angle deviates from 90° [116] (see figure 4.13(b)). Therefore, to find $F(t)$, the relation

$$F(t) = \int_t^\infty \left[\dot{\mathcal{E}}(t') - \dot{\mathcal{E}}_\infty\right] \mathrm{d}t' + \mathcal{E}_0 \tag{4.15}$$

was used. Figure 4.14 shows the resulting energy landscapes, which is presented as parametric plots of $F(t)$ *vs* $X(t)$ at different θ_e and β. The asymmetry in the curves shows that the liquid barrel is subject to a stronger restitutive force upon and inwards displacement (as opposed to an outwards displacement) due to the effect of confinement. The overall increase in the curvature of the landscapes at lower θ_e arises from the same effect; at low θ_e the barrels equilibrate closer to the apex of the wedge (where confinement is strongest). The increase in curvature at large β implies a stronger restitutive force; this is due to a larger projection of the net restitutive force along the direction of motion, and a higher rate of distortion of the interface shape in wider wedges.

To compare the lattice-Boltzmann results to the analytical model §3.1.1, the energy landscapes obtained in Eq. (3.59) to the simulation results (see figure 4.14) are superimposed. It was found that, on occasions, the theoretical curve is below the simulations.

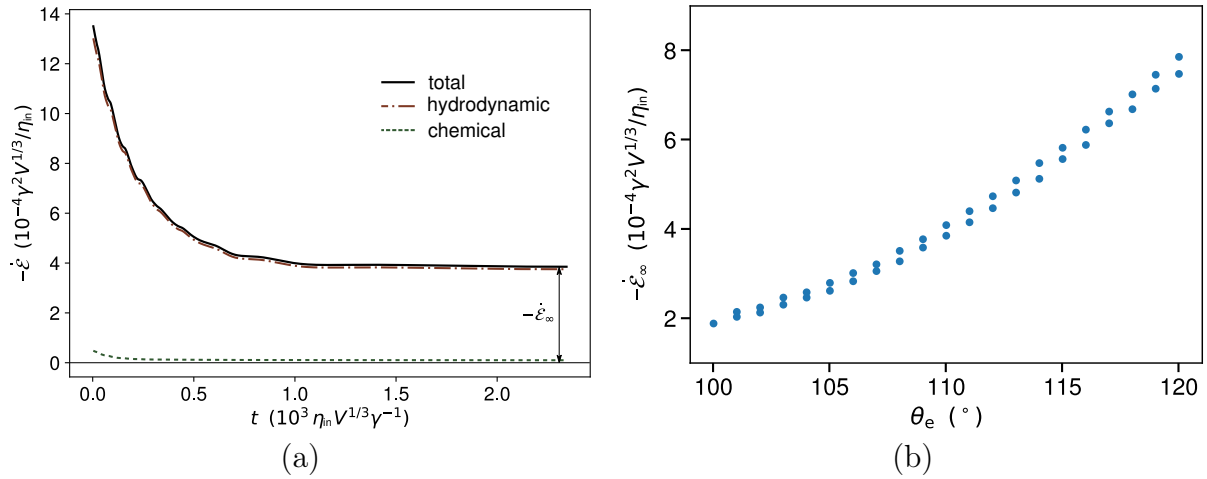

(a) (b)

Figure 4.13: Energy dissipation as a function of time and residual dissipation. In (a), the solid line indicates the total energy dissipation. The viscous hydrodynamic dissipation is shown as a dotted-dashed line and the chemical dissipation as a dotted line. The residual dissipation is indicated with a double arrow. (b) Dependence of the residual dissipation on the equilibrium contact angle. The simulation parameters are $M = 0.005$ and $\eta_{in} = 1/3$.

This is expected, as initial configurations of the droplet that have a higher initial energy compared to the liquid barrel. This occurs when the initial condition of the droplet is closer to equilibrium. It is reasonable to conclude that the liquid barrel is a low-energy interfacial shape. In contrast, when the droplet travels for a longer distance, it can be observed that the theoretical curve lies above the one obtained from the simulations. This is also expected since, as the droplet moves, the variation in the contact angle changes the fluid-fluid interface. Since it is a dissipative process, regardless of the direction of motion and change in the contact angle, this effect reduces instantaneous energy compared to the liquid barrel.

The analytical value of the restitution constant, k, Eq. (3.145), was also compared with the one obtained from the simulations. In the simulations, k was obtained by fitting the energy landscape curves of figure 4.14 to a third-degree polynomial (fixing the constant and linear terms to coincide with the energy minima in the simulations). It was found that the curve fitting gave a good representation of the data by considering data points within a region close to the equilibrium position. The measurements show a decrease of k with increasing θ_e and decreasing β, in qualitative agreement with the theory (see figure 4.15). Moreover, there is a reasonable agreement with the magnitude of k; the overall larger k values obtained from the simulations imply a larger total energy than the surface energy accounted for in the analytical model. This is expected, as the initial configuration of the liquid in the simulations has a larger surface area than the barrel shape proposed in §3.1.1.

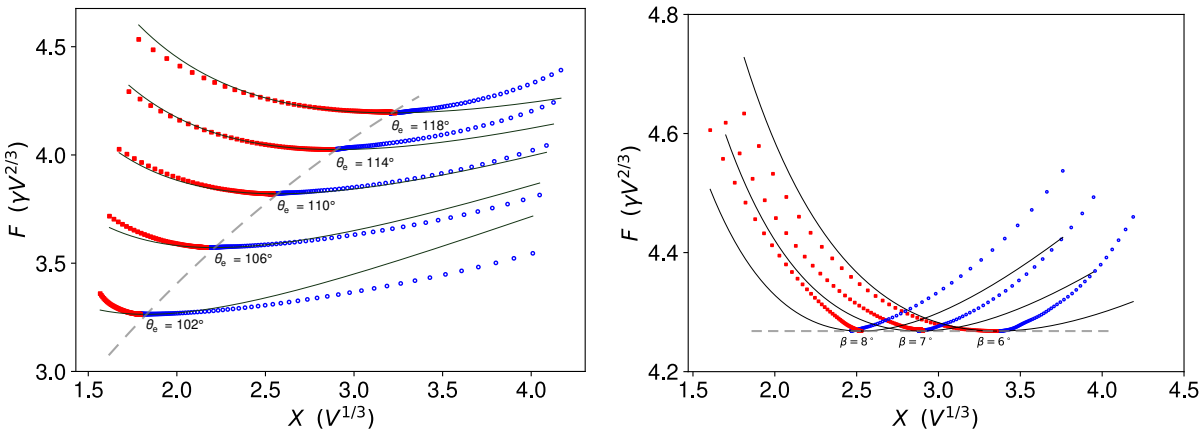

Figure 4.14: Energy landscapes of the liquid barrel for (a) different values of the contact angle at fixed $\beta = 6°$, and (b) different values of the wedge angle at $\theta_e = 120°$. The symbols correspond to inwards motion (○) and outwards motion (■). The solid lines correspond to the energy of the liquid barrel. The dashed line corresponds to the zero-point energy. The thin solid lines show third-degree polynomials used to fit the data. The simulation parameters are $\eta_{in} = 1/3$ and $M = 0.005$.

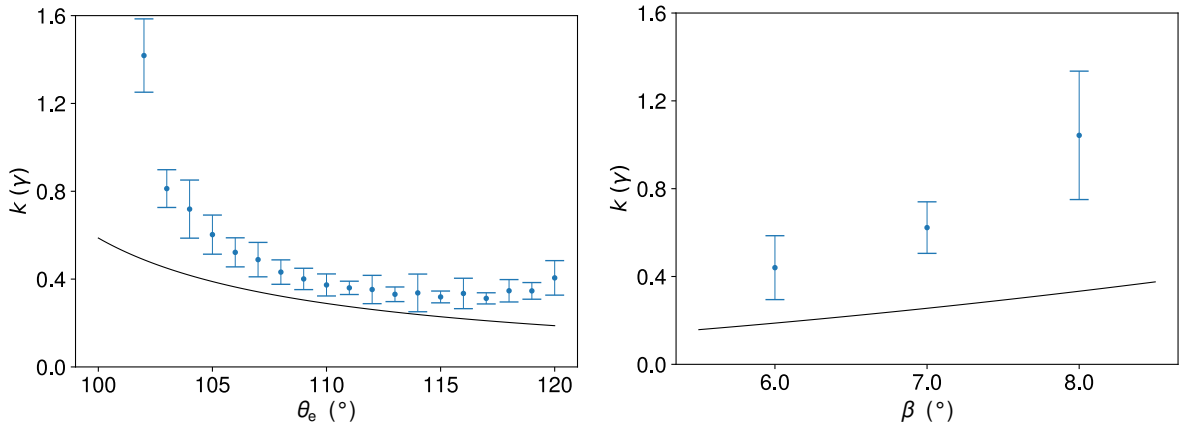

Figure 4.15: Restitution constant as a function of θ_e at $\beta = 6°$ (a), and as a function of β at $\theta_e = 120°$ (b). In both plots, the symbols represent the numerical calculation and the solid lines represent the theoretical prediction. The error bars are the root-mean-square error of the least-squares algorithm used to determine k.

4.2.7 The Relaxation Time and the Friction Coefficient

As explained in §3.3.5, the time-scale of the relaxation of the droplet is set by the competition between the driving (capillary) force and the dissipative (friction) forces, i.e.,

$$\tau \overset{\text{def}}{=} \frac{\nu_X}{k}, \tag{4.16}$$

where ν_X is the friction coefficient (see §3.3.5). Since diffusion of momentum and mass are irreversible processes, the constants η_{in} and M can only affect dissipative forces. Therefore, any effect that these constants have on the relaxation time, must emerge from the friction coefficient, since by construction, k is conservative.

Considering the contributions to energy dissipation (as stated in §3.3.5) and the dynamic behaviour of the contact angle (as presented in §4.2.5), it is expected that the dissipation function is of the form

$$\dot{\mathcal{E}} \sim \left[a' + b' \log(M\eta_{\text{in}}) + \frac{c'}{M}\right] \dot{X}^2, \tag{4.17}$$

where a', b', and c' are parameters yet to be determined that depend on the viscosity of the inner and outer phase, the contact angle and the wedge angle. Therefore, comparing Eq. (4.17) with the results of §4.2.2, the relaxation time is expected be proportional to the term inside the brackets of Eq. (4.17) up to a dependence on $\sin^{-2}\beta$ and independent of θ_{e}, i.e.,

$$\tau \approx \frac{\eta_{\text{in}} V^{1/3}}{\gamma \sin^2\beta}\left[a + b\,\log(M\eta_{\text{in}}) + \frac{c}{M}\right], \tag{4.18}$$

where a, b and c are constants that depend only on the viscosities of both phases.

From the simulations, it was found that τ increases linearly with the viscosity of the inner phase, η_{in} (see figure 4.16(a)). This implies that all three contributions to the drag coefficient (and thus all a, b, and c) scale with η_{in}. The extrapolation of the relaxation time to a finite value ($\tau > 0$) as $\eta_{\text{in}} \to 0$ is due to the non-zero viscosity of the outer phase.

The dependence of τ on the mobility coefficient, M, is presented in figure 4.16(b). A monotonic decrease of τ with M is found, which can be reasoned in terms of both a larger microscopic length-scale ℓ_{m}, and a smaller contact-line friction coefficient at higher M (second and third term in Eq. (4.18)). More quantitatively, the simulation data to fit Eq. (4.18) is used, treating the constants a, b and c as fitting parameters. The functional form is in good agreement with the simulation data for the set of parameter values $a = 3.15$, $b = -0.196$, and $c = 9.71 \times 10^{-5}$. In fact, it was found that none of the terms in Eq. (4.18) is negligible: a fit, fixing $b = 0$ (dotted line in figure 4.16(b)) or $c = 0$ (dotted-dashed line in the same figure), gives a qualitatively incorrect representation of the simulation data.

4.3 Concluding remarks

In this chapter, lattice-Boltzmann simulations were carried out to analyse the dynamics of droplets in wedges and further support the liquid barrel shape in dynamic situations. First, the simulation results for the equilibrum shape and position of droplets on wedges

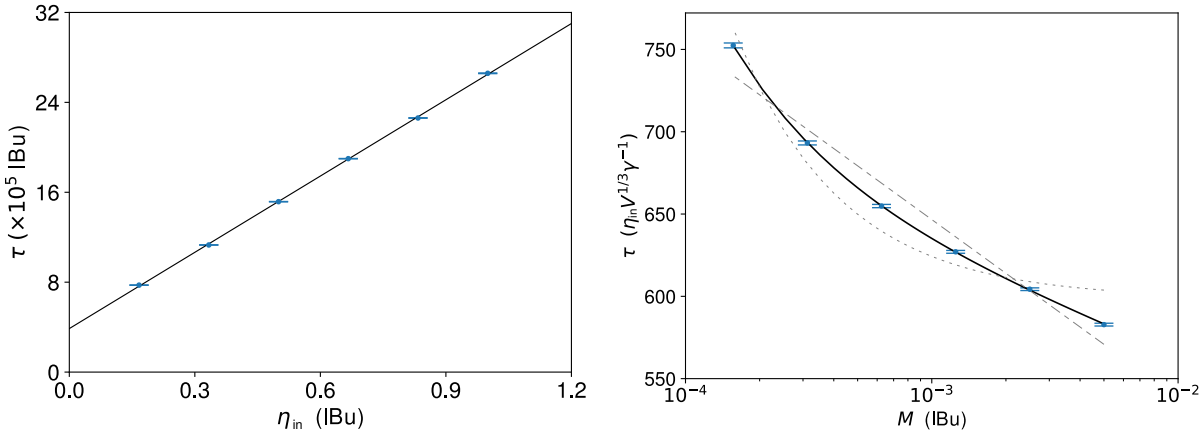

(a) (b)

Figure 4.16: Dependence of the translational relaxation time of a liquid barrel on the viscosity and coefficient of mobility. (a) τ as a function of η_{in} at fixed $M = 0.005$. The solid line a linear fit. (b) τ as function of M at fixed $\eta_{\text{in}} = 1/3$. The continuous lines correspond to three curve fittings of Eq. (4.18), corresponding contributions to dissipation from the bulk and corner flow (dotted-dashed line), bulk and contact line (dotted line), and bulk, corner and contact line (solid line). The simulation parameters are $\theta_{\text{e}} = 110°$ and $\beta = 5°$.

were obtained. Then, the translational motion of droplets in hydrophobic wedges is analysed. This is done by observing the driving forces and the flow field and comparing these findings with previous analysis. Moreover, the restitutive forces are compared against the theoretical model by reconstructing the energy landscapes.

The dissipative forces involved in the relaxation process are then examined. This is done by first noting how the advancing and receding contact angles change due to the motion of the droplet, a consequence of the motion of the contact lines. The analysis concludes by looking at the relaxation time, that is, the characteristic time in which the droplet approaches equilibrium, which shows the three contributions to the dissipative forces. This is in good agreement with the liquid barrel model proposed in the previous chapter.

Chapter 5

Droplet Manipulation in a Wedge Geometry

The theoretical description and simulations developed in § 3 and § 4 give a framework to study applications of the motion of a liquid droplet inside a wedge. In this chapter, the possibility of droplet manipulation by changing the geometry of the wedge is assessed, where the knowledge gained by the theoretical analysis and simulations is applied to explain recent experimental results.

5.1 Experiments on Liquid Barrels

Experimentally, a smooth translation of a droplet in a wedge upon reconfiguration of the boundaries is only possible in the absence of contact angle hysteresis. In that way, a consistent equilibrium configuration can be found and thus, the behaviour of the droplet can be modelled by the liquid-barrel model. Slippery liquid-infused porous surfaces (SLIPS) [117], also known as lubricant-impregnated porous surfaces [118], provide an excellent framework for these purposes [119] (see figure 5.1).

A SLIPS consists of a porous surface that is covered by a thin liquid layer that acts as a lubricant. In the experiments[1], the underlying surface consists of a flat silicon wafer with a square grid of SU-8 photolithographic resin pillars of $90 \times 90\,\mu\mathrm{m}^2$ with $100\,\mu\mathrm{m}$ of separation that produce the porous texture. The porous surface is coated with a nano-particle solution making it superhydrophobic—repelling water, but not oil [120]—and then infused with a thin layer of lubricating oil [119, 95].

When a water droplet sits on a SLIPS, a small oil meniscus of a few hundred microns, is observed in place of a contact line. This suggests that the droplet is cloaked by oil. This is further confirmed by surface tension measurements of a sessile droplet in air, $\gamma \approx 63\,\mathrm{mN\,m^{-1}}$, which is a value lower than the surface tension of water and air alone ($\gamma < 71\,\mathrm{mN\,m^{-1}}$); thus indicating the presence of oil in the water-air interface which decreases the surface tension. Except for the oil meniscus, a water droplet in contact with a SLIPS adopts a spherical shape. Extrapolating the spherical cap up to the intersection with the solid surfaces defines the apparent contact angle, $\theta_\mathrm{e} = 100^\circ \pm 5^\circ$, in equilibrium.

A direct contact between the water phase and the solid surface is prevented due to the nano-particle coating, thus practically eliminating the contact angle hysteresis [118,

[1] The experiments were carried out by Jian Hui Guan whom I thank for kindly sharing his results.

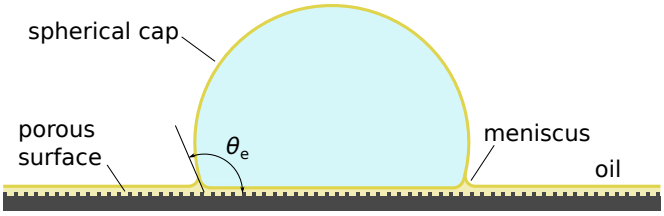

Figure 5.1: Schematics of a SLIPS surface with a sessile droplet of water.

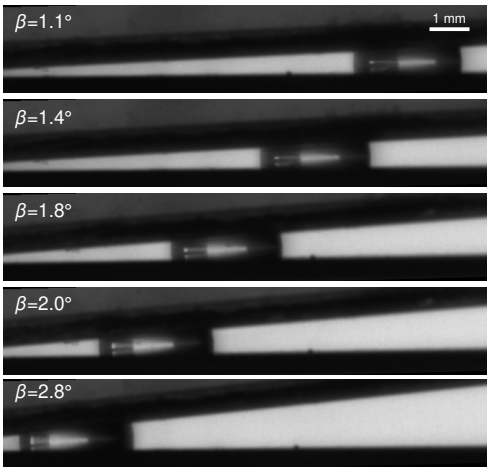

Figure 5.2: Droplet morphology in equilibrium. A $4\,\mu$L water droplet equilibrates at different positions within a SLIPS wedge by adjusting the opening angle.

121, 119]. This is verified by placing a droplet on top of a tilted SLIPS and allowing it to roll off by the force of gravity. The sliding angle, i.e., the minimum tilting angle in which motion occurs, was less than 1° for a droplet of $3\,\mu$L.

The experimental set-up consists of two SLIPS surfaces indistinguishable in their fabrication; one fixed, parallel to the horizontal and facing up, and the other one, facing down and forming a wedge of an angle 2β, where β was varied within $1.1° \leq \beta \leq 2.8°$. Then, a droplet of water of volume V ($2\,\mu\text{L} \leq V \leq 5\,\mu\text{L}$) is placed inside the wedge bridging the two surfaces (see figure 5.2).

Experiments were conducted to measure the equilibrium shape of the droplet for initial positions closer to the apex and farther out from the expected equilibrium state. After all visible motion ceased ($\sim 100\,$s), measurements were taken for the height-to-width aspect ratio and droplet radius.

The height-to-width aspect ratio, h, is a dimensionless number that characterises the shape of the droplet. This is illustrated in figure 5.3, which shows a diagram of the different filling regimes for a wedge with the contact angle as the bifurcation parameter. The energy landscapes reported in § 3.3.5 suggest that the spherical droplet shape corresponds to global minima in the surface energy, and therefore distortions to such shapes will always relax back to equilibrium. Henceforth, in equilibrium, the height-to-width aspect ratio, $h_e = -\cos(\theta_e - \beta)$, plays the role of an attractor. For $\theta_e < 90° + \beta$, $h_e = 0$, corresponding to the complete filling states studied by Concus and Finn [90, 89] and Brinkmann and Blossey [91]. For $\theta_e = 90° + \beta$, one obtains the onset of droplet detachment from the apex. For $\theta_e > 90° + \beta$, the aspect ratio becomes finite ($h_e > 0$), corresponding to the liquid barrel domain (see § 3.1.1). Increasing the equilibrium contact angle leads to a limiting

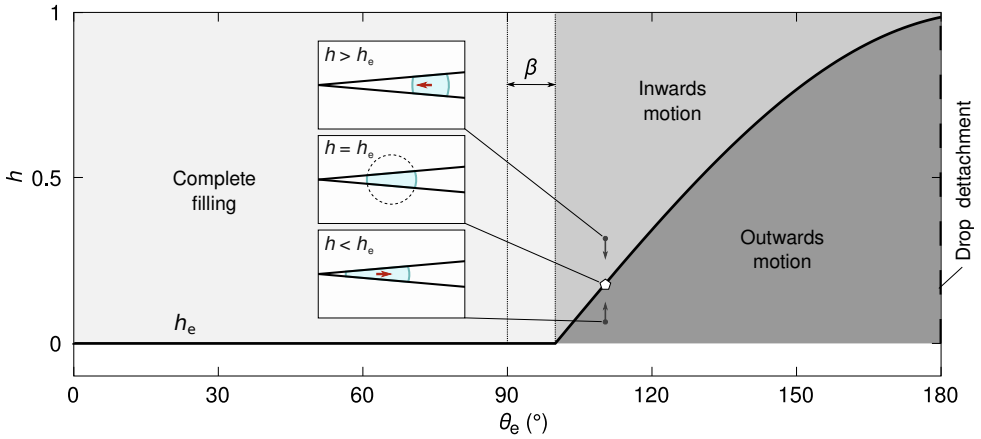

Figure 5.3: Bifurcation diagram of the filling states of liquid droplets in a solid wedge. The solid line denotes the equilibrium height-to-width ratio, or attractor. The vertical arrows indicate the direction of the trajectories of the system for fixed values of θ_e and β. The dotted line ($\theta_e = 90° + \beta$) shows the bifurcation, or onset of edge blobs. Examples of the morphology of the droplet are shown as insets. For clarity, the volume in the examples is not the same.

barrel configuration, where $\theta_e = 180°$ and $h_e = \cos\beta$. In such a limit, the contact area between the liquid and the solid vanishes, and the liquid forms a suspended droplet.

Out of equilibrium, the instantaneous aspect ratio characterises the inwards and outwards modes of motion for a liquid barrel, is given by

$$h = \frac{\xi - 1}{\alpha - 1} h_e. \tag{5.1}$$

A displacement of the liquid towards the apex of the wedge will result in a vertical compression of the droplet (see lower inset in figure 5.3), this corresponds to $h < h_e$. In contrast, a displacement towards the wide end of the wedge causes a vertical extension in the shape of the droplet, and corresponds to $h > h_e$. As the only attractor, at constant contact angle and geometry of the wedge, all trajectories move as vertical lines towards h_e as shown in figure 5.3.

Further examination of the equilibrium state can be performed to asses the final position of the droplet. In this case the parameter q is measured, which is proportional to the position of the droplet. It is a positive quantity that decreases when the droplet is closer to the apex of the wedge and it becomes identical to the droplet radius in equilibrium (from Eqs. (3.66) and (3.51)),

$$R_e = q_e = -\frac{\sin\beta}{\cos\theta_e} X_e = \left[\frac{6V}{\pi(\cos 3\theta_e - 9\cos\theta_e)}\right]^{1/3}. \tag{5.2}$$

The experiments were carried out for droplets at positions closer to the apex and further out as initial conditions. The results are shown in figure 5.4 and are in good agreement with the analytical prediction. That is, for a given contact angle, the radius of the droplet does not depend on the wedge angle. Moreover, it also shows that the position in which the droplet relaxes is invariant to initial conditions and is consistent with the analytical prediction. This is most important for an accurate control of the droplet during actuation.

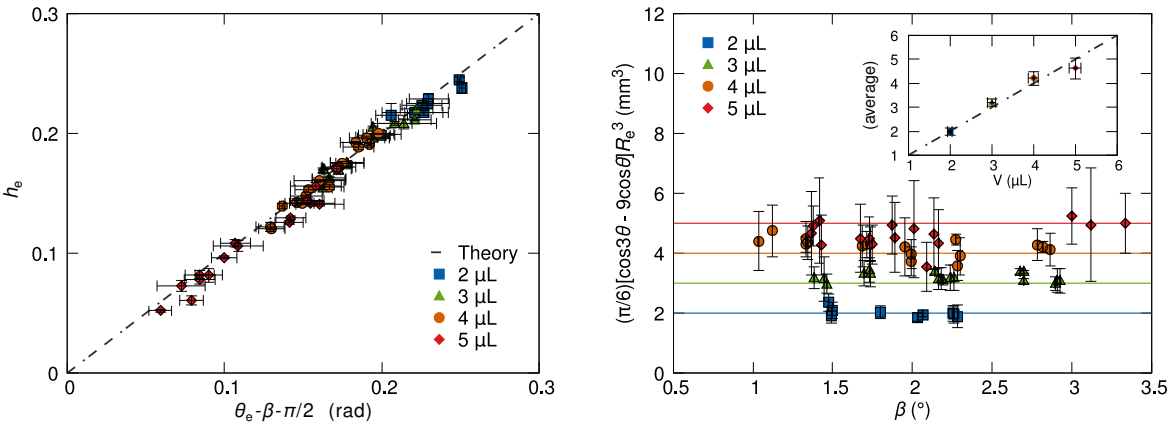

(a) (b)

Figure 5.4: Measurements of the equilibrium state of the droplet. (a) Data collapse of the height-to-width ratio of droplets of different volumes and contact angles confined in wedges with different opening angles. (b) Radius of droplets of volumes from $2\,\mu$L to $5\,\mu$L. The data has been collapsed to eliminate differences due to the small variations of the contact angle.

In order to study the dynamic behaviour of the droplets, the translation of the droplet as the system relaxes to equilibrium will now be studied. In this set of experiments, the droplet was filmed during its translation to the equilibrium position (see figure 5.5). The position of the droplet was tracked by finding the centre of the osculating circle to the interface of the droplet. Figure 5.6(a) shows that the distance to the equilibrium position decreases exponentially, according to Eq. (3.150),

$$X(t) - X_e = [X(0) - X_e]e^{-t/\tau}. \tag{5.3}$$

In the absence of a contact line, the main drag force is assumed to stem from the bulk hydrodynamic dissipation (see § 3.3.4). In other words, the dissipative contributions from the corner flow and contact-line, as formulated in Eq. (3.141), do not appear. This is equivalent to setting $\ell_m = \ell_M$ and $\zeta_0 = 0$ in the drag coefficient of Eq. (3.141) when evaluating the relaxation time in Eq. (3.144). This leads to the following scaling of the relaxation time,

$$T(V, \theta_e, \beta) = \frac{V^{1/3}\,\cos\theta_e \csc^2\beta}{(\cos 3\theta_e - 9\cos\theta_e)^{4/3}}\left[1 + \frac{2\cos^2\theta_e(\cos 2\theta_e - 5)}{(2\theta_e - \pi - \sin 2\theta_e)^2}\right]^{-1}. \tag{5.4}$$

The experimental value for the relaxation time, τ_{exp}, can be measured via curve fitting from the time series of the position, $X = X(t)$. The experimental relaxation time is compared with Eq. (5.4) in figure 5.6(b). As it can be observed, this model gives a good scaling of the experimental data over the range of parameters considered. The details of the motion of the droplet, in contact with the lubricating layer, affects the pre-factor in the relaxation time, which the dynamic model of the liquid-barrel model in §3.3.5 does not capture.

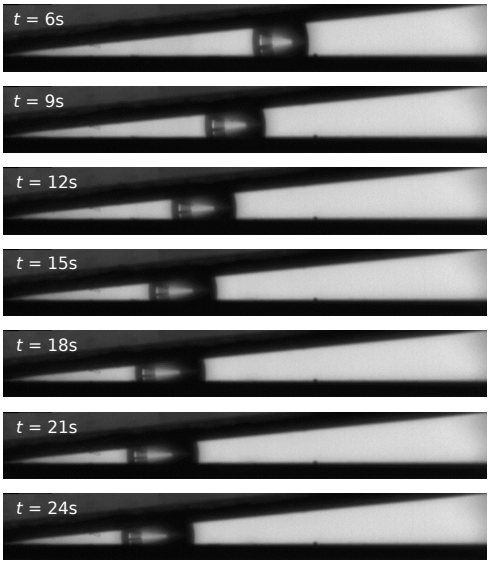

Figure 5.5: Sequence of snapshots of a 4 μL droplet relaxing to equilibrium.

5.2 Droplet Manipulation

The possibility of actuating the droplet by introducing a change in the on the geometry of the set-up will now be considered. For simplicity, the actuation is restricted in such a way to produce translation in a single dimension. The axis of translation, or *principal axis*, designates the line that bisects the wedge and that is perpendicular to the apex. Furthermore, changes in the geometry of the wedge produced by a combination of a change in the wedge angle, β, and a rigid displacement of the planes (see figure 5.7) are considered.

From the wedge angle, $\beta(t) \to \beta$, has the effect of moving h_e and thus producing vertical trajectories that aim at the moving equilibrium point. A rigid displacement of the solid planes, $d(t)$, has the effect of shifting the position of the apex relative to the laboratory frame of reference, and modifies the instantaneous aspect ratio, h.

An example of droplet translation was carried out experimentally by manually controlling the geometry of the wedge [95]. This is shown in figure 5.8(a). In the absence of pinning, no threshold force is necessary to overcome, and the motion of the droplet follows immediately. The position of the droplet with respect to the laboratory frame of reference (lower plane in figure 5.8(a)) is tracked, see dashed curve in figure 5.8(b).

The motion of the droplet can be analysed in the Lagrangian formalism. Following Eq. (3.108), the Lagrangian function is

$$L(X,t) = -F_V(X,t), \tag{5.5}$$

which now depends explicitly on time. The equation of motion, as discussed in § 3.3.1, is

$$\nu_X \dot{X} = -\frac{\mathrm{d}F_V}{\mathrm{d}X}, \tag{5.6}$$

and reduces to

$$\dot{X} = -\frac{1}{\tau(t)}[X - X_\mathrm{e}(t)], \tag{5.7}$$

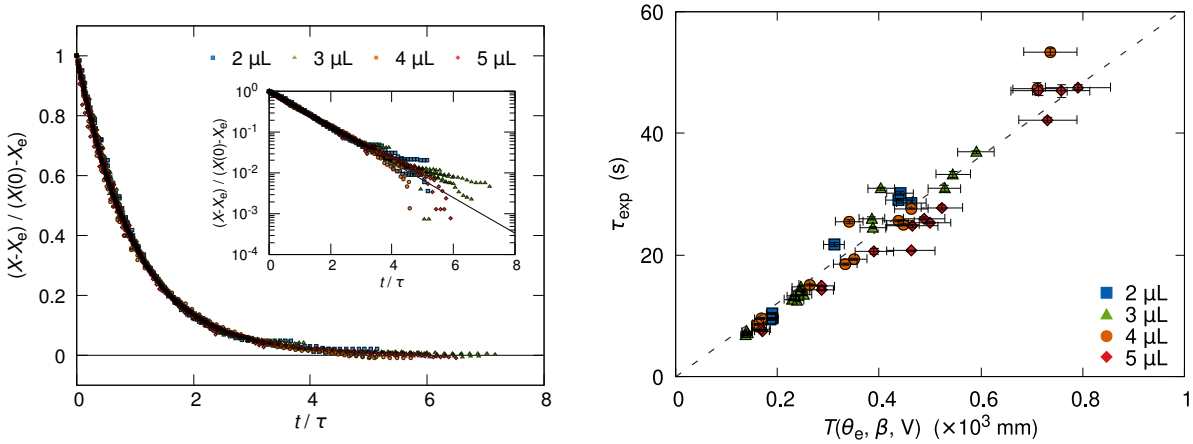

(a) (b)

Figure 5.6: Relaxation to equilibrium. (a) Data collapse of the position of the droplet against time. (b) Comparision of the experimental relaxation time against the theoretical prediction at $V_{\text{eff}} = V/2$, $\ell_{\text{m}} = \ell_{\text{M}}$, and $\zeta_0 = 0$.

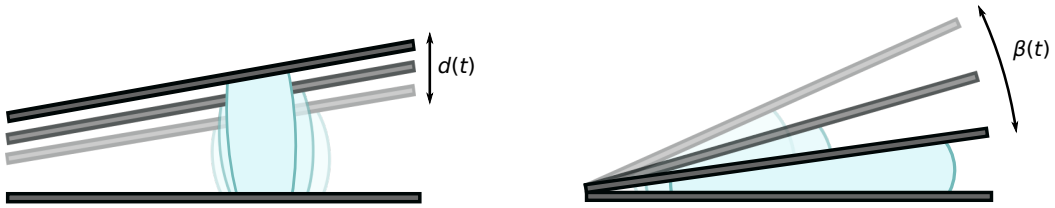

(a) (b)

Figure 5.7: The two ways of actuation of the geometry of the set-up that were used for droplet translation: (a) a vertical displacement of the upper plane, and (b) a change in the dihedral angle.

if the system is kept close to equilibrium (see § 3.3.5). However, the equilibrium position and the relaxation time of the system now depend on time explicitly. The equilibrium position becomes the driver of the droplet, i.e., a *signal*, and is given by

$$X_{\text{e}}(t) = -\frac{\cos\theta_{\text{e}}}{\sin\beta(t)}\left[\frac{6V}{\pi(\cos 3\theta_{\text{e}} - 9\cos\theta_{\text{e}})}\right]^{1/3} - d(t)\cot 2\beta(t). \tag{5.8}$$

The relaxation time, being the ratio between the drag and restitution coefficients becomes

$$\tau(t) = \frac{\nu_X}{k \circ \beta(t)}, \tag{5.9}$$

where ν_X can be express in terms of the volume of the liquid and contact angle, as in Eq. (3.149), making it independent of t.

Eq. (5.7) is a linear first-order differential equation, and it can be solved by introducing an integrating factor [122], i.e., multiplying Eq. (5.7) by

$$g(t) = \exp\left[\int_{t_0}^{t} \frac{\mathrm{d}t'}{\tau(t')}\right]. \tag{5.10}$$

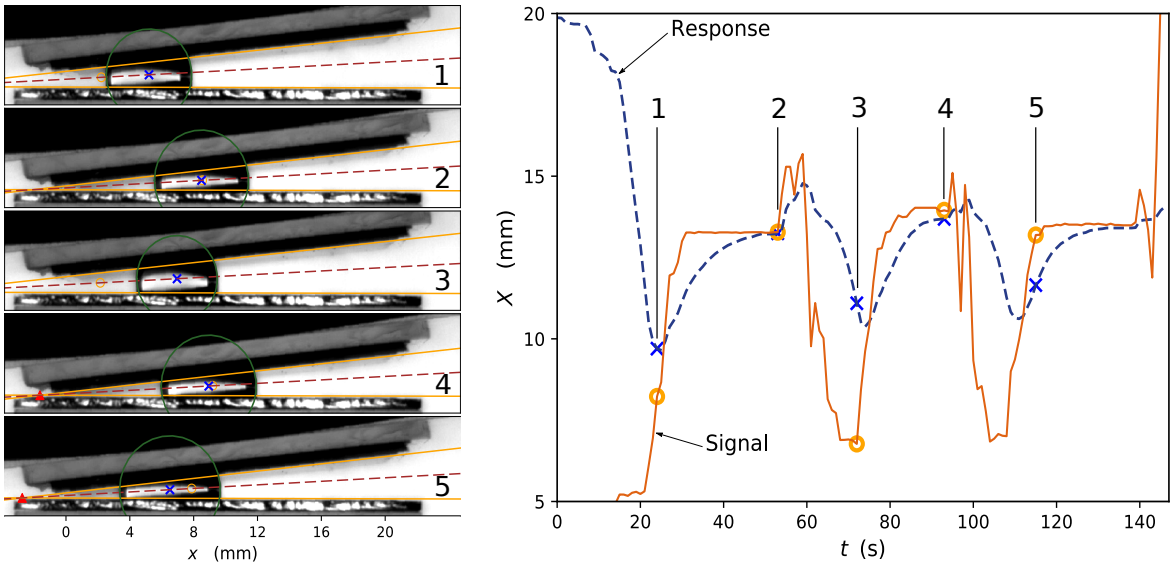

(a) (b)

Figure 5.8: Actuation of a droplet by reconfiguration of the wedge geometry. (a) The actuation signal, driven by the hand of the experimentalist, shifts the relative position of the apex of the wedge (▲). The new prescribed position (○) if followed by the centre of the droplet (×). (b) Equilibrium position and droplet trajectory for the sequence shown in (a). The droplet trajectory, here tracked by measuring the position of the centre of the osculating circle (green) in the frame of reference of the laboratory, X, follows the imposed signal with a lag determined by the friction force acting on the liquid.

Without loss of generality, it is assumed that the initial time is zero, $t_0 = 0$, the solution to Eq. (5.7) can be written as,

$$X(t) = [\, X(0) - X_\mathrm{e}(0) \,]\, e^{-\int \mathrm{d}t/\tau} + X_\mathrm{e}(t) - \frac{1}{g(t)} \int \dot{X}_\mathrm{e}\, g(t)\, \mathrm{d}t. \tag{5.11}$$

The first term in the right hand side of Eq. (5.11) can be interpreted as the effect of the initial conditions, which, in the long run, will fade out. The second term reveals that the position of the droplet will follow the equilibrium value with a delay given by the velocity of the signal, which is given by the third term. Note that for constant τ and X_e the more familiar solution of Eq. (5.3) is recovered.

The change in the energy of the system is given by,

$$\dot{\mathcal{E}} = \frac{\partial F_V}{\partial t} - \nu_X \dot{X}^2, \tag{5.12}$$

which is used to quantify the energy consumed during the actuation. The first term in the right-hand side of the equation stands for the power needed to produce the translation of the droplet; the second term is the dissipation term.

From the aforementioned experiments, the energy change as a function of time is reconstructed and is shown in figure 5.9. It was observed that when actuation takes place, there is a peak in the potential energy of the droplet. This occurs when the actuation time-scale is much faster than the relaxation time; henceforth resulting in accumulation of potential energy that will later on will be dissipated during motion. Moreover, if

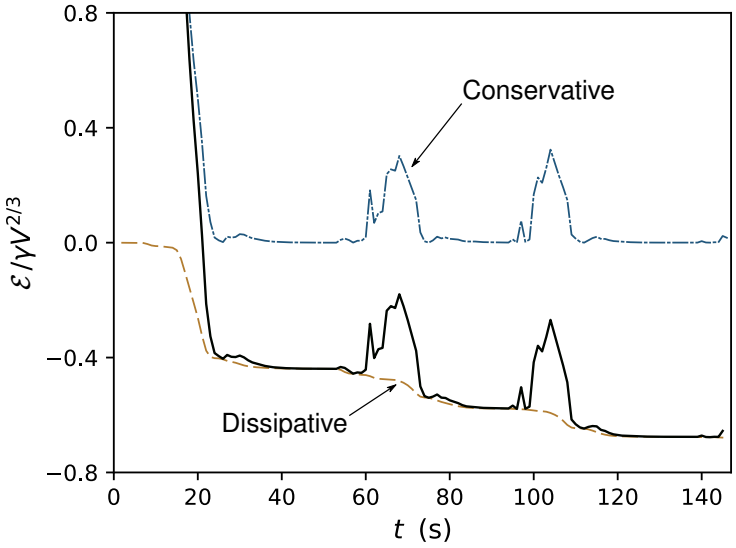

Figure 5.9: Evolution of the energy of the droplet upon manipulation within the SLIPS wedge. The total energy (solid line) is composed of the conservative energy (dashed line) which relaxes asymptotically to zero, and the dissipative energy (dot-dashed line) which decreases most when the velocity of the droplet is highest.

the driving force acts slowly, the energy remains close to its ground state, therefore the dissipation of energy can be arbitrarily small.

The overall change in energy is obtained by integrating Eq. (5.12) throughout the span of actuation time, i.e., from the initial time, $t = 0$, until the end, $t = T$.

$$\Delta\mathcal{E} = \Big[F_V(t)\Big]_0^T - \nu_X \int_0^T \dot{X}^2 \,\mathrm{d}t. \tag{5.13}$$

The first term in the right hand side of Eq. (5.13) is the energy difference between the initial and final configuration states.

Close to equilibrium, Eq. (3.146),

$$F_V(X,t) = F_\mathrm{e} + \frac{1}{2}k(t)[X - X_\mathrm{e}(t)]^2 + O(X - X_\mathrm{e})^3, \tag{5.14}$$

is valid. The ground state energy F_e depends only on the volume of the droplet and its contact angle, quantities kept constant during actuation. Then, if the droplet is set in equilibrium at both initial and final states of the actuation, the term in brackets of Eq. (5.13) is equal to zero. This is true, regardless of the initial and final positions, $X(0) \neq X(T)$, as long as these are equilibrium states. Consequently, the total change in energy is burnt in viscous dissipation.

Using the Eq. (5.11) in Eq. (5.13), and assuming that the starting and final states are in equilibrium, the total amount of energy dissipated is

$$\Delta\mathcal{E} = -\nu_X \int_0^T \left[\frac{1}{\tau g}\int \dot{X}_\mathrm{e}\, g \,\mathrm{d}t'\right]^2 \mathrm{d}t. \tag{5.15}$$

Eq. (5.15) shows the dissipation of energy in terms of the velocity of the driving signal, $\dot{X}_\mathrm{e}$, and the delay given by the function g. If the velocity of the signal is small, the term

inside the brackets of Eq. (5.15) is small, and therefore dissipation is almost negligible. This can be observed in figure 5.8 at frames 2 and 4, which corresponds to the plateaus in the conservative energy (dot-dashed curve of figure 5.9).

In contrast, when the equilibrium position of the droplet is drastically changed and the droplet speeds up (see figure 5.8, frames 1 and 5), a large dissipation takes place (see figure 5.9). Consequently, the total energy decreases by the release of the potential energy and but also by dissipation, and thus, $\Delta\mathcal{E}$ decreases from plateau to plateau.

5.3 Concluding remarks

In this chapter, experimental results of the statics and dynamics of droplets in wedges is reported. Good agreement with the theoretical description was made possible by using SLIPS surfaces as the bounding planes. This surfaces provide an ideal test bed for the model since they allow mobility of sessile droplets at virtually no pinning.

Finally, the possibility of droplet manipulation is explored. Relying on the theoretical framework constructed in previous chapters, the behaviour of a droplet, when actuating on the geometry of its confinement, can be predicted and controlled. In this case, it can be concluded that, since the initial and final states that a droplet acquire are energetically identical, the energy dissipated during actuation can be arbitrarily reduced.

Conclusions of Part I

In this part, the static and dynamics of partially wetting droplets in wedges is studied. The analysis is based on the sharp-interface formalism and, the shape of a droplet is proposed to simplify model, the liquid barrel. Then, lattice-Boltzmann simulations were carried out. These revealed details in the behaviour of this system, and also to compare the liquid barrel assumption. Finally, these concepts were applied with the purpose of droplet manipulation by means of actuating on the geometry of the confinement.

During the relaxation of the liquid barrels towards equilibrium, the motion of the liquid is driven by a distribution of the curvature of the interface which creates a pressure gradient. The resulting flow field in the bulk of the droplet is laminar. Near the contact lines, the flow field changes to the treadmill pattern described by Dussan and Davies [32]. The motion of the contact lines is driven by differences in the chemical potential caused by the out-of-equilibrium interface curvature [39]. The viscous stress and the chemical-potential imbalance make the dissipation density peak at the contact lines. This causes the contact angle to deviate from its equilibrium value and thus produce a force that opposes the motion.

The energy landscape experienced by the liquid barrel upon a translation from its equilibrium position reveals the effect of geometry on the restitutive force. This force is larger for a displacement towards the narrow portion of the wedge because of an increase in confinement. The same effect explains the decrease in the force as a function of the wetting angle; droplets with a higher contact angle tend to equilibrate further away from the apex of the wedge. The increase of the force with the wedge angle can be attributed to an increased rate of distortion of the shape of the droplet and the growth in the horizontal projection of the force.

The simulations to the model in §3 were compared, assessing the expressions of the relaxation time of the liquid barrel including the effect of the hydrodynamic dissipation of the bulk flow and the corner flow near the contact line, and the dissipation arising from the motion of the contact line itself. The scaling of the relaxation time is expressed in terms of the diffuse-interface model parameters. The results confirm the presence of the three contributions to the relaxation time.

The relative contribution of the contact-line and corner-flow dissipation (to the bulk dissipation) is governed by the size of the interface. In the simulations, this length scale is two orders of magnitude smaller than the size of the droplet, which contrasts with millimetre-sized droplets of molecular liquids (such as water) where the interface thickness is several orders of magnitude smaller than the typical macroscopic length scale of the flow. Qualitatively, however, the scaling relation for the relaxation time is expected to hold, and, thus, the results presented might help guide experiments to identify the contribution of the different sources of dissipation in this system.

The presence of parasitic effects due to numerical gave rise to inaccuracies in the

simulations. These manifest as the non-vanishing spurious currents that surround the interface droplet and the small amplitude oscillations in the translation of the droplet due to discretisation error of the solid boundary. The forces acting on the droplet in the immediacy of equilibrium are arbitrarily small, and any perturbation, which may stem from numerical errors, might interrupt its relaxation. Nonetheless, these numerical errors did not affect significantly motion of the flow and allowed the droplet to reach the expected equilibrium.

Further details in the behaviour of the droplet remain an open question. These include a unified and consistent structure of the flow of the inner and the outer phase in connection with the corner flow. The spurious currents had the effect of distorting the flow field that surrounds the droplet, thus obscuring the effect that the side vortices, predicted by the theory, have in the motion of the droplet. The discretisation error, or aliasing of the solid boundaries had a considerable impact in the velocity of the droplet, and for that reason, details on what affects the dynamic contact angle were not conclusive, and thus finer details of the dissipation function. Experiments, in order to avoid contact line pinning, made use of SLIPS surfaces, thus preventing measurements about the dynamics of a contact line.

Pathways for droplet actuation at no potential energy cost were presented, which can be accomplished at arbitrarily low energy dissipation. It is worth highlighting the relevance of these ideas in the design of new microfluidic devices that require the actuation of liquids. The example of droplet manipulation presented in this chapter might inspire more experiments [94] to further understand the behaviour and shape of droplets in wedge geometries. But also to further understand the behaviour of the system beyond the assumptions that were considered, e.g., when a true contact line is present or when the viscosity of the outer fluid is non negligible.

Part II

Evaporation of Droplets on Smooth Wavy Surfaces

Introduction to Part II

Although the evaporation of sessile droplets appears to be a simple diffusion problem, a significant amount of research is invested to predict and control this phenomenon [75, 123]. Important applications of droplet evaporation are Microcontact Printing [124] and Immersion Lithography [125, 126], which are highly effective techniques for microstructure patterning on surfaces. The miniaturisation of these technologies is only possible due to a highly controlled evaporation of specialised inks and solidification of resins that are deposited on a smooth substrate. In Microcontact Printing, the shape that the ink acquires during its evaporation has several consequences on the deposition of the material that the ink carries [124]. At the same time, the topography of the surface may also affect the morphology of the deposited ink [127]. In Immersion Lithography, water droplets, which are difficult to avoid, may stay in contact with the substrate and cause watermarks that damage the quality of the lithography [128]. Henceforth, controlling the location and morphology of the droplets as they evaporate is of paramount importance to these technologies.

Closely related to evaporation is condensation, as several features observed in evaporation persist in condensation. There are considerable reasons to motivate research along this line; for example, harvesting water out of humid air via dewing can provide a viable solution to the water shortage problem in arid regions [129]. Another example is in de-humidifiers, which use the same principle of condensation to reduce the concentration of water in ambient air. In such devices, the humidity-collecting surface is topographically patterned with grooves in order to increase the surface area for condensation, and thus the efficiency of the device [130]. These mechanism has been widely inspired by surfaces observed in nature, for example, the green frog in tropical Australia [131], the *Stenocara* beetle[129, 132], and some plants[133]. Nonetheless, by introducing the grooves, other effects affecting the behaviour of the condensing phase also take place [134]. Therefore, understanding how droplets behave on grooved surfaces presents the possiblity to further increase the efficiency of water-harvesters and de-humidifiers.

To date, four different "modes" of evaporation have been documented (see figure 5.10). Picknett and Bexon first proposed a model based on two modes to explain the behaviour of evaporating sessile droplets on solid surfaces [135]. These are, the *constant contact angle* or *slide mode* and the *constant area* or *stick mode*. In the slide mode of evaporation, the shape of the droplet remains constant as the droplet shrinks in size by the loss of mass. This requires that the contact lines are free to move, and therefore, the surface to be smooth and homogeneous [18]. In contrast, in the stick mode of evaporation, for the contact to remain constant, it is necessary that the contact lines maintain their position, thus the droplet becomes thinner and thinner with time [136]. This is commonly observed, for example, in the coffee rings, where, due to eddy flows, small coffee particles deposit at the contact lines leaving a ring-shaped stain [137].

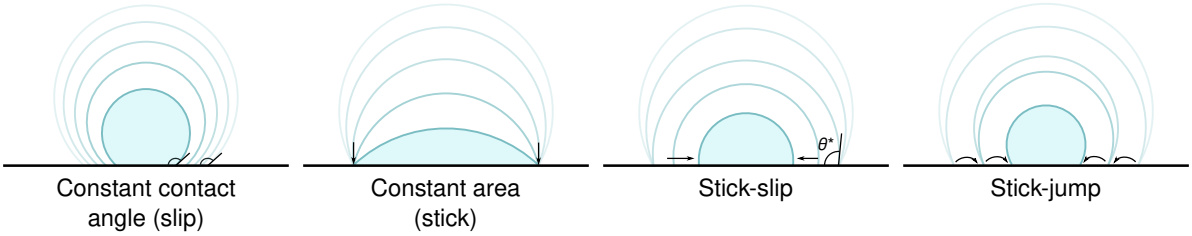

Figure 5.10: Four modes of evaporation of sessile droplets. Higher opacity in the liquid-gas interface of the droplets indicate later stages in the evaporation process.

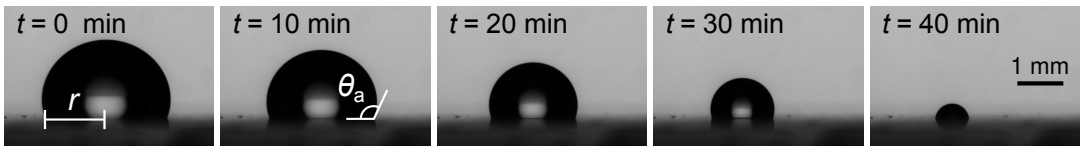

(a)

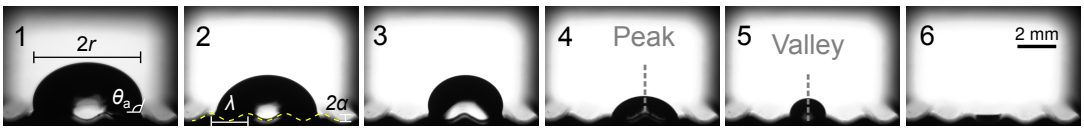

(b)

Figure 5.11: Snapshots of two water droplets evaporating. (a) An 8 μL water droplet on a flat LIR surface undergoing the slide mode of evaporation. (b) An 80 μL sessile droplet on a sinusoidal LIR surface with wavelength, $\lambda = 2$ mm, and amplitude $\epsilon = 200\,\mu$m undergoing snap evaporation.

It is also possible that the droplet undergoes a combination of constant area and constant angle modes, i.e., a *stick-slide* mode. This occurs when a droplet begins evaporating under the constant area mode until the contact angle reaches a critical value, θ^* in figure 5.10. After this point, the mode changes into a slip mode of evaporation, thus, the footprint radius of the droplet decreases but the contact angle stays fixed [138].

A fourth mode of evaporation has been reported, the *stick-jump* mode [139]. This occurs when a sessile droplet on a flat non-homogeneous surface undergoes a pinning and jumping mechanism in which the droplet keeps a constant area until a critical angle is reached, then it jumps acquiring a new radius and the contact angle is restored. The jumps occurs at discrete intervals of time until the droplet evaporates completely [140].

The focus of the next chapters is directed to the case of a droplet in contact with a surface which has a smooth sinusoidal topography. The droplet would be able to slide off if the surface was flat, nevertheless, due to the topography, it sits in a discrete set of locations. An experimental demonstration[2] of this effect is shown in figure 5.11. The surfaces used for the experiments are Liquid-Infused Rough (LIR) surfaces . Similar to the SLIPS (see §5.1), LIR surfaces consist of a 3D-printed surface coated with a superhydrophobic solution, and infused with a thin layer of oil.

When a droplet is in contact with a flat LIR surface, it undergoes a slide mode of evaporation, where the droplet keeps a constant contact angle for the most part of the evaporation process. That is, until the end, when the size of the droplet is comparable to

[2]I thank Gary G. Wells for providing the experimental images and plots.

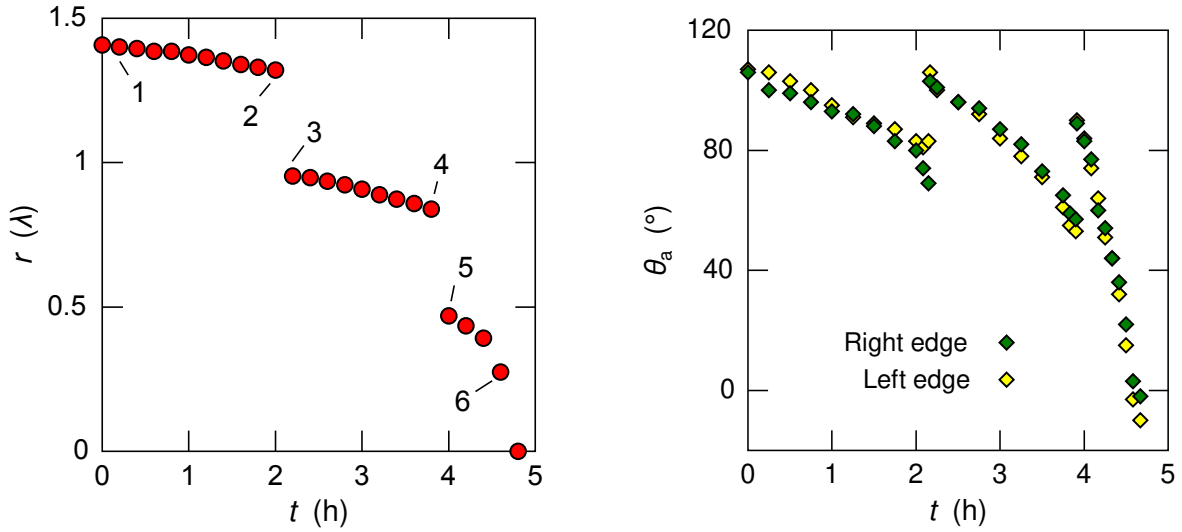

Figure 5.12: Time evolution of a droplet evaporating on a wavy LIR surface. (a) Plot of the radius as a function of time. The numbers correspond to the snapshots of figure 5.11(b). (b) Plot of the apparent contact angle as a function of time.

the height of the oil meniscus, thus affecting the shape of the droplet.

When the droplet sits on the wavy LIR surface, depending on its volume, it centres itself either at a peak or a trough of the topography (see figure 5.11(b)). During the most part of the evaporation process, the droplet smoothly changes its contact area and the apparent contact angle (see figure 5.12). However, there are times in which the droplet undergoes abrupt changes in its configuration: contracting its footprint radius and alternating from peak to trough or vice versa. This is a different mode of evaporation from any of the aforementioned, since both the footprint radius and contact angle are changing smoothly for most of the time, and discontinuously at moments. This new mode will be referred as *snap evaporation*.

In this part, the causes of snap evaporation are studied. The approach taken in §6, is to replicate the snap evaporation of droplets under lattice-Boltzmann simulations. Then, in §7, an analytical model based on the sharp-interface formalism is constructed. Finally, the conclusions of this part are presented.

Chapter 6

Lattice-Boltzmann Simulations

To better understand the mechanism of snap evaporation, numerical simulations of the coupled hydrodynamic and diffusion equations were carried out using the lattice-Boltzmann algorithm presented in §2. The aim will be to look into more detail at the conditions and the mechanism of the snap transition.

As detailed in §1, the governing equation for the evaporation of droplets is the Cahn-Hilliard equation (Eq. (1.26)),

$$(\partial_t + \boldsymbol{u} \cdot \boldsymbol{\nabla})\, \phi = M \nabla^2 \mu, \tag{6.1}$$

which models diffusive process driven by gradients in the chemical potential, μ. The latter is defined by a phase field, ϕ, according to Eq. (1.12) as,

$$\mu = B\phi(\phi^2 - 1) - K\nabla^2\phi, \tag{6.2}$$

where the parameters K and B can be adjusted by Eqs. (1.20) and (1.16) to give value to the surface tension and the interface thickness. Although we expect a quasi-static process, the velocity field, $\boldsymbol{u}$, which produces advective currents, cannot be neglected at this point. The velocity field is governed by the Navier-Stokes equation (Eq. (1.27)),

$$\rho\,(\partial_t + \boldsymbol{u} \cdot \boldsymbol{\nabla})\, \boldsymbol{u} = -\boldsymbol{\nabla} \cdot \mathbf{P} + \eta \nabla^2 \boldsymbol{u} + \rho \boldsymbol{g}. \tag{6.3}$$

where the pressure tensor, $\mathbf{P}$, is also defined by the phase field according to Eq. (2.20),

$$\mathbf{P} = \left[\frac{1}{4}B(\phi^2 - 1)(3\phi^2 + 1) - K\phi\nabla^2\phi - \frac{1}{2}K|\boldsymbol{\nabla}\phi|^2\right]\mathbf{I} + K\boldsymbol{\nabla}\phi\boldsymbol{\nabla}\phi, \tag{6.4}$$

and $\boldsymbol{g}$ is included to model the gravitational acceleration.

The wettability of the sinusoidal surface is tuned by introducing the boundary condition of Eq. (1.23),

$$K\hat{\boldsymbol{n}} \cdot \boldsymbol{\nabla}\phi = \chi, \tag{6.5}$$

where, the wetting potential, χ, is specified by the equilibrium contact angle, θ_e, according to Eq. (1.25).

Following §2, the coupled Cahn-Hilliard and Navier-Stokes equations are integrated by a lattice-Boltzmann algorithm.

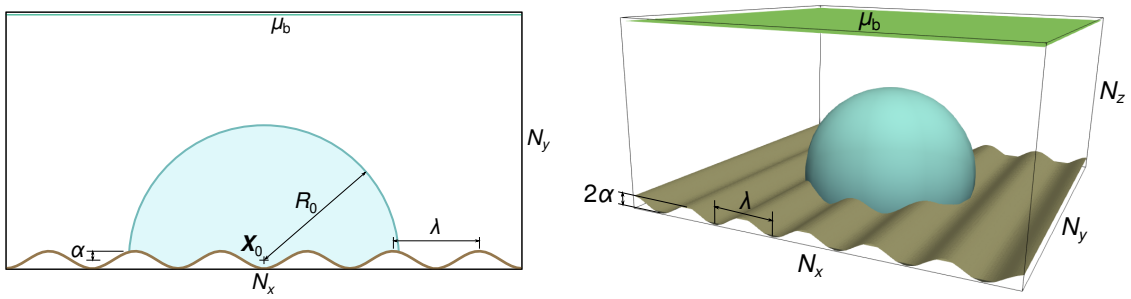

(a) (b)

Figure 6.1: Schematics of the 2D (a) and 3D (b) simulation set-up. At the bottom, the curved line (surface) represents the solid surface. At the top, a horizontal line (plane) representing the evaporation boundary condition where the value of the chemical potential is prescribed to μ_b.

6.1 Simulation Set-Up

For an evaporating sessile droplet on a topographically patterned surface, a simulation set-up similar to the one described in §2.3.6 is used; these are, 2D and 3D lattice-Boltzmann simulations of a binary fluid. The geometry of the lattice is a D2Q9 or a D3Q15 grid for the 2D and 3D simulations, respectively. The domain of the simulation is contained in a box of dimensions $N_x \times N_y(\times N_z)$. The sides of the simulation box have a periodic topology. At the bottom, the domain is bounded by the surface defined by the topography of the solid, whose local height is

$$h(x) = |\alpha| - \alpha \cos\left[2\pi(x - N_x/2)/\lambda\right] + 0.5. \tag{6.6}$$

An upper horizontal plane is fixed at the top of the simulation box, in which boundary conditions to promote evaporation are prescribed (see figure 6.1). Following §2.3.6, along the upper bounding surface the chemical potential is fixed to a constant value, μ_b.

Small inhomogeneities are introduced to the wettability solid surface in order to break the symmetry of the set-up. In the diffuse interface model, the surface energy of the solid, χ, is prescribed as a boundary condition [25]. In the lattice-Boltzmann simulations (see §2.2), the value of χ, can be specified in terms of the contact angle, θ', i.e.,

$$\chi(\theta') = \frac{3}{2}\gamma\,\mathrm{sgn}(\pi/2 - \theta')\sqrt{a(\theta')\left[1 - a(\theta')\right]}, \tag{6.7}$$

where $a(\theta') = \cos[\arccos(\sin^2\theta')/3]$, and $\mathrm{sgn}(x)$ gives the sign of x [26]. Therefore, it is possible to introduce inhomogeneities to the solid surface by randomly prescribing θ' at every boundary node. For this, a random number generator of normal distribution is used, whose mean and variance are θ_e and $\Delta\theta$, respectively. Small values of $\Delta\theta$ are chosen so that the deviation of the contact angle from θ_e is negligible, however, enough to create small perturbations that break the symmetry of the set-up.

Additionally, to replicate the effect of the gravitational acceleration observed in the experiments, a body force of the form was added,

$$\boldsymbol{g}(\boldsymbol{x}) = \frac{\phi(\boldsymbol{x}) + 1}{2}\, g_0\, \hat{\boldsymbol{e}}_z. \tag{6.8}$$

Table 6.1: List of parameters for the 2D and 3D simulations.

Common simulation paramters

Parameter	*Value*	*Parameter*	*Value*	*Parameter*	*Value*
γ	0.001	ℓ	2.12	μ_b	-1×10^{-5}
θ_e	105°	ρ	1	λ	$N_x/6$
$\Delta\theta$	0—1°	η	1/6	α	$\pm 0.1\lambda$

2D

Parameter	*Value*
N_x	240
N_y	120
M	8
g	0

3D

Parameter	*Value*
N_x	120
N_y	120
N_z	60
M	1
g	$-2 \times 10^{-}6$

The value of constant $g_0 = -2.0 \times 10^{-6}$ is chosen to match the Bond number ($Bo \approx 1.8$) of an 80 μL water droplet (~ 3 mm in radius).

As an initial condition, the fluid is at rest, and the shape of the droplet is spherical with centre at $\boldsymbol{X}_0$ and radius, $R_0 = 3\lambda/2$. In terms of the velocity field, $\boldsymbol{u}$, and order parameter, ϕ, the initial condition reads

$$\boldsymbol{u}(x, t = 0) = 0, \tag{6.9}$$

$$\phi(x, t = 0) = \tanh\left[\frac{R_0 - |\boldsymbol{x} - \boldsymbol{X}_0|}{\sqrt{2}\ell}\right]. \tag{6.10}$$

$\boldsymbol{X}_0$ is placed at the geometric centre of the surface $h(x)$, i.e.,

$$\boldsymbol{X}_0 = 0.5N_x\hat{\boldsymbol{e}}_x + (|\alpha| + 0.5)\hat{\boldsymbol{e}}_y, \tag{6.11}$$

for 2D simulations, and

$$\boldsymbol{X}_0 = 0.5N_x\hat{\boldsymbol{e}}_x + 0.5N_y\hat{\boldsymbol{e}}_y + (|\alpha| + 0.5)\hat{\boldsymbol{e}}_z, \tag{6.12}$$

for the 3D simulations, respectively. This generally renders the initial configuration of the droplet out of equilibrium, however, after a short transient, which was discarded, the droplet finds the stable equilibrium configuration.

The values of the simulation parameters used are summarised in table 6.1. Under these conditions, the typical time for the droplet to evaporate completely was found to be $\sim 10^7$ iterations for 2D simulations, and $\sim 10^5$ for 3D.

In order to characterise the behaviour of a 2D evaporating droplet on the wavy topography, as formulated in §7, the footprint radius, cross-sectional area, and interfacial energy were measured. To calculate these quantities, first, it is necessary to find the interface of the droplet, this is the set of points, I, that belong to the contour curve, $\phi = 0$, of the order parameter, i.e.,

$$I = \left\{\boldsymbol{x}_i = (x_i,\, y_i) \,|\, \phi(\boldsymbol{x}_i) = 0\right\}_{i=1}^{n}, \tag{6.13}$$

where $\boldsymbol{x}_1$ and $\boldsymbol{x}_n$ are the two contact points, n is the number of interface points on the set, and $\phi(\boldsymbol{x})$ is a linear interpolation of the order parameter field. The footprint radius

is obtained from the distance between the two contact points, i.e.,

$$r = \frac{|\boldsymbol{x}_1 - \boldsymbol{x}_n|}{2}. \tag{6.14}$$

The position of the droplet can be measured by averaging the position of the two contact points,

$$X = \frac{x_n + x_1}{2}. \tag{6.15}$$

The cross-sectional area can be calculated using the *shoelace* algorithm [141], [1] Following Eq. (1.8), the interfacial energy in two-dimensions was calculated by approximating the arc length of the fluid-fluid circular section and the arc length of the fluid-solid surface, i.e.,

$$F = \gamma \sum_{i=1}^{n} \left\{ |\boldsymbol{x}_{i+1} - \boldsymbol{x}_i| - \cos\theta_{\mathrm{e}} \sqrt{[x_{i+1} - x_i]^2 + [h(x_{i+1}) - h(x_i)]^2} \right\}, \tag{6.17}$$

where it is understood that the set I is sorted, that is, the interface points make a progressive sequence from $\boldsymbol{x}_1$ to $\boldsymbol{x}_n$, according to the rule

$$(\boldsymbol{x}_{i+1} - \boldsymbol{x}_i) \cdot (\boldsymbol{x}_i - \boldsymbol{x}_{i-1}) > 0, \quad \text{for } i = 2, ..., n-1. \tag{6.18}$$

For accuracy, the search for interface points is done until the distance between adjacent points is less than two lattice spacings, i.e.,

$$|\boldsymbol{x}_{i+1} - \boldsymbol{x}_i| < 2, \qquad \text{for } i = 1, ..., n-1. \tag{6.19}$$

6.2 Simulation Results

In order to assert agreement with the experimental results, full 3D simulations with the effect of gravity and inhomogeneities in the energy of the solid surface were carried out. In figure 6.2, the snapshots of the experiments and simulations at the moments previous and after the snap events are presented. In both cases, the evaporation sequence is normalised by the total evaporation time. As it can be observed, qualitatively, the morphology and position of the droplet is in good agreement with the experimental observations.

In an ideal situation, since the equilibrium state of the droplet appears to be symmetric, the droplet should not break the symmetry during the snap events. This, however, has not been observed in the experiments, and implies that the alternation in the position of the droplet, which renders an effective translation to the nearby sites, can only be possible if the symmetry is broken. Therefore, two situations of snap evaporation were examined: one in which all symmetries are preserved, and one in which noise on the surface energy of the solid is introduced as the only source of asymmetry.

To further simplify the system, 2D simulations where the effect of gravity has been removed were performed. Since symmetry in the transverse direction to the grooves is discrete it is expect that the snap events will persist in a two-dimensional system.

[1] The shoelace algorithm consists of adding the areas of the triangles cast by the corners of a polygon, in summary,

$$A = \frac{1}{2} \sum_{i=0}^{n} \left\{ \det \begin{vmatrix} x_i & x_{i+1} \\ y_i & y_{i+1} \end{vmatrix} + \det \begin{vmatrix} x_i & x_{i+1} \\ h(x_i) & h(x_{i+1}) \end{vmatrix} \right\}, \tag{6.16}$$

where the point $\boldsymbol{x}_0$ is identified with $\boldsymbol{x}_n$.

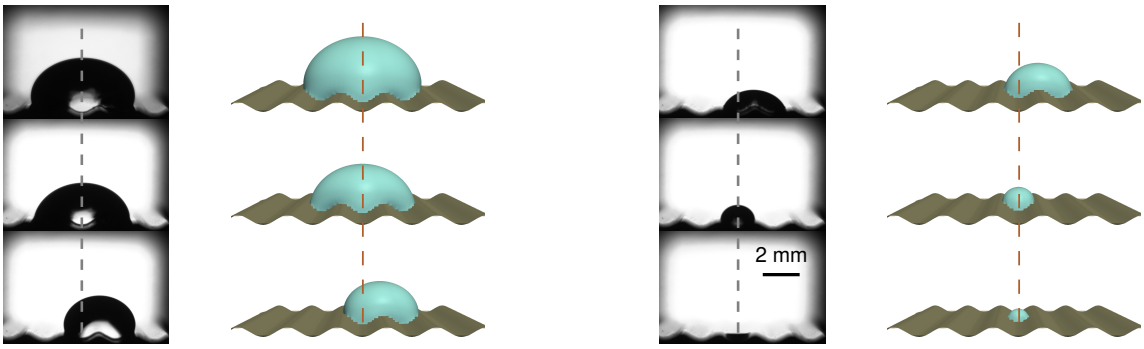

Figure 6.2: 3D simulation of a droplet undergoing a sequence of snaps during its evaporation. To the left of each frame, the experimental snapshot is presented for comparision.

6.2.1 2D Simulations Preserving Symmetry

Initially, the droplet begins evaporating in a symmetric configuration and centering itself either at a peak or at a valley of the surface pattern (see figure 6.3(a)). Then, as the mass of the droplet begins to decrease, the footprint radius slowly decreases, until reaching a point in which the footprint radius drops down at a faster pace. During this short period, it can be observed that the droplet builds pressure gradients in its core and, therefore, it is no longer in mechanical equilibrium (see figure 6.3(b)). At this time, a reconfiguration process of the droplet leads to a new equilibrium. Since the centre of the droplet stays at either a trough or a peak, it can be concluded that a *symmetric snap* has occurred.

Looking in more detail at the time interval where the symmetric snap takes place 6.3(c), it can be observed that, as the contact points get past the critical footprint radius, the contact points begin to move towards the centre of the droplet. This increases the pressure at both sides of the droplet which in turn creates a gradient forces the fluid to move to the centre of the droplet. Moreover, two side vortices on top of the interface appear, elevating the central part of the droplet and reducing its width. The snap event terminates when the flows die out and the droplet sits still on top of a trough, with its contact points resting near the peaks of the topography.

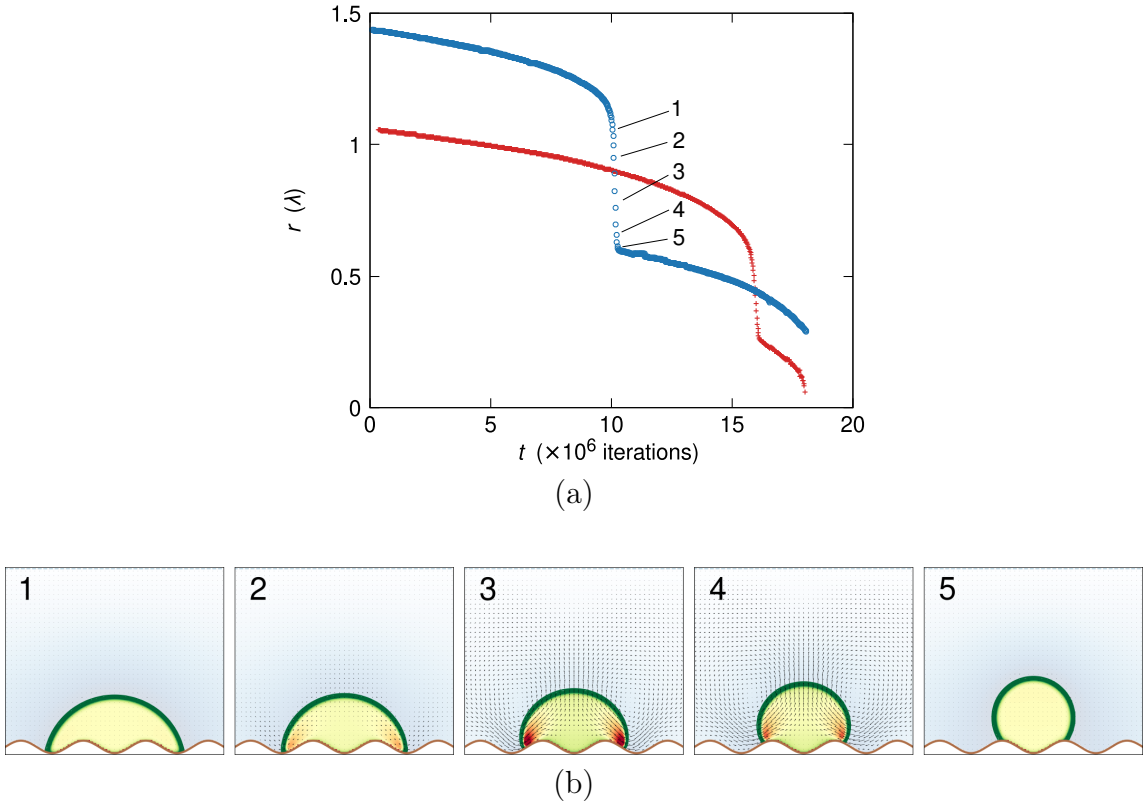

Figure 6.3: Evolution of a 2D sessile droplet on a homogeneous surface. (a) Plot of the time evolution of the footprint radius. The symbols correspond to droplets centred in a valley (○) or in a peak (+) of the periodic topography. (b) Sequence of snapshots during a symmetric snap of a droplet centred in valley. The velocity of the fluids is shown as a vector field. The colour maps represent the pressure inside the droplet, in a green (low) to red (high) gradient, and the chemical potential of the surrounding region, with a white (low) to blue (high) gradient.

6.2.2 2D Simulations with Noisy Surfaces

Now, the effect of the static noise in the evolution of the droplet will be examined. At the beginning of the simulation, the droplet is centred either at a peak or a trough (see figure 6.4(a)). As the droplet evaporates, it slowly begins to decrease its footprint radius keeping its shape unaltered by the inhomogeneities in the surface of the solid. This implies that the fluctuations in the equilibrium contact angle do not produce a significant change in the equilibrium state of the droplet. Consequently, the fluctuations produce perturbations to the state of the droplet, however, these equilibrium states are stable.

As the droplet evaporates, the footprint radius shows an evolution similar to the symmetric system, until the footprint radius reaches a point where a snap takes place. At the onset of the snap, however, the noise in the energy of the solid surface has a strong effect on the course of the relaxation to the new equilibrium configuration. The droplet snaps asymmetrically, reducing its footprint radius and shifting its centre to a side, this will be referred as an *asymmetric snap* (see figure 6.4(b)).

The sequence of snapshots of figure 6.4(b) that show the snap transition reveal details of the asymmetric snap. It can be observed that the contact point on the right is the first to move; this can also be recognised by the local increase in pressure (colour map).

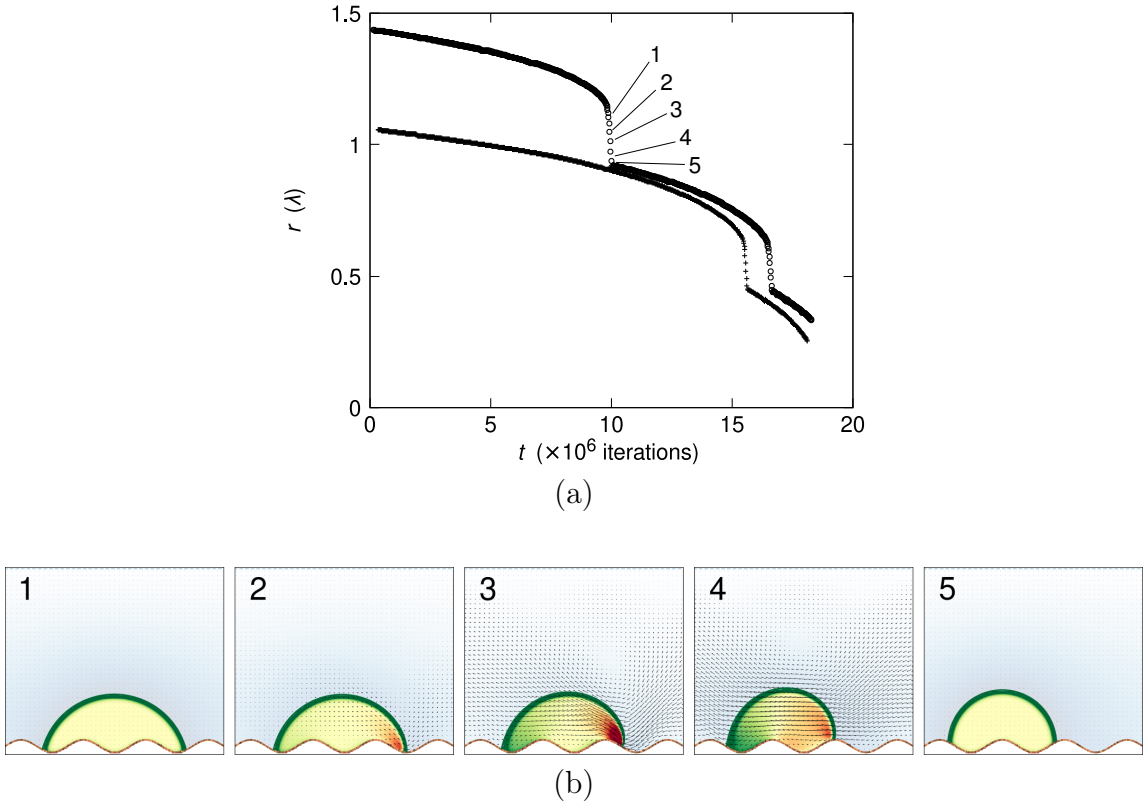

Figure 6.4: Evolution of a droplet sitting on a non-homogeneous wavy surface. (a) Time evolution of the footprint radius of the droplet. The symbols correspond to droplets initially centred at a valley (○) or at a peak (+) of the solid surface. (b) A sequence of snapshots during the asymmetric snap of a droplet previously centred in valley. The vector and colour maps have the same meaning as in figure 6.3.

Due to the motion of the right contact line, the pressure on the left side of the droplet decreases, and thus the left contact point moves away from the centre. In contrast to the symmetric snap, a single vortex appears at the right side, the fluid inside the droplet is propelled to the left resulting in a net translation leaving the droplet centred at a peak.

Comparing figures 6.3(b) and 6.4(b), it can be observed that the course of asymmetric the snaps is determined at an early stage. This is also observed in the experiments, since no symmetric snap has been observed.

6.3 Concluding remarks

Lattice-Boltzmann simulations of snapping droplets were successfully carried out. It was shown that the 3D simulations, with the effect of gravity, correctly match the sequence of states of an evaporating droplet on a wavy surface observed in the experiments. Furthermore, 2D simulations were carried out, these reveal that the phenomenon can be studied in two dimensions since the snaps transitions, and the rest of the evaporation process is well preserved. From the simulations, it was observed that the droplet undergoes two distinct snap transitions: the symmetric, in which the droplet remains in position, and asymmetric, in which the droplet switches to a nearby position.

Chapter 7

Analytical Model

7.1 Sharp-Interface Formulation

To further understand the causes for the snap events, a two-dimensional, sharp-interface model that captures the main features of the system will be constructed.

In the aforementioned experiments, it can be seen that for an $80\,\mu$L water droplet, at room temperature, and relative humidity of $\sim 20\%$, the time-lapse of evaporation is about 5 hours. On the other hand, any perturbation to the equilibrium state of the droplet will fade out due to viscous dissipation; presumably, after a few seconds [27, 96] for a water droplet of the same volume and in the same conditions. The high contrast between the evaporation and mechanical relaxation time-scales ensures that, during evaporation, the system is in mechanical equilibrium and the process can be considered quasi-static. This is a reasonable approximation except for the few instants in which the snaps occur, which will be considered instantaneous. This also implies that the cross-sectional area of the droplet, equivalent to the droplet volume, can regarded as the control parameter, instead of analysing the time evolution of the system explicitly.

For mechanical equilibrium to be possible, the pressure inside the fluid must be uniform, thus, according to the Young-Laplace law [3], the mean curvature of the interface must be constant for a quasi-static droplet configuration. Consequently, for a two-dimensional droplet, the shape of the interface must be circular. Additionally, assuming that the surface is ideal—free from pinning of the contact lines—implies that the intersection angle of the liquid-gas with the solid surface is equal to the equilibrium contact angle, θ_e, defined by the Young-Dupré relation (see figure 7.1).

On this basis, the problem is reduced to finding the set of circular arc shaped droplets of a prescribed cross-section area, A, and intersection angle θ_e.

Let the topography of the solid be parametrised as

$$h(x) = -\alpha \cos \frac{2\pi x}{\lambda}, \tag{7.1}$$

where α is the amplitude, and λ is the wavelength. Note that Eq. (7.1) is an even function, and advantage of this symmetry is taken by placing the centre of the droplet in the y axis. This implies that, $\alpha > 0$ represents a droplet sitting on top of a trough, whereas $\alpha < 0$ corresponds to a droplet sitting on a peak.

The liquid-gas interface is described by a circle of radius R, and centre at a point $(0, y_0)$. The intersection of the liquid-gas interface and the solid surface occurs at the

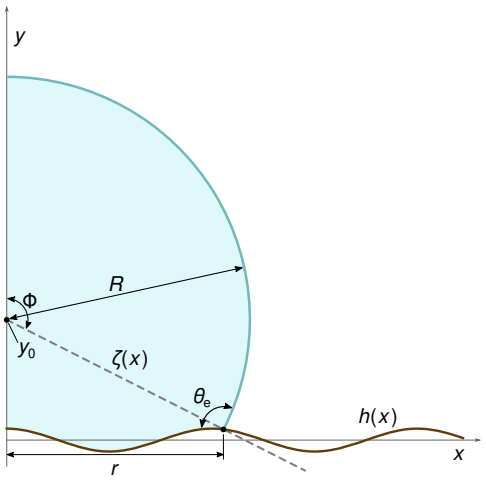

Figure 7.1: Schematics of a 2-D sessile droplet on a sinusoidal surface.

contact point which is at a distance r from the axis of symmetry, thus, defining the footprint radius (see figure 7.1).

Let $\zeta = \zeta(x)$, be the straight line that joins the centre of the droplet with the contact point. The angle opening from the y axis to the line ζ will be denoted as Φ. Then, the cross-sectional area of the droplet is obtained by adding the area of the of the truncated circle, delimited by Φ, and the area bounded by the curves $\zeta(x)$ and $h(x)$, i.e.,

$$A(r) = \Phi R^2 + 2\int_0^r [\zeta(x) - h(x)]\, dx. \tag{7.2}$$

Therefore, to evaluate the cross-sectional area, it is necessary to determine the opening angle, the radius of the droplet and the slope of the line ζ in terms of the footprint radius. The opening angle reads

$$\Phi(r) = \theta_\mathrm{e} - \arctan h'(r). \tag{7.3}$$

Then, the radial line ζ can be expressed as,

$$\zeta(x) = h(r) + (x - r)\, \cot \Phi(r), \tag{7.4}$$

where the slope, expressed in terms of θ_e and r, is

$$\cot \Phi(r) = \frac{1 + h'(r) \tan \theta_\mathrm{e}}{\tan \theta_\mathrm{e} - h'(r)}. \tag{7.5}$$

The relation between the radius of the droplet and contact point follows by noting that $r = R \sin \Phi$, and using Eq. (7.3), which leads to

$$R = \frac{r\sqrt{1 + h'(r)^2}}{\sin \theta_\mathrm{e} - h'(r) \cos \theta_\mathrm{e}}. \tag{7.6}$$

The apparent contact angle, as measured in the experiments (see figure 5.11), is

$$\theta_\mathrm{a} = \Phi. \tag{7.7}$$

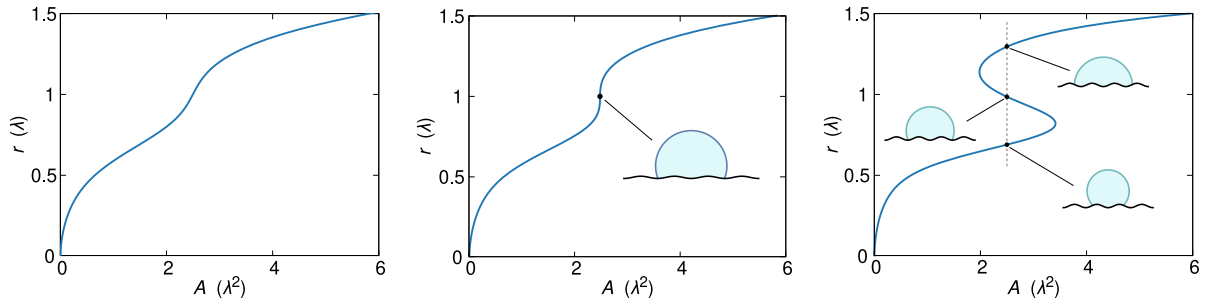

(a) (b) (c)

Figure 7.2: Cusp bifurcation in the relation of the radius of the droplet, r, and the cross-sectional area, A: (a) at low amplitude of the pattern ($\alpha = 0.013\lambda$), (b) at the bifurcation point ($\alpha \approx 0.033\lambda$), (c) and at high amplitude ($\alpha = 0.073\lambda$). The contact angle is $\theta_e = 110°$.

7.2 Equilibrium States

Having established the geometry of the system, the corresponding equilibrium state for a given cross-sectional area can now be determined. By virtue of Eqs. (7.1), and (7.3)–(7.6) Eq. (7.2) can be evaluated and thus give

$$A(r) = \Phi(r)\, R^2 - 2r\alpha \cos\frac{2\pi x}{\lambda} - r^2 \cot\Phi(r) + \frac{\alpha\lambda}{\pi}\sin\frac{2\pi r}{\lambda}. \tag{7.8}$$

In figure 7.2, r vs A is plotted for different values of the undulation amplitude of the solid, α. At small amplitude, the base radius grows monotonically with A in the range shown in figure 7.2(a). Consequently, as the droplet evaporates and A decreases, the radius can follow the decrement smoothly. In contrast, at large amplitude (see figure 7.2(c)), the footprint radius is not always unique for a given droplet area, i.e., the system is *multistable* [142].

In the context of dynamical systems, the emergence (or disappearance) of equilibria as a control parameter varies, is called a *bifurcation*. In this case, it is a *cusp* type bifurcation, which corresponds to the onset of multiple equilibrium states [142], and is triggered by the bifurcation parameter, α/λ, as can be seen from figure 7.2. Later, it will be clarified that the cusp bifurcation is not the mechanism that produces the snap events, however, it is a necessary condition.

The bifurcations are found to be characterised by the loss of monotonicity in the $A(r)$ curve. This implies that, when multiple equilibrium states emerge, A develops an inflection point, thus satisfying

$$\partial_r^2 A = 0. \tag{7.9}$$

Moreover, a minimum and a maximum appears at the sides of the inflection point. As the bifurcation parameter is decreased, the two extrema approach each other until they merge. This implies that,

$$\partial_r A = 0, \tag{7.10}$$

is passed on to the bifurcation point [143]. In other words, Eqs. (7.9) and (7.10) yield the necessary conditions for the bifurcation, and algebraically determine the value of the bifurcation parameters, α^* and r^*.

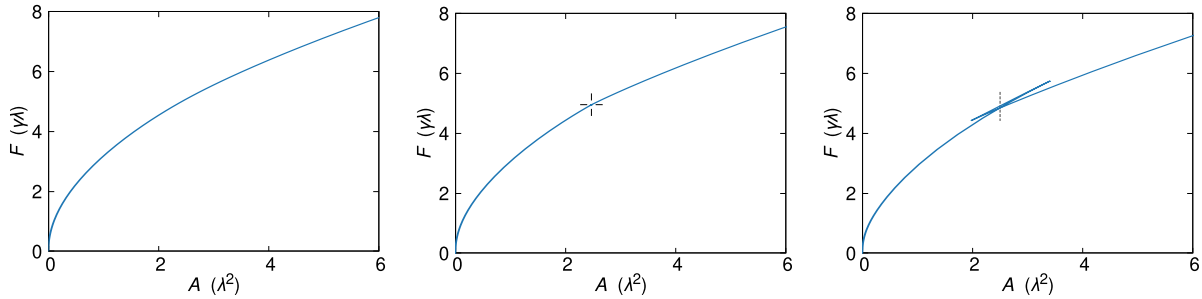

(a) (b) (c)

Figure 7.3: Plot of the energy *vs* cross-sectional area of the droplet parametrised by the footprint radius for pattern amplitude (a) below the bifurcation ($\alpha = 0.013\lambda$), (b) at the bifurcation point ($\alpha \approx 0.033\lambda$), and (c) above the bifurcation ($\alpha = 0.073\lambda$) for a contact angle, $\theta_e = 110°$. The bifurcation point is indicated by the cross mark in (b), and area of the multistable equilibria from figure 7.2(c) is presented by the vertical dashed line in (c).

7.3 Stability of Equilibria

To analyse the stability of the system, the energy of the equilibrium droplet configurations will be calculated. The interfacial energy is calculated from the two arc lengths of the liquid-gas and the solid-liquid interface,

$$F(r) = 2\gamma\Phi R - 2\gamma\cos\theta_e \int_0^r \sqrt{1 + h'(x)^2}\,\mathrm{d}x, \tag{7.11}$$

which, by virtue of Eqs. (7.1), and (7.3)–(7.6), can be evaluated, i.e.,

$$F(r) = 2\gamma\Phi R - \frac{2\gamma\lambda\cos\theta_e}{2\pi} E\left(\frac{2\pi r}{\lambda}, \mathrm{i}\frac{2\pi\alpha}{\lambda}\right), \tag{7.12}$$

where E is the incomplete elliptic integral of the second kind, and $\mathrm{i} = \sqrt{-1}$.

In figure 7.3, F *vs* A is plotted, parametrised by r, for different values of the amplitude of the pattern. It can be observed that, when the amplitude is below the bifurcation value (figure 7.3(a)), the scaling of the energy is approximately the square-root of the cross-sectional area. For this value of the amplitude, the grooves have a weak effect on the shape of the droplet, therefore, the area roughly grows as the square radius, and the energy linearly, therefore $F \sim A^{1/2}$. At the bifurcation (see figure 7.3), the derivative

$$\frac{\mathrm{d}F}{\mathrm{d}A} = \frac{\partial_r F}{\partial_r A}, \tag{7.13}$$

presents a discontinuity (see Eq. (7.10)). Further increasing the amplitude produces a bow-like structure in the energy curve (figure 7.3(c) and close-up of the bow structure in figure 7.4).

Figure 7.4 shows a closer look to the behaviour of the system at large amplitudes, where the loop in the energy curve appears. In this plot, the equilibrium curves of both valley-centred and peak-centred droplets are included. Consider an evaporating droplet on a surface of amplitude $\alpha > \alpha^*$, and consider that the area of the droplet is well above the inflection point as in state (1) of figure 7.4. As the droplet evaporates, the system

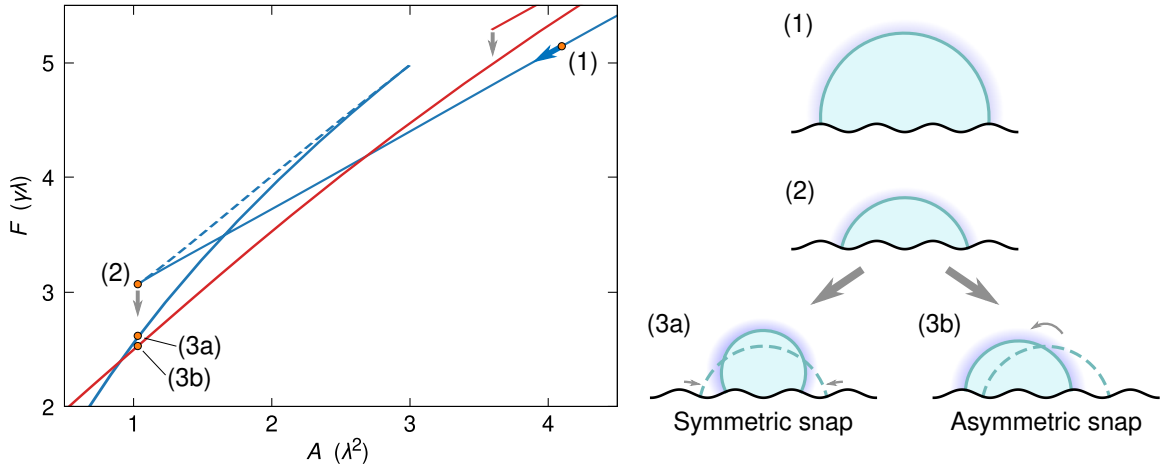

Figure 7.4: Trajectory of an evaporating droplet in the energy space. Initially, a large droplet starts at state (1) and moves along the solid blue line until it reaches state (2). After (2), the system is driven to a new configuration state with lower energy, which could be either (3a) or (3b). The dashed line represents the states with higher energy in the metastable region.

stays in equilibrium and the trajectory follows the solid line until reaching state (2). This is a critical point, since $\partial_r A = 0$. A further (infinitesimal) loss in the area brings the droplet out of equilibrium. At that moment, the trajectory goes downwards, decreasing its energy, to either state (3a) or (3b) in an "instantaneous" transition, i.e., the *snap*.

If the symmetry of the system is preserved, the centre of droplet remains in place and the transition to the new equilibrium state (e.g., (3a)) is a *symmetric snap*. However, if the symmetry of the system is broken, e.g., by fluctuations or by inhomogeneities in the solid surface, the transition results in an *asymmetric snap* (e.g. (3b)). In this case, the droplet moves sideways, switching its centre from a valley to a peak, as exemplified in the figure, or *vice versa* depending on the former configuration.

As shown in figure 7.4 by the dashed segment, the region joining the two extrema of the multistable region has a higher energy. States with higher energy are disfavoured compared to those with lower energy, and therefore, it is expected that the stability of these states is lower.

7.4 Comparison with the Simulations

Looking at the simulation results for the 2D droplet, the trajectory that the system draws in the r–A and F–A space can be observed. More details of the snap transitions can be found With the aid of the simulations.

In figure 7.5(a, b), the footprint radius as a function of the cross-sectional area, A, can be observed during the evaporation of the droplet. At the beginning of the simulations, both valley- and peak-centred droplets, have a high value in A, and follow their equilibrium branch until they reach their critical points. At that point, the droplet loses its equilibrium state and is forced to jump to a new equilibrium state. Since the symmetry is preserved throughout the simulations, the droplets maintain their positions, thus resuming the evaporation process in the same equilibrium branch.

Figure 7.5(c, d) shows the effect that noise to the energy of the solid surface produces. In the beginning of the trajectory, no difference from a symmetric system is evident, until the critical point is reached whence the snap transitions reveal the asymmetry. During the course of the snap, the base radius is reduced, however, to the other equilibrium branch, which corresponds to a peak if the droplet was initially centred in a valley.

7.5 Bifurcations Induced by the Cross-Sectional Area

The 2D simulations presented in §6.2.2, indicate that the droplet configuration sequence is determined at the early stages of the snap transition. Therefore, fluctuations in the contact angle reveal that the symmetric transition is unlikely due to an instability that precedes slightly before the symmetric snap. This is further confirmed in figure 7.6(a), note that the trajectory of a sessile droplet on noisy surface does not quite reach the critical point and begins to depart from the equilibrium branch in a symmetric snap. This is evidence that the stable equilibrium branch now has lost stability at some value of A before the critical value, repelling the trajectory from the current branch, and now being attracted by the side branches (see figure 7.6). Due to the topology of the of the solutions of a continuous dynamical system, this requires that two unstable equilibrium points at the sides of this branch merge with it and breaking its stability [144]. In the language of the dynamical systems, this is called a *subcritical pitchfork bifurcation* [142].

On the other hand, if the symmetry is not broken, lateral motion is forbidden, and the trajectory goes past the pitchfork bifurcation. This implies that, the equilibrium branch does not show any instability if symmetry is preserved. Consequently, the section of the equilibrium branch from the pitchfork bifurcation to the critical point is stable to variations of the footprint radius, but unstable to lateral perturbations, i.e., a *saddle* [143].

As the evaporation of a droplet on a homogeneous surface continues and A reaches the critical point, the local equilibrium configurations suddenly disappear. This is due to a *fold bifurcation* [142], and consists of a collision of a saddle point and an unstable point. It occurs at the critical value, where the curve $A(r)$ reaches a minimum or a maximum. In this case, the unstable point belongs to the high energy section of the branch as shown in figure 7.4.

7.6 Concluding remarks

In this chapter, a two-dimensional sharp-interface model has been constructed to elucidate the origin of the snap transitions that droplets undergo when placed on wavy surfaces. First, it was found that the number equilibrium states that the droplet can acquire depend on the amplitude of the topography: at low values of the amplitude, the relation is unique, however at higher values, multiple configurations for a given volume can be found. The latter gives the requirement for the snap transitions, that is to say, if the amplitude of the topography is small enough, the evaporation of the droplet will follow a quasi-static evolution.

It was found that the transition between these two behaviours is due to a cusp bifurcation. The cusp bifurcation is accompanied by a fork bifurcation, which is transited as the mass of the droplet is reduced by evaporation. The fold bifurcation gives rise to symmetric snaps. Moreover, with the aid of the lattice-Boltzmann simulations, a third

bifurcation was found, a pitchfork bifurcation, which precedes the fold bifurcation and corresponds to the asymmetric snaps.

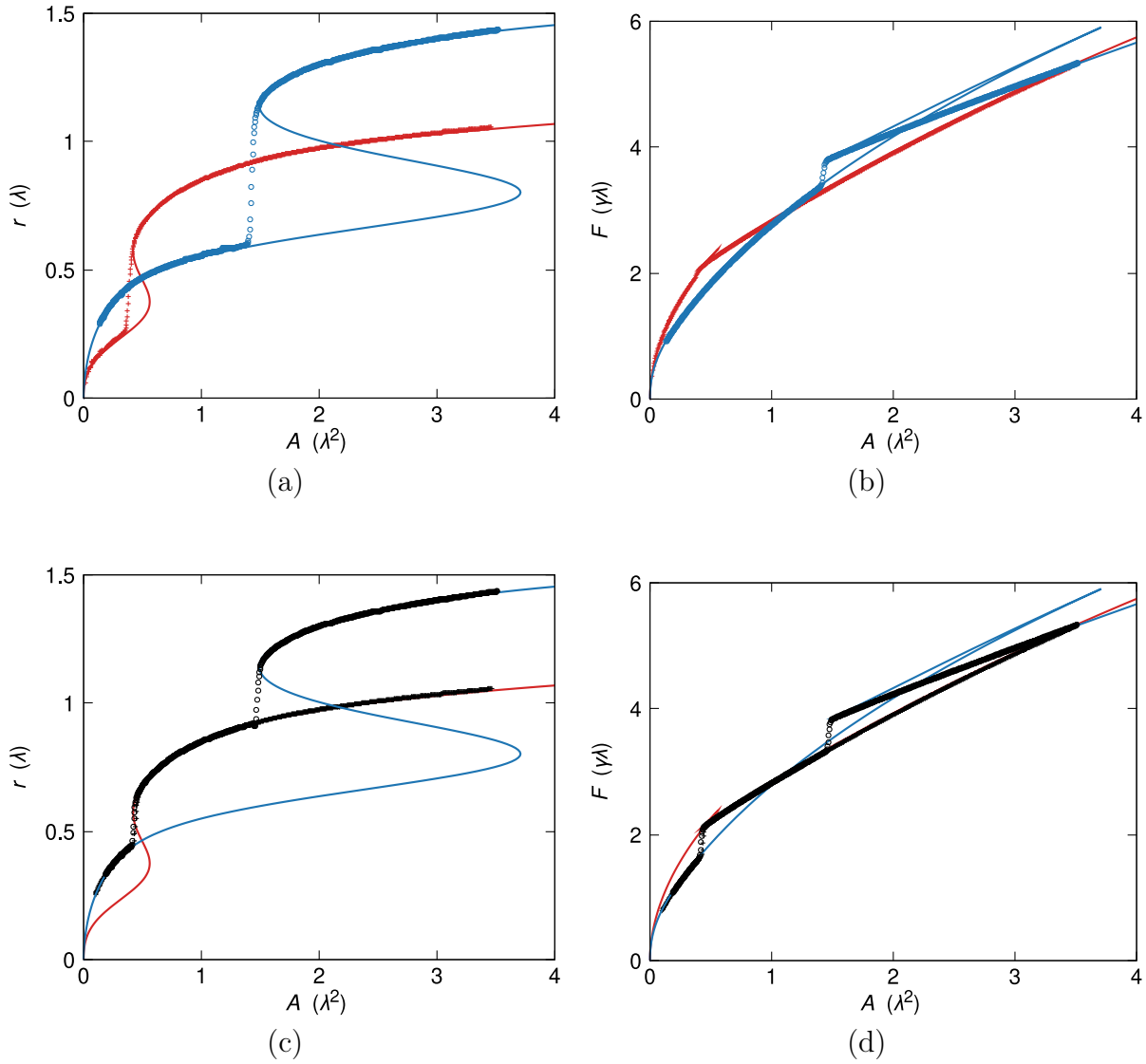

Figure 7.5: Evolution of a 2D system. (a, c) Plot of the footprint radius against the cross-sectional area and (b, c) plot of the interfacial energy as function of the area. In (a) and (b) the system preserves it symmetry, whereas in (c) and (d) noise in the surface energy of the solid is introduced to give rise to asymmetric snaps. The blue and red curves correspond to the equilibrium branches of a valley-centred droplet ($\alpha = 0.1$) and a peak-centred droplet ($\alpha = -0.1$), respectively. The symbols have the same meaning as in figures 6.3 and 6.4.

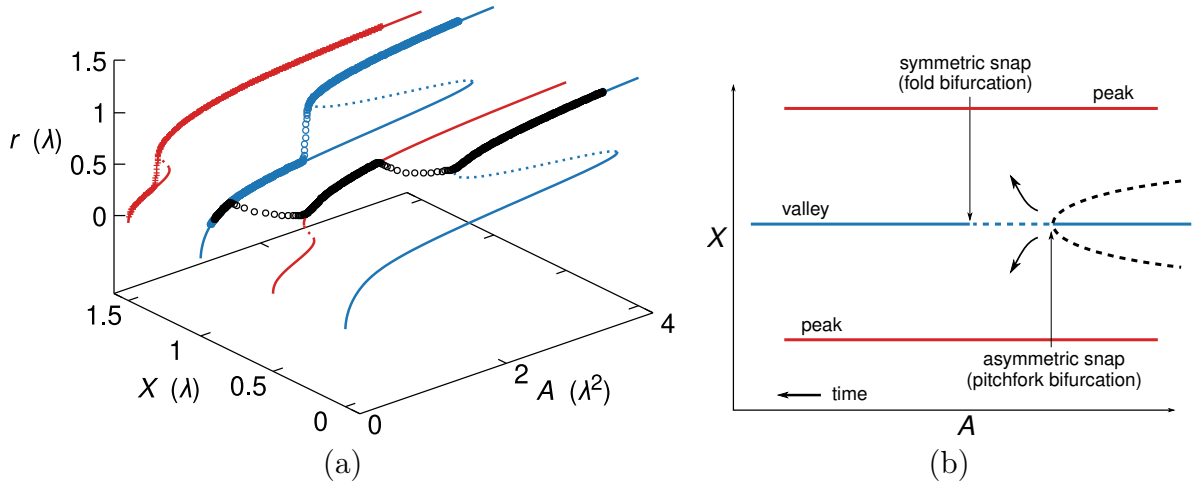

Figure 7.6: Bifurcations in the evolution of snap evaporation. (a) Simulation trajectories projected as shown in the A–X–r space. Symmetric trajectories stay with a constant position, X, unlike noisy trajectories that switch from branch to branch. (b) Caricature of the bifurcation diagram of the position of the droplet with respect to the bifurcation parameter, A. The stable equilibria of the branches is depicted by a solid line, the saddle points are represented by a dashed line.

Conclusions of Part II

The evaporation of sessile droplets on a sinusoidal patterned surface was studied using lattice-Boltzmann simulations and an analytical model based on a sharp-interface formalism. During the course of its evaporation, the base radius and contact angle of the droplet smoothly changes except for the few sudden events dubbed snaps. The snap events occur when the amplitude of the surface undulation is big enough, and are caused by a bifurcation in the stability of the equilibrium configuration.

Two types of snaps transitions; corresponding to symmetric and asymmetric snaps were identified. The symmetric snap, only observed in the simulations, occurs when the system is symmetric upon reflections about the centre of the droplet. It can be described as a quick contraction of the contact lines leaving the position of the droplet unaltered. This transition is the consequence of a fold bifurcation which annihilates the local equilibrium state. The asymmetric snap, in contrast, is the one observed in the experiments, and consists of a lateral displacement of the droplet together with the contraction of its footprint radius. It is caused by a pitchfork bifurcation that precedes the fold bifurcation in the course of the evaporation, and because of this, the symmetric snaps are not observed in experimental situations.

The pitchfork and fold bifurcations are triggered by the cross-sectional area of the droplet, A/λ^2, which is the relevant control variable of the two-dimensional system since it is proportional to the current mass of the droplet as it evaporates. Nonetheless, due to the relation between the footprint radius and the cross-sectional area, the first can be used as a bifurcation parameter as well.

A third type of bifurcation was found, a cusp bifurcation, which is triggered by the amplitude of the surface undulations, α/λ. This bifurcation, creates multistability in the equilibrium curves, and thus the emergence of the fold bifurcations. Due to the relation of the footprint radius, r, with the cross-sectional area, A of the droplet, r can also be used as the bifurcation parameter. The bifurcation diagram, r–α, can be used to visualise the stable and unstable branches for droplet of a given footprint radius (see figure 7.7). It can be observed that for $|\alpha|$ above any cusp bifurcation, a curve separating the stable and unstable region is born. This corresponds to the set of fold bifurcations that give rise to the symmetric snaps. The bifurcation diagram shows how the sinusoidal pattern determines the valid solutions for the base radius of the droplet. [145, 146].

A two-dimensional system has revealed the richness and details of the snap evaporation in the experimental set-up. Figure 7.8 shows a comparision of the analytical model with the experimental data. The evolution of the footprint radius in the experiments shows that the snap occurs before the fold bifurcation, further contrasting the presence of the pitchfork bifurcation. However, the apparent contact angle presents higher discrepancies from the analytical model. This may be due to a change in the height of the oil meniscus in relation to the size of the droplet that occurs in the LIR surfaces used in the

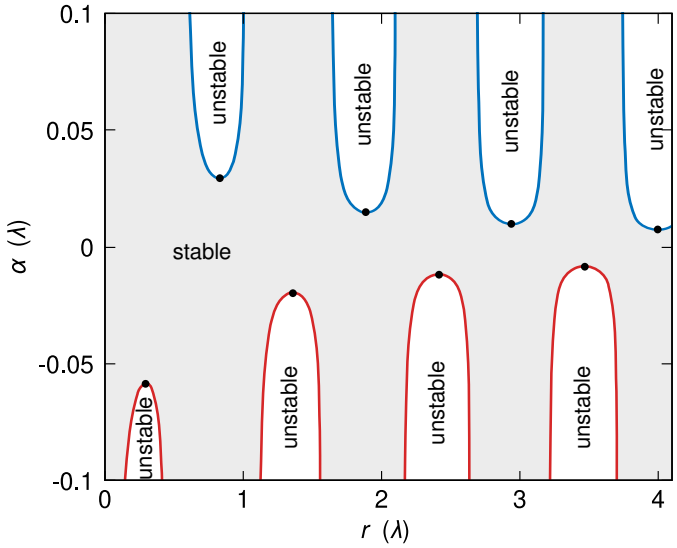

Figure 7.7: Bifurcation diagram r–α. Fold bifurcations shown as coloured solid lines, and correspond to the critical points that lead to symmetric snaps. The shaded (or white) areas represent the location of stable (or unstable) equilibria. The coloured regions correspond to the equilibrium branch of a valley-centred (blue), peak-centred (red). The cusp bifurcations are shown as black dots. The contact angle is set to $\theta_e = 120°$ to produce this plot.

experiments [147, 119].

The 3D simulations with the effect of gravity did not present any qualitatively difference in the behaviour with respect to the 2D simulations. This is expected since weak gravitational field only distort the shape of the droplet, however, maintaining the contact angles unaltered. Because of this, the contact area of the droplet can be matched by a droplet of a different volume unaffected by gravity, at least in the cross section. Therefore, the present model may still be valid. Although, the relation of the footprint radius and the cross-sectional area of a droplet may be distorted by gravity, it is not expected any qualitative difference to arise.

The time evolution of the cross-sectional area of a droplet that undergoes snap evaporation is monotonic, and continuous (see figure 7.9(a)). Since the evaporation rate of the droplet depends on the exposed surface area [135], the evolution of A is smooth most of the time, except at the snap transitions, where the curves present a sudden change in slope as the droplet is subject to a quick reduction of its interface area.

Moreover, it can be observed that the droplet that undergoes a series of asymmetric snaps evaporates at a lower pace compared to the other two symmetric cases. This is expected, since after an asymmetric snap, a lateral leap of the droplet allows it to sit in a configuration with a larger base radius and thus, less exposed surface area. Therefore, droplet that undergo asymmetric snaps take a longer time to evaporate.

Considering that the fluctuations that affect the droplet are unpredictable, it can assume that, because of the asymmetric snaps, the droplet jumps with equal probability to any of its neighbouring sides. This implies that the trajectory of the position of the droplet is not unique, thus the initial conditions cannot be traced back, nor the future evolution is fully determined. Therefore, the evolution of the position of the droplet is a stochastic process, discrete both in time and space.

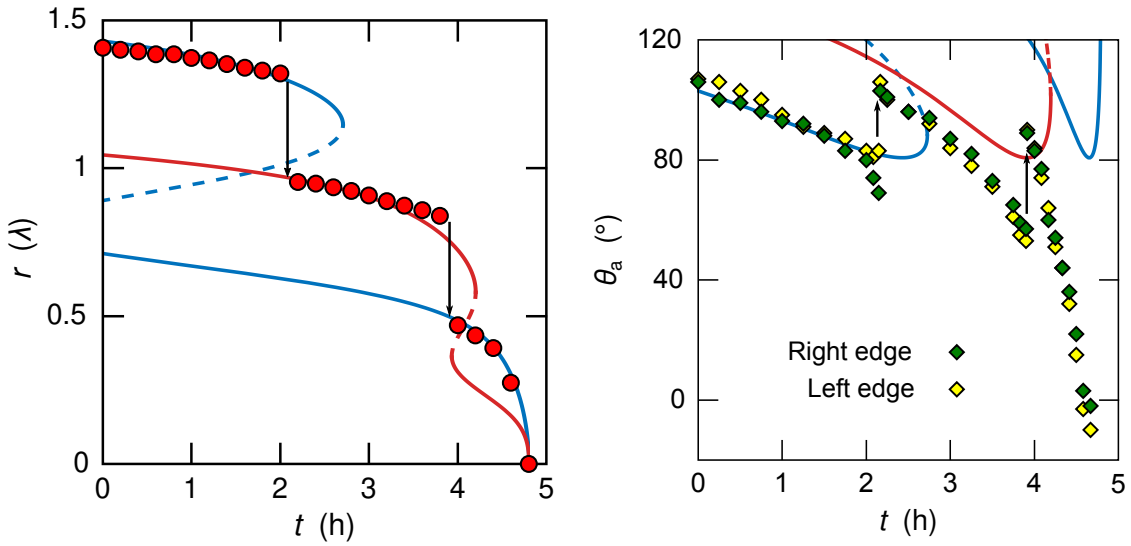

(a) (b)

Figure 7.8: Time evolution of (a) the base radius, r, and (b) the apparent contact angle, θ_a, measured in the experiments compared to the analytical model. To produce these plots, it has been assumed that, in 3D, the cross-sectional area decreases at a constant rate. The constant of proportionality is adjusted by matching the initial configuration with the moment when the droplet has evaporated.

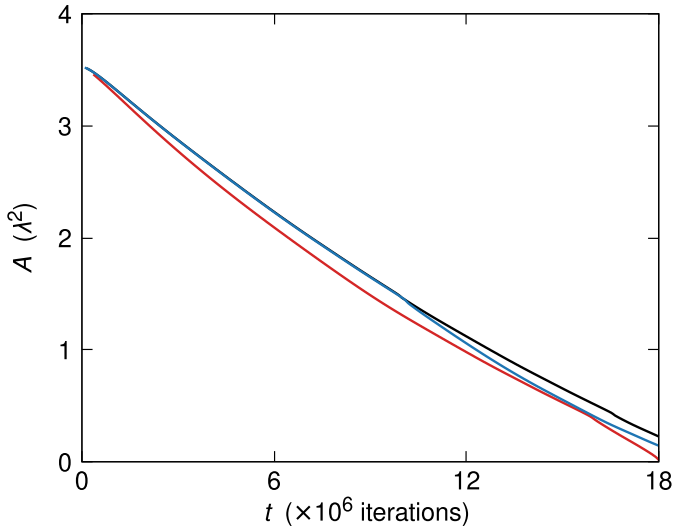

Figure 7.9: Time evolution of (a) the cross-sectional area of 2D droplets undergoing snap evaporation. The black line corresponds to a droplet undergoing asymmetric snaps, the blue and red curves represents a valley-centred and a peak-centred droplet, respectively.

General Conclusions

In this work, the statics and dynamics of capillary surfaces in contact with solid boundaries using analytical and numerical models have been studied. For this, a lattice-Boltzmann method (LBM) that models open boundaries which allow mass transfer by means of diffusive or advective currents was developed. An algorithm to model the dynamic wetting of the fluids on smooth solid boundaries of an arbitrary shape was also introduced.

The statics and dynamics of a droplet inside a wedge was analysed. A model for the shape of the droplet was put forward, which can be found with the name "liquid barrel". Using this assumption, the energy and pressure of the droplet at different positions within the wedge were computed. This allowed the calculation of the forces that the droplet exerts to restore its equilibrium position. Using a Lagrangian formulation, and estimating dissipative forces, the translational motion in which the droplet relaxes to equilibrium was studied. It was found that the equilibration process obeys an exponential trend, which is characteristic of overdamped motion. This implies that the characteristic time in which this occurs is determined by the quotient of friction and restitutive coefficients.

The liquid barrel assumption was validated by comparing the analytical results with LBM simulations and with experiments. The simulations confirm that the energy dissipated by the droplet during its translational motion can be attributed to the friction forces operating at three different length-scales. The macroscopic length-scale corresponds to the viscous dissipation of the flows in the bulk of both phases. In the intermediate length-scale, the dissipation is due to the corner flow, which corresponds to the hydrodynamic friction arising due to the motion of the fluids in the close vicinity of the contact line. This source of friction links to the microscopic scale since it depends on diffusive processes that escape a purely hydrodynamic description. At the microscopic level, the diffuse-interface approximation predicts a third source of dissipation, which is inversely proportional to the mobility. This mechanism has an interesting implication: although diffusion is an irreversible process, and thus dissipative, the diffusion of the chemical potential has a lubricating effect which facilitates the motion of the droplet.

The applicability of the liquid-barrel model in the manipulation of a droplet confined in a wedge was also demonstrated. This consisted on actuating the geometry of the wedge confinement in order to achieve translational motion. It was shown that by decreasing the speed of the droplet, one can approach the limit of translational invariant motion.

The behaviour of an evaporating sessile droplet on a wavy surface was also studied. Due to the patterned topography, the droplet rests in equilibrium on a discrete set of positions. The stability and emergence of these states depend on the volume of the droplet, therefore, as the droplet evaporates, the equilibrium configuration is suddenly lost. As a consequence the droplet relaxes to a new configuration changing its shape and position. Those transitions were named "snaps", because the footprint radius of the droplet always decreases in a much shorter timescale than evaporation. LBM simulations

were carried out and then an analytical model was constructed to understand the causes for these transitions. It was found that such events can to occur due to a bifurcation in the equilibrium configuration of the droplet, and this bifurcation is triggered by the amplitude of the surface topography. Therefore, at sufficiently low amplitudes in the surface pattern, snap events can be prevented. Moreover, it was found that the actual snap transition occurs due to other bifurcations which are triggered by the volume of the droplet. Therefore, as the droplet evaporates, the reduction of its volume induce an instability that drive the droplet to a new configuration.

Some lessons on the physics of contact lines are worth mentioning. When modelling the motion of a contact line from a hydrodynamic approach, it is assumed that a fluid is in a local thermodynamic equilibrium. For that reason, a slip-length is artificially included to produce the effect that is experimentally observed. This assumption must be used with caution, since it is know to fail under several circumstances [31, 109].

In the diffuse-interface formulation of phase transitions, the motion of a triple line is possible due to diffusive flows of chemical gradients. This provides an advantage since the slip-length becomes a consequence of the model rather than a requirement. It is then left to the diffusive coefficient as the tuning parameter to match the experimental evidence. However, when this is carried out, the values obtained are much larger than what is expected for normal diffusive processes [42, 9], and once again, caution must be taken. Therefore, despite the success of the diffuse interface approach, it can be said that the problem of contact line dynamics lies at a deeper level, in which kinetic effects at molecular level are dominant [33, 148]. In that context, the spontaneous motion of droplets in wedges may provide a plausible alternative for experimental examination on the motion of contact lines. That is because the opening angle of the wedge can be tuned to amplify the effect of the dissipative forces acting on the droplet and thus allowing fine measurements on the progression of the contact lines.

On the other hand, the snap transitions observed in the evaporation of droplets on wavy surfaces provide an interesting insight on the problem of contact line hysteresis. By construction, the surfaces in which the experiments are conceived allow a smooth motion of the contact lines, nonetheless, before any snap event, the contact angle reaches a minimum value. A similar effect occurs for condensation of droplets, in which case, the contact angle would reach a maximum value before the sudden spreading of the droplet. Therefore, hysteresis in the contact angle is induced by the topography of the surface. From the bifurcation diagram in figure 7.7, it can be seen that in order to avoid these sudden transitions, for large droplets ($r \gg \lambda$), the amplitude of the topography must be decreased at a higher rate. In other words, if the grooves of the surface are shrunk while maintaining their aspect ratio, contact angle hysteresis is inevitable. This would explain the difficulties in producing surfaces completely free from pinning, since roughness is always found at a microscopic level.

Appendix A

LBM Constants

Table A.1 containst a list of the lattice-Boltzmann velocity sets and table A.2 geometric factors for the D2Q9, D3Q15, and D319 models.

Table A.1: Lattice-Boltzmann velocity sets for the models:

D2Q9

q	$(c_q)_x$	$(c_q)_y$
0	0	0
1	-1	0
2	0	-1
3	0	1
4	1	0
5	-1	-1
6	-1	1
7	1	-1
8	1	1

D3Q15

q	$(c_q)_x$	$(c_q)_y$	$(c_q)_z$
0	0	0	0
1	1	0	0
2	-1	0	0
3	0	1	0
4	0	-1	0
5	0	0	1
6	0	0	-1
7	1	1	1
8	1	1	-1
9	1	-1	1
10	-1	1	1
11	1	-1	-1
12	-1	1	-1
13	-1	-1	1
14	-1	-1	-1

D3Q19

q	$(c_q)_x$	$(c_q)_y$	$(c_q)_z$
0	0	0	0
1	1	0	0
2	-1	0	0
3	0	1	0
4	0	-1	0
5	0	0	1
6	0	0	-1
7	1	1	0
8	1	-1	0
9	1	0	1
10	1	0	-1
11	-1	1	0
12	-1	-1	0
13	-1	0	1
14	-1	0	-1
15	0	1	1
16	0	1	-1
17	0	-1	1
18	0	-1	-1

Table A.2: Lattice Boltzmann weighting factors. ($w(|\boldsymbol{c}_q|^2) \stackrel{\text{def}}{=} w_q$.)

Model	$w(0)$	$w(1)$	$w(2)$	$w(3)$	c_s^2
D2Q9	4/9	1/9	1/36	0	1/3
D3Q15	2/9	1/9	0	1/72	1/3
D3Q19	1/3	1/18	1/36	0	1/3

Appendix B

The Jeffery-Hamel Flow

The flow within a wedge geometry, including inertial effects, was addressed by Rosenhead [74]. Here, a similar procedure in the low-Reynolds number is followed to obtain behaviour of the flow. Using polar coordinates, the velocity field is expressed as $\boldsymbol{u} = u_r\hat{\boldsymbol{r}} + u_\theta\hat{\boldsymbol{\theta}}$, and the angular flow is assumed to vanish, i.e., $u_\theta = 0$.

The continuity equation, Eq. (1.36), reads,

$$\frac{1}{r}\frac{\partial r u_r}{\partial r} = 0, \tag{B.1}$$

which has the general solution,

$$u_r(r,\theta) = \frac{f(\theta)}{r} \tag{B.2}$$

where f depends only on θ. The explicit form of f can be found using the Stokes equations, Eq. (1.35). In polar coordinates, and using (B.2), these read

$$\eta\frac{f''}{r^3} - \frac{\partial p}{\partial r} = 0, \tag{B.3}$$

$$2\eta\frac{f'}{r^3} - \frac{1}{r}\frac{\partial p}{\partial \theta} = 0. \tag{B.4}$$

Integrating (B.4) with respect to θ gives the pressure profile,

$$p(r,\theta) = \frac{2\eta}{r^2}f(\theta) + g(r), \tag{B.5}$$

where g only depends on r. Substituting this result into (B.3) gives the equation,

$$\frac{\mathrm{d}^2 f}{\mathrm{d}\theta^2} + 4f = \frac{r^3}{\eta}\frac{\mathrm{d}g}{\mathrm{d}r}. \tag{B.6}$$

The left hand side only depends on θ, whereas the right hand side only depends on r. This can only happen if both sides are equal to a constant, c_1. Therefore,

$$g(r) = -\frac{c_1\eta}{2r^2} + c_2, \qquad \text{and} \qquad f(\theta) = \frac{c_1}{4} + c_3\cos 2\theta + c_4\sin 2\theta. \tag{B.7}$$

The constants c_i, $i = 1, ..., 4$ can be found by imposing boundary conditions to the flow. Due to symmetry, the flow profile must be an even function of θ, therefore $c_4 = 0$. Imposing a no-slip boundary condition at the walls of the wedge fixes $c_1 = -4c_3\cos 2\beta$.

Setting the pressure to $p(r_1) = p_1$ and $p(r_2) = p_2$ at two arbitrary points, r_1 and r_2, fixes $c_2 = (p_1 r_1^2 - p_2 r_2^2)/(r_1^2 - r_2^2)$ and $c_3 = (p_2 - p_1) r_1^2 r_2^2 / 2\eta(r_1^2 - r_2^2)$. Finally, the velocity of the flow reads,

$$\boldsymbol{u}(r, \theta) = \frac{1}{2\eta} \frac{p_2 - p_1}{r_2 - r_1} \frac{r_1^2 r_2^2}{r_1 + r_2} \frac{\cos 2\beta - \cos 2\theta}{r} \hat{\boldsymbol{r}}, \tag{B.8}$$

and the pressure field is,

$$p(r, \theta) = -\frac{p_2 r_2^2 - p_1 r_1^2}{r_2^2 - r_1^2} + \frac{1}{r^2} \frac{p_2 - p_1}{r_2 - r_1} \frac{r_1^2 r_2^2}{r_2 + r_1} \cos\theta. \tag{B.9}$$

Appendix C

Coefficients of the Volume and Free Energy Polynomial Forms

Changing back to the (φ, ϑ)-parametrisation of the liquid barrel, the liquid-gas surface element is,

$$\mathrm{d}\boldsymbol{A}_{\mathrm{lg}} = (\partial_\varphi \boldsymbol{x} \times \partial_\vartheta \boldsymbol{x}_{\mathrm{lg}})\,\mathrm{d}\vartheta\mathrm{d}\varphi \tag{C.1}$$

Using Eq. (3.32) and integrating with respect to ϑ gives,

$$\begin{aligned} V = \frac{1}{3}\int_0^{2\pi} R\,\{2(X\partial_\varphi r \sin\varphi + r^2 + Xr\cos\varphi)\sin\psi + R[r(3\psi + \sin\psi\cos\psi) \\ +X(\psi + \sin\psi\cos\psi)\cos\varphi] + 2X\partial_\varphi R\psi\sin\varphi + 2R^2\sin\psi\}\;\mathrm{d}\varphi, \end{aligned} \tag{C.2}$$

Following the Eq. (3.10) and Eq. (3.11), the radii r and R read

$$r(\varphi) = \frac{q\epsilon\alpha}{\cos\varphi + \alpha}, \tag{C.3}$$

$$R(\varphi) = q\left(1 + \frac{\epsilon\cos\varphi}{\cos\varphi + \alpha}\right). \tag{C.4}$$

Substituting Eqs. (C.3) and (C.4) into Eq. (C.2) results in a polynomial of ϵ where the coefficients are,

$$a_0 = \frac{1}{3}\int_0^{2\pi} \{2\sin\psi + \alpha[\psi + \sin\psi\cos\psi]\cos\varphi\}\;\mathrm{d}\varphi, \tag{C.5}$$

$$\begin{aligned} a_1 = \frac{1}{6}\int_0^{2\pi} (\cos\varphi + \alpha)^{-3}\,\{&4\alpha^4\cos\varphi\sin\psi \\ &+ \alpha^3[(4\psi + 2\sin\psi + \sin 2\psi)\cos 2\varphi + 6(\psi + \sin\psi) + 2\sin 2\psi] \\ &+ 2\alpha^2[(\{3\psi + \sin 2\psi\}\cos 2\varphi + 7\psi + 4\{2 + \cos\psi\}\sin\psi)\cos\varphi] \\ &+ \alpha[(2\psi + \sin 2\psi)\cos 2\varphi + 8\psi + 4(6 + \cos\psi)\sin\psi]\cos^2\varphi \\ &+ 12\cos^3\varphi\sin\psi\}\;\mathrm{d}\varphi, \end{aligned} \tag{C.6}$$

$$a_2 = \frac{1}{12}\int_0^{2\pi} (\cos\varphi+\alpha)^{-3}\left\{4\alpha^3[\cos 2\varphi+3]\sin\psi \right. \\ +\alpha^2[(6\psi+\sin 2\psi)\cos 2\varphi+22\psi+16\sin\psi+5\sin 2\psi]\cos\varphi \\ +\alpha[(2\psi+\sin 2\psi)\cos 2\varphi+26\psi+24\sin\psi+5\sin 2\psi]\cos^2\varphi \\ \left.+24\cos^3\varphi\sin\psi\right\}\,\mathrm{d}\varphi, \tag{C.7}$$

and

$$a_3 = \frac{1}{6}\int_0^{2\pi} (\cos\varphi+\alpha)^{-3}\left\{4\alpha^2\cos\varphi\sin\psi \right. \\ +\alpha\left[6\psi+\sin 2\psi\right]\cos^2\varphi \\ \left.+4\cos^3\varphi\sin\psi\right\}\,\mathrm{d}\varphi. \tag{C.8}$$

The evaluation of the integrals requires an explicit expression of the angle ψ, using Eq. (3.8) gives

$$\tan\psi = \frac{\tan\beta}{\alpha^2\tan^2\beta-1}\left[\alpha\sqrt{1+(\cos^2\varphi-\alpha^2)\tan^2\beta}+\cos\varphi\right]. \tag{C.9}$$

Using (C.9) and expanding in powers of β leads to (3.56).

To compute the interfacial energy, it is first noted that (3.46) is composed of two terms, the first being

$$\int_0^{2\pi}\int_{-\psi}^{\psi}|\mathrm{d}\boldsymbol{A}_{\mathrm{lg}}| = \int_0^{2\pi}\int_{-\psi}^{\psi} R\left[R^2\cos^2\vartheta+2Rr\cos\vartheta+r^2+(\partial_\varphi R+\partial_\varphi r\cos\vartheta)^2\right]^{1/2}\,\mathrm{d}\vartheta\mathrm{d}\varphi. \tag{C.10}$$

The integral in ϑ can be expressed in terms of elliptic functions. Then, substituting R and r using Eqs. (C.3) and (C.4), gives an expression in terms of q and ϵ. This is then complemented by Eq. (3.48), and after making a third order Taylor expansion ϵ, leads to Eq. (3.58).

Appendix D

Bulk Dissipation of the Liquid Barrel

By substituting Eq. (3.118) in Eq. (3.130), the energy dissipation in the bulk of the droplet can be determined. First, the gradient of the velocity field is

$$\boldsymbol{\nabla u}_{\text{bulk}} = \frac{\dot{X}\beta(s_1+s_2)}{s^2(2\beta\cos 2\beta - \sin 2\beta)}\begin{bmatrix}\cos 2\omega - \cos 2\beta & \sin 2\omega \\ 0 & \cos 2\beta - \cos 2\omega\end{bmatrix}, \tag{D.1}$$

which leads to the bulk energy dissipation density

$$\dot{\varepsilon} = -\frac{\eta}{2}(\boldsymbol{\nabla u}_{\text{bulk}} + \boldsymbol{\nabla u}_{\text{bulk}}^T)^2 = \frac{2\eta\dot{X}^2\beta^2(s_1+s_2)^2(3+\cos 4\beta - 4\cos 2\beta\cos 2\omega)}{s^4(2\beta\cos 2\beta - \sin 2\beta)^2}. \tag{D.2}$$

To obtain the total dissipation, Eq. (D.2) needs to be integrated over a volume $V_{\text{eff}} < V$, that corresponds to the region where the Jeffery-Hamel is adequate and thus the bulk dissipation of the barrel takes place.

V_{eff} is approximated as a toroidal section, of major radius equal to the distance X, and a minor diameter $R'_o = R_o(1-\delta)$, for some positive $\delta \leq 1$. Therefore, the bulk dissipation is

$$\dot{\mathcal{E}}_{\text{bulk}} = \int \dot{\varepsilon}\,\mathrm{d}V_{\text{eff}} = \int_{-\beta}^{\beta}\int_{X-R'_o}^{X+R'_o}\int_{-\sqrt{R'^2_o-(s-X)^2}}^{\sqrt{R'^2_o-(s-X)^2}} \dot{\varepsilon}\,\mathrm{d}y\,s\mathrm{d}s\,\mathrm{d}\omega, \tag{D.3}$$

which evaluates to

$$\dot{\mathcal{E}}_{\text{bulk}} = -16\,\pi\,\eta\frac{\xi^2}{(\xi^2-1)^{3/2}}\frac{[\beta\,(\cos 4\beta + 3) - \sin 4\beta]\,\beta^2}{(2\beta\cos 2\beta - \sin 2\beta)^2}\,R'_o\,\dot{X}^2. \tag{D.4}$$

From Eq. (D.4) the effective volume can be redefined as $V_{\text{eff}} \overset{\text{def}}{=} V(1-\delta)$, and with this replace R'_o. Then, taking a Laurent series expansion in β of Eq. (D.4) leads to Eq. (3.131).

Appendix E

The Contour Integral of the Velocity of the Contact Line

To calculate the closed-loop integral in Eqs. (3.137), and (3.140), v_{cl}, the projection of the velocity perpendicular to the contact line must be first obtained. This can be done by obtaining a parametrisation of the contact line. Points belonging to the contact line can be reached through three displacements from the origin, that is,

$$\boldsymbol{x}_{\mathrm{cl}} = X\hat{\boldsymbol{e}}_x + X\sin\beta\,\hat{\boldsymbol{n}} + \boldsymbol{r}_{\mathrm{cl}}. \tag{E.1}$$

The first displacement lands in the centre of the droplet, from there, the next displacement moves to the nearest point in the top solid surface, concluding with a coplanar displacement to the triple line represented by the vector $\boldsymbol{r}_{\mathrm{cl}}$. This vector can be obtained using Eq. (3.4) evaluated at the solid boundary. Then, $\boldsymbol{r}_{\mathrm{cl}} = \boldsymbol{x}_{\mathrm{lg}}(\varphi, \vartheta = \psi) - X\hat{\boldsymbol{x}} - X\sin\beta\,\hat{\boldsymbol{n}}$, which gives the radius of the contact line,

$$\begin{aligned} r_{\mathrm{cl}} = \frac{q}{2(\alpha+\cos\varphi)}\Big[&2(1+\epsilon)^2 + \alpha^2(3-2\alpha^2+4\epsilon^2) - 4\alpha\{\alpha^2 - 2(1+\epsilon)\}\cos\varphi \\ &+ 2\alpha\cos 2\beta(\alpha+\cos\varphi)^2 + \{2(1+\epsilon)^2 - \alpha^2\}\cos 2\varphi \\ &+ 8\alpha\epsilon\{\alpha + (1+\epsilon)\cos\varphi\}\cos\psi\Big]^{1/2}, \end{aligned} \tag{E.2}$$

where the relation $\sin\psi = (\alpha + \cos\varphi\cos\psi)\tan\beta$ that results from Eq. (3.8), was used to simplify the expression. Substituting Eq. (C.9), the contact line radius can be expressed in series form,

$$r_{\mathrm{cl}} = q(1+\epsilon) - \frac{1}{2}q\alpha\beta^2(\alpha + \epsilon\cos\varphi) + O(\beta^3). \tag{E.3}$$

Notice that at $\epsilon = 0$, the variation in φ from Eq. (E.2), is lost and the contact line becomes a circle. From Eq. (E.3), it can be seen the that dependence in φ is weak, since it is proportional to $\alpha\beta^2\epsilon \sim \beta\epsilon$.

After obtaining the magnitude of the vector $\boldsymbol{r}_{\mathrm{cl}}$, its direction can be expressed by the unitary vector $\hat{\boldsymbol{r}}_{\mathrm{cl}} = \boldsymbol{r}_{\mathrm{cl}}/r_{\mathrm{cl}}$. From Eqs. (E.1), (C.9), and (E.2), it can be seen that

$$\hat{\boldsymbol{r}}_{\mathrm{cl}} = \frac{(\cos\varphi,\ \sin\varphi,\ \tan\beta\cos\varphi)}{\sqrt{1+\tan^2\beta\cos^2\varphi}} + \boldsymbol{O}(\beta^4, \epsilon). \tag{E.4}$$

This a vector collinear to the intersection of the solid plane wall, and a vertical slice at the angle φ from the x axis.

The velocity of the points in the contact line can be calculated by the derivative with respect to time of Eq. (E.1); using Eqs. (3.57), (E.2), and (E.4), this is,

$$\begin{aligned}\boldsymbol{v}_{\rm cl} =&\Big(\frac{1}{2}\big[q\cos\varphi\{2-\beta^2\cos^2\varphi\}\dot\epsilon - \dot q\{(\alpha^2\beta^2-2)\cos\varphi + 2\alpha(\beta^2-1)+\beta^2\cos^3\varphi\\ &+\qquad \epsilon\cos\varphi(\beta^2\cos^2\varphi-2)\}\big],\\ &-\frac{1}{2}\sin\varphi[\dot q\{\alpha^2\beta^2+\beta^2\cos^2\varphi+\epsilon\left(\beta^2\cos^2\varphi-2\right)-2\}+q\left(\beta^2\cos^2\varphi-2\right)\dot\epsilon],\\ &\beta\left[\dot q(\alpha+\epsilon\cos\varphi+\cos\varphi)+q\cos\varphi\dot\epsilon\right]\Big)+\boldsymbol{O}(\beta^3)\end{aligned} \tag{E.5}$$

To calculate the projection of the velocity in the perpendicular direction to the contact line, the vector $\hat{\boldsymbol{b}}\equiv\hat{\boldsymbol{t}}\times\hat{\boldsymbol{n}}$ is defined, where $\hat{\boldsymbol{t}}=\partial_\varphi\boldsymbol{r}_{\rm cl}/|\partial_\varphi\boldsymbol{r}_{\rm cl}|$. For the sake of simplicity, $\hat{\boldsymbol{b}}=\hat{\boldsymbol{r}}_{\rm cl}$ is used, which is a valid approximation for small values of β and ϵ. Then, the projected velocity reads,

$$v_{\rm cl}\approx\boldsymbol{v}_{\rm cl}\cdot\hat{\boldsymbol{r}}_{\rm cl}=q\dot\epsilon-\frac{\dot q}{4}\left[2\alpha^2\beta^2+\alpha\left(\beta^2(1+\cos(2\varphi))-4\right)\cos\varphi-4(1+\epsilon)\right]+O(\beta^3). \tag{E.6}$$

Now, all the ingredients are gathered to compute the circuit integral. The infinitesimal length $\mathrm{d}l$ becomes $r_{\rm cl}\mathrm{d}\varphi$, and the integration is performed over the interval $[0,\,2\pi]$. The integral in (3.137) can be evaluated in series form,

$$\begin{aligned}\oint_{\rm cl} v_{\rm cl}^2\,\mathrm{d}l\approx\int_0^{2\pi}v_{\rm cl}^2\,r_{\rm cl}\,\mathrm{d}\varphi=&\pi\,q\,(1+\epsilon)\Big[\left\{\alpha^2+2(1+\epsilon)^2\right\}\dot q^2+4\,q\,(1+\epsilon)\,\dot\epsilon\,\dot q+2\,q^2\,\dot\epsilon^2\Big]\\ &-\frac{\pi}{4}\alpha^2\beta^2q\Big[\left\{2\alpha^2+3(1+\epsilon)(5+4\epsilon)\right\}\dot q^2\\ &+16\,q\,(1+\epsilon)\,\dot\epsilon\,\dot q+4q^2\,\dot\epsilon^2\Big]\quad+O(\beta^4)\end{aligned} \tag{E.7}$$

Keeping terms up to linear order in β and ϵ, Eq. (3.138) is finally obtained.

Appendix F

List of publications

Peer-reviewed publications:

- Ruiz-Gutiérrez, É., Semprebon, C., McHale, G., & Ledesma-Aguilar, R. (2018). *Statics and dynamics of liquid barrels in wedge geometries.* Journal of Fluid Mechanics, 842, 26-57.

- Ruiz-Gutiérrez, É., Guan, J. H., Xu, B., McHale, G., Wells, G. G., & Ledesma-Aguilar, R. (2017). *Energy invariance in capillary systems.* Physical review letters, 118(21), 218003.

- Guan, J. H., Ruiz-Gutiérrez, É., Xu, B. B., Wood, D., McHale, G., Ledesma-Aguilar, R., & Wells, G. G. (2017). *Drop transport and positioning on lubricant-impregnated surfaces.* Soft matter, 13(18), 3404-3410.

- Wells, G. G., Ruiz-Gutiérrez, É., Le Lirzin, Y., Nourry, A., Orme, B. V., Pradas, M., & Ledesma-Aguilar, R. (2018). *Snap evaporation of droplets on smooth topographies.* Nature communications, 9(1), 1380.

For future submission:

- Ruiz-Gutiérrez, É., and Ledesma-Aguilar, R. *Liquid barrels in wedges: a diffuse-interface approach.*

Bibliography

[1] T. M. Squires and S. R. Quake. Microfluidics: Fluid physics at the nanoliter scale. *Rev. Mod. Phys.*, 77:977–1026, Oct 2005.

[2] D. Quéré. Rough ideas on wetting. *Physica A: Statistical Mechanics and its Applications*, 313(1–2):32–46, 2002. Fundamental Problems in Statistical Physics.

[3] P.-G. de Gennes, F. Brochard-Wyart, and D. Quéré. *Capillarity and wetting phenomena: drops, bubbles, pearls, waves*. Springer Science & Business Media, 2013.

[4] J. S. Rowlinson and B. Widom. *Molecular theory of capillarity*. Courier Corporation, 2013.

[5] J. D. Van Der Waals and J. S. Rowlinson. *On the continuity of the gaseous and liquid states*. Courier Corporation, 2004.

[6] A. J. C. Ladd and R. Verberg. Lattice-boltzmann simulations of particle-fluid suspensions. *Journal of Statistical Physics*, 104(5-6):1191–1251, 2001.

[7] T. Lee and C.-L. Lin. A stable discretization of the lattice Boltzmann equation for simulation of incompressible two-phase flows at high density ratio. *Journal of Computational Physics*, 206(1):16–47, 2005.

[8] I. Ginzburg. Equilibrium-type and link-type lattice Boltzmann models for generic advection and anisotropic-dispersion equation. *Advances in Water Resources*, 28(11):1171–1195, 2005.

[9] F. Magaletti, F. Picano, M. Chinappi, L. Marino, and C. M. Casciola. The sharp-interface limit of the Cahn–Hilliard/Navier–Stokes model for binary fluids. *Journal of Fluid Mechanics*, 714:95–126, 2013.

[10] M. R. Swift, E. Orlandini, W. R. Osborn, and J. M. Yeomans. Lattice Boltzmann simulations of liquid-gas and binary fluid systems. *Physical Review E*, 54(5):5041, 1996.

[11] H. B Callen. *Thermodynamics and an Introduction to Thermostatistics*. John wiley & sons, 2006.

[12] R. K. Pathria and P. D. Beale. *Statistical Mechanics*. Butterworth, Heinemann, Elsevier, 3 edition, 2009.

[13] D. A. McQuarrie. *Statistical Mechanics*. University Science Books, 2000.

[14] L. E Reichl. *A modern course in statistical physics; 4th ed.* Wiley-VCH, Weinheim, 2016.

[15] A. J. M. Yang, P. D. Fleming, and J. H. Gibbs. Molecular theory of surface tension. *The Journal of Chemical Physics*, 64(9):3732–3747, 1976.

[16] A. J. Bray. Theory of phase-ordering kinetics. *Advances in Physics*, 43(3):357–459, 1994.

[17] L. M. Pismen. Mesoscopic hydrodynamics of contact line motion. *Colloids and Surfaces A: Physicochemical and Engineering Aspects*, 206(1–3):11–30, 2002.

[18] P. G. de Gennes. Wetting: statics and dynamics. *Rev. Mod. Phys.*, 57:827–863, Jul 1985.

[19] R. Evans. The nature of the liquid-vapour interface and other topics in the statistical mechanics of non-uniform, classical fluids. *Advances in Physics*, 28(2):143–200, 1979.

[20] J. W. Cahn and J. E. Hilliard. Free energy of a nonuniform system. I. Interfacial free energy. *The Journal of chemical physics*, 28(2):258–267, 1958.

[21] L. D. Landau and E. M. Lifshitz. *Statistical Physics, Part 1*, volume 5 of *Course of Theoretical Physics*. Butterworth-Heinemann, Oxford, 1980.

[22] M. J. P. Nijmeijer, A. F. Bakker, C. Bruin, and J. H. Sikkenk. A molecular dynamics simulation of the lennard-jones liquid–vapor interface. *The Journal of Chemical Physics*, 89(6):3789–3792, 1988.

[23] B. V. Derjaguin and N. V. Churaev. On the question of determining the concept of disjoining pressure and its role in the equilibrium and flow of thin films. *Journal of Colloid and Interface Science*, 66(3):389 – 398, 1978.

[24] M. Röger and Y. Tonegawa. Convergence of phase-field approximations to the gibbs–thomson law. *Calculus of Variations and Partial Differential Equations*, 32(1):111–136, May 2008.

[25] J. W. Cahn. Critical point wetting. *The Journal of Chemical Physics*, 66(8):3667–3672, 1977.

[26] A. J. Briant, A. J. Wagner, and J. M. Yeomans. Lattice Boltzmann simulations of contact line motion. I. Liquid-gas systems. *Phys. Rev. E*, 69:031602, Mar 2004.

[27] L. D. Landau and E. M. Lifshitz. *Fluid Mechanics*, volume 6 of *Course of Theoretical Physics*. Elsevier, 2013.

[28] C. Pozrikidis. *Boundary integral and singularity methods for linearized viscous flow*. Cambridge University Press, 1992.

[29] G. K. Batchelor. *An Introduction to Fluid Dynamics*. Cambridge Mathematical Library. Cambridge University Press, 2000.

[30] E. M. Purcell. Life at low reynolds number. volume 1, pages 47–67. World Scientific, 2014.

[31] P. G. de Gennes, X. Hua, and P. Levinson. Dynamics of wetting: local contact angles, 1990.

[32] V. E. B. Dussan and S. H. Davis. On the motion of a fluid-fluid interface along a solid surface. *Journal of Fluid Mechanics*, 65(01):71–95, 1974.

[33] T. D. Blake and J. M. Haynes. Kinetics of liquid-liquid displacement. *Journal of colloid and interface science*, 30(3):421–423, 1969.

[34] R. G. Cox. The dynamics of the spreading of liquids on a solid surface. part 1. viscous flow. *Journal of Fluid Mechanics*, 168:169–194, 1986.

[35] O. V. Voinov. Hydrodynamics of wetting. *Fluid Dynamics*, 11(5):714–721, 1976.

[36] J. H. Snoeijer. Free-surface flows with large slopes: Beyond lubrication theory. *Physics of Fluids*, 18(2):021701, 2006.

[37] L. Bocquet and J.-L. Barrat. Hydrodynamic boundary conditions, correlation functions, and kubo relations for confined fluids. *Phys. Rev. E*, 49:3079–3092, Apr 1994.

[38] J. H. Snoeijer and B. Andreotti. Moving Contact Lines: Scales, Regimes, and Dynamical Transitions. *ANNUAL REVIEW OF FLUID MECHANICS*, 45:269–292, 2013.

[39] A. J. Briant and J. M. Yeomans. Lattice Boltzmann simulations of contact line motion. II. Binary fluids. *Phys. Rev. E*, 69:031603, Mar 2004.

[40] P. Yue, C. Zhou, and J. J. Feng. Sharp-interface limit of the Cahn–Hilliard model for moving contact lines. *J. Fluid Mech.*, 645:279–294, 2010.

[41] P. Seppecher. Moving contact lines in the Cahn-Hilliard theory. *International Journal of Engineering Science*, 34(9):977–992, 1996.

[42] D. Jacqmin. Contact-line dynamics of a diffuse fluid interface. *Journal of Fluid Mechanics*, 402:57–88, 2000.

[43] P. Yue and J. J. Feng. Wall energy relaxation in the Cahn–Hilliard model for moving contact lines. *Physics of Fluids*, 23(1):012106, 2011.

[44] T. Qian, X. P. Wang, and P. Sheng. A variational approach to moving contact line hydrodynamics. *J. Fluid Mech.*, 564:333–360, 2006.

[45] H. Kusumaatmaja, E. J. Hemingway, and S. M. Fielding. Moving contact line dynamics: from diffuse to sharp interfaces. *Journal of Fluid Mechanics*, 788:209–227, 12 2015.

[46] W. B. Hardy. III. The spreading of fluids on glass. *The London, Edinburgh, and Dublin Philosophical Magazine and Journal of Science*, 38(223):49–55, 1919.

[47] C. Wu, T. Qian, and P. Sheng. Droplet spreading driven by van der Waals force: a molecular dynamics study. *Journal of Physics: Condensed Matter*, 22(32):325101, 2010.

[48] M. J. de Ruijter, J. De Coninck, and G. Oshanin. Droplet spreading: Partial wetting regime revisited. *Langmuir*, 15(6):2209–2216, 1999.

[49] M. J. de Ruijter, T. D. Blake, and J. De Coninck. Dynamic wetting studied by molecular modeling simulations of droplet spreading. *Langmuir*, 15(22):7836–7847, 1999.

[50] J. De Coninck, M. J. de Ruijter, and M. Voué. Dynamics of wetting. *Current Opinion in Colloid and Interface Science*, 6(1):49–53, 2001.

[51] S. Succi. *The lattice Boltzmann equation: for fluid dynamics and beyond*. Oxford university press, 2001.

[52] R. L. Liboff. *Kinetic theory*. Springer, 1983.

[53] S. Chapman and T. G. Cowling. *The mathematical theory of non-uniform gases: an account of the Kinetic Theory of viscosity, thermal conduction and diffusion in gases*. Cambridge university press, 1970.

[54] A. Satoh. *Introduction to practice of molecular simulation: molecular dynamics, Monte Carlo, Brownian dynamics, Lattice Boltzmann and dissipative particle dynamics*. Elsevier, 2010.

[55] X. He and L. S. Luo. A priori derivation of the lattice Boltzmann equation. *Phys. Rev. E*, 55:R6333–R6336, Jun 1997.

[56] X. He, S. Chen, and R. Zhang. A lattice boltzmann scheme for incompressible multiphase flow and its application in simulation of rayleigh–taylor instability. *Journal of Computational Physics*, 152(2):642–663, 1999.

[57] A. J. C. Ladd. Numerical simulations of particulate suspensions via a discretized Boltzmann equation. Part 1. Theoretical foundation. *Journal of Fluid Mechanics*, 271:285–309, 7 1994.

[58] X. He, X. Shan, and G. D. Doolen. Discrete Boltzmann equation model for nonideal gases. *Physical Review E*, 57(1):R13, 1998.

[59] P. L. Bhatnagar, E. P Gross, and M. Krook. A model for collision processes in gases. I. Small amplitude processes in charged and neutral one-component systems. *Physical review*, 94(3):511, 1954.

[60] T. Lee and L. Liu. Lattice Boltzmann simulations of micron-scale drop impact on dry surfaces. *Journal of Computational Physics*, 229(20):8045–8063, 2010.

[61] J. C. Desplat, I. Pagonabarraga, and P. Bladon. LUDWIG: A parallel Lattice-Boltzmann code for complex fluids. *Computer Physics Communications*, 134(3):273–290, 2001.

[62] T. Krüger, H. Kusumaatmaja, A. Kuzmin, O. Shardt, G. Silva, and E. M. Viggen. *The Lattice Boltzmann Method: Principles and Practice*. Springer, 2016.

[63] T. Inamuro, N. Konishi, and F. Ogino. A Galilean invariant model of the lattice Boltzmann method for multiphase fluid flows using free-energy approach. *Computer Physics Communications*, 129(1):32–45, 2000.

[64] D. J. Holdych, D. Rovas, J. G. Georgiadis, and R. O. Buckius. An Improved Hydrodynamics Formulation for Multiphase Flow Lattice-Boltzmann Models. *International Journal of Modern Physics C*, 09(08):1393–1404, 1998.

[65] C. M. Pooley and K. Furtado. Eliminating spurious velocities in the free-energy lattice Boltzmann method. *Phys. Rev. E*, 77:046702, Apr 2008.

[66] I. Ginzburg. Generic boundary conditions for lattice Boltzmann models and their application to advection and anisotropic dispersion equations. *Advances in Water Resources*, 28(11):1196–1216, 2005.

[67] M. Bouzidi, M. Firdaouss, and P. Lallemand. Momentum transfer of a Boltzmann-lattice fluid with boundaries. *Physics of Fluids*, 13(11):3452–3459, 2001.

[68] M. Hecht and J. Harting. Implementation of on-site velocity boundary conditions for D3Q19 lattice Boltzmann. *Journal of Statistical Mechanics: Theory and Experiment*, 13, 2010.

[69] I. Ginzburg, F. Verhaeghe, and D. d'Humieres. Two-relaxation-time lattice Boltzmann scheme: About parametrization, velocity, pressure and mixed boundary conditions. *Communications in computational physics*, 3(2):427–478, 2008.

[70] D. Yu, R. Mei, L.-S. Luo, and W. S. Viscous flow computations with the method of lattice Boltzmann equation. *Progress in Aerospace Sciences*, 39(5):329–367, 2003.

[71] B.J. Noye and R.J. Arnold. Accurate finite difference approximations for the Neumann condition on a curved boundary. *Applied Mathematical Modelling*, 14(1):2–13, 1990.

[72] P. K. Kundu and I. M. Cohen. Fluid mechanics. *Academic, Calif*, 1990.

[73] L. E. Fraenkel. Laminar Flow in Symmetrical Channels with Slightly Curved Walls. I. On the Jeffery-Hamel Solutions for Flow Between Plane Walls. *Proceedings of the Royal Society of London A: Mathematical, Physical and Engineering Sciences*, 267(1328):119–138, 1962.

[74] L. Rosenhead. The steady two-dimensional radial flow of viscous fluid between two inclined plane walls. *Proceedings of the Royal Society of London A: Mathematical, Physical and Engineering Sciences*, 175(963):436–467, 1940.

[75] A. M. Cazabat and G. Guéna. Evaporation of macroscopic sessile droplets. *Soft Matter*, 6:2591–2612, 2010.

[76] M. Prakash, D. Quéré, and J. W. M. Bush. Surface tension transport of prey by feeding shorebirds: The capillary ratchet. *Science*, 320(5878):931–934, 2008.

[77] Q. Wang, X. Yao, H. Liu, D. Quéré, and L. Jiang. Self-removal of condensed water on the legs of water striders. *Proceedings of the National Academy of Sciences*, 112(30):9247–9252, 2015.

[78] L. Bocquet, É. Charlaix, and F. Restagno. Physics of humid granular media. *Comptes Rendus Physique*, 3(2):207–215, 2002.

[79] Z. Grof, C. J. Lawrence, and F. Štěpánek. The strength of liquid bridges in random granular materials. *Journal of Colloid and Interface Science*, 319(1):182–192, 2008.

[80] T. P. Farmer and J. C. Bird. Asymmetric capillary bridges between contacting spheres. *Journal of Colloid and Interface Science*, 454:192 – 199, 2015.

[81] P. Renvoisé, J. W. M. Bush, M. Prakash, and D. Quéré. Drop propulsion in tapered tubes. *EPL (Europhysics Letters)*, 86(6):64003, 2009.

[82] E. Reyssat. Drops and bubbles in wedges. *Journal of Fluid Mechanics*, 748:641–662, 6 2014.

[83] R. Dangla, S. C. Kayi, and C. N. Baroud. Droplet microfluidics driven by gradients of confinement. *Proceedings of the National Academy of Sciences*, 110(3):853–858, 2013.

[84] M. Ataei, T. Tang, and A. Amirfazli. Motion of a liquid bridge between nonparallel surfaces. *Journal of Colloid and Interface Science*, 492:218 – 228, 2017.

[85] J. Lv, Y. Liu, J. Wei, E. Chen, L. Qin, and Y. Yu. Photocontrol of fluid slugs in liquid crystal polymer microactuators. *Nature*, 537(7619):179–184, Sep 2016. Article.

[86] C. Luo and X. Heng. Separation of oil from a water/oil mixed drop using two nonparallel plates. *Langmuir*, 30(33):10002–10010, 2014.

[87] F. Hauksbee. An Account of an Experiment Touching the Direction of a Drop of Oil of Oranges, between Two Glass Planes, towards Any Side of Them That is Nearest Press'd Together. By Mr. Fr. Hauksbee, F. R. S. *Philosophical Transactions*, 27(325-336):395–396, 1710.

[88] P. Concus and R. Finn. On the behavior of a capillary surface in a wedge. *Proceedings of the National Academy of Sciences of the United States of America*, 63(2):292, 1969.

[89] P. Concus, R. Finn, and J. McCuan. Liquid bridges, edge blobs, and Scherk-type capillary surfaces. *Indiana University mathematics journal*, 50(1):411–441, 2001.

[90] P. Concus and R. Finn. Discontinuous behavior of liquids between parallel and tilted plates. *Physics of Fluids*, 10(1):39–43, 1998.

[91] M. Brinkmann and R. Blossey. Blobs, channels and "cigars": Morphologies of liquids at a step. *The European Physical Journal E*, 14(1):79–89, 2004.

[92] F. P. Bretherton. The motion of long bubbles in tubes. *Journal of Fluid Mechanics*, 10(2):166–188, 1961.

[93] C. W. Park, S. Gorell, and G. M. Homsy. Two-phase displacement in Hele-Shaw cells: Experiments on viscously driven instabilities. *Journal of Fluid Mechanics*, 141:257–287, 1984.

[94] D. Baratian, A. Cavalli, D. van den Ende, and F. Mugele. On the shape of a droplet in a wedge: new insight from electrowetting. *Soft Matter*, 11:7717–7721, 2015.

[95] É. Ruiz-Gutiérrez, J. H. Guan, B. Xu, G. McHale, G. G. Wells, and R. Ledesma-Aguilar. Energy invariance in capillary systems. *Phys. Rev. Lett.*, 118:218003, May 2017.

[96] C. A. Miller and L. E. Scriven. The oscillations of a fluid droplet immersed in another fluid. *Journal of Fluid Mechanics*, 32:417–435, 5 1968.

[97] O.-Y. Zhong-Can and W. Helfrich. Instability and deformation of a spherical vesicle by pressure. *Phys. Rev. Lett.*, 59:2486–2488, Nov 1987.

[98] P. Moon and D. E. Spencer. *Field theory handbook: including coordinate systems, differential equations and their solutions*. Springer, 2012.

[99] H. Kusumaatmaja and R. Lipowsky. Equilibrium morphologies and effective spring constants of capillary bridges. *Langmuir*, 26(24):18734–18741, 2010.

[100] M. Andrews. Alternative separation of Laplace's equation in toroidal coordinates and its application to electrostatics. *Journal of Electrostatics*, 64(10):664–672, 2006.

[101] K. A. Brakke. The Surface Evolver. *Experimental Mathematics*, 1(2):141–165, 1992.

[102] H. Goldstein, C. P. Poole, and J. L. Safko. *Classical mechanics*. Addison Wesley, 3 edition, 2001.

[103] D. Bonn, J. Eggers, J. Indekeu, J. Meunier, and E. Rolley. Wetting and spreading. *Rev. Mod. Phys.*, 81:739–805, May 2009.

[104] G.B. Jeffery. The two-dimensional steady motion of a viscous fluid. *Philosophical Magazine Series 6*, 29(172):455–465, 1915.

[105] Georg Hamel. Spiralförmige bewegungen zäher flüssigkeiten. *Jahresbericht der Deutschen Mathematiker-Vereinigung*, 25:34–60, 1917.

[106] O. Sano and H. Hasimoto. The effect of two plane walls on the motion of a small sphere in a viscous fluid. *Journal of Fluid Mechanics*, 87:673–694, August 1978.

[107] B Levich and L Landau. Dragging of liquid by a plate. *Acta Physiochim*, 17:42–54, 1942.

[108] A. Oron, S. H. Davis, and S. G. Bankoff. Long-scale evolution of thin liquid films. *Rev. Mod. Phys.*, 69:931–980, Jul 1997.

[109] S. R. Ranabothu, C. Karnezis, and L. L. Dai. Dynamic wetting: Hydrodynamic or Molecular-Kinetic? *Journal of Colloid and Interface Science*, 288(1):213–221, 2005.

[110] L. Bocquet and J.-L. Barrat. Flow boundary conditions from nano- to micro-scales. *Soft Matter*, 3:685–693, 2007.

[111] L. Bocquet and E. Charlaix. Nanofluidics, from bulk to interfaces. *Chemical Society Reviews*, 39(3):1073–1095, 2010.

[112] H. Bruus. *Theoretical microfluidics. Oxford master series in condensed matter physics*. Oxford University Press Oxford, 2008.

[113] Š. Šikalo, C. Tropea, and E.N. Ganić. Dynamic wetting angle of a spreading droplet. *Experimental Thermal and Fluid Science*, 29(7):795–802, 2005. Two Phase FlowThird International Symposium on Two Phase Flow Modelling and Experimentation.

[114] S. P. Thampi, I. Pagonabarraga, R. Adhikari, and R. Govindarajan. Universal evolution of a viscous–capillary spreading drop. *Soft Matter*, 12(28):6073–6078, 2016.

[115] S. O. Unverdi and G. Tryggvason. A front-tracking method for viscous, incompressible, multi-fluid flows. *Journal of Computational Physics*, 100(1):25 – 37, 1992.

[116] C. M. Pooley, H. Kusumaatmaja, and J. M. Yeomans. Contact line dynamics in binary lattice Boltzmann simulations. *Phys. Rev. E*, 78:056709, Nov 2008.

[117] T.-S. Wong, S. H. Kang, S. K. Y. Tang, E. J. Smythe, B. D. Hatton, A. Grinthal, and J. Aizenberg. Bioinspired self-repairing slippery surfaces with pressure-stable omniphobicity. *Nature*, 477(7365):443–447, Sep 2011.

[118] J. D. Smith, R. Dhiman, S. Anand, E. Reza-Garduno, R. E. Cohen, G. H. McKinley, and K. K. Varanasi. Droplet mobility on lubricant-impregnated surfaces. *Soft Matter*, 9:1772–1780, 2013.

[119] J. H. Guan, G. G. Wells, B. Xu, G. McHale, D. Wood, J. Martin, and S. Stuart-Cole. Evaporation of sessile droplets on Slippery Liquid-Infused Porous Surfaces (SLIPS). *Langmuir*, 31(43):11781–11789, 2015. PMID: 26446177.

[120] A. Marmur. From hygrophilic to superhygrophobic: Theoretical conditions for making high-contact-angle surfaces from low-contact-angle materials. *Langmuir*, 24(14):7573–7579, 2008.

[121] F. Schellenberger, J. Xie, N. Encinas, A. Hardy, M. Klapper, P. Papadopoulos, H.-J. Butt, and D. Vollmer. Direct observation of drops on Slippery Lubricant-Infused Surfaces. *Soft Matter*, 11:7617–7626, 2015.

[122] G. B. Arfken, H. J. Weber, and F. E. Harris. *Mathematical methods for Physicists, A Comprehensive guide, Seventh Edison*. Elsevier, London, 2013.

[123] H. Y. Erbil. Evaporation of pure liquid sessile and spherical suspended drops: A review. *Advances in Colloid and Interface Science*, 170(1–2):67–86, 2012.

[124] A. Perl, D. N. Reinhoudt, and J. Huskens. Microcontact printing: Limitations and achievements. *Advanced Materials*, 21(22):2257–2268, 2009.

[125] D. Kawamura, T. Takeishi, K. Sho, K. Matsunaga, N. Shibata, K. Ozawa, S. Shimura, H. Kyoda, T. Kawasaki, S. Ishida, T. Toshima, Y. Oonishi, and S. Ito. Influence of the watermark in immersion lithography process, 2005.

[126] K.H. Lee, S.M. Kim, H. Jeong, and G.Y. Jung. Spontaneous nanoscale polymer solution patterning using solvent evaporation driven double-dewetting edge lithography. *Soft Matter*, 8:465–471, 2012.

[127] D. Losic, J. G. Shapter, and J. J. Gooding. Influence of surface topography on alkanethiol sams assembled from solution and by microcontact printing. *Langmuir*, 17(11):3307–3316, 2001.

[128] C.Y. Chang, D. C. Yu, J. C. H. Lin, and B. J. Lin. Watermark defect formation and removal for immersion lithography, 2006.

[129] B. White, A. Sarkar, and A.-M. Kietzig. Fog-harvesting inspired by the stenocara beetle-an analysis of drop collection and removal from biomimetic samples with wetting contrast. *Applied Surface Science*, 284:826–836, 2013.

[130] X. Heng and C. Luo. Bioinspired plate-based fog collectors. *ACS Applied Materials & Interfaces*, 6(18):16257–16266, 2014. PMID: 25192549.

[131] C. R. Tracy, N. Laurence, and K. A. Christian. Condensation onto the skin as a means for water gain by tree frogs in tropical australia. *The American Naturalist*, 178(4):553–558, 2011.

[132] T. Nørgaard and M. Dacke. Fog-basking behaviour and water collection efficiency in namib desert darkling beetles. *Frontiers in Zoology*, 7(1):23, 2010.

[133] M. Ebner, T. Miranda, and A. Roth-Nebelsick. Efficient fog harvesting by stipagrostis sabulicola (namib dune bushman grass). *Journal of Arid Environments*, 75(6):524–531, 2011.

[134] Anna Lee, Myoung-Woon Moon, Hyuneui Lim, Wan-Doo Kim, and Ho-Young Kim. Water harvest via dewing. *Langmuir*, 28(27):10183–10191, 2012. PMID: 22731870.

[135] R.G. Picknett and R. Bexon. The evaporation of sessile or pendant drops in still air. *Journal of Colloid and Interface Science*, 61(2):336 – 350, 1977.

[136] H. Hu and R. G. Larson. Evaporation of a sessile droplet on a substrate. *The Journal of Physical Chemistry B*, 106(6):1334–1344, 2002.

[137] H. B. Eral, D. J. C. M. 't Mannetje, and J. M. Oh. Contact angle hysteresis: a review of fundamentals and applications. *Colloid and Polymer Science*, 291(2):247–260, 2013.

[138] Stauber, J. M. and Wilson, S. K. and Duffy, B. R. and Sefiane, K. On the lifetimes of evaporating droplets. *Journal of Fluid Mechanics*, 744, 2014.

[139] D. Debuisson, A. Merlen, V. Senez, and S. Arscott. Stick-Jump (SJ) Evaporation of Strongly Pinned Nanoliter Volume Sessile Water Droplets on Quick Drying, Micropatterned Surfaces. *Langmuir*, 32(11):2679–2686, 2016.

[140] E. Dietrich, E. S. Kooij, X. Zhang, H. J. W. Zandvliet, and D. Lohse. Stick-Jump Mode in Surface Droplet Dissolution. *Langmuir*, 31(16):4696–4703, 2015. PMID: 25835057.

[141] B. Braden. The surveyor's area formula. *The College Mathematics Journal*, 17(4):326–337, 1986.

[142] S. H. Strogatz. *Nonlinear dynamics and chaos: with applications to Physics, Biology, Chemistry, and Engineering*. Westview Press, 2014.

[143] G. Teschl. *Ordinary differential equations and dynamical systems*, volume 140. American Mathematical Society Providence, 2012.

[144] M. Nakahara. *Geometry, topology and physics*. CRC Press, 2003.

[145] P. L. Boyland. Bifurcations of circle maps: Arnol'd tongues, bistability and rotation intervals. *Comm. Math. Phys.*, 106(3):353–381, 1986.

[146] L. Glass, M. R. Guevara, A. Shrier, and R. Perez. Bifurcation and chaos in a periodically stimulated cardiac oscillator. *Physica D: Nonlinear Phenomena*, 7(1):89 – 101, 1983.

[147] J. H. Guan, E. Ruiz-Gutierrez, B. B. Xu, D. Wood, G. McHale, R. Ledesma-Aguilar, and G. G. Wells. Drop transport and positioning on lubricant-impregnated surfaces. *Soft Matter*, 13:3404–3410, 2017.

[148] James E. Sprittles. Air entrainment in dynamic wetting: Knudsen effects and the influence of ambient air pressure. *Journal of Fluid Mechanics*, 769:444–481, 2015.